中国科学技术大学

博士学位论文

RHIC 重离子碰撞中质子数涨落的研究

作者姓名：　司凡
学科专业：　粒子物理与原子核物理
导师姓名：　张一飞 教授　许怒 教授　江角晋一 教授
完成时间：　二〇二四年十月三十日

University of Science and Technology of China
A dissertation for doctor's degree

Study of Proton Number Fluctuations in Heavy-Ion Collisions at RHIC

Author: Fan Si

Speciality: Particle Physics and Nuclear Physics

Supervisors: Prof. Yifei Zhang, Prof. Nu Xu, Prof. ShinIchi Esumi

Finished time: October 30, 2024

中国科学技术大学学位论文原创性声明

本人声明所呈交的学位论文，是本人在导师指导下进行研究工作所取得的成果。除已特别加以标注和致谢的地方外，论文中不包含任何他人已经发表或撰写过的研究成果。与我一同工作的同志对本研究所做的贡献均已在论文中作了明确的说明。

作者签名：司凡　　　　签字日期：2024.10.30

中国科学技术大学学位论文授权使用声明

作为申请学位的条件之一，学位论文著作权拥有者授权中国科学技术大学拥有学位论文的部分使用权，即：学校有权按有关规定向国家有关部门或机构送交论文的复印件和电子版，允许论文被查阅和借阅，可以将学位论文编入《中国学位论文全文数据库》等有关数据库进行检索，可以采用影印、缩印或扫描等复制手段保存、汇编学位论文。本人提交的电子文档的内容和纸质论文的内容相一致。

控阅的学位论文在解密后也遵守此规定。

☑公开　□控阅（____年）

作者签名：司凡　　　　导师签名：张飞

签字日期：2024.10.30　　　　签字日期：2024.10.30

摘 要

理解由量子色动力学（QCD）主导的强相互作用物质的相结构是高能核物理领域中的基本科学目标之一。QCD 相图总结了基于温度（T）和重子化学势（μ_B，系统增加一个重子所需的能量）的强相互作用物质相的区域，包括：强子相，其中夸克和胶子被限制在强子内；夸克-胶子等离子体（QGP）相，其中夸克和胶子在极高的温度和重子密度下解禁闭。QGP 被认为曾存在于宇宙大爆炸后的早期宇宙，因此实验学家进行相对论重离子碰撞，通过创造极端条件以重新产生 QGP，并通过改变碰撞能量（以下涉及的能量均为质心能量 $\sqrt{s_{\mathrm{NN}}}$）来探索相图中的不同区域。

强子相与 QGP 相之间相变的性质是 QCD 相结构的重要研究内容。格点 QCD 的计算预期在小 μ_B 处的相变表现为平滑过渡，而基于 QCD 的模型则表明在较大 μ_B 处其为一阶相变。因此，在这两种相变之间可假设存在一个 QCD 临界点。理论预言表明，当系统接近临界点时，发散的关联长度会显著增强守恒荷（如净重子数、净电荷数和净奇异数等）的涨落，并使得这些涨落在重离子碰撞实验中表现为逐事件净质子数（净重子数的替代）高阶累积矩（C_r）的非单调行为。此外，理论预测超高阶累积矩在平滑过渡区域应表现为负值。在较宽能量范围内探测这些信号将为 QCD 相结构提供强有力的证据。

相对论重离子对撞机（RHIC）完成了束流能量扫描计划的第一阶段（BES-I），针对 7.7–200 GeV 的金核-金核碰撞。STAR 实验观测到净质子数 C_4/C_2 对碰撞能量的非单调依赖（3.1σ 显著性），这与预期的临界信号定性一致；3 GeV 的 C_4/C_2 返回基线，表明临界区域只可能存在于 3 GeV 以上的重离子碰撞中；从 200 GeV 降至 7.7 GeV，C_6/C_2 表现为绝对值越来越大的负值，这一趋势符合对平滑过渡的预测。然而，这些结果在较低能量的不确定度较大，并且在 3 GeV 和 7.7 GeV 之间存在测量空白。因此，RHIC 进行了统计量更高的第二阶段（BES-II），包括 7.7–27 GeV 的对撞实验和 3–13.7 GeV 的固定靶实验。

本论文分析了从 BES-II 对撞实验的 7.7 GeV 和 11.5 GeV 的金核-金核碰撞中收集的数据，利用约 15 倍于 BES-I 的事件数，详细研究了 RHIC 重离子碰撞中的质子（包括反质子和净质子）数涨落。STAR 探测器系统包括时间投影室（TPC）和飞行时间探测器（TOF），并且 BES-II 的内 TPC（iTPC）升级提供了更高的测量准确性和效率以及更大的接受度。分析涉及几个关键步骤：数据选择和质量保证、中心性确定、对有限中心度区间宽度和探测效率的修正以及对统计和系统不确定度的评估。相对于 BES-I，我们引入了若干全新的数据分析技术：（1）重新刻度 TPC 对径迹能量损失的测量参数，提高粒子鉴别（PID）的准确性。（2）研

究 TPC 和 TOF 的（反）质子接受度受到事件原初顶点位置和 TPC 径迹拟合点数的影响。（3）详细估计质子和反质子的纯度，要求它们在任意相空间区间中高于 90%。（4）考虑接受度和纯度，定义多种 PID 判选条件，确保探测器在每个事件中完整覆盖测量的相空间，并且质子和反质子始终具有高纯度。（5）得益于 iTPC，使用两种参考带电粒子多重数来确定碰撞中心度等级：一种保持与 BES-I 相同的动力学判选条件，另一种扩大赝快度范围以提供更好的中心度分辨率。（6）计算探测效率时，对 TPC 寻迹效率和 TOF 匹配效率考虑更为精确的四维依赖，包括中心度，原初顶点位置，快度（y）和横动量（p_{T}），并且增加 PID 判选条件的效率，以描述相关的径迹丢失。（7）不同于 BES-I 的相空间平均效率修正法，采用保留效率微分形式的逐径迹效率修正法。（8）对系统误差估计，改变径迹质量筛选条件、PID 筛选条件和效率，通过 Barlow 检查来提取测量结果的系统性变化。

净质子、质子和反质子数的累积矩以及质子和反质子数的阶乘累积矩（κ_r）的结果展示了对碰撞中心度的依赖（至高六阶）以及对快度和横动量的依赖（至高四阶）。测量的默认接受度为 [$0.4\ \mathrm{GeV}/c < p_{\mathrm{T}} < 2.0\ \mathrm{GeV}/c, |y| < 0.5$]；在研究快度依赖时，测量净/反质子和质子的快度范围分别扩展至 $|y| < 0.6$ 和 0.7。更好的中心度分辨率产生更低的累积矩及比值，然而中心事件的 C_4/C_2 显示出微弱的中心度分辨率效应。净质子数 C_4/C_2 的结果与 BES-I 在 $\sim 1\sigma$ 范围内一致，并且其统计和系统误差被显著压低至 BES-I 的 1/5 至 1/3。最终，我们得到了关于能量依赖的重要物理结果，包括 0–5% 和 70–80% 中心度的净质子数累积矩比值以及质子和反质子数阶乘累积矩比值，并将其与几种不含临界点的模型基线相比较，如 HRG CE、Hydro EV 和 UrQMD（0–5%）。相对于多种无临界的参考，包括边缘事件和这些模型，中心事件中的净质子数 C_4/C_2 在约 19.6 GeV 处出现偏差为 2–5σ 的低谷，并且在 7.7–27 GeV 的整体偏离至高可达 5.4σ 的显著性。质子数的 κ_2/κ_1 和 κ_3/κ_1 在约 11.5 GeV 处分别表现为可能的谷值和峰值，并且有迹象表明 κ_4/κ_1 在 17.3 GeV 附近呈现低谷。这些非单调行为无法被无临界的参考重现，表明其中可能蕴含来自临界区域的信号。

这项工作聚焦于 QCD 中相变动力学的实验探索。与 BES-I 相比，本研究利用增大的统计量、升级的探测器和改进的数据分析技术，获得了更好的中心度分辨率、更好的统计精度、更好的系统误差控制和更好的接受度覆盖，观测到了非单调和偏离基线的高阶涨落。这些发现对我们理解 QCD 相结构，尤其是对临界点的寻找，做出了重要贡献，并为相关理论研究和未来实验提供了宝贵的参考。

关键词：重离子碰撞　QCD 相图　QCD 临界点　涨落　累积矩

ABSTRACT

Understanding the phase structure of strongly interacting matter, as governed by Quantum Chromodynamics (QCD), is one of the fundamental scientific objectives in the field of high-energy nuclear physics. The QCD phase diagram summarizes strongly interacting matter regions based on temperature (T) and baryonic chemical potential (μ_B, energy required to add a baryon to the system), including the hadronic phase, where quarks and gluons are limited within hadrons, and the quark-gluon plasma (QGP) phase, where quarks and gluons are deconfined under extremely high temperatures and baryon densities. QGP is believed to have existed in the early universe following the Big Bang, so experimentalists conduct relativistic heavy-ion collisions to recreate QGP by creating extreme conditions and to explore different regions of the phase diagram by varying the collision energy (energies involved below represent center-of-mass energies $\sqrt{s_{\mathrm{NN}}}$).

The nature of the phase transition between the hadronic phase and the QGP phase is an important research topic of the QCD phase structure. Lattice QCD calculations predict a smooth crossover as the phase transition at small μ_B, while QCD-based models suggest a first-order phase transition at larger μ_B. Hence, a conjectured QCD critical point is located between the two types of phase transitions. Theoretical predictions indicate that as the system approaches the critical point, the diverged correlation length can significantly enhance fluctuations of conserved charges, such as net-baryon, net-electric-charge and net-strangeness numbers, and make these fluctuations manifest in heavy-ion collision experiments as a non-monotonic behavior in higher-order cumulants (C_r) of the event-by-event net-proton number (proxy for the net-baryon number). Additionally, theories predict that hyper-order cumulants should exhibit negative values in the crossover region. Detecting such signals across a wide energy range would provide strong evidence for the QCD phase structure.

Relativistic Heavy Ion Collider (RHIC) completed the first phase of the Beam Energy Scan program (BES-I) for Au+Au collisions at 7.7–200 GeV. The STAR experiment observed a non-monotonic $\sqrt{s_{\mathrm{NN}}}$ dependence of the net-proton number C_4/C_2 with a significance of 3.1σ, qualitatively consistent with the expected critical signal; C_4/C_2 at 3 GeV returns to the baseline, suggesting that the critical region can only exist at energies higher than 3 GeV if created in heavy-ion collisions; C_6/C_2 as $\sqrt{s_{\mathrm{NN}}}$ behave to be increasingly negative as energies decrease from 200 GeV to 7.7 GeV, the trend of which aligns with predictions for the crossover. However, these results come with large uncertainties at relatively low energies and have a measurement gap between 3 GeV and 7.7 GeV. Therefore, RHIC conducted the second phase (BES-II) with much higher statistics, including collider experiments at 7.7–27 GeV and fixed-target experiments at 3–13.7 GeV.

This dissertation presents a detailed study of proton (including antiproton and net-proton) number fluctuations in heavy-ion collisions at RHIC, analyzing data collected in Au+Au collisions at 7.7 GeV and 11.5 GeV from BES-II collider experiments with about 15 times more statistics than BES-I. The STAR detector system includes Time Projection Chamber (TPC) and Time-Of-Flight detector (TOF), and the upgrade of the inner TPC (iTPC) for BES-II provides higher accuracy and efficiency of measurements and larger acceptance. The analysis involves several critical steps: data selection and quality assurance, centrality determination, corrections for finite centrality bin width and detection efficiency and statistical and systematic uncertainty estimations. Compared to BES-I, we introduce several new data analysis techniques: (1) The TPC measured parameter of the track energy loss is recalibrated to improve the PID accuracy. (2) Dependences of (anti)proton acceptances from TPC and TOF on the event primary vertex position and the number of TPC track fitting points are studied. (3) Proton and antiproton purities are estimated in details and required to be higher than 90% in each phase space bin. (4) Considering acceptance and purity, multiple PID selection criteria are defined to ensure that detectors fully cover the measured phase space in each event and that proton and antiproton purities are always high. (5) Taking advantage of iTPC, two reference charged-particle multiplicities are utilized to determine the collision centrality class: one keeps the same kinematic cut as BES-I, and the other extends the pseudorapidity window, providing better centrality resolution. (6) As detection efficiency is calculated, more precise four-dimensional dependence of TPC tracking efficiency and TOF matching efficiency are considered, including centrality, primary vertex position, rapidity (y) and transverse momentum (p_{T}), and the PID cut efficiency is introduced to describe related track loss. (7) Different from the bin-by-bin efficiency correction in BES-I, the track-by-track efficiency correction maintaining the differential form of the efficiency is performed. (8) For the systematic uncertainty estimation, the track quality cuts, PID selection criteria and efficiency are varied to extract the systematic variations of the measured quantities through the Barlow check.

Net-proton, proton and antiproton number cumulants, as well as proton and antiproton number factorial cumulants (κ_r), are presented with respect to collision centrality (up to the sixth order), rapidity and p_{T} (up to the fourth order). The default acceptance of the measurement is [0.4 GeV/c < p_{T} < 2.0 GeV/c, $|y| < 0.5$]; the rapidity window is extended to $|y| < 0.6$ and 0.7 for net/anti-proton and proton measurements, respectively, when studying rapidity dependence. Better centrality resolution produces lower cumulants and ratios, but C_4/C_2 in central events shows a weak centrality resolution effect. Net-proton number C_4/C_2 results agree with BES-I within $\sim 1\sigma$, and statistical and systematic errors are significantly suppressed to 1/5 to 1/3 of BES-I. Finally, the importance physical results of the energy dependence are presented, including net-proton number cumulant ratios and proton and antiproton number factorial cumulant ratios from the 0–5% and 70–80% centrality classes, along with several model baselines without a critical point for comparison, such as HRG CE, Hydro EV and UrQMD (0–5%). Relative to various non-critical references, including peripheral events and these models, net-proton number C_4/C_2 in central events shows a dip at ~19.6 GeV with a deviation of 2–5σ, and the overall deviation at 7.7–27 GeV reaches a significance level of up to 5.4σ. Proton number κ_2/κ_1 and κ_3/κ_1 likely exhibit a dip and a peak at ~11.5 GeV, respectively, with a hint that κ_4/κ_1 shows a dip around 17.3 GeV. These non-monotonic behaviors cannot be reproduced by non-critical references, indicating potential signals from the critical region.

This work focuses on experimental exploration of the phase transition dynamics in QCD. Compared to BES-I, utilizing enlarged statistics, upgraded detectors and improved data analysis techniques, this study benefits from better centrality resolution, better statistical precision, better control over systematics and better acceptance coverage, with non-monotonic higher-order fluctuations deviating from baselines observed. The findings contribute significantly to our understanding of the QCD phase structure, especially in the search for the critical point, and provide valuable references for related theoretical studies and future experiments.

Key Words: Heavy-Ion Collision, QCD Phase Diagram, QCD Critial Point, Fluctuation, Cumulant

Contents

List of Figures

List of Tables

Notation

T	temperature
μ_B	baryonic chemical potential
$\sqrt{s_{\mathrm{NN}}}$	center-of-mass energy per nucleon pair in a collision
m	rest mass
p	total momentum
p_{T}	transverse momentum
η	pseudorapidity
y	rapidity
ξ	correlation length
χ_r	rth-order susceptibility
μ	mean
σ	standard deviation
S	skewness
κ	kurtosis
m_r	rth-order moment
μ_r	rth-order central moment
f_r	rth-order factorial moment
C_r	rth-order cumulant
κ_r	rth-order factorial cumulant
$\langle q \rangle$	expectation of stochastic variable q
$\langle q^r \rangle_{\mathrm{f}}$	rth-order factorial moment of stochastic variable q
$\langle q^r \rangle_{\mathrm{c}}$	rth-order cumulant of stochastic variable q
$\langle q^r \rangle_{\mathrm{fc}}$	rth-order factorial cumulant of stochastic variable q

Chapter 1 Introduction

1.1 Standard Model

As is well known, there are four fundamental interactions in the universe: the strong force, the electromagnetic force, the weak force, and the gravity, listed from strongest to weakest. Standard Model (SM) of particle physics, based on the gauge group SU(3)×SU(2)×U(1), is a comprehensive framework that describes the fundamental particles and their interactions, excluding gravity. The strong interaction corresponds to the SU(3) component, while the electroweak interaction is described by SU(2)×U(1).

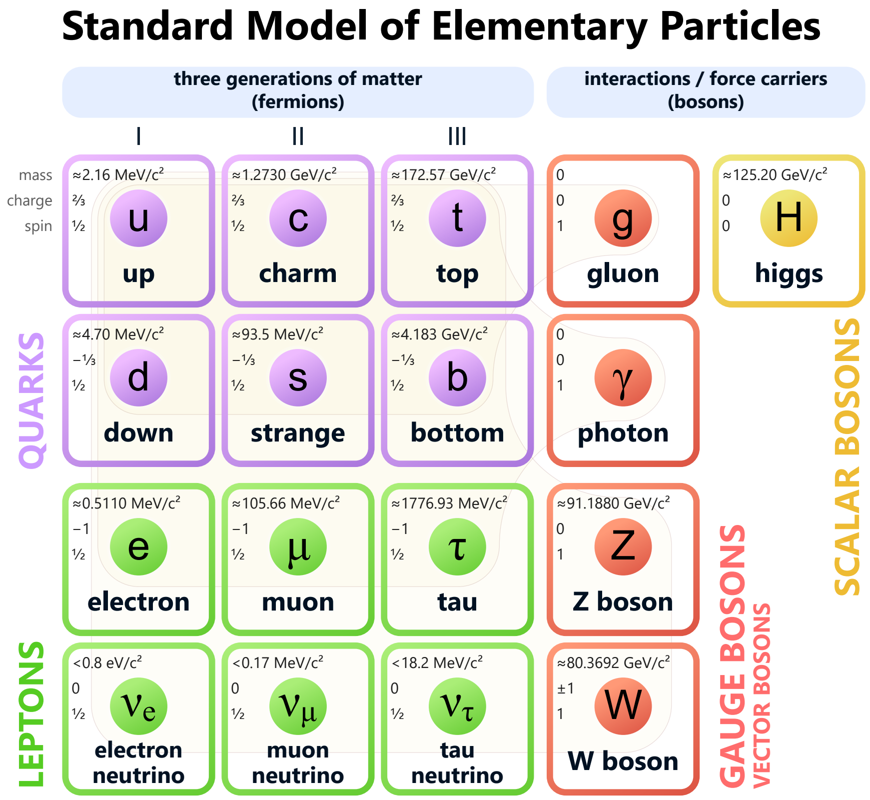

Figure 1.1 (Color online) Standard Model of elementary particles. Mass, charge and spin are labelled for each particle. Figure is taken from Reference [1].

Standard Model classifies all known fundamental particles into two main categories: fermions with half-integer spins and bosons with integer spins, as shown in Figure 1.1 [1]. Fermions are the building blocks of matter and are divided into quarks and leptons, each with three generations. For quarks, there are two flavors in each generation, and the total six flavors are: up (u), down (d), charm (c), strange (s), top (t) and bottom (b). They combine to form hadrons under the strong interaction, which are further classified into baryons, such as protons and neutrons, and mesons, such as pions and kaons. Each baryon is composed of three quarks, while mesons consist of a quark and an antiquark. For leptons, each generation consists of one charged lepton, which is electron (e), muon (μ) or tauon (τ), and one charge-neutral lepton, called neutrino, corresponding to each charged lepton, named by electron neutrino (ν_e), muon neutrino (ν_μ) or tauon neutrino (ν_τ).

Bosons are classified into vector bosons with a spin equal to one and scalar bosons with zero spin. Vector bosons, or gauge bosons, are the force carriers that mediate the fundamental interactions. Gluons (g) mediate the strong force between color-charged particles, which are quarks and gluons; photons (γ) mediate the electromagnetic force between particles carrying electric charges; and $\mathrm{W}^\pm$ and Z bosons mediate the weak force. Scalar bosons represent Higgs bosons, responsible for giving masses to fermions and $\mathrm{W}^\pm$ and Z bosons through the Higgs mechanism.

Developed in the mid-20th century, the Standard Model has successfully predicted and explained a wide range of phenomena in high-energy physics and continues to be the foundation for understanding the behavior of subatomic particles. All fundamental particles predicted by the Standard Model have been discovered experimentally, the last of which is the Higgs boson, observed in 2012 by the ATLAS [2] and CMS [3] experiments at Large Hadron Collider (LHC) at European Organization for Nuclear Research (CERN). However, there are still limitations and open questions within the Standard Model. For instance, it does not include gravity or explain the mechanism behind non-zero neutrino masses.

1.2 Quantum Chromodynamics

Quantum Chromodynamics (QCD) [4-6], developed in the early 1970s, is the fundamental theory describing the strong interaction and explaining how quarks and gluons interact and form hadrons as a key component of Standard Model. QCD is based on the concept of color charge and the SU(3) gauge symmetry group. A quark carries one color charge of the three types: red, green and blue, while each gluon carries a combination of a color charge and an anticolor charge. Gluons couple with color charges with the coupling constant is defined by [7]

$$\alpha_\mathrm{s}(Q^2) = \frac{g_\mathrm{s}^2}{4\pi} \approx \frac{1}{\beta_0 \ln\left(Q^2 \middle/ \Lambda_\mathrm{QCD}^2\right)}, \tag{1.1}$$

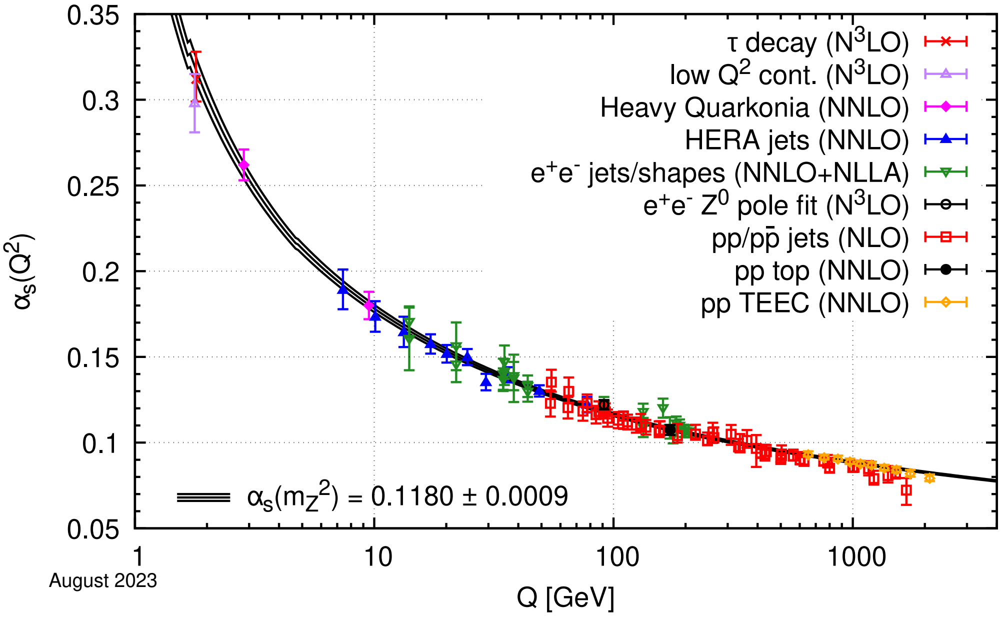

Figure 1.2 (Color online) Measurements of the coupling constant (α_s) of the strong interaction as a function of the energy scale (Q). $\alpha_s\left(m_Z^2\right)$ is computed from the current average taken by Particle Data Group. Figure is taken from Reference [8].

as a function of the energy or momentum transfer (Q^2), where Λ_{QCD} represents the QCD scale parameter, and

$$\beta_0 = \frac{11N_c - 2N_f}{12\pi} \tag{1.2}$$

with $N_c = 3$ and N_f as the numbers of quark colors and flavors, respectively. Figure 1.2 [8] summarizes measurements of α_s as a function of the respective energy scale Q. As Q grows, the running α_s decreases, meaning that the strength of the strong interaction is reduced at higher energy scales. For the case of a small distance ($r \to 0$) or a large momentum transfer ($Q^2 \gg \Lambda_{\mathrm{QCD}}^2$), quarks and gluons interact weakly with quite small α_s and are allowed to behave almost as free particles. This is called asymptotic freedom, one of the characteristics of QCD. On the contrary, at a large distance ($r \to \infty$) or an energy scale close to the QCD scale ($Q \to \Lambda_{\mathrm{QCD}}$), the large α_s represents the strong interaction among quarks and gluons, which makes them bounded together and confined within hadrons. This is called color confinement, the other critical characteristic of QCD.

1.3 QCD Phase Diagram

Through the strong interaction, quarks and gluons form various states of matter making up the fabric of the universe. The conjectured QCD phase diagram shown in Figure 1.3 [9] maps out these states of matter under different conditions of temperature

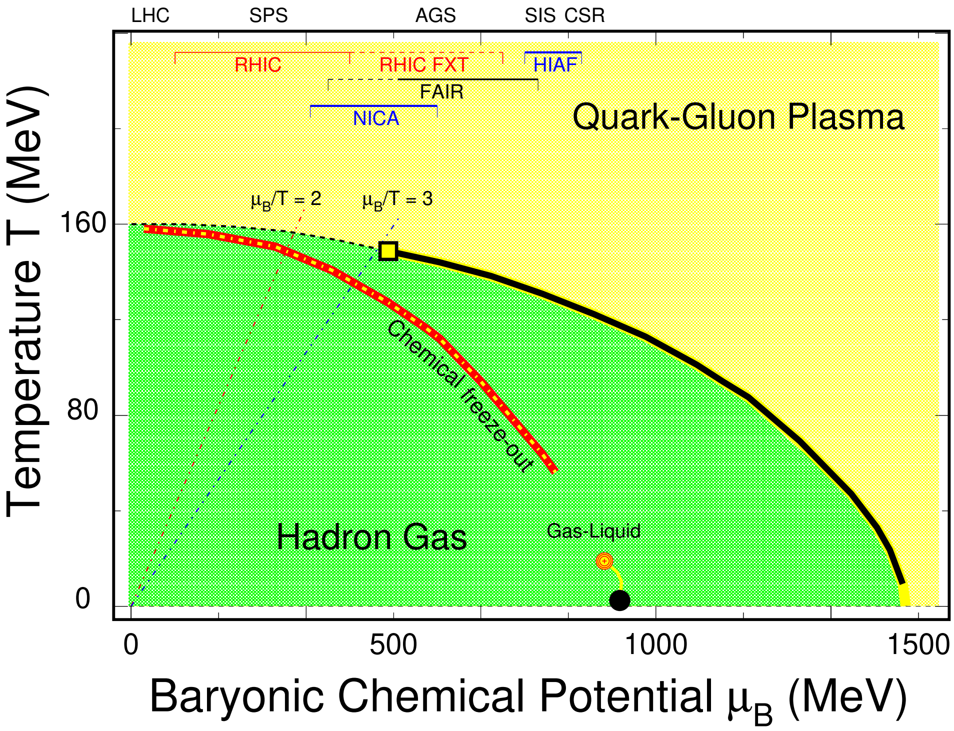

Figure 1.3 (Color online) Conjectured QCD phase diagram of temperature (T) versus baryonic chemical potential (μ_B). The phase boundary between hadronic and Quark-Gluon Plasma (QGP) phases consists of the crossover (dashed curve) at small μ_B and the first-order phase transition (solid curve) at large μ_B, between which a conjectured critical point is drawn. Figure is taken from Reference [9].

(T) and baryonic chemical potential (μ_B). μ_B is defined by the change in the free energy of a system described by the grand canonical ensemble when an additional baryon is introduced, which can reflect the net-baryon number density. This diagram offers a comprehensive framework for understanding the behavior and the phase structure of strongly interacting matter across a wide range of environments.

1.3.1 Hadronic Phase

In the green area in Figure 1.3, where both μ_B and T are low enough, quarks and gluons are confined within color-neutral hadrons, as $r \to \infty$ or $Q \to \Lambda_{\mathrm{QCD}}$ in Equation (1.1). This state of matter is known as the hadronic phase, the current phase of matter in the universe under standard conditions. In this phase, matter primarily exists in the form of hadrons, indicating that the effective degrees of freedom are hadrons.

There is a liquid-gas transition in the green area, which has a first-order phase transition (yellow curve) connecting a second-order critical point (red circle) and the ground state of the nuclear matter ($T \sim 0$ and $\mu_B \sim 925$ MeV) [10].

1.3.2 Quark-Gluon Plasma Phase

As μ_B and/or T increase and enter the yellow area in Figure 1.3, quarks and gluons weakly interact and become deconfined, forming a new state of matter known as the Quark-Gluon Plasma (QGP), which is theoretically predicted by QCD. In the QGP phase, quarks and gluons are no longer confined within individual hadrons but move freely over larger volumes, and the fundamental degrees of freedom turn to quarks and gluons. According to the history of the universe shown in Figure 1.4 [11], QGP is believed to have existed in the early universe about 10^{-6} s after the Big Bang and then cooled down to hadrons.

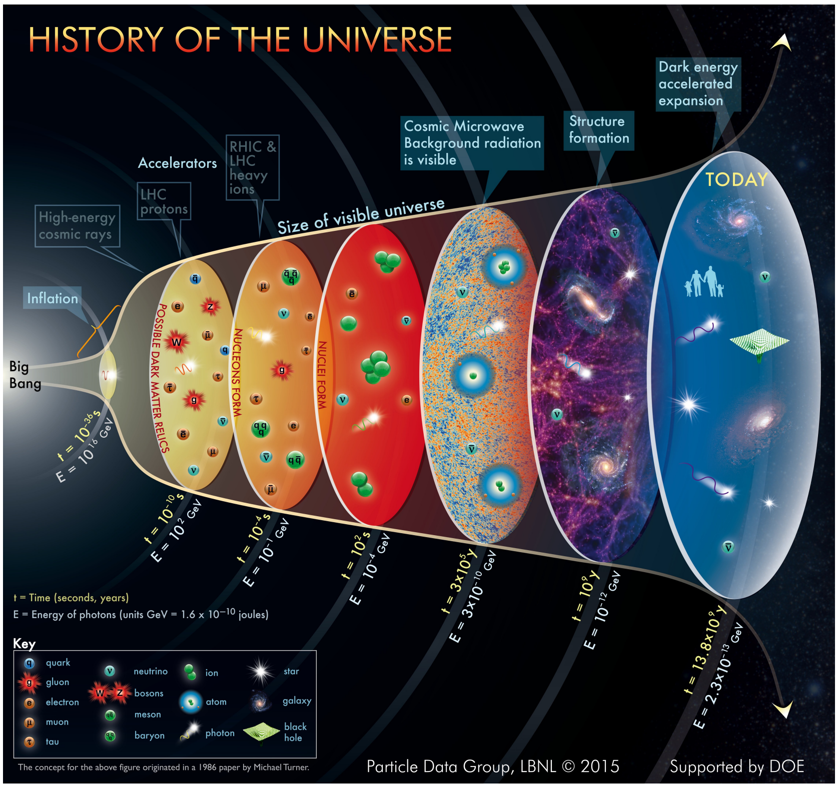

Figure 1.4 (Color online) A sketch of the expected history of the universe. The Quark-Gluon Plasma (QGP) may have existed shortly after the Big Bang and cooled down to hadrons. Relativistic heavy-ion collisions can simulate the Big Bang by creating similar forms of matter. Figure is taken from Reference [11].

Several experimental evidences consistent with theoretical predictions demonstrate that QGP can be recreated in relativistic heavy-ion collisions [12-17], and related measurements reveal that it behaves as a nearly perfect fluid with several key properties, including strong coupling and small viscosity [18-20].

1.3.3 Crossover

A phase transition takes place at the phase boundary between the hadronic phase and the QGP phase. At low μ_B and high T, there is predicted to be a crossover transition, without a sharp or distinct phase boundary. The approximate location of the crossover region is indicated by the black dashed curve in Figure 1.3. In the smooth crossover, hadronic matter and the deconfined state of quarks and gluons gradually and continuously transform into each other. Lattice QCD [21], a non-perturbative solution of QCD from first principles on a discretized space-time lattice, provides strong predictions for the existence of the crossover at $\mu_B = 0$ [22-26], and a new calculation for the temperature of the transition is $T = 156.5 \pm 1.5$ MeV.

1.3.4 First-Order Phase Transition

At high μ_B and relatively low T, several effective QCD-based models suggest that the phase transition is of the first order [27-30], and the phase boundary is drawn as a black solid curve in Figure 1.3. Lattice QCD calculations could also support the prediction of the first-order phase transition [31-32], even though they are usually difficult to be performed at non-zero μ_B due to the sign problem. The first-order phase transition exhibits a distinct first-order phase boundary in the QCD phase diagram, involving the coexistence of the hadronic and QGP phases in a mixed-phase region.

1.3.5 Critical Point

Considering the predictions of the crossover at low μ_B and the first-order phase transition at high μ_B, there is expected to be an end point, called QCD critical point. The yellow square in Figure 1.3 represents the critical point at a conjectured position. It terminates the first-order phase boundary, beyond which the transition between phases is the smooth crossover. For a system at the critical state, its correlation length (ξ) is believed to diverge, indicating long-range correlations and enhanced fluctuations.

The study of the critical point can significantly improve our understanding of the QCD theory, and the possible confirmation of its existence or inexistence should become a milestone in our exploration of the QCD phase structure. Extensive efforts have been dedicated to theoretically determining the location of the critical point with applying approximation, assumption or estimation through lattice QCD [31,33-35] and various QCD-based models, such as Nambu–Jona-Lasinio (NJL) [36], Polyakov-Nambu-Jona-Lasinio (PNJL) [37], Dyson-Schwinger Equations (DSE) [38], Functional Renormalization Group (FRG) [39]. Figure 1.5 [40] summarizes several theoretical predictions for the location of the critical point, which distribute within a quite wide range of T = 40–180 MeV and μ_B = 200–1100 MeV. Considering the large uncertainties and differences from the theoretical and model predictions through different approaches, it

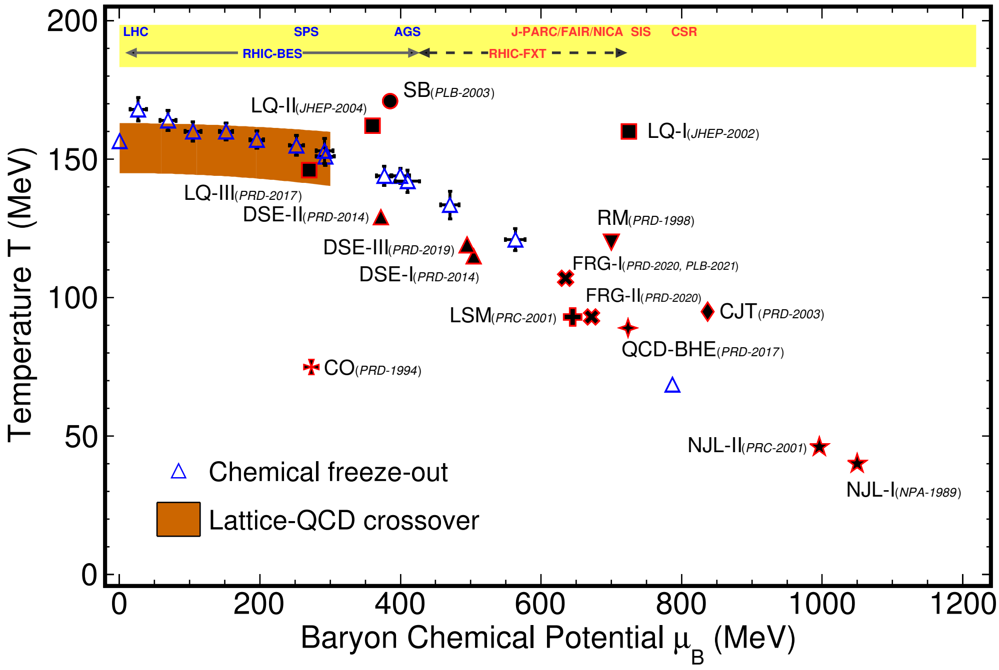

Figure 1.5 (Color online) Theoretical predictions for the location of the critical point (solid markers) in the QCD phase diagram. Locations of the crossover from lattice QCD (brown band) and the chemical freeze-out from statistical model fits of measurements (blue open triangles) are also shown. Figure is taken from Reference [40].

is crucial to look for the answer about the existence and location of the critical point in experiments.

1.4 Relativistic Heavy-Ion Collisions

As we mentioned before, QGP is theorized to have formed shortly after the Big Bang. In the current universe, which has since cooled significantly, QGP no longer exists under natural conditions. To simulate the Big Bang and the system shortly after it shown in Figure 1.4, physicists design relativistic heavy-ion collisions, creating the conditions of extremely high temperatures and energy densities capable of the QGP formation. Therefore, relativistic heavy-ion collisions are also called as the little Bang.

1.4.1 System Evolution

Figure 1.6 [41] illustrates various stages of the system evolution in relativistic heavy-ion collisions with corresponding time scales labelled. Two atomic nuclei are accelerated to velocities approaching the speed of light and directed towards each other. Due to Lorentz contraction in the direction of the beam, these nuclei appear significantly flattened, like pancakes. Upon collision, a substantial amount of energy is deposited in the interaction zone, placing the system at a pre-equilibrium state. The energy density

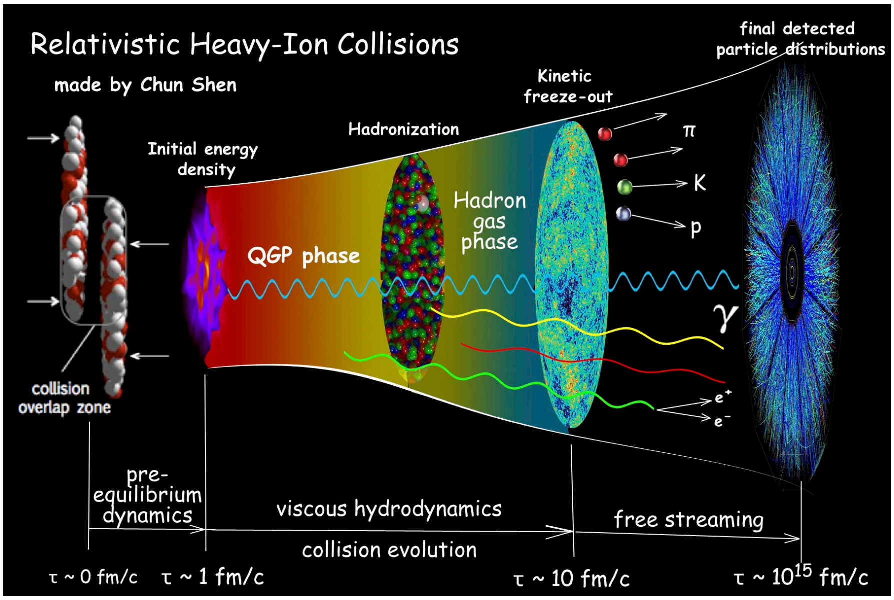

Figure 1.6 (Color online) A sketch of relativistic heavy-ion collisions, including various stages of the collision system evolution. Figure is taken from Reference [41].

peaks approximately 1 fm/c after the collision, and the system reaches the state of local thermal equilibrium. Under such extreme conditions, hadrons break into deconfined quarks and gluons and undergo a phase transition into a state of hot and dense nuclear matter known as QGP, in which complex strong interactions take place.

As the system evolves, it experiences expansion and cooling. The hadronization process begins when quarks and gluons recombine into hadrons. During this phase, hadrons continue both inelastic and elastic interactions until the temperature and density drop sufficiently. The system starts its chemical freeze-out when inelastic collisions cease, and the relative abundances of different hadron species are fixed. The chemical freeze-out position in the QCD phase diagram is shown as red-yellow dotted curve in Figure 1.3, which is obtained from the fits of experimental particle yields using a thermal model. Around 10 fm/c after the collision, kinetic freeze-out occurs when elastic collisions stop, and the momentum spectra of the hadrons no longer change. Finally, these hadrons at a free state continue to travel until they are accepted by detectors.

1.4.2 Experiments

Many accelerators for relativistic heavy-ion collisions have been built, such as the Bevatron, Alternating Gradient Synchrotron (AGS), Super Proton Synchrotron (SPS) and Schwerionensynchrotron (SIS), and several others, including Nuclotron-based Ion Collider fAcility (NICA), Facility for Antiproton and Ion Research (FAIR) and High Intensity Heavy Ion Accelerator Facility (HIAF), have been designed or are currently in construction. The two largest running facilities are Relativistic Heavy Ion Collider

(RHIC) at Brookhaven National Laboratory (BNL) in the USA since the year 2000 and LHC at CERN in Switzerland since the year 2010.

Two of the most important initial settings are the types of the colliding nuclei and the collision energy. For the nuclei types, RHIC commonly selects Au, as well as U, Ru, Zr, Cu, Al, and O, and LHC prefers Pb and Xe. Light ions, such as protons (p), deuterons (d), and ^{3}He, are also used in collisions with either light or heavy ions to study small collision systems. The p+p collisions, which are not considered to have enough energy density to create QGP, are always used as a baseline reference for heavy-ion collisions.

For the collision energy, it is always quantified by $\sqrt{s_{\mathrm{NN}}}$, centre-of-mass energy per colliding nucleon pair. Here,

$$s = \left(E_{\text{projectile}} + E_{\text{target}}\right)^2 - \left(\boldsymbol{p}_{\text{projectile}} + \boldsymbol{p}_{\text{target}}\right)^2, \tag{1.3}$$

which is expressed by the energies and momentum vectors of the colliding particles. RHIC has the capability to perform Au+Au collisions at $\sqrt{s_{\mathrm{NN}}}$ from 3 to 200 GeV and p+p collisions up to 510 GeV. LHC operates at TeV-level collision energies, for Pb+Pb collision at $\sqrt{s_{\mathrm{NN}}}$ = 2.76, 5.02 and 5.36 TeV through several upgrades, and in the near future, is going to achieve its designed maximum energy of 14 TeV for p+p collisions and 5.5 TeV for Pb+Pb collisions [42].

In experiments, each collision is referred to as an event, and the location where the collision occurs is known as the primary vertex. The three-dimensional geometry is always based on a right-handed Cartesian coordinate system, with the z-axis aligned along the beam line and the positive y axis pointing upward. The parameters of a particle, including its three-momentum $\left(p_x, p_y, p_z\right)$ and rest mass m, are defined by

$$p_{\mathrm{T}} = \sqrt{p_x^2 + p_y^2}, \tag{1.4}$$

$$m_{\mathrm{T}} = \sqrt{p_{\mathrm{T}}^2 + m^2}, \tag{1.5}$$

$$p = \sqrt{p_{\mathrm{T}}^2 + p_z^2}, \tag{1.6}$$

$$E = \sqrt{p^2 + m^2}, \tag{1.7}$$

$$\varphi = \arctan \frac{p_y}{p_x}, \tag{1.8}$$

$$\theta = \arctan \frac{p_{\mathrm{T}}}{p_z}, \tag{1.9}$$

$$\eta = \frac{1}{2} \ln \frac{p + p_z}{p - p_z} = -\ln\left(\tan\frac{\theta}{2}\right), \tag{1.10}$$

$$y = \frac{1}{2} \ln \frac{E + p_z}{E - p_z} \tag{1.11}$$

as the transverse momentum, transverse mass, total momentum, energy, azimuthal angle, polar angle, pseudorapidity and rapidity, respectively.

1.4.3 Exploring Phase Diagram

Note that relativistic heavy-ion collisions are the only experimental method available to humans for creating QGP. Thus, these experiments offer an indispensable opportunity to study QGP and explore the QCD structure. To scan the QCD phase diagram by reaching different positions of T and μ_B, an effective approach is to vary $\sqrt{s_{\mathrm{NN}}}$. As discussed, the formation of QGP requires extreme conditions of temperature and density. Simply put, the former mainly relies on vacuum heating, while the latter primarily results from matter compression. In collisions at the higher energy, the larger amount of energy is deposited, and the stronger heating process increases T. In lower-energy collisions, due to the baryon stopping effect that the colliding nuclei slow down more significantly and overlap for a longer duration, the net-baryon number density is

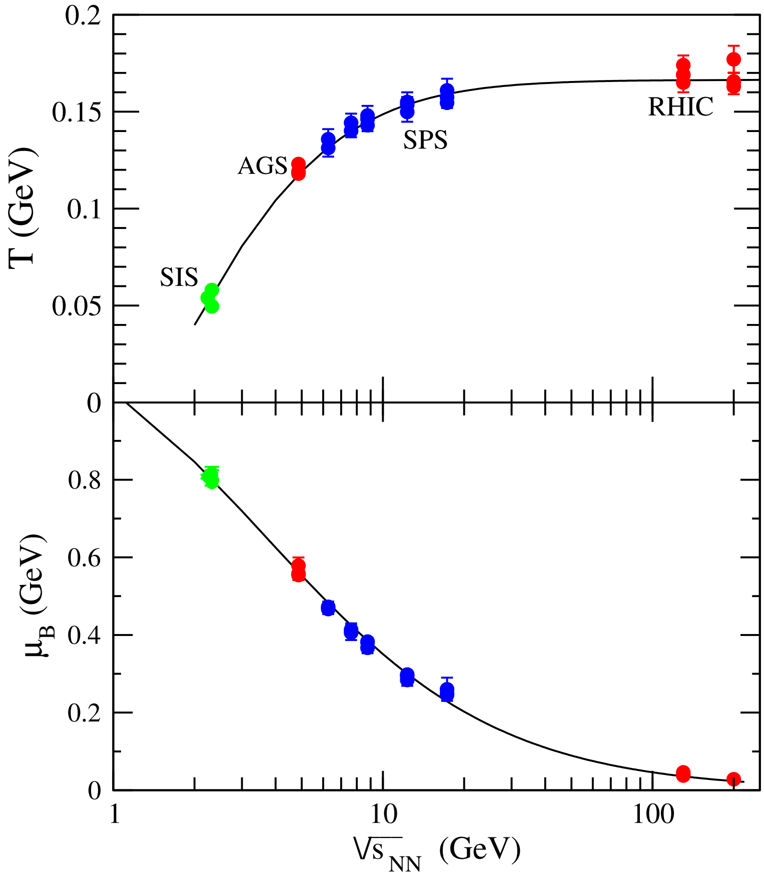

Figure 1.7 (Color online) Collision energy ($\sqrt{s_{\mathrm{NN}}}$) dependence of T (top) and μ_B (bottom) at the chemical freeze-out. Markers are obtained from statistical-thermal model fits for particle yield measurements from experiments at SIS (green), AGS (red), SPS (blue) and RHIC (red), and curves represent the functional parameterization. Figure is taken from Reference [43].

concentrated in the central collision zone, which highly enhances μ_B.

Figure 1.7 [43] summarizes T and μ_B at the chemical freeze-out as functions of $\sqrt{s_{\mathrm{NN}}}$ obtained from statistical-thermal model fits for particle yield measurements from various collider experiments. It is obvious that T increases and μ_B decreases as $\sqrt{s_{\mathrm{NN}}}$ rises. The parameterization formulae [43] are listed below

$$T\left(\mu_B\right) = a - b\mu_B^2 - c\mu_B^4, \tag{1.12}$$

$$\mu_B\left(\sqrt{s_{\mathrm{NN}}}\right) = \frac{d}{1 + e\sqrt{s_{\mathrm{NN}}}}, \tag{1.13}$$

where

$$a = 0.166 \pm 0.002\ \mathrm{GeV}, \tag{1.14}$$

$$b = 0.139 \pm 0.016\ \mathrm{GeV}^{-1}, \tag{1.15}$$

$$c = 0.053 \pm 0.021\ \mathrm{GeV}^{-3}, \tag{1.16}$$

$$d = 1.308 \pm 0.028\ \mathrm{GeV}, \tag{1.17}$$

$$e = 0.273 \pm 0.008\ \mathrm{GeV}^{-1}. \tag{1.18}$$

Equation (1.12) can roughly describe the curve of the chemical freeze-out in the QCD phase diagram. Equation (1.13) provides an important support for experimentally scanning the QCD phase diagram by varying $\sqrt{s_{\mathrm{NN}}}$.

1.5 Experimental Observables

According to the statistical physics, ξ of a thermodynamic system in equilibrium describes the range over which a physical quantity is related or the fluctuation is correlated. The most characteristic feature of a system at a critical point is the divergence of ξ in the idealized thermodynamic limit, meaning the correlations influence the entire system. This leads to the divergence of the specific heat (c_V) and the susceptibility (χ). The enhanced ξ near the critical point can also induce long-range correlations and large fluctuations in the system.

Both of ξ and χ are theoretically calculable. However, it is impossible to obtain them directly in relativistic heavy-ion collision experiments, as we cannot observe the QCD matter in the collision region during its brief existence. The only approach is to infer these properties from measurable quantities of the particles detected at the final state.

Since fluctuations and correlations in a system strongly depend on ξ and χ, they are believed to be acutely sensitive to the QCD phase structure [44-48]. These properties can be quantified by statistical measures, including cumulants (C_r) and factorial cumulants (κ_r, irreducible correlation functions), where $r = 1, 2, \cdots$ indicates the order. Through processes governed by the strong interaction within a closed system, the net-baryon (B), net-electric-charge (Q) and net-strangeness (S) numbers remain conserved, collectively called as the conserved quantum charge ($q = B, Q, S$). Their fluctuations in a grand canonical ensemble can vary significantly under different phase conditions and are deeply studied and highly suggested to explore the phase structure [49-53]. Experimentally, net-particle numbers at the final state can be directly measured on the event-by-event basis. The net-proton, net-charged-hadron and net-charged-kaon numbers are considered to be proxies for B, Q and S, respectively, and their higher-order cumulants and factorial cumulants are selected as the observables, expected to reflect related behaviors of the conserved charges according to several theoretical and model studies [54-59]. In this analysis, we focus on higher-order fluctuations of event-by-event net-proton numbers.

The definitions and properties of statistical measures will be discussed in Section 1.8. Connections of the correlation length and susceptibility to the cumulant of the conserved charge will be discussed in Sections 1.5.1 and 1.5.2.

1.5.1 Susceptibility and Cumulant

In a system of thermal equilibrium for a grand canonical ensemble, the susceptibility of the conserved charge can be marked as $\chi^{B,Q,S}_{i,j,k}$, where i, j and k are the corresponding orders for B, Q and S. It can be connected to the derivative of the dimensionless thermodynamic pressure $\left(P/T^4\right)$ with respect to the reduced chemical potential $\left(\mu_q/T\right)$ as [24,60-61]

$$\chi^{B,Q,S}_{i,j,k} = \frac{\partial^{i+j+k}\left(P/T^4\right)}{\partial\left(\mu_B/T\right)^i \partial\left(\mu_Q/T\right)^j \partial\left(\mu_S/T\right)^k}. \tag{1.19}$$

The dimensionless thermodynamic pressure on the right-hand side can be given by the logarithm of the QCD partition function (Z) as

$$\frac{P}{T^4} = \frac{1}{VT^3}\ln Z\left(V, T, \mu_B, \mu_Q, \mu_S\right), \tag{1.20}$$

where V is the volume of the system. We can also have the relation between the cumulant ($C^{B,Q,S}_{i,j,k}$) of the B, Q, S distribution and the QCD partition function

$$C^{B,Q,S}_{i,j,k} = \frac{\ln Z\left(V, T, \mu_B, \mu_Q, \mu_S\right)}{\partial\left(\mu_B/T\right)^i \partial\left(\mu_Q/T\right)^j \partial\left(\mu_S/T\right)^k}. \tag{1.21}$$

Thus, with the combination of the above three equations, the cumulant of the conserved charge, an observable capable to be measured in experiments, is connected to the susceptibility of the collision system by

$$C_{i,j,k}^{B,Q,S} = VT^3 \chi_{i,j,k}^{B,Q,S}. \tag{1.22}$$

Both univariate (diagonal) and multivariate (off-diagonal) cases are included in the equation. To cancel the trivial contributions from the volume and temperature, it is easy to take the ratio of cumulants to obtain the direct connection to the susceptibility

$$\frac{C_{i,j,k}^{B,Q,S}}{C_{i\prime,j\prime,k\prime}^{B,Q,S}} = \frac{\chi_{i,j,k}^{B,Q,S}}{\chi_{i\prime,j\prime,k\prime}^{B,Q,S}}. \tag{1.23}$$

For the univariate cumulant C_r of q, the above two equations degenerate into the following forms

$$C_r^q = VT^3 \chi_r^q, \tag{1.24}$$

$$\frac{C_r^q}{C_{r\prime}^q} = \frac{\chi_r^q}{\chi_{r\prime}^q}. \tag{1.25}$$

Figure 1.8 [50] shows the clear peak structure of χ_B near the critical point predicted by the NJL model.

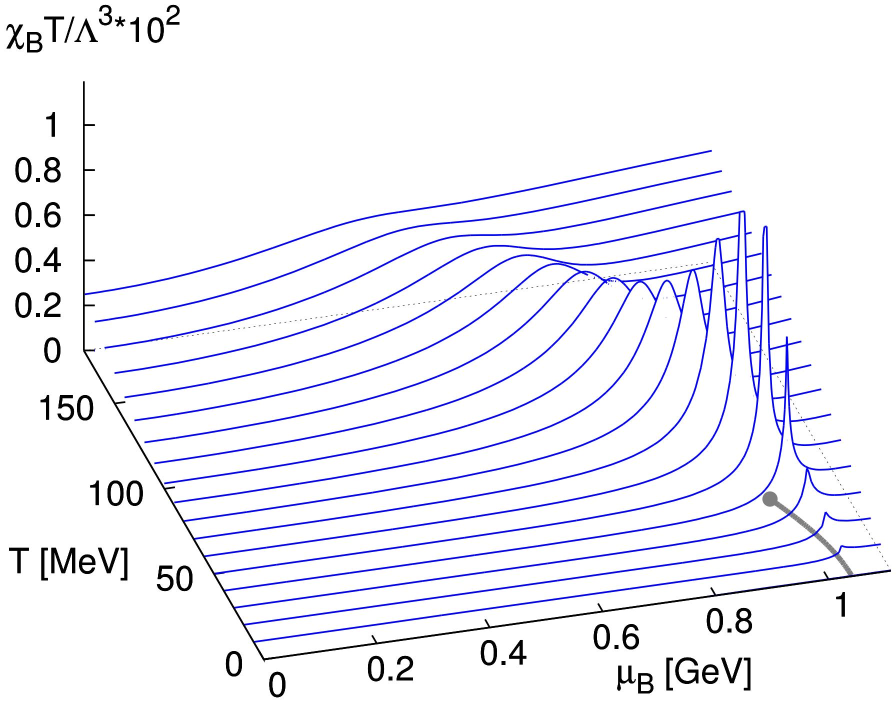

Figure 1.8 (Color online) Net-baryon number susceptibility (χ_B) multiplied by T as a function of T and μ_B in the Nambu–Jona-Lasinio (NJL) model. The gray curve on the bottom surface represents the first-order phase boundary with an end point as the critical point. Figure is taken from Reference [50].

1.5.2 Correlation Length and Cumulant

The σ field model [48,51,55,62] is applied for the study, based on the order parameter field quantified by the critical mode $\sigma(\boldsymbol{x})$. The fluctuation near a critical point is described by the probability distribution

$$P(\sigma) \sim \exp\left(-\frac{\Omega(\sigma)}{T}\right), \tag{1.26}$$

Here, Ω is the effective action or free energy functional for the σ field, and it can be expanded in terms of σ as

$$\Omega(\sigma) = \int \mathrm{d}^3\boldsymbol{x}\left(\frac{(\nabla\sigma)^2}{2} + \frac{m_\sigma^2}{2}\sigma^2 + \frac{\lambda_3}{3}\sigma^3 + \frac{\lambda_4}{4}\sigma^4 + \cdots\right), \tag{1.27}$$

where $m_\sigma = 1/\xi$ and λ_i $(i = 3, 4, \cdots)$ denote the σ-field screening mass and the interaction coupling parameter, respectively.

For the zero momentum mode

$$\sigma_V \equiv \int \sigma(\boldsymbol{x})\,\mathrm{d}^3\boldsymbol{x} \tag{1.28}$$

in a system of volume V, the cumulants are given by

$$C_2^{\sigma_V} = VT\xi^2, \tag{1.29}$$

$$C_3^{\sigma_V} = 2VT^2\lambda_3\xi^6, \tag{1.30}$$

$$C_4^{\sigma_V} = 6VT^3\left(2\left(\lambda_3\xi\right)^2 - \lambda_4\right)\xi^8, \tag{1.31}$$

Since the system is near the critical point, we have $\xi \to \infty$ and vanishing λ_3 and λ_4 given by

$$\lambda_3 = \tilde{\lambda}_3 T^{-1/2}\xi^{-3/2}, \tag{1.32}$$

$$\lambda_4 = \tilde{\lambda}_4 T^{-1}\xi^{-1}, \tag{1.33}$$

where $\tilde{\lambda}_3$ and $\tilde{\lambda}_4$ are dimensionless, universal and independent of ξ. After combining above four equations, we have

$$C_3^{\sigma_V} = 2VT^{3/2}\tilde{\lambda}_3\xi^{9/2}, \tag{1.34}$$

$$C_4^{\sigma_V} = 6VT^2\left(2\tilde{\lambda}_3^2 - \tilde{\lambda}_4\right)\xi^7. \tag{1.35}$$

The σ field model study concludes that the higher-order cumulant, with a higher power of the correlation length, could diverge faster near the critical point.

For the net-baryon number cumulant, Reference [48] also derives

$$C_r^B \sim \xi^{5r/2-3}, \tag{1.36}$$

indicating that the higher-order fluctuations depend more sensitively on the correlation length.

1.5.3 Acceptance and (Factorial) Cumulant

Experimental measurements are usually performed within finite acceptances, for example, of y-p_{T}, and theoretical studies are needed to understand the expected acceptance dependence of fluctuation measures.

Based on the simplest idealized Bjorken model [63] of a boost invariant fireball, the dependence on the rapidity acceptance window Δy is introduced [64]. Considering the event-by-event particle number of interest marked by N, its mean is proportional to Δy due to the boost invariance as

$$\langle N\rangle \sim \Delta y. \tag{1.37}$$

Related to the range of correlations in rapidity, Δy_{corr}, two qualitatively different regimes, $\Delta y \gg \Delta y_{\mathrm{corr}}$ and $\Delta y \ll \Delta y_{\mathrm{corr}}$, are distinguished.

If $\Delta y \gg \Delta y_{\mathrm{corr}}$, cumulants grow as linear functions of Δy based on the additivity of cumulants from uncorrelated contributions, which will be proved in Section 1.8.4. The normalized cumulant by the trivial mean

$$\omega_r \equiv \frac{C_r}{\langle N\rangle} \tag{1.38}$$

accepts contribution of physical correlations to deviate from unity, which saturates at a constant value for $\Delta y \gg \Delta y_{\mathrm{corr}}$. Furthermore, the rth-order factorial cumulant, as a linear combination of cumulants up to the rth order, quantifying the strength of the r-particle correlation [64-65], behaves like

$$\kappa_r \sim \Delta y \sim \langle N\rangle. \tag{1.39}$$

If $\Delta y \ll \Delta y_{\mathrm{corr}}$ with $\Delta y \sim \langle N\rangle \to 0$, the fluctuation measures approach the Poisson limit. Thus, we have

$$\kappa_r \sim (\Delta y)^r \sim \langle N\rangle^r, \tag{1.40}$$

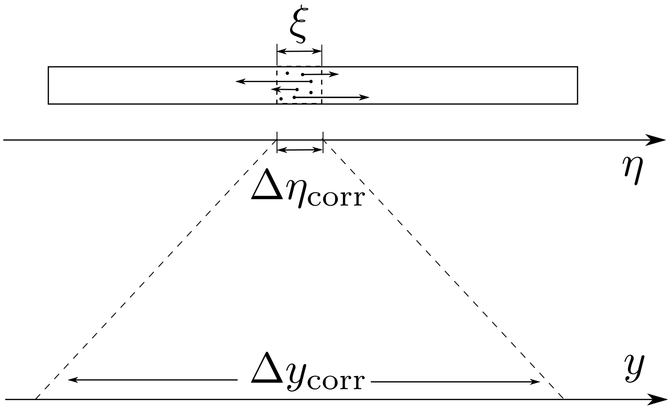

Figure 1.9 A sketch of effect of the thermal broadening or the freeze-out smearing from the spatial (Bjorken) rapidity η to the kinematic rapidity y. Figure is taken from Reference [64].

and the dependence of cumulants on Δy is polynomial and more complicated.

Figure 1.9 [64] illustrates the effect of the thermal broadening or the freeze-out smearing on the relation between the spatial (Bjorken) rapidity η and the kinematic rapidity y. The correlation length controls $\Delta\eta_{\mathrm{corr}}$, and the translation of the spatial correlations into kinematic correlations induces $\Delta y_{\mathrm{corr}} \ll \Delta\eta_{\mathrm{corr}}$. By taking a measurement in a wider acceptance window of y, and also p_{T}, more particles within the correlated

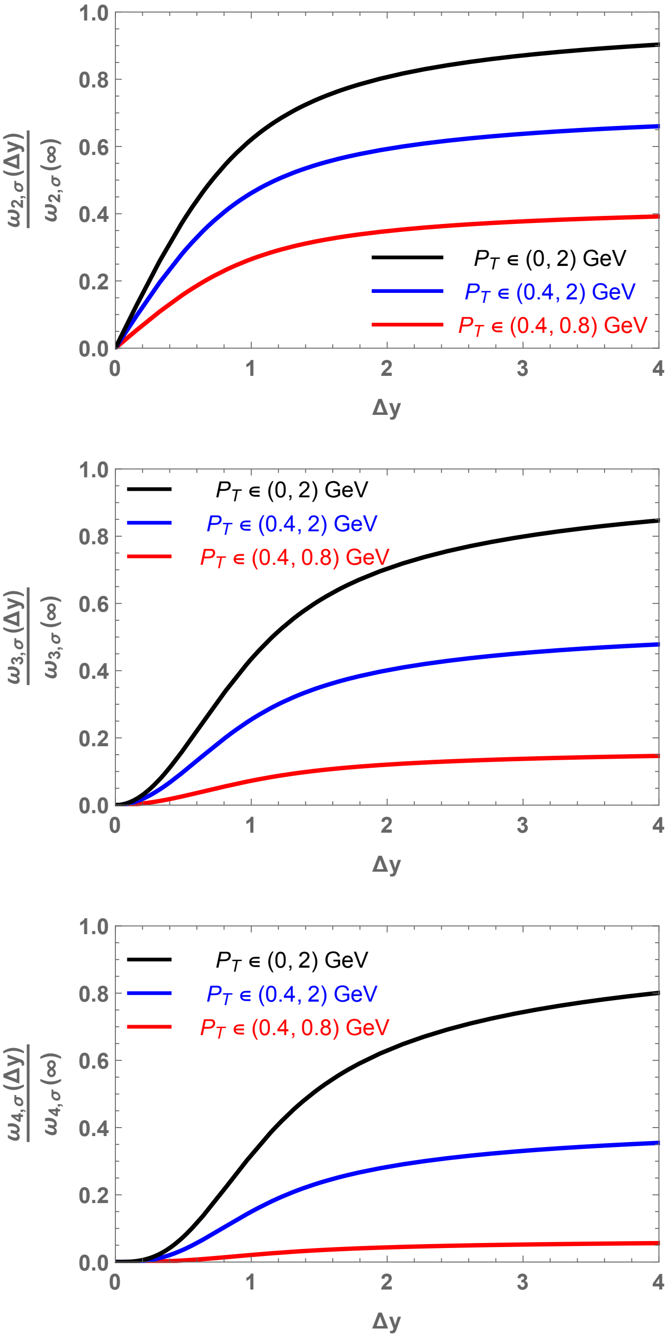

Figure 1.10 (Color online) Expected acceptance dependence of normalized second-, third- and fourth-order cumulants ($\omega_{2,3,4}$) induced by the critical contribution from the σ field model with $\Delta y_{\mathrm{corr}} \sim 1$. Figure is taken from Reference [64].

spatial volume are included, and the physical contribution could be significantly larger. Figure 1.10 [64] shows the Δy dependence of $\omega_{2,3,4}$ within various p_{T} windows relative to those in the full phase space expected by the σ field model with $\Delta y_{\mathrm{corr}} \sim 1$. For small $\Delta y \ll 1$, $\omega_r \sim (\Delta y)^{r-1}$, while for large Δy, a saturation is observed.

1.6 Expected Signatures

Theorists have made lots of efforts to predict signatures of various QCD phase structures including the critical point and the crossover, which provide important suggestions and directions for the experimental analysis. It is also important to have studies on baselines to help us understand the signatures through comparisons.

1.6.1 Signal for Critical Point

As discussed, during the relativistic heavy-ion system evolution, abundances of various hadron species are fixed when hadrons stop their inelastic interactions at the chemical freeze-out. In other words, the information about the particle numbers at the final state, including net-particle number fluctuations, comes from the chemical freeze-out. How the behavior of ξ around the critical point influences the experimental measurement has been theoretically studied.

Figure 1.11 [48] shows the conjectured QCD phase structure, including possible information on the correlation length. Considering the divergence of ξ at the critical

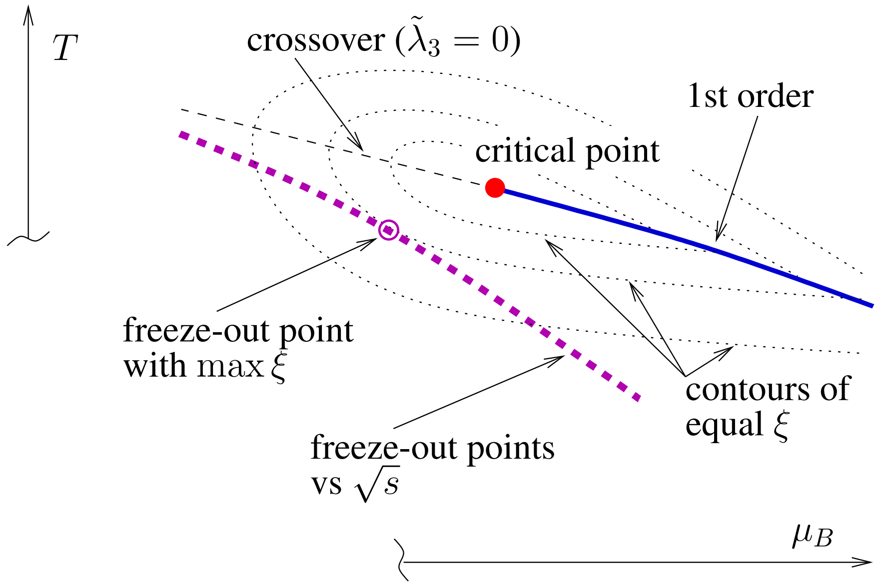

Figure 1.11 (Color online) Illustration of the phase structure and the correlation length (ξ) in the QCD phase diagram. Possible relative positions of equal-ξ contours and maximum-ξ freeze-out point are shown. Figure is taken from Reference [48].

point, several possible contours of equal ξ are drawn surrounding the critical point. A diverged ξ might not be observed at the chemical freeze-out, but this suggests a freeze-out position with a maximum ξ. Since μ_B and T at the chemical freeze-out vary as functions of the initial collision energy, $\sqrt{s_{\mathrm{NN}}}$ dependence of higher-order fluctuations could show a non-monotonic behavior depending on the freeze-out position with respect to the critical point. Measurements in heavy-ion collisions by scanning $\sqrt{s_{\mathrm{NN}}}$ can help extract information related to the structure.

Here, we continue to present the study based on the σ field model [48,51,55] following Section 1.5.2. For a system away from the critical point, characterized by $\xi^3 \ll V$, Central Limit Theorem dictates that the probability distribution of σ_V approaches a Gaussian distribution, with higher-order cumulants vanishing beyond the second order. However, if the system is near the critical point, the distribution develops a non-Gaussian shape. In Equations (1.34) and (1.35), the dimensionless couplings $\tilde{\lambda}_3 = 0 - {\sim}8$ and $\tilde{\lambda}_3 = {\sim}4 - {\sim}20$, depending on whether the approach to the critical point is from the crossover side or first-order transition side, as derived from the Ising universality class. Therefore, according to Equation (1.35), for a system in the vicinity of the critical point, we can estimate a negative $C_4^{\sigma_V}$ on the crossover side, while it becomes positive on the first-order transition side. The left panel of Figure 1.12 represents the density plot of the expected $C_4^{\sigma_V}$ as a function of T and μ_B near the critical point, with red and blue colors indicating negative and positive values, respectively.

The fluctuations of the σ field and the observable quantity, the number of given charged particles N as a example, can be connected by

$$C_4^N = C_1^N + C_4^{\sigma_V}\left(\frac{gd}{T}\int_p \frac{n_p}{\gamma_p}\right)^4 + \cdots, \tag{1.41}$$

where $\gamma_p = 1\Big/\dfrac{\mathrm{d}E_p}{\mathrm{d}m}$ denotes the relativistic γ-factor of a particle with the momentum vector $\boldsymbol{p}$ and mass m. Here, d is the degeneracy factor (e.g., number of spin or charge states of the particle), and n_p represents the equilibrium distribution for a particle. The coupling g is defined by the infinitesimal change of the field $\delta\sigma$ leading to a change of the effective mass of the particle by $\delta m = g\delta\sigma$. The first term on the right-hand side of the equation is the Poisson contribution considered as the statistical baseline. Thus, the sign of the normalized fourth-order cumulant $\omega_4 = C_4\big/C_1$ of the observable, relative to the baseline, is governed by $C_4^{\sigma_V}$. The right panel of Figure 1.12 illustrates the expected qualitative dependence of $\omega_4 - \omega_4^{\mathrm{baseline}}$ on μ_B along the freeze-out trajectory shown as the dashed green curve in the left panel. As $\sqrt{s_{\mathrm{NN}}}$ decreases and the chemical freeze-out μ_B increases, when the system remains within the crossover region, the fourth-order cumulant of the observable runs down and away from the baseline due to the negative contribution. If the system approaches the critical point, the fourth-order cumulant will receive a positive contribution and rise up across the baseline. After the system enters the first-order phase transition side and moves far away from the critical point, the negative contribution will become weaker, resulting in the fourth-order cumulant returning to the baseline.

This theoretical study provides a reasonable expectation for the signature of the critical point and serves as a key guide for experimental measurements. An effective approach involves scanning $\sqrt{s_{\mathrm{NN}}}$ to search for non-monotonic behavior in higher-order fluctuations relative to the baseline. It is necessary to note that the conditions in theories may not exactly match experiments. Theoretical systems are typically infinite and in equilibrium, whereas heavy-ion collision systems are rapidly expanding where the fluctuations are impacted by the non-equilibrium environment [67-69] with finite size and time [70-71]. For instance, the maximum correlation length can only be comparable to the system size, limiting its ideal divergence. Additionally, numerous effects, including diffusion and hadronic rescatterings [72-74], resonance decays [74-76] and net-baryon number conservation [77-78], can also influence the measured fluctuations and the associated baselines.

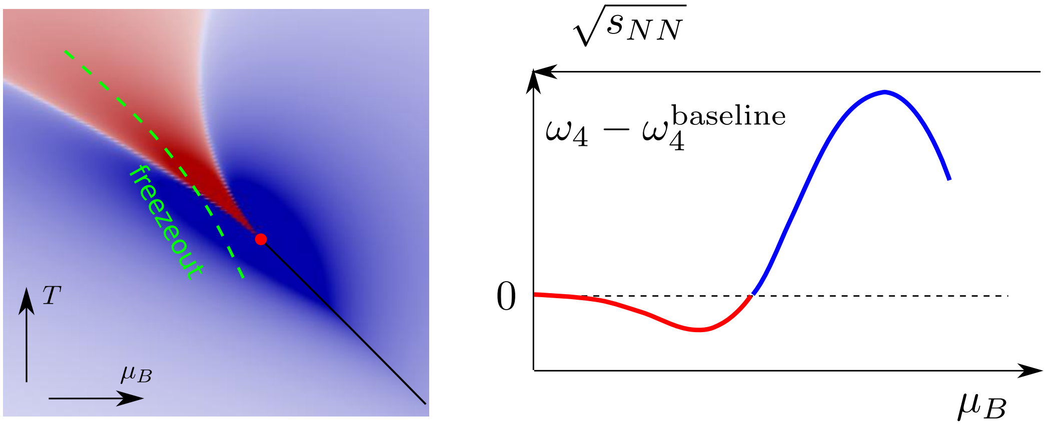

Figure 1.12 (Color online) Equilibrium expectation for the fourth-order cumulant, relative to the baseline, as a function of T and μ_B in the QCD phase diagram (left) and as a function of μ_B along the freeze-out trajectory (dashed green curve in the left panel) (right). Red and blue regions and curves reflect the negative and positive signs of the fourth-order cumulant, respectively. Figures are taken from Reference [66].

1.6.2 Signal for Crossover

Figures 1.13 [79] and 1.14 [80] present the predictions for hyper-order cumulant (beyond the fourth order) ratios by the lattice QCD calculation and the FRG approach, respectively. Both of the theoretical results, considering the smooth crossover transition, obtain negative signs of C_5 and C_6. In other words, the signature of the crossover is expected to be negative hyper-order cumulants.

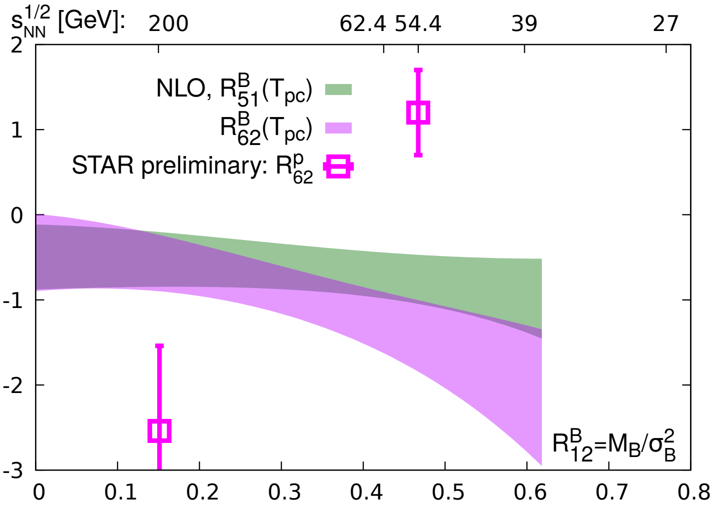

Figure 1.13 (Color online) Net-baryon number C_5/C_1 (R_{51}) and C_6/C_2 (R_{62}) as functions of C_1/C_2 (R_{12}) evaluated along the pseudo-critical line from lattice QCD. The STAR preliminary measurement of net-proton number C_6/C_2 [81-82] is shown for comparison. Figure is taken from Reference [79].

1.6.3 Statistical Baselines

The Poisson and Gaussian distributions are usually considered to be the statistical baselines. Their properties will be discussed in Section 1.8.

For the Poisson baseline, where no correlation is taken into account, $C_r/C_{r'} \equiv 1$ ($r, r' \geqslant 1$) and $\kappa_r \equiv 0$ ($r \geqslant 2$), meaning that high-order factorial cumulants characterize the correlations.

If we measure the difference between the numbers of two particle species (N_1 and N_2), the Poisson baseline is turned to the Skellam baseline. We have $C_{\text{odd}}/C_{\text{odd}} \equiv 1$ and $C_{\text{even}}/C_{\text{even}} = C_{\text{even}}/\langle N_1 + N_2\rangle \equiv 1$, where the sign $\langle\cdot\rangle$ represents the expectation.

For the Gaussian baseline, $C_r \equiv 0$ ($r \geqslant 3$), which indicates that the high-order cumulants describe the non-Gaussian fluctuations.

1.6.4 Model Baselines

The baseline can also be understood from model calculations without considering a phase transition or a critical point, such as the Hadron Resonance Gas (HRG) model [85-

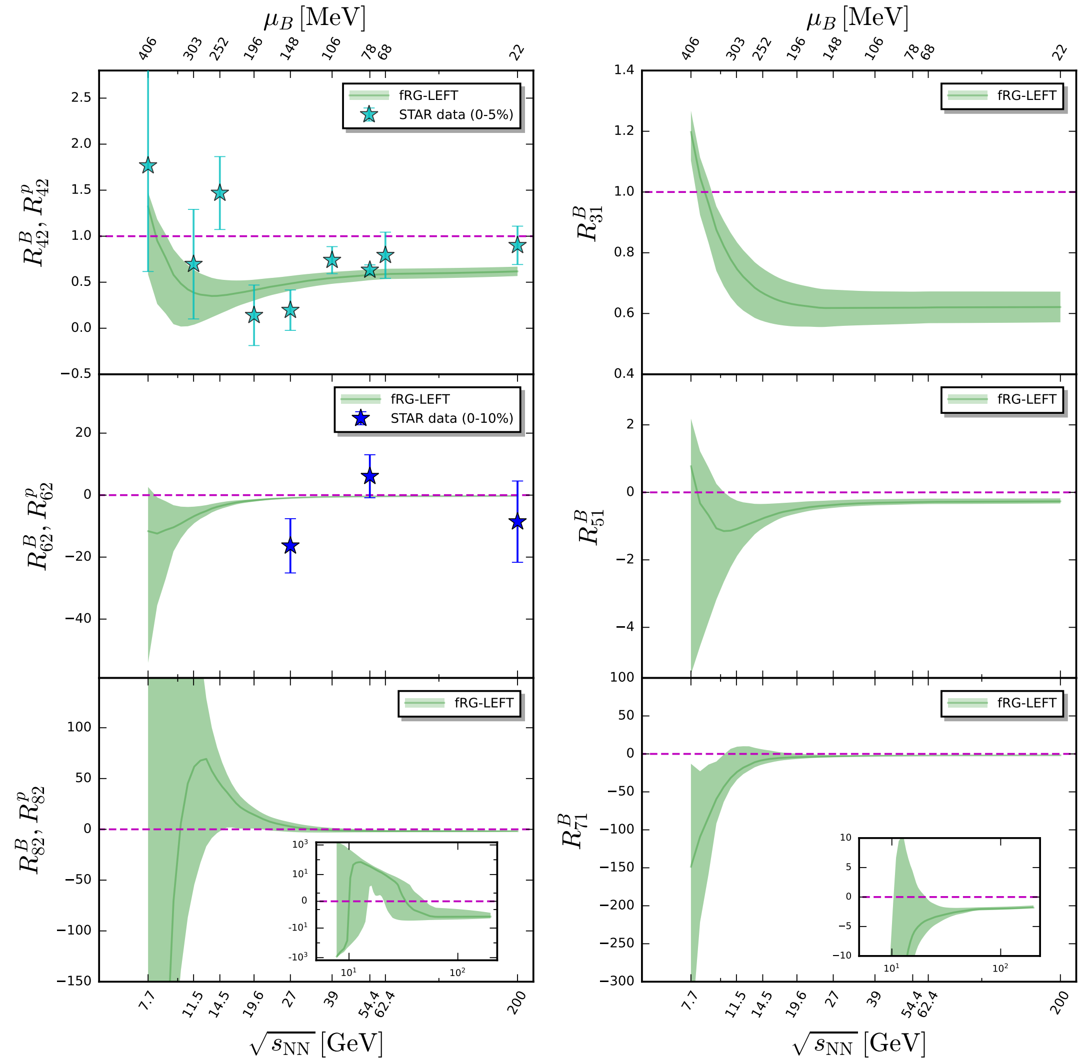

Figure 1.14 (Color online) Net-baryon number cumulant ratios as functions of $\sqrt{s_{\rm NN}}$ evaluated on the pseudo-critical line from the functional renormalization group (FRG) approach. The STAR measurements of net-proton number C_4/C_2 [83] and C_6/C_2 [84] are shown for comparison. Figure is taken from Reference [80].

86] and the Ultra-relativistic Quantum Molecular Dynamics (UrQMD) model [87-89]. By comparing results from experiments and models, key information on the QCD phase structure could be extracted from a possible difference or consistency. Studies from these models will be discussed in Section 1.7.

1.7 Useful Models

Models are developed by theorists to describe the condition or evolution of the heavy-ion collision system based on a certain comprehension. Predictions from those with no phase transition or critical point can serve as baselines for the QCD phase structure. Moreover, models provide good opportunities to understand various processes irrelevant to the realistic QCD phase structure that influence the measured quantities, including: (a) difference between fluctuations of net-baryon and net-proton numbers, (b) effect of resonance decays, (c) effect of finite acceptance (d) effect of net-baryon number conservation.

1.7.1 HRG

The HRG model [85-86] is well-known to describe the hadronization characteristics of the system at the time of freeze-out in heavy-ion collisions, and its calculated thermal abundances of various hadrons show a good agreement with experimental data. In the model, the basic degree of freedom is the confined hadronic matter, and only the interactions resulting in resonance formation are implicitly included, which are constrained by the thermal creation of hadronic resonances based on their Boltzmann factor [90-91]. Since the measured higher-order fluctuations of net-particle numbers also come from the chemical freeze-out, the HRG calculations can serve as a theoretical non-critical baseline under a thermal condition [77,92-94].

1. Baseline Study

For a grand canonical ensemble with the Boltzmann approximation, Equation (1.20) can derive a simple form as [90]

$$\frac{P}{T^4} = \frac{1}{\pi^2} \sum_i g_i \left(\frac{m_i}{T}\right)^2 K_2\left(\frac{m_i}{T}\right) \cosh\left(\frac{\mu_i}{T}\right), \tag{1.42}$$

where $K_2(x)$ denotes the modified Bessel function of the second kind, and the summation is taken for stable hadrons and resonances, each labelled by i. The degeneracy factor and mass of the ith particle are marked by g_i and m_i, respectively, and $\mu_i = B_i\mu_B + Q_i\mu_Q + S_i\mu_S$ represents the total chemical potential for the ith particle carrying B_i, Q_i and S_i as its baryon, electric-charge and strangeness numbers. Using Equation 1.19, we can calculate the net-baryon number susceptibility by

$$\chi^B_{\mathrm{odd}} = \sum_{i\in\mathrm{baryons}} g_i \left(\frac{m_i}{T}\right)^2 K_2\left(\frac{m_i}{T}\right) \sinh\left(\frac{\mu_B + Q_i\mu_Q + S_i\mu_S}{T}\right), \tag{1.43}$$

$$\chi^B_{\mathrm{even}} = \sum_{i\in\mathrm{baryons}} g_i \left(\frac{m_i}{T}\right)^2 K_2\left(\frac{m_i}{T}\right) \cosh\left(\frac{\mu_B + Q_i\mu_Q + S_i\mu_S}{T}\right), \tag{1.44}$$

In other words, susceptibility ratios between orders of the same parity

$$\frac{\chi^B_{\mathrm{odd}}}{\chi^B_{\mathrm{odd}}} = \frac{\chi^B_{\mathrm{even}}}{\chi^B_{\mathrm{even}}} \equiv 1, \tag{1.45}$$

which follows the statistical baseline from the Skellam distribution as discussed before. At zero μ_Q and μ_S, we have

$$\frac{\chi^B_{\text{odd}}}{\chi^B_{\text{even}}} = \tanh\frac{\mu_B}{T}. \tag{1.46}$$

Also for a grand canonical ensemble with the Boltzmann approximation, the probability function of the net-baryon number is proved to be expressed solely in terms of the mean numbers of baryons (b) and antibaryons ($\bar{b} = b - B$) by [92]

$$P(B) = \mathrm{e}^{-\left(b+\bar{b}\right)} \left(\frac{b}{\bar{b}}\right)^{B/2} I_B\left(2\sqrt{b\bar{b}}\right), \tag{1.47}$$

with $I_B(x)$ representing the modified Bessel function of the first kind. This is exactly the Skellam distribution with b and $\bar{b}$ as its two parameters, which will be introduced in Section 1.8.7.

Then considering a system described by a canonical ensemble, the mean baryon and antibaryon numbers can be expressed by [94]

$$b = z\frac{I_{B-1}(2z)}{I_B(2z)}, \tag{1.48}$$

$$\bar{b} = z\frac{I_{B+1}(2z)}{I_B(2z)}, \tag{1.49}$$

where $z = \sqrt{z_b z_{\bar{z}}}$, and z_b and $z_{\bar{z}}$ denote the single-particle partition functions for baryons and antibaryons, respectively. The net-baryon number is always conserved in the whole system as $B = b - \bar{b}$. In a subsystem, corresponding to the acceptance defined in experiments, it is found that

$$b_{\mathrm{A}} = \alpha_b b, \tag{1.50}$$

$$\bar{b}_{\mathrm{A}} = \alpha_{\bar{b}} \bar{b}, \tag{1.51}$$

where the subscript A stands for the quantity in the acceptance, and $\alpha_b = z_{b,\mathrm{A}} \big/ z_b$ and $\alpha_{\bar{b}} = z_{\bar{b},\mathrm{A}} \big/ z_{\bar{b}}$ are the acceptance parameters. The probability distribution of the net-baryon number in the acceptance is derived as

$$\begin{aligned} P_{\mathrm{A}}\left(B_{\mathrm{A}}\right) = &\left(\frac{\alpha_b}{\alpha_{\bar{b}}}\right)^{B_{\mathrm{A}}/2} \left(\frac{1-\alpha_b}{1-\alpha_{\bar{b}}}\right)^{\left(B-B_{\mathrm{A}}\right)/2} \\ &\times \frac{I_{B_{\mathrm{A}}}\left(2z\sqrt{\alpha_b \alpha_{\bar{b}}}\right) I_{B-B_{\mathrm{A}}}\left(2z\sqrt{\left(1-\alpha_b\right)\left(1-\alpha_{\bar{b}}\right)}\right)}{I_B(2z)}, \end{aligned} \tag{1.52}$$

and its cumulant of any order can be calculated accordingly.

2. Effect Study

For a grand canonical ensemble, the logarithm of the partition function follows Equation 1.20. In the HRG model, it is formed by contributions from all stable hadrons and resonances including antiparticles, which can be separated into contributions from baryons and mesons as [93]

$$\ln Z\left(V, T, \mu_B, \mu_Q, \mu_S\right) = \sum_{i \in \text{baryons}} \ln Z_i^{+}\left(V, T, \mu_i\right) + \sum_{i \in \text{mesons}} \ln Z_i^{-}\left(V, T, \mu_i\right), \tag{1.53}$$

where i runs for all particles, and $\mu_i = B_i \mu_B + Q_i \mu_Q + S_i \mu_S$ for the ith particle with B_i, Q_i and S_i. The contribution from the ith particle is expressed by

$$\ln Z_i^{\pm}\left(V, T, \mu_i\right) = \pm \frac{V g_i}{2\pi^2} \int \mathrm{d}^3 \boldsymbol{p} \ln\left(1 \pm \exp\left(\frac{\mu_i - E}{T}\right)\right) \tag{1.54}$$

with g_i representing the degeneracy factor of the ith particle. Hence, we have

$$\frac{P}{T^4} = \frac{1}{VT^3} \ln Z_i = \pm \frac{g_i}{2\pi^2 T^3} \int \mathrm{d}^3 \boldsymbol{p} \ln\left(1 \pm \exp\left(\frac{\mu_i - E}{T}\right)\right), \tag{1.55}$$

and using Equation 1.19, the generalized susceptibilities for baryons can be obtained as

$$\chi_{r,\text{baryon}}^{q} = \frac{q^r}{VT^3} \int \mathrm{d}^3 \boldsymbol{p} \sum_{k=0}^{\infty} (-1)^k (k+1)^{r-1} \exp\left(-\frac{(k+1)E}{T}\right) \exp\left(\frac{(k+1)\mu_q}{T}\right) \tag{1.56}$$

$$\chi_{r,\text{meson}}^{q} = \frac{q^r}{VT^3} \int \mathrm{d}^3 \boldsymbol{p} \sum_{k=0}^{\infty} (k+1)^{r-1} \exp\left(-\frac{(k+1)E}{T}\right) \exp\left(\frac{(k+1)\mu_q}{T}\right), \tag{1.57}$$

where $q = B, Q, S$ of the ith particle and r denotes the order. The total generalized susceptibility is the summed contributions of baryons and mesons as

$$\chi_r^q = \sum \chi_{r,\text{baryon}}^{q} + \sum \chi_{r,\text{meson}}^{q}. \tag{1.58}$$

The HRG results [93] show the cumulant ratios C_2/C_1, C_3/C_2 and C_4/C_2 of net-proton and net-baryon numbers as functions of $\sqrt{s_{\mathrm{NN}}}$ in Figure 1.15. Left panels introduce various p_{T} acceptances and obtain small differences in the results. Right panels compare the cumulant ratios from net-proton numbers with resonance decays, net-proton numbers and net-baryon numbers, all of which show the qualitatively consistent trend in the $\sqrt{s_{\mathrm{NN}}}$ dependence. For C_4/C_2, the effect of resonance decays becomes stronger at lower energies.

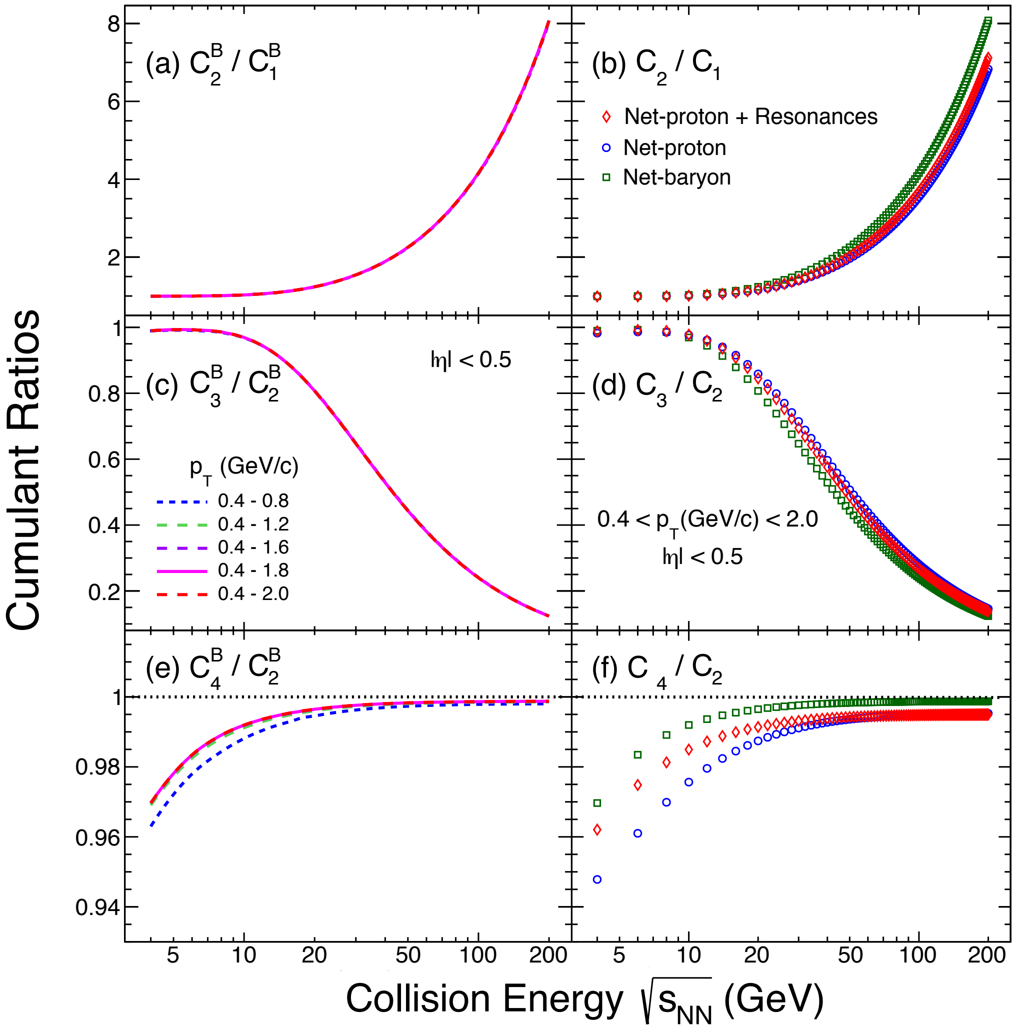

Figure 1.15 (Color online) Net-baryon number cumulant ratios in various transverse momentum (p_T) acceptances (left) and comparison between net-proton and Net-baryon number cumulant ratios (right) as functions of $\sqrt{s_{NN}}$ from the Hadron Resonance Gas (HRG) model. Figure is taken from Reference [93].

1.7.2 UrQMD

The UrQMD model [87-89] is a microscopic model developed to simulate relativistic heavy-ion collisions in a wide energy range from Bevalac and SIS up to AGS, SPS and RHIC. It processes transports and interactions of hadrons, including binary scatterings, formation of color strings and resonance decays, starting from the collision. About 100 species of hadrons are included in the model, the transport trajectories of which are treated to be classical.

The model includes several features also held by the realistic experiments. For example, the baryon, electric-charge and strangeness numbers are always conserved during the simulation, which is also expected in the QCD matter. Besides, a stronger baryon stropping phenomenon exists at lower energies in the model, as also observed in realistic collisions. One critical difference from the experiments is that the model refuses to simulate the deconfinement for hadrons or the thermal QCD medium. In other words, there is no QCD phase transition. Therefore, the UrQMD model provides an excellent comparison to data as the baseline without a critical point taken into account.

1.8 Statistical Measures and Distributions

In statistics, statistical measures, including moments and cumulants, are used to characterize distributions of stochastic variables and quantify their fluctuations of various orders. In this section, definitions and properties of statistical measures, which are relevant to this analysis, will be introduced from a statistical perspective, follower by introductions to several commonly used distributions.

1.8.1 Moment

For a stochastic variable marked by X following the probability mass function $P(X)$, the moment generating function is given by

$$G(\theta) = \sum_{X} P(X)\mathrm{e}^{\theta X} = \left\langle \mathrm{e}^{\theta X} \right\rangle . \tag{1.59}$$

If X is a continuous variable, the summation for the probability mass function should be replaced with the integral of the probability density function, which will not be repeated henceforth. The rth-order moment, also called the moment about the origin, is defined by

$$m_r = \langle X^r \rangle = \partial_\theta^r G(\theta)\big|_{\theta=0} , \tag{1.60}$$

where ∂_θ represents $\dfrac{\partial}{\partial\theta}$.

The four fundamental statistical measures, mean (μ), variance (σ^2), skewness (S) and kurtosis (κ), can be expressed in terms of moments as

$$\mu = m_1, \tag{1.61}$$

$$\sigma^2 = m_2 - m_1^2, \tag{1.62}$$

$$S = \frac{m_3 - 3m_2m_1 + 2m_1^3}{\sigma^3}, \tag{1.63}$$

$$\kappa = \frac{m_4 - 4m_3m_1 + 6m_2m_1^2 - 3m_1^4}{\sigma^4} - 3. \tag{1.64}$$

If we discuss a multivariate case, for example, a bivariate case, two stochastic variables, X and Y, follow the probability mass function $P(X, Y)$, and the moment is defined using its generating function by

$$G(\theta, \eta) = \sum_{X,Y} P(X, Y)\mathrm{e}^{\theta X+\eta Y} = \left\langle \mathrm{e}^{\theta X+\eta Y} \right\rangle, \tag{1.65}$$

$$m_{r,s} = \langle X^r Y^s \rangle = \partial_\theta^r \partial_\eta^s G(\theta, \eta)\big|_{\theta=\eta=0}. \tag{1.66}$$

The generating definitions for more stochastic variables are similar.

1.8.2 Central Moment

The *r*th-order central moment of X, or the moment about the mean, is given by

$$\mu_r = \langle (X - \langle X \rangle)^r \rangle \tag{1.67}$$

with $\mu_1 \equiv 0$.

The variance, skewness and kurtosis can be derived as

$$\sigma^2 = \mu_2, \tag{1.68}$$

$$S = \frac{\mu_3}{\sigma^3}, \tag{1.69}$$

$$\kappa = \frac{\mu_4}{\sigma^4} - 3, \tag{1.70}$$

respectively.

For a bivariate case involving X and Y, the central moment can be defined similarly by

$$\mu_{r,s} = \langle (X - \langle X \rangle)^r (Y - \langle Y \rangle)^s \rangle, \tag{1.71}$$

and $\mu_{1,1}$ is specifically the covariance between X and Y.

1.8.3 Factorial Moment

The *r*th-order factorial moment of X is derived from its generating function by

$$G_\mathrm{f}(u) = \sum_X P(X)u^X = \left\langle u^X \right\rangle, \tag{1.72}$$

$$f_r = \langle X^r \rangle_\mathrm{f} = \partial_u^r G_\mathrm{f}(u)\big|_{u=1}. \tag{1.73}$$

By setting $G = G_\mathrm{f}$ with $\theta = \ln u$, the second-order factorial moment, for example, is calculated by

$$\left\langle X^2 \right\rangle_\mathrm{f} = \partial_u \left(\partial_u\theta\partial_\theta G\right)\big|_{u=1} = \left(\partial_u\theta\right)^2 \partial_\theta^2 G\Big|_{u=1} + \partial_u^2\theta\partial_\theta G\big|_{u=1} = \left\langle X^2 \right\rangle - \langle X \rangle. \tag{1.74}$$

The relations between moments and factorial moments can be summarized as

$$\langle X^r \rangle_\mathrm{f} = \langle X(X-1)\cdots(X-r+1) \rangle. \tag{1.75}$$

1.8.4 Cumulant

For the rth-order cumulant of X, its generating function and definition are

$$G_{\mathrm{c}}(\theta) = \ln G(\theta) = \ln \sum_X P(X) \mathrm{e}^{\theta X} = \ln \left\langle \mathrm{e}^{\theta X} \right\rangle , \tag{1.76}$$

$$C_r = \langle X^r \rangle_{\mathrm{c}} = \partial_\theta^r G_{\mathrm{c}}(\theta)\big|_{\theta=0} . \tag{1.77}$$

For example, the second-order cumulant is calculated by

$$\langle X^r \rangle_{\mathrm{c}} = \partial_\theta^2 \ln G\big|_{\theta=0} = \left.\frac{\partial_\theta^2 G}{G}\right|_{\theta=0} - \left.\frac{\left(\partial_\theta G\right)^2}{G^2}\right|_{\theta=0} = \left\langle X^2 \right\rangle - \langle X \rangle^2. \tag{1.78}$$

Cumulants up to the sixth order can be expressed by the mean and central moments as

$$C_1 = \mu, \tag{1.79}$$

$$C_2 = \mu_2, \tag{1.80}$$

$$C_3 = \mu_3, \tag{1.81}$$

$$C_4 = \mu_4 - 3\mu_2^2, \tag{1.82}$$

$$C_5 = \mu_5 - 10\mu_3\mu_2, \tag{1.83}$$

$$C_6 = \mu_6 - 15\mu_4\mu_2 - 10\mu_3^2 + 30\mu_2^3, \tag{1.84}$$

and can also be calculated recursively by

$$C_r \ (r \geqslant 1) = m_r - \sum_{i=1}^{r-1} \binom{r-1}{i-1} m_{r-i} C_i, \tag{1.85}$$

$$C_r \ (r \geqslant 2) = \mu_r - \sum_{i=2}^{r-2} \binom{r-1}{i-1} \mu_{r-i} C_i. \tag{1.86}$$

Fundamental statistical measures can be derived by

$$\mu = C_1, \tag{1.87}$$

$$\sigma^2 = C_2, \tag{1.88}$$

$$S = \frac{C_3}{\sigma^3}, \tag{1.89}$$

$$\kappa = \frac{C_4}{\sigma^4}, \tag{1.90}$$

and also form cumulant ratios as

$$\frac{C_2}{C_1} = \frac{\sigma^2}{\mu}, \tag{1.91}$$

$$\frac{C_3}{C_1} = \frac{S\sigma^3}{\mu}, \tag{1.92}$$

$$\frac{C_3}{C_2} = S\sigma, \tag{1.93}$$

$$\frac{C_4}{C_2} = \kappa\sigma^2. \tag{1.94}$$

Figure 1.16 [95-96] illustrates skewness and kurtosis. Skewness quantifies the asymmetry of a distribution, while kurtosis measures the sharpness of the peak or the heaviness of the tails relative to a normal distribution, or called "peakedness" or "tailedness". C_3 and C_4 also carry similar information.

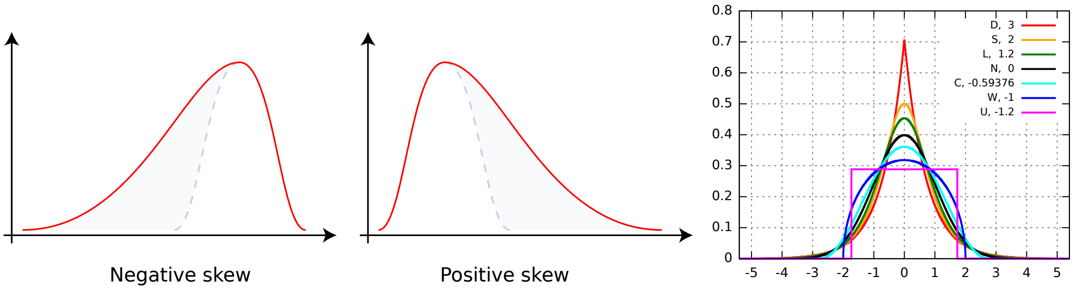

Figure 1.16 (Color online) Illustrations of skewness (left) and kurtosis (right) for various distributions. Figure is taken from References [95-96].

A critical property of the cumulant is the additivity. Suppose X_1 and X_2 are independent and do not correlate, so the moment generating function for $X_1 \pm X_2$ is expressed by

$$G^{X_1 \pm X_2}(\theta) = \left\langle \mathrm{e}^{\theta(X_1 \pm X_2)} \right\rangle = \left\langle \mathrm{e}^{\theta X_1} \right\rangle \left\langle \mathrm{e}^{\pm\theta X_2} \right\rangle = G^{X_1}(\theta) G^{X_2}(\pm\theta), \tag{1.95}$$

and the cumulant generating function can be decomposed as

$$G_{\mathrm{c}}^{X_1 \pm X_2}(\theta) = \ln G^{X_1 \pm X_2}(\theta) = \ln G^{X_1}(\theta) + \ln G^{X_2}(\pm\theta) = G_{\mathrm{c}}^{X_1}(\theta) + G_{\mathrm{c}}^{X_2}(\pm\theta). \tag{1.96}$$

Thus, we have

$$\begin{aligned} \left\langle (X_1 \pm X_2)^r \right\rangle_{\mathrm{c}} &= \partial_\theta^r G_{\mathrm{c}}^{X_1}(\theta) \Big|_{\theta=0} + \partial_\theta^r G_{\mathrm{c}}^{X_2}(\pm\theta) \Big|_{\theta=0} \\ &= \partial_\theta^r G_{\mathrm{c}}^{X_1}(\theta) \Big|_{\theta=0} + (-1)^r \, \partial_\theta^r G_{\mathrm{c}}^{X_2}(\theta) \Big|_{\theta=0} \\ &= \left\langle X_1^r \right\rangle_{\mathrm{c}} + (-1)^r \left\langle X_2^r \right\rangle_{\mathrm{c}}, \end{aligned} \tag{1.97}$$

or

$$C_r^{X_1 \pm X_2} = C_r^{X_1} + (-1)^r C_r^{X_2} \tag{1.98}$$

for independent X_1 and X_2.

For a bivariate case, the cumulant of X and Y is defined as

$$G_{\mathrm{c}}(\theta,\eta)=\ln G(\theta,\eta)=\ln\sum_{X,Y}P(X,Y)\mathrm{e}^{\theta X+\eta Y}=\ln\left\langle \mathrm{e}^{\theta X+\eta Y}\right\rangle, \tag{1.99}$$

$$C_{r,s}=\langle X^rY^s\rangle_{\mathrm{c}}=\partial_\theta^r\partial_\eta^s G_{\mathrm{c}}(\theta,\eta)\big|_{\theta=\eta=0}, \tag{1.100}$$

where $C_{1,1}=\mu_{1,1}$ is equal to the covariance. The additive property remains for the multivariate case.

1.8.5 Factorial Cumulant

The definition of the rth-order factorial cumulant of X using its generating function is

$$G_{\mathrm{fc}}(u)=\ln G_{\mathrm{f}}(u)=\ln\sum_{X}P(X)u^X=\ln\left\langle u^X\right\rangle, \tag{1.101}$$

$$\kappa_r=\langle X^r\rangle_{\mathrm{fc}}=\partial_u^r G_{\mathrm{fc}}(u)\big|_{u=1}. \tag{1.102}$$

The relations between cumulants and factorial cumulants are similar to those between moments and factorial moments, which can be summarized as

$$\langle X^r\rangle_{\mathrm{fc}}=\langle X(X-1)\cdots(X-r+1)\rangle_{\mathrm{c}}, \tag{1.103}$$

and those up to the sixth order are listed here

$$\kappa_1=C_1, \tag{1.104}$$

$$\kappa_2=C_2-C_1, \tag{1.105}$$

$$\kappa_3=C_3-3C_2+2C_1, \tag{1.106}$$

$$\kappa_4=C_4-6C_3+11C_2-6C_1, \tag{1.107}$$

$$\kappa_5=C_5-10C_4+35C_3-50C_2+24C_1, \tag{1.108}$$

$$\kappa_6=C_6-15C_5+85C_4-225C_3+274C_2-120C_1. \tag{1.109}$$

1.8.6 Poisson Distribution

The Poisson distribution is a fundamental distribution for a non-negative integer stochastic variable, which describes the number of events occurring within a fixed interval of time/space, given that these events happen with a known constant mean rate and independently of the time since the last event. If $X\sim\mathrm{Poisson}(\lambda)$, the probability mass function is

$$P(X=k)=\frac{\lambda^k\mathrm{e}^{-\lambda}}{k!} \tag{1.110}$$

with one parameter $\lambda > 0$ as the mean rate per interval. $k = 0, 1, \cdots$ is the number of events.

The cumulant generating function and cumulant are given by

$$G_{\mathrm{c}}(\theta) = \ln\left(\mathrm{e}^{-\lambda}\sum_{k=0}^{\infty}\frac{\left(\lambda \mathrm{e}^{\theta}\right)^k}{k!}\right) = \lambda\left(\mathrm{e}^{\theta}-1\right), \tag{1.111}$$

$$C_r = \lambda. \tag{1.112}$$

The factorial-cumulant generating function and factorial cumulant are given by

$$G_{\mathrm{fc}}(u) = \ln\left(\mathrm{e}^{-\lambda}\sum_{k=0}^{\infty}\frac{(\lambda u)^k}{k!}\right) = \lambda u, \tag{1.113}$$

$$\kappa_r = \begin{cases}\lambda & \text{if } r = 1,\\ 0 & \text{if } r \geqslant 2.\end{cases} \tag{1.114}$$

Thus, for the Poisson distribution, all the cumulants are equal, leading to the cumulant ratios always at unity. The factorial cumulants from the second order onward are zero. In other words, higher-order factorial cumulants quantify non-Poisson fluctuations.

1.8.7 Skellam Distribution

The Skellam distribution is a distribution for an integer stochastic variable describing the difference between two independent Poisson-distributed stochastic variables. If $X_1 \sim \text{Poisson}\left(\lambda_1\right)$ and $X_2 \sim \text{Poisson}\left(\lambda_2\right)$ are independent, $X_1 - X_2$ follows $\text{Skellam}\left(\lambda_1, \lambda_2\right)$ with the probability mass function

$$P(X = k) = \mathrm{e}^{-\left(\lambda_1+\lambda_2\right)}\left(\frac{\lambda_1}{\lambda_2}\right)^{k/2} I_k\left(2\sqrt{\lambda_1\lambda_2}\right), \tag{1.115}$$

where $I_k(x)$ is the modified Bessel function of the first kind.

Using the additive property, the cumulant can be derived from the Poisson distribution as

$$C_r = \begin{cases}\lambda_1 - \lambda_2 & \text{if } r \text{ is odd},\\ \lambda_1 + \lambda_2 & \text{if } r \text{ is even}.\end{cases} \tag{1.116}$$

It is easy to see that the cumulant ratios between orders of the same parity are always unity.

1.8.8 Binomial Distribution

The Binomial distribution is a commonly used distribution for a non-negative integer stochastic variable. It describes the number of successes in a fixed number of independent Bernoulli trials, each with the same probability of success. If $X \sim \text{Binomial}(n, p)$, the probability mass function is

$$P(X = k) = \binom{n}{k} p^k (1 - p)^{n-k}, \tag{1.117}$$

with two parameters: $n = 0, 1, \cdots$ as the number of Bernoulli trials and $0 \leqslant p \leqslant 1$ as the probability of success on each trial. $k = 0, 1, \cdots, n$ is the number of successes.

The cumulant generating function and cumulant can be expressed as

$$G_{\mathrm{c}}(\theta) = \ln \sum_{k=0}^{n} \binom{n}{k} \left(p\mathrm{e}^{\theta}\right)^k (1 - p)^{n-k} = n \ln\left(1 - p + p\mathrm{e}^{\theta}\right), \tag{1.118}$$

$$C_r = \begin{cases} np & \text{if } r = 1, \\ np(1 - p) & \text{if } r = 2, \\ np(1 - p)(1 - 2p) & \text{if } r = 3, \\ np(1 - p)\left(1 - 6p + 6p^2\right) & \text{if } r = 4, \\ np(1 - p)\left(1 - 14p + 36p^2 - 24p^3\right) & \text{if } r = 5, \\ np(1 - p)\left(1 - 30p + 150p^2 - 240p^3 + 120p^4\right) & \text{if } r = 6, \\ \cdots. \end{cases} \tag{1.119}$$

Similarly, the factorial-cumulant generating function and factorial cumulant are given by

$$G_{\mathrm{fc}}(u) = \ln \sum_{k=0}^{n} \binom{n}{k} (pu)^k (1 - p)^{n-k} = n \ln(1 - p + pu), \tag{1.120}$$

$$\kappa_r = (-1)^{k-1}(k - 1)!np^k. \tag{1.121}$$

1.8.9 Negative Binomial Distribution

The negative binomial distribution (NBD), as a probability distribution for a non-negative integer stochastic variable, describes the number of failures required to achieve a specified number of successes in a sequence of independent Bernoulli trials with the same probability of success. The probability mass function is

$$P(X = k) = \binom{k + r - 1}{k} p^r (1 - p)^k, \tag{1.122}$$

with two parameters: $r = 0, 1, \cdots$ as the number of successes and $0 \leqslant p \leqslant 1$ as the probability of success on each trial. $k = 0, 1, \cdots$ is the number of failures.

The cumulant is derived from its generating function as

$$G_{\mathrm{c}}(\theta) = \ln \sum_{k=0}^{\infty} \binom{k+r-1}{k} p^r \left((1-p)\mathrm{e}^{\theta}\right)^k = r \ln \frac{p}{1-(1-p)\mathrm{e}^{\theta}}, \tag{1.123}$$

$$C_r = \begin{cases} \dfrac{r(1-p)}{p} & \text{if } r = 1, \\ \dfrac{r(1-p)}{p^2} & \text{if } r = 2, \\ \dfrac{r(1-p)(2-p)}{p^3} & \text{if } r = 3, \\ \dfrac{r(1-p)(6-6p+p^2)}{p^4} & \text{if } r = 4, \\ \cdots . \end{cases} \tag{1.124}$$

1.8.10 Gaussian Distribution

The Gaussian distribution, also known as the normal distribution, is one of the most important probability distributions for real-valued stochastic variables, related to many natural phenomena. If $X \sim \mathrm{Gaus}\left(\mu, \sigma^2\right)$, the probability density function is

$$f(x) = \frac{1}{\sqrt{2\pi}\sigma} \exp\left(-\frac{(x-\mu)^2}{2\sigma^2}\right). \tag{1.125}$$

The cumulant generating function and cumulant are

$$G_{\mathrm{c}}(\theta) = \mu\theta + \frac{1}{2}\sigma^2\theta^2 + \ln \int_{-\infty}^{+\infty} \mathrm{d}x f\left(x - \sigma^2\theta\right) = \mu\theta + \frac{1}{2}\sigma^2\theta^2, \tag{1.126}$$

$$C_r = \begin{cases} \mu & \text{if } r = 1, \\ \sigma^2 & \text{if } r = 2, \\ 0 & \text{if } r \geqslant 3. \end{cases} \tag{1.127}$$

All the Gaussian cumulants from the third order onward are zero, so higher-order cumulants quantify non-Gaussian fluctuations.

1.9 Motivation

Mapping the QCD phase diagram as a function of T and μ_B is one of the fundamental goals of high-energy nuclear physics including both theoretical and experimental researches. The QCD critical point, expected by related theories, is a distinct singular phase structure. Search for the critical point, confirming its existence and locating it in the phase diagram, would provide deep insights into the nature of the strong interaction, as well as the behavior of QCD matter under extreme conditions of temperature and density. Moreover, it would also enhance our understanding on the early universe, where similar conditions existed shortly after the Big Bang.

Higher-order fluctuations of conserved charges, such as net-baryon, net-electric-charge and net-strangeness numbers, are theoretically predicted to be sensitive to the QCD phase structure [45]. A non-monotonic $\sqrt{s_{\mathrm{NN}}}$ dependence of C_4/C_2 would serve as a clear signal of the critical region [51]. Net-proton number fluctuations are believed to reflect the magnitude of the net-baryon number [54], making their higher-order cumulants and factorial cumulants effective experimental observables [48]. Theoretical predictions also indicate that fluctuations in larger acceptances would carry significantly stronger signatures of critical fluctuations and correlations [64].

RHIC has completed the Beam Energy Scan (BES) program including the first phase (BES-I, 2010–2017) and the second phase (BES-II, 2018–2021) by performing Au+Au collision experiments at $\sqrt{s_{\mathrm{NN}}}$ = 3–200 GeV [97]. This program provides a critical opportunity to explore the QCD phase diagram over a wide region of T and μ_B ranging approximately from 25 to 750 MeV. The STAR experiment has published the measurement of the net-proton number fluctuations from $\sqrt{s_{\mathrm{NN}}}$ = 7.7, 11.5, 14.5, 19.6, 27, 39, 54.4, 62.4 and 200 GeV from BES-I [83,98], and C_4/C_2 in central collisions shown in Figure 1.17 [99] exhibits a non-monotonic dependence on $\sqrt{s_{\mathrm{NN}}}$ with a significance of 3.1σ. The shape of the energy dependence agrees with the theoretical predictions shown in the right panel of Figure 1.12 and deviates from several models that do not include a critical point, suggesting a signal of the possible critical region. The most recent result from $\sqrt{s_{\mathrm{NN}}}$ = 3 GeV [99-100], also shown in Figure 1.17, is dramatically lower than the BES-I measurement but consistent with the UrQMD model calculation. This indicates that C_4/C_2 returns to the baseline, so the matter created at $\sqrt{s_{\mathrm{NN}}}$ = 3 GeV could be predominantly hadronic, and the critical region is not likely to exist in heavy-ion collisions at energies lower than 3 GeV.

The hyper-order cumulant ratios C_5/C_1 and C_6/C_2 are presented in Figure 1.18 [102]. The progressively negative C_6/C_2 in central collisions as $\sqrt{s_{\mathrm{NN}}}$ decreases down to 7.7 GeV represents a qualitative consistency with the theoretical predictions from lattice QCD shown in Figure 1.13 and FRG shown in Figure 1.14. The UrQMD calculation is either positive or consistent with zero as a baseline. This observation supports a crossover signature near the energy region. The significantly positive hyper-order cumulants from $\sqrt{s_{\mathrm{NN}}}$ = 3 GeV also support the hadronic matter as sug-

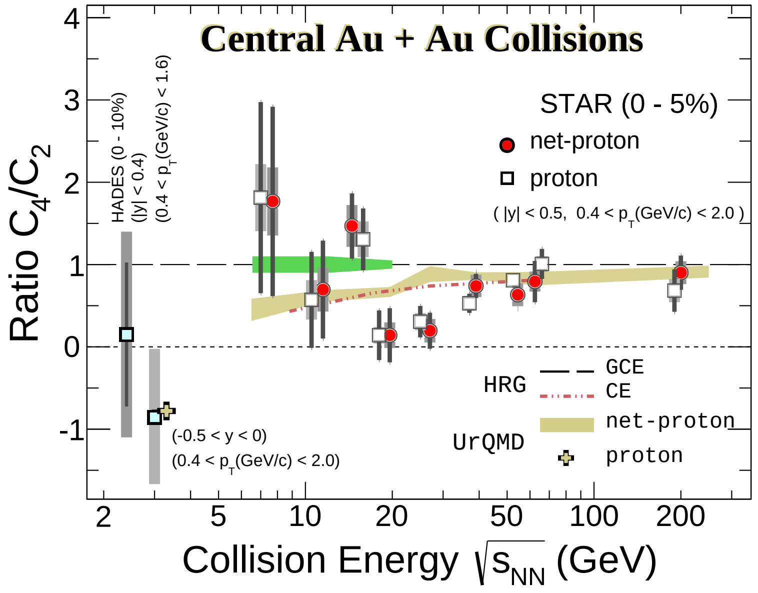

Figure 1.17 (Color online) $\sqrt{s_{\rm NN}}$ dependence of net-proton number C_4/C_2 in central Au+Au collisions. Experimental results are measured by the STAR [83,98-100] and HADES [101] experiments are compared to HRG and UrQMD model calculations as baselines. Figure is taken from Reference [99].

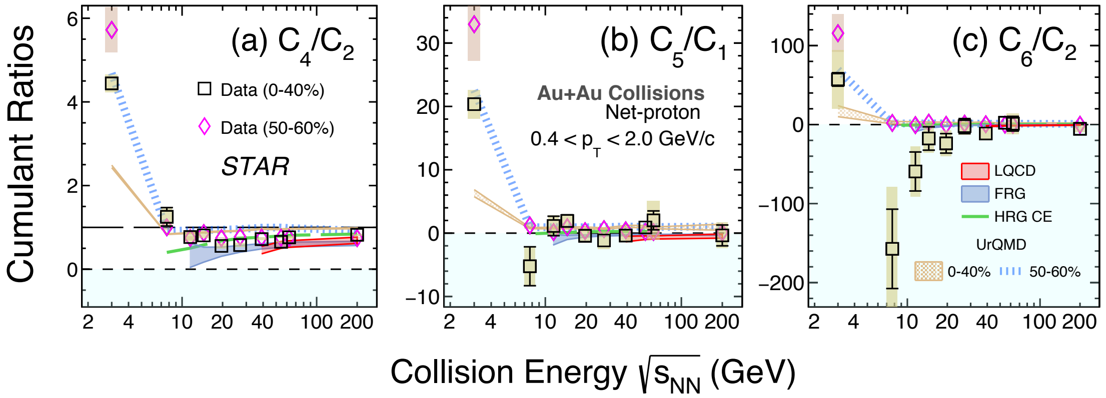

Figure 1.18 (Color online) $\sqrt{s_{\rm NN}}$ dependence of net-proton number C_4/C_2, C_5/C_1 and C_6/C_2 in Au+Au collisions. Experimental results measured by the STAR experiment [84,102] are compared to calculations from lattice QCD, FRG and HRG and UrQMD models. Figure is taken from Reference [102].

gested by C_4/C_2.

However, cumulants and factorial cumulants up to the sixth order have quite large uncertainties in the range of $\sqrt{s_{\rm NN}}$ = 7.7–27 GeV, and a strong gap exists in measured energy range between 3 GeV and 7.7 GeV, making it difficult to draw strong conclusions. The BES-II program focuses on the high-baryon-density region at relatively low collision energies with 7–18 times more events than BES-I. Fixed-target experiments fill in the collision energy range from $\sqrt{s_{\rm NN}}$ = 3 to 13.7 GeV, and collider experiments are taken from $\sqrt{s_{\rm NN}}$ = 7.7 to 27 GeV with two new energies, 9.2 GeV and

17.3 GeV [103]. Furthermore, the STAR detector system has been upgraded with three new detectors, iTPC [104], eTOF [105] and EPD [106], to improve the data quality and enlarge the acceptance coverage.

This analysis is motivated by the goal of measuring net-proton number fluctuations utilizing the new data collected by STAR from the RHIC BES-II collider experiments. With the enhanced statistics, the upgraded detector system and the improved analysis techniques recent years, we are expected to have a significantly higher precision and reliability on the result compared to BES-I and an opportunity to observe the acceptance dependence in a broader range. The new measurement would provide us a better understanding on the QCD phase structure including the existence or inexistence of the critical point and its possible approximate location in the phase diagram.

The thesis is organized as follows: Chapter 1 provides an the introduction to the QCD phase diagram and reviews theoretical and experimental efforts of the exploration. Theorists describe the brief picture of the phase structure and find effective observables and potential signatures, such as higher-order fluctuations of conserved charges. Experimentalists design relativistic heavy-ion collisions and achieve many invaluable measurements. Necessary conclusions of statistics are also presented in this chapter. Chapter 2 details the experimental facilities and program involved. An accelerator, RHIC, and a detector system, STAR, are introduced, explaining where and how the data used in this analysis were collected. Additionally, the BES program, where the data originate, is also covered. Chapter 3 focuses on the analysis techniques and procedures. It discusses methods for selecting high-quality runs, events, and tracks, as well as strategies for mitigating negative effects and noise in the measurement of high-order fluctuations. A study based on the UrQMD model is also included, providing an important reference for the experimental analysis. Chapter 4 presents the results, including net-proton, proton and antiproton number distributions, cumulants and factorial cumulants. It also includes comparisons with theoretical models. Chapter 5, the last chapter, concludes the dissertation with a summary of the analysis and discussions on the findings. An outlook on future measurements and experiments is also given.

Chapter 2 Experimental Setup

2.1 The RHIC Complex

RHIC [107-108] is one of the most significant scientific facilities to accelerate heavy ions to relativistic collisions for studying the formation and properties of nuclear matter at extreme temperatures and densities. Figure 2.1 [109] shows a chain of accelerators at BNL, where RHIC is located. It consists of two superconducting magnet rings, each with a circumference of 3.8 km. Within these rings, particle beams travel in opposite directions: clockwise in the "blue" ring and counter-clockwise in the "yellow" ring. Both rings are capable of accelerating ions to relativistic speeds and storing them for several hours. There are six intersection points where the two beams can collide, providing locations for various detectors used in experiments. When RHIC began operations in 2000, it hosted four major experiments: BRAHMS [110] at 2 o'clock, STAR [111] at 6 o'clock, PHENIX [112] at 8 o'clock, and PHOBOS [113] at 10 o'clock. The PHOBOS, BRAHMS, and PHENIX experiments concluded in 2005, 2006, and 2016, respectively. However, the STAR experiment continues to operate and contribute valuable data. In 2023, a new experiment called sPHENIX [114] was initiated by installing a new detector at the former location of PHENIX.

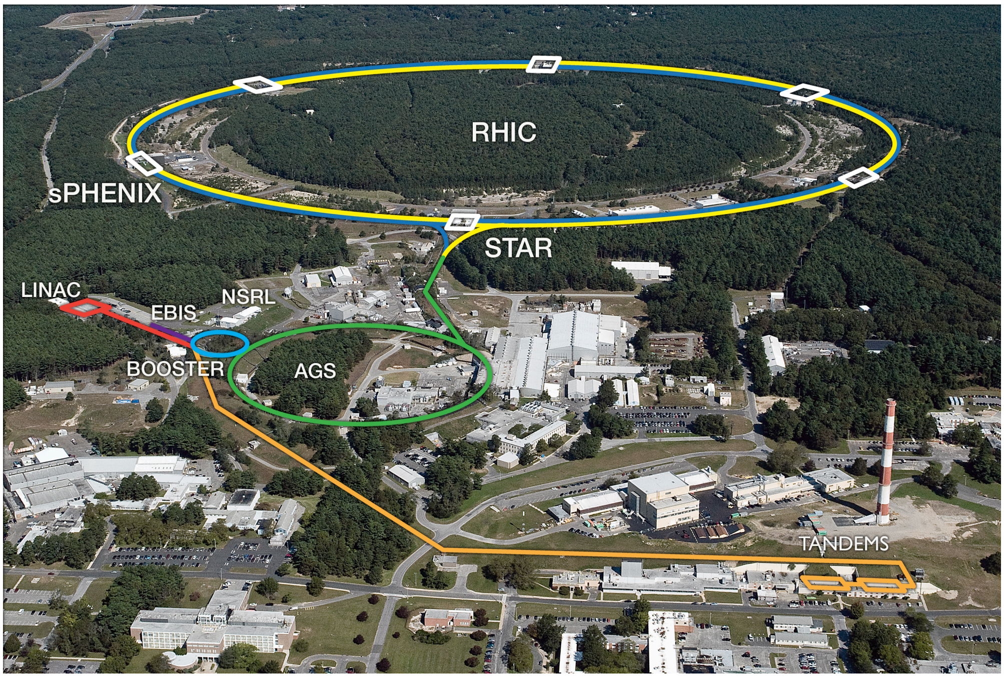

Figure 2.1 (Color online) A chain of accelerators at BNL for protons or atomic nuclei including Relativistic Heavy Ion Collider (RHIC). Detectors of the running experiments, STAR and sPHENIX, are installed in two of the six intersection points where beam pairs collide. Figure is taken from Reference [109].

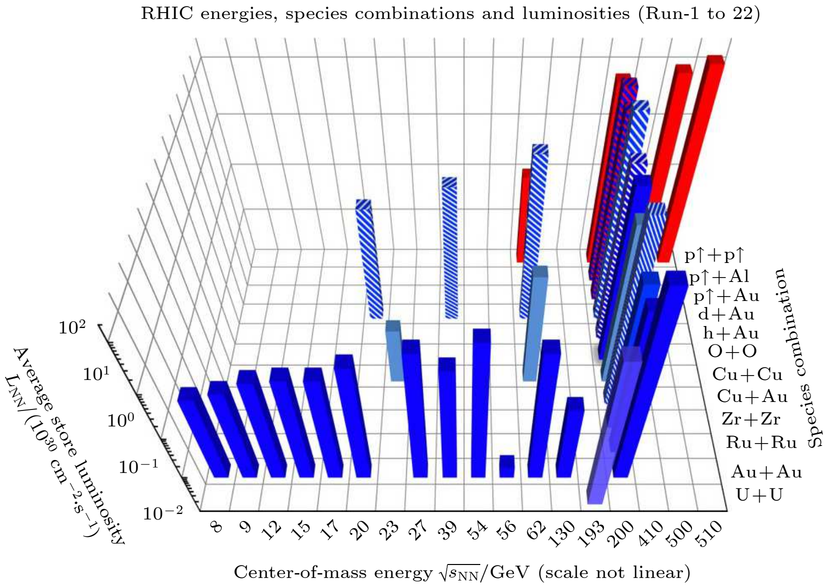

Figure 2.2 (Color online) Relativistic ion collision experiments of various systems and energies performed at RHIC from Run-1 to Run-22. Figure is taken from Reference [115].

The idea for RHIC emerged in the late 1980s as the need to explore QGP and the condition of the early universe became evident. The construction began in 1991, leveraging the existing infrastructure at BNL from previous accelerators, such as AGS, which played a pivotal role in pre-accelerating ions. RHIC was fully built in 1999 and started its first operation in the next year, with the initial runs focusing on search for QGP signatures in relativistic heavy-ion collisions. Plans are underway to switch the RHIC infrastructure into Electron-Ion Collider (EIC) within the next few years, and RHIC may conduct its final run in 2025 to prepare for the construction of EIC.

RHIC primarily collides $^{197}\mathrm{Au}^{79+}$, which are densely packed with nucleons and originate from one of the heaviest common nuclei. Other ions, such as $^{238}\mathrm{U}^{92+}$, $^{96}\mathrm{Ru}^{44+}$, $^{96}\mathrm{Zr}^{40+}$, $^{63+}\mathrm{Cu}^{29+}$, $^{27+}\mathrm{Al}^{13+}$, $^{16}\mathrm{O}^{8+}$, $^{3}\mathrm{He}^{2+}$, d and p, from heaviest to lightest, are also selected by RHIC to create systems of different sizes. Here, $^{96}\mathrm{Ru}^{44+}$ and $^{96}\mathrm{Zr}^{40+}$ belong to an isobaric state due to the same mass number, providing opportunity to study the chiral magnetic effect [116]. It is worth mentioning that RHIC is currently the only collider for high-energy beams of spin-polarized protons to explore the proton spin structure [117]. The beam energy of RHIC for Au is designed to reach a maximum of 100 AGeV and can be adjusted over a wide range, down to 3.85 AGeV. In other words, RHIC is capable of conducting Au+Au collisions at $\sqrt{s_{\mathrm{NN}}}$ = 7.7–200 GeV in the collider mode or $\sqrt{s_{\mathrm{NN}}}$ = 3–13.7 GeV in the fixed-target (FXT) mode. The top collision energy is 510 GeV for p+p collisions. Figure 2.2 [115] summarizes the system and energy dependences of relativistic ion collision experiments performed at RHIC from Run-1 to Run-22.

RHIC uses a complex chain of accelerators, shown in Figure 2.1, before the beam injection. Taking Au as an example, the first step was two Tandem van de Graaff accelerators generating Au^{31+} ions. Now this work is turned over to the Electron Beam Ion Source accelerator accelerator (EBIS) with significantly better performance, which provides Au^{32+} ions with the kinetic energy of 2 AMeV. Ions then enter a small and circular synchrotron called Booster. Here, they are accelerated to about 37% the speed of light with the the kinetic energy of 95 AMeV and become Au^{77+} with more electron removed. The beam is fed into AGS, where the kinetic energy reaches 8.86 AGeV, corresponding to 99.7% the speed of light, and ions are fully stripped to be Au^{79+}. Finally, they are sent to the AGS-to-RHIC transfer line (AtR) with a switching magnet at the end to direct ion bunches to either of the RHIC rings. This setup allows for flexibility in choosing different ions and collision energies. For experiments requiring polarized protons, the first step is replaced by Brookhaven Linear Accelerator (Linac) producing a beam of 200 MeV.

2.2 The STAR Experiment

The Solenoidal Tracker at RHIC (STAR) [111] is one of the major experiments conducted at RHIC. The main goal of STAR is investigating the formation and characteristics of QGP and studying the evolution of the collision system under extreme conditions of temperature and density. Figure 2.3 [118] illustrates a schematic of the STAR detector system, which is designed to operate in the environment of high particle multiplicities and energy densities created by heavy-ion collisions at RHIC energies. The system is centered around the beamline, oriented along the east-west axis, and comprises several subsystems as shown in the figure. From the inside out, the central region includes inner Time Projection Chamber (iTPC) [104], Time Projection Chamber (TPC) [119], barrel Time-Of-Flight detector (TOF, or bTOF) [120], Barrel Electromagnetic Calorimeter (BEMC) [121], the magnet [122] and Muon Telescope Detector (MTD) [123]. Additional components are positioned on the east and/or west sides, such as End-cap Electromagnetic Calorimeter (EEMC) [124], end-cap Time-Of-Flight detector (eTOF) [105], and Event Plane Detector (EPD) [106]. Other detectors like Beam-Beam Counter (BBC) [125], Vertex Position Detector (VPD) [126] and Zero-Degree Calorimeter (ZDC) [127] are present but not labelled in the figure. Three new detectors were installed for the BES-II program: EPD ready in 2018, iTPC and eTOF ready in 2019, photos of which are shown in Figure 2.4.

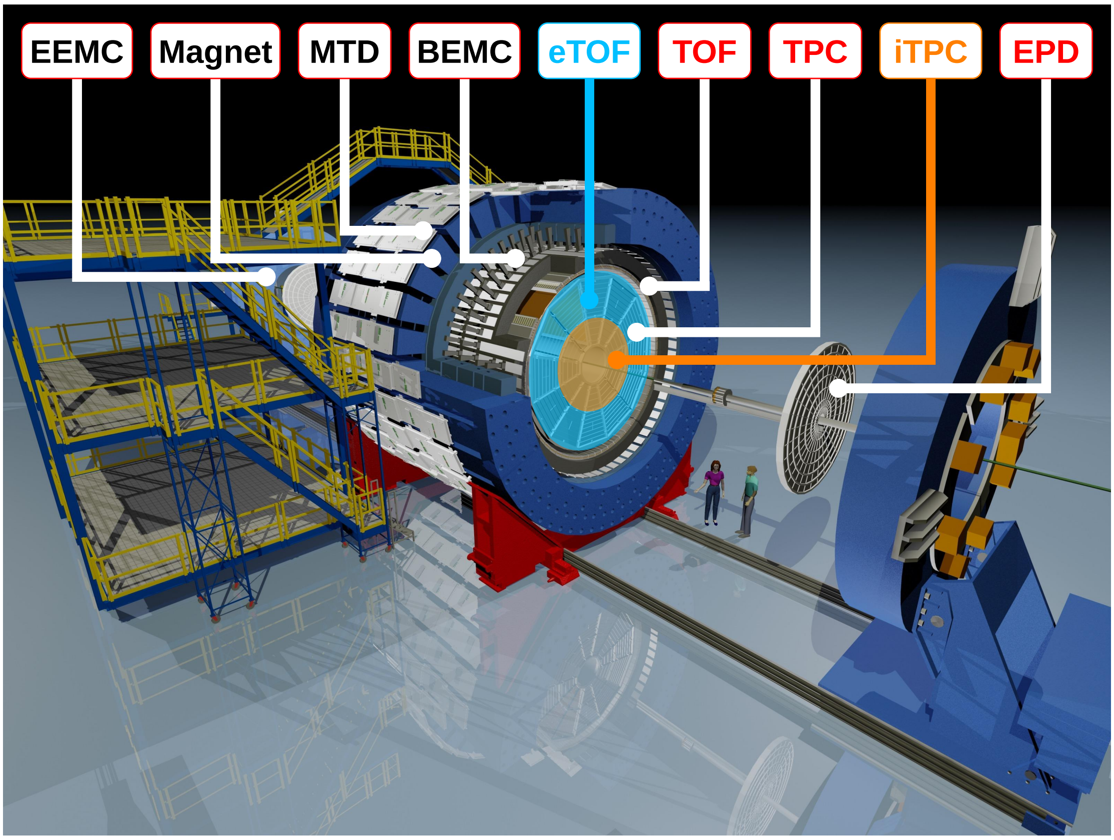

Figure 2.3 (Color online) A sketch of the STAR detector system. The labelled detectors are: End-cap Electromagnetic Calorimeter (EEMC), Muon Telescope Detector (MTD), Barrel Electromagnetic Calorimeter (BEMC), end-cap Time-Of-Flight detector (eTOF), barrel Time-Of-Flight detector (TOF, or bTOF), Time Projection Chamber (TPC), inner Time Projection Chamber (iTPC) and Event Plane Detector(EPD). Figure is taken from Reference [118].

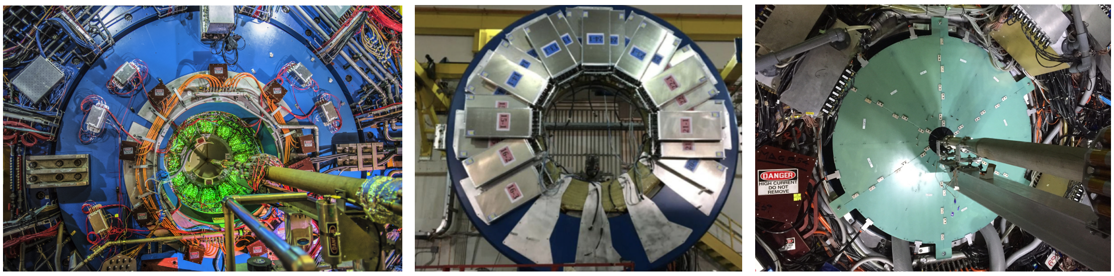

Figure 2.4 (Color online) Photos of the STAR iTPC (left), eTOF (middle) and EPD (right) installed for BES-II. Figure is taken from STAR.

The solenoidal magnet produces a uniform magnetic field along the direction of the beam line, reaching up to 0.5 T. Each detector is responsible for measuring distinct quantities: TPC is the primary component for event primary-vertex construction, charged-particle tracking, momentum measurement and particle identification (PID). TOF and eTOF focus on PID by measuring the time of flight at mid-rapidities and backward rapidities, respectively. BEMC and EEMC detect energy deposition through electromagnetic interactions between charged particles and detector material, while MTD specializes in muon identification. VPD supplements TPC by determining the event primary-vertex position. BBC, ZDC and EPD help reconstruct the event plane using forward particles and, along with VPD, serve as triggers of events to activate other detectors for data collection.

In the coordinate system of the STAR experiment, the positive z-direction points west along the beam line; the y-direction points vertically upward; and the positive x-direction points horizontally south, forming a right-handed coordinate system. The origin, with the coordinate (0, 0, 0), is located at the center of the detector system on the beam line.

The detector system features a wide and uniform acceptance, providing excellent tracking and PID capabilities, along with modest data rates. Several key detectors, which will be discussed in the following sections, contribute to these characterizes.

2.2.1 TPC

The STAR TPC [119] is the primary detector of the system, playing a crucial role in reconstructing primary vertices of events, tracking charged particles, measuring their momenta and identifying particle species with high precision. A sketch of the STAR TPC is shown in Figure 2.5 [119]. It is a cylindrical detector with a length of 420 cm, a inner diameter of 100 cm and a out diameter of 400 cm, and its center is located at the coordinate (0, 0, 0). The chamber is filled with the P10 gas (90% argon and 10% methane) regulated at 2 mbar above the atmospheric pressure as the working gas, providing optimal conditions for ionization and drift of electrons generated by passing

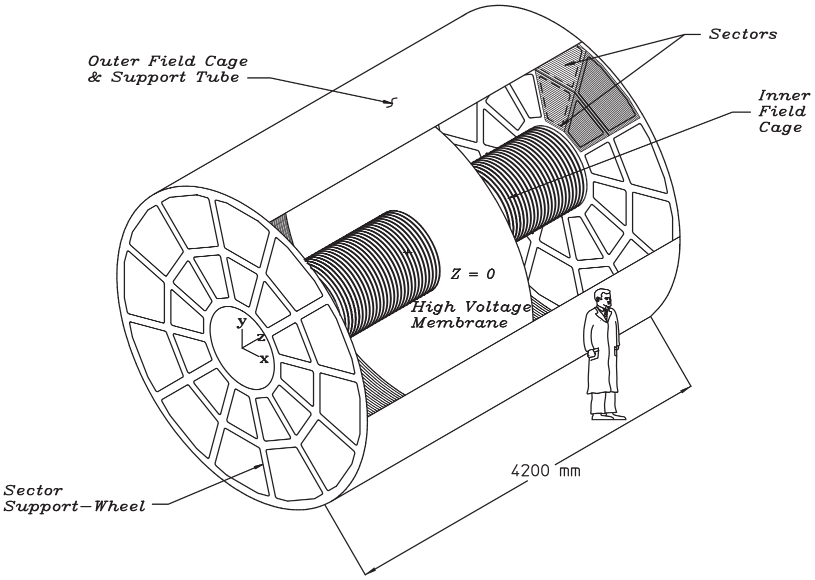

Figure 2.5 A sketch of the STAR TPC. Figure is taken from Reference [119].

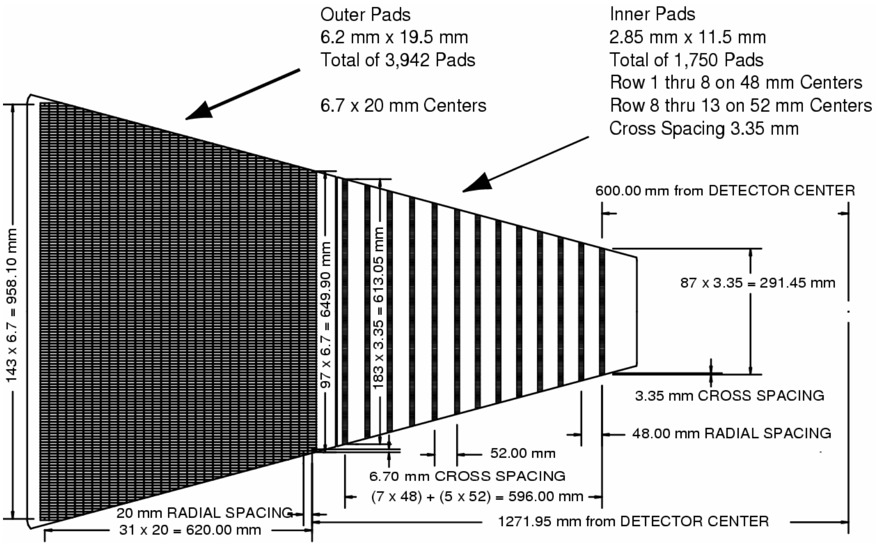

Figure 2.6 A sketch of a full sector in the anode pad plane of TPC before the iTPC upgrade. On the right is the inner sub-sector, with small pads arranged in widely spaced rows. On the left is the outer sub-sector, densely packed with larger pads. Figure is taken from Reference [119].

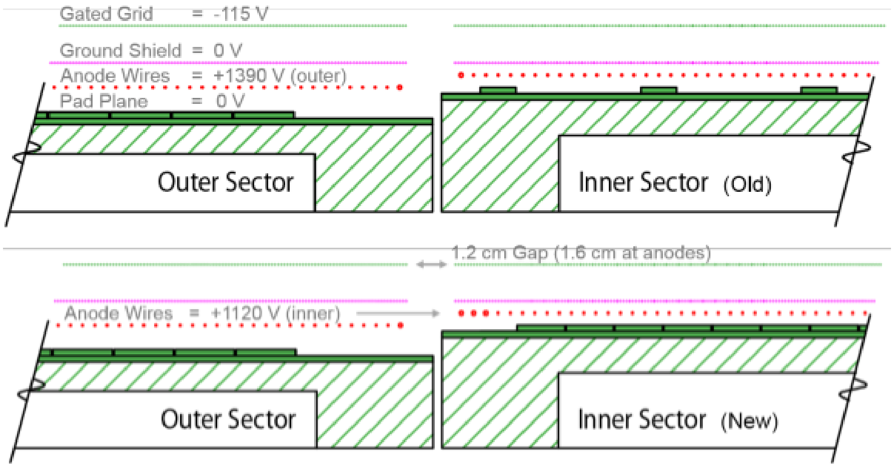

Figure 2.7 (Color online) A side view of a STAR TPC sector before (top) and after (bottom) the iTPC upgrade. The outer sub-sector configuration remains the same, but larger pads are placed in more rows with no gap in the inner sub-sector. Figure is taken from Reference [104].

charged particles. It is symmetrically divided by a central membrane into two halves located on either side of the z-axis, one to the east and one to the west. The central membrane serves as a cathode with a voltage of 28 kV relative to the anode planes at the end caps. An electric field is produced to be 133 keV/cm long the beam line, but the direction is opposite in the east and west halves of TPC. The magnetic field maintained by the magnet sub-system is also along the beam line. In each anode plane, 12 identical sectors are divided with one Multi-Wire Proportional Chambers (MWPC) installed in each. MWPCs are connected to the Front-End Electronic cards (FEEs) and Readout Boards (RDOs) to record electronics about the position and timing and provide them to the Data Acquisition system (DAQ), which can process the vast amount of data generated during collisions, handling high event rates and allowing real-time data analysis.

Figure 2.6 [119] shows a full sector in the anode pad plane of TPC before the iTPC upgrade. A sector is further divided into an inner sub-sector and an outer sub-sector. There were 13 pad rows in each inner sectors and 32 rows in each outer sector. The outer pads are clearly larger and denser without space. Because the particle multiplicities emerging from RHIC collisions at $\sqrt{s_{\mathrm{NN}}}$ = 200 GeV were not known when TPC was designed in 1993–1995, smaller and sparse inner pads were designed to help relieve track merging at small radii in case of very high multiplicities. With the iTPC upgrade ready in 2019, all inner sub-sectors were replaced by 40 new ones, which are fully instrumented, and the outer sub-sectors were not changed. Thus, the total number of the pad rows in each full sector increases from 45 to 72. Figure 2.7 [104] compares the pad rows before and after the iTPC upgrade. It is clear that the new pads are larger and denser with no gap. Besides, there are a few more upgrades in the new pads summarized in Reference [104].

The charged particles flying through TPC can ionize the atoms of the working gas along their trajectories to creating electron-ion pairs. These freed electrons, of which the primary source is argon, drift under the electric field force towards the anode plane. The drift velocity of freed electrons is typically 5.45 cm/μs and can be determined by a laser experiment. Note that the accuracy of electron drift is highly dependent on the uniformity of the electric field. When electrons approach MWPCs at the anode, they are capable of triggering an avalanche effect, making the signal of charges highly amplified to be detected by the readout electronics.

Positions of pads which read the ionization electrons provide x- and y-coordinates of charged-particle paths, and a z-coordinates can be calculated using the drift time and the velocity. The three-dimensional trajectory of each charged particle can be obtained by collecting and fitting coordinates of several points. Bent by the magnetic field, each charged particles flies along a helix, determining the sign of the electric charge by the curvature direction and allowing for the momentum measurement. The momentum can be calculated by

$$p = |q|BR, \tag{2.1}$$

with q, B and R as the electric charge, magnetic field and radius of the helix curvature, respectively.

TPC also measures the energy loss ($\mathrm{d}E/\mathrm{d}x$, or $-\langle \mathrm{d}E/\mathrm{d}x\rangle$) of a charged particle

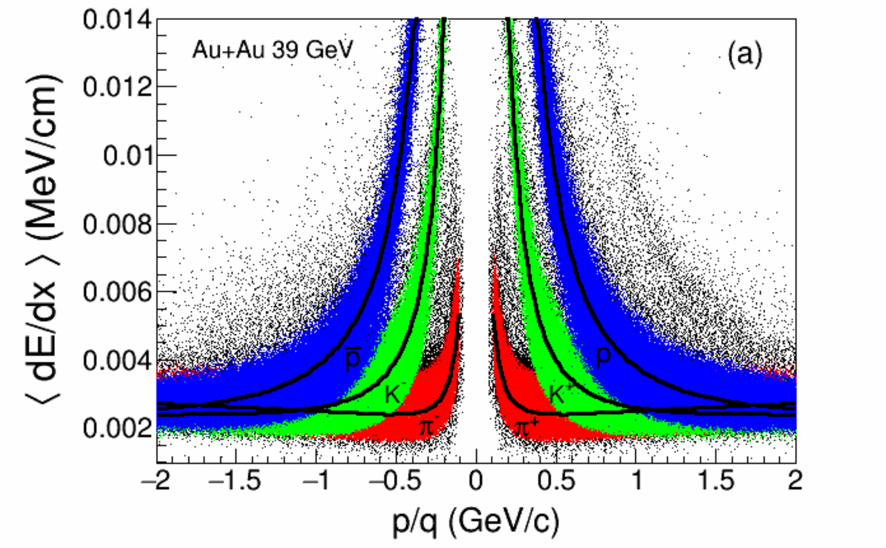

Figure 2.8 (Color online) Momentum (p) dependence of the energy loss ($\mathrm{d}E/\,\mathrm{d}x$) for positively ($q > 0$) and negatively ($q < 0$) charged particles measured by TPC. The black curves represent the expected values for pions, kaons and (anti)protons. Figure is taken from Reference [129].

in the working gas by analyzing the total ionization energy deposited along the trajectory and the distance of the track. The strength of the electronic signal is generally proportional to the number of the primary ionization electrons, which in turn reflects the ionization energy. The theoretical $\mathrm{d}E/\,\mathrm{d}x$ of a particle as a function of p can be described by the Bethe-Bloch formula

$$\frac{\mathrm{d}E}{\mathrm{d}x} = Kz^2\frac{Z}{A}\frac{1}{\beta^2}\left(\frac{1}{2}\ln\frac{2m_\mathrm{e}c^2\beta^2\gamma^2T_\mathrm{max}}{I^2} - \beta^2 - \frac{\delta(\beta\gamma)}{2}\right), \tag{2.2}$$

where $K = 4\pi N_\mathrm{A}r_\mathrm{e}^2m_\mathrm{e}c^2 \approx 0.307075\ \mathrm{MeV{\cdot}mol^{-1}{\cdot}cm^2}$ is a constant; z is the charge number of the incident particle; Z and A are the atomic number and atomic mass of the absorber, respectively; T_max is the maximum transferable energy; I is the material-dependent characteristic ionization constant; and δ is the density effect correction. This function clearly accounts for the mass and charge of particles, enabling the differentiation of various particle species based on their $\mathrm{d}E/\,\mathrm{d}x$ patterns. Note that STAR employs the Bichsel function [128] developed to model $\mathrm{d}E/\,\mathrm{d}x$ in TPC.

Figure 2.12 [129] shows the p dependence of $\mathrm{d}E/\,\mathrm{d}x$ for charged particles measured by TPC. Bands from pions, kaons and protons are labelled by red, green and blue colors, respectively, and the theoretical values are drawn as black solid curves. It can be seen that the bands are going to overlap together at high p due to the comparable theoretical values. This figure indicates that the STAR TPC can separate pions and kaons at $p \lesssim 0.6$ GeV/c, and kaons and protons at $p \lesssim 1$ GeV/c.

With its large volume and high granularity, the TPC provides full azimuthal cov-

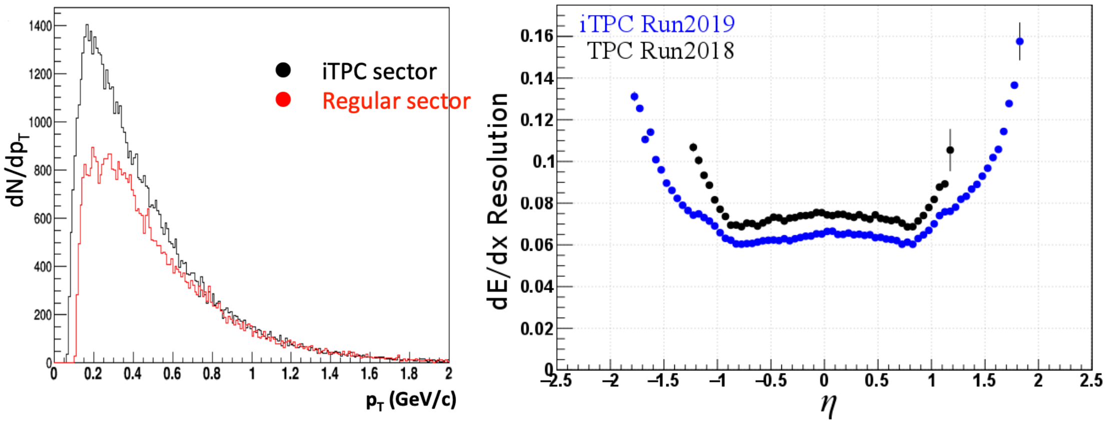

Figure 2.9 (Color online) Comparison of the TPC performance before and after the iTPC upgrade. A lower p_{T} threshold, high tracking efficiency, larger η acceptance and better $\mathrm{d}E/\mathrm{d}x$ resolution are obtained taking advantage of iTPC. Figure is taken from Reference [130].

erage and a large acceptance within $|\eta| \lesssim 1.0$ prior to the iTPC, as well as excellent spatial resolution. These capabilities enable precise tracking of thousands of particles produced in each collision, which is crucial for analyzing complex events in heavy-ion collisions.

After the iTPC upgrade completed in 2019, due to much more pads installed in the inner sub-sectors, the performance of TPC is further improved, reflected by Figure 2.9 [130]. The measured track $\mathrm{d}N/\mathrm{d}p_{\mathrm{T}}$ distributions in the left panel indicate that the p_{T} threshold is reduced from 0.125 GeV/c down to 0.06 GeV/c, and the detection efficiency is enhanced, especially for low-p_{T} tracks. The right panel presents an obviously larger η coverage, effectively extended to $|\eta| \lesssim 1.6$, and a better $\mathrm{d}E/\mathrm{d}x$ resolution. The larger acceptance makes it possible to perform measurements at forward rapidities. The better reconstruction of low-p_{T} tracks, the higher efficiency and the larger acceptance, strongly result in counting much more charged particles, which is expected to improve the centrality resolution, crucial to the fluctuation-related analysis. Furthermore, taking advantage of more track fitting points, the position and momentum resolutions are improved other than the $\mathrm{d}E/\mathrm{d}x$ resolution, which provide higher data quality and accuracy.

2.2.2 TOF

The STAR TOF [120] is designed to complement TPC by aiding in the identification of high-p particles, and It is configured as a cylindrical shell around the TPC, providing full azimuthal coverage and an acceptance range of $|\eta| \lesssim 0.9$, similar to TPC.

TOF utilizes the technique of Multi-gap Resistive Plate Chamber (MRPC) developed from Resistive Plate Chamber (RPC). It consists of 120 trays, each containing

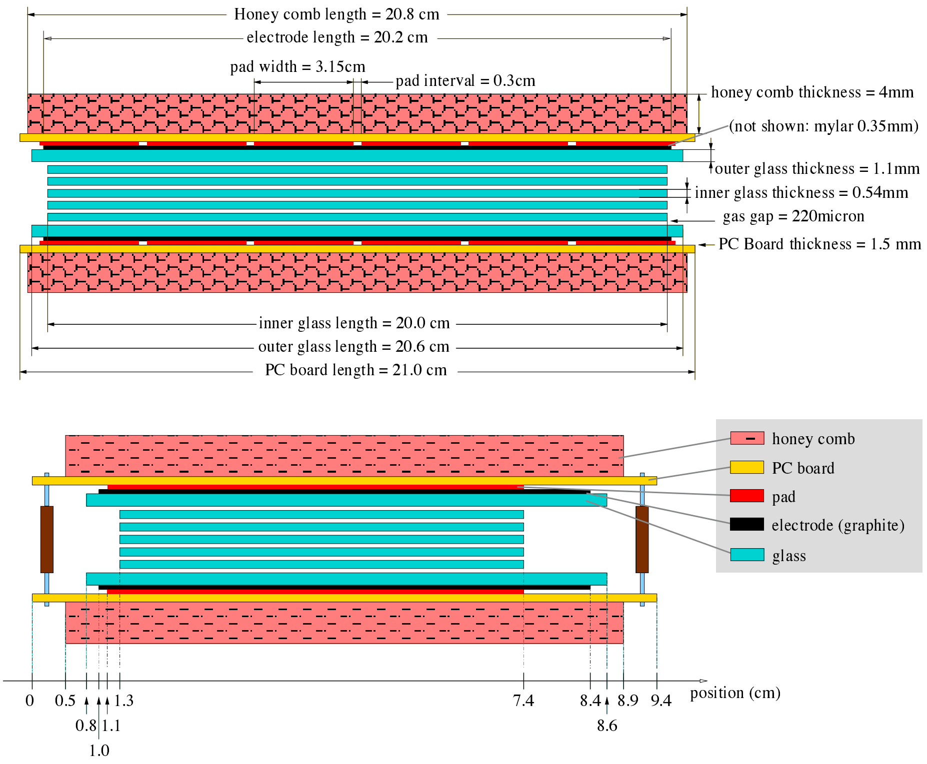

Figure 2.10 (Color online) Two different side views of the STAR TOF MRPC module. The upper and lower ones show the long and short edges of different scales, respectively. Figure is taken from Reference [120].

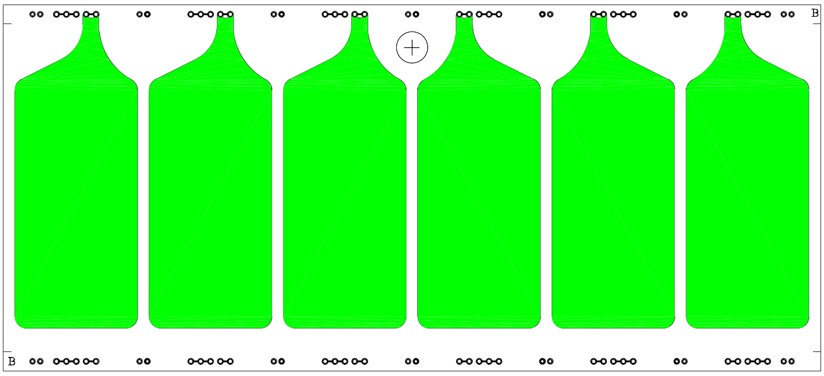

Figure 2.11 (Color online) A sketch of the circuit board with the copper read-out pads of the STAR TOF MRPC module. Figure is taken from Reference [120].

32 MRPC modules. A schematic of the MRPC module structure is illustrated in Figure 2.10 [120]. Each MRPC module comprises seven stacked resistive plates with six uniform gas gaps between consecutive plates. These gaps are filled with a gas mixture of 95% R-134a and 5% iso-Butane [131]. The resistive plates are made of high-resistivity glass, typically around 10^{13} Ω/cm, with the outer plates being thicker than the inner ones. The outer surfaces of these plates are coated with electrodes made of graphite tape, featuring a surface resistivity of 10^5 Ω. These electrodes are connected to six cop-

per read-out pads, as depicted in Figure 2.11 [120], which are used for signal recording. A high voltage across the electrodes generates a strong electric field within the module, causing the inner plates to float electrically.

Once a charged particle traverses the chamber, avalanches take place in the gas gaps. Due to the high resistivity of the glass plates and graphite electrodes, these components are transparent to the charge induction resulting from these avalanches. Consequently, avalanches occurring in all gas gaps contribute to a cumulative signal on the read-out pads.

TOF has an excellent intrinsic time resolution of approximately 80–95 ps [132]. It measures the timing of the charged particle at the end of its trajectory with an excellent resolution and operates together with two identical VPDs, each 5.4 m away from the TPC center along the beam line, which determine the start time by measuring the forward particles [133]. The time of flight is calculated as the difference

$$\Delta t = t_{\text{TOF}} - t_{\text{VPD}}. \tag{2.3}$$

The time resolution of the system is usually found to be around 100 ps [132]. By accurately matching the TPC track with the TOF hit corresponding to the same particle, the

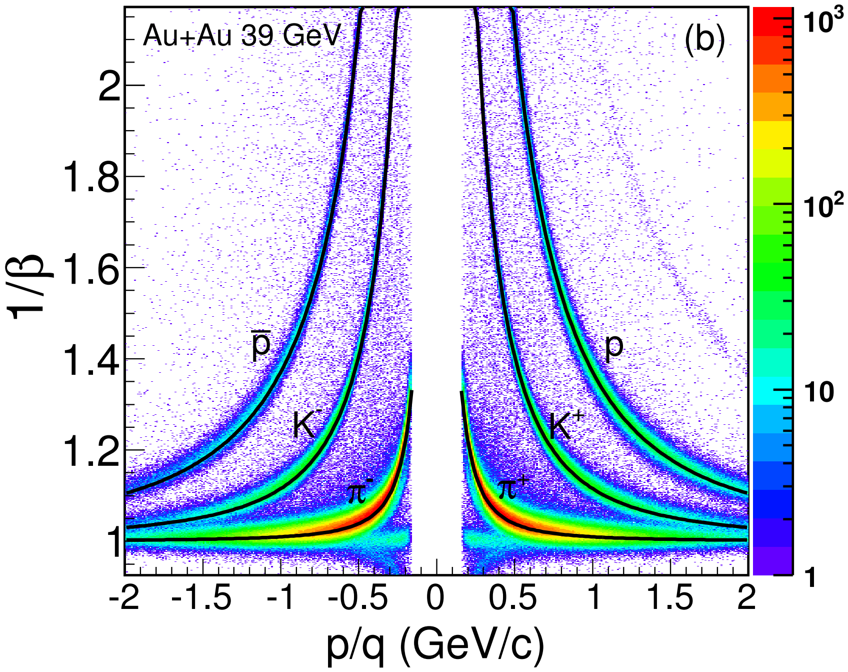

Figure 2.12 (Color online) Momentum (p) dependence of the inverse velocity ($1/\beta$) for positively ($q > 0$) and negatively ($q < 0$) charged particles measured by TOF. The black curves represent the expected values for pions, kaons and (anti)protons. Figure is taken from Reference [129].

flight distance can be computed from the track helix measured by the TPC. The velocity of the particle is then derived by

$$\beta = \frac{L}{c\Delta t}, \tag{2.4}$$

where L is the distance of flight. Using p provided by the TPC, the squared mass can be obtained by

$$m^2 = p^2\left(\frac{1}{\beta^2} - 1\right) \tag{2.5}$$

for the particle identification.

Figure 2.12 [129] shows the p dependence of $1/\beta$ for the charged particles measured by TOF. The pion and kaon bands merge at a higher momentum compared to the $\mathrm{d}E/\mathrm{d}x$ distributions in Figure 2.8. In other words, TOF can separate pions and kaons at $p \lesssim 1.6$ GeV/c, which is highly extended compared to TPC.

2.3 Beam Energy Scan Program

As discussed, T and μ_B at the chemical freeze-out from relativistic heavy-ion collisions generally follow functions of $\sqrt{s_{\mathrm{NN}}}$ in Equations 1.12 and 1.13. To map the QCD phase diagram and explore the phase structure, RHIC has successfully conducted the BES-I program in 2010–2017 and the BES-II program in 2018–2021. By varying the beam energy in the widest possible range of RHIC, Au+Au collisions at $\sqrt{s_{\mathrm{NN}}}$ from 7.7 to 200 GeV in the collider mode and from 3 to 13.7 GeV in the FXT mode were performed. Tables 2.1 and 2.2 list the information of all the collider and FXT data sets included in BES, respectively. The numbers of events from BES-I and BES-II in the collider mode and the Run-18 $\sqrt{s_{\mathrm{NN}}} = 3$ GeV FXT data set represent the statistics used in the net-proton number fluctuation analyses [98,100,134-135], while the numbers of events from other FXT data sets denote those of good events taken from Reference [103]. It is obvious that in BES-II, we have many new collision energies, including two collider energies, 9.2 GeV and 17.3 GeV, and 7–18 times more statistics compared to BES-I.

So far, measurements of net-proton number fluctuations from BES-I and the Run-18 $\sqrt{s_{\mathrm{NN}}} = 3$ GeV FXT data set have been completed. In this thesis, we focus on the analysis utilizing the BES-II collider data sets.

Table 2.1 Information of data sets in the collider mode included in the first (BES-I) and second (BES-II) phases of the Beam Energy Scan program. The numbers of BES-I and BES-II events are taken from References [98,134-135].

Beam Energy (AGeV)	$\sqrt{s_{\mathrm{NN}}}$ (GeV)	μ_B (MeV)	Run (Year 20xx)	Events (Million)
100	200	25	10	238
31.2	62.4	75	10	47
27.2	54.4	85	17	550
19.5	39	112	10	86
13.5	27	156	11	30
			18	220
9.8	19.6	206	11	15
			19	270
8.65	17.3	230	21	116
7.3	14.6	262	14	20
			19	178
5.75	11.5	316	10	6.6
			20	110
4.59	9.2	372	20	78
3.85	7.7	420	10	3
			21	45

Table 2.2 Information of data sets in the fixed-target (FXT) mode included in the Beam Energy Scan program (BES). The numbers of events from the Run-18 $\sqrt{s_{\mathrm{NN}}} = 3$ GeV data set and other data sets are taken from Reference [100] and Reference [103], respectively.

Beam Energy (AGeV)	$\sqrt{s_{\mathrm{NN}}}$ (GeV)	μ_B (MeV)	Run (Year 20xx)	Events (Million)
100	13.7	280	21	51
70	11.5	316	21	52
44.5	9.2	372	21	54
31.2	7.7	420	19	51
			20	112
26.5	7.2	440	18	155
			20	317
			21	89
19.5	6.2	490	20	118
13.5	5.2	540	20	103
9.8	4.5	590	20	108
7.3	3.9	633	20	53
			19	117
5.75	3.5	670	20	116
4.59	3.2	699	19	201
3.85	3	750	18	140
			21	2103

Chapter 3 Analysis Details

3.1 Data Sets

In this thesis, we analyze the data collected by the STAR experiment from Au+Au collisions in the collider mode from RHIC BES-II. The information of the used data sets is summarized in Table 3.1.

Table 3.1 Information of the data sets used in this analysis.

System	$\sqrt{s_{\mathrm{NN}}}$ (GeV)	Year	Trigger Setup	Stream	Production	Library
Au+Au	7.7	2021	production_7p7GeV_2021	st_physics(_adc)	P22ib	SL22b
	11.5	2020	production_11p5GeV_2020	st_physics(_adc)	P23ia	SL23a

Here, we explain some parameters defined in the STAR data sets.

1. Event level
    (a) V_x: x-coordinate of the reconstructed primary vertex position
    (b) V_y: y-coordinate of the reconstructed primary vertex position
    (c) V_r: $\sqrt{\left(V_x - V_x^{\text{center}}\right)^2 + \left(V_y - V_y^{\text{center}}\right)^2}$
    (d) V_z: z-coordinate of the reconstructed primary vertex position
    (e) RefMult: official reference multiplicity of charged particles within $|\eta| < 0.5$
    (f) RefMult3: reference multiplicity of charged particles excluding protons and antiprotons within $|\eta| < 1.0$
    (g) RefMult3X: reference multiplicity of charged particles excluding protons and antiprotons within $|\eta| < 1.6$
    (h) nTofMatch: number of TOF hits matched with a TPC track
2. Track level
    (a) nHitsFit: number of hit points of TPC used for the track trajectory fit
    (b) nHitsPoss: number of hit points of TPC possible for the track
    (c) nHitsDedx: number of hit points of TPC used for the track $\mathrm{d}E/\mathrm{d}x$ calculation
        - nHitsDedx $= 0 \Leftrightarrow \mathrm{d}E/\mathrm{d}x = 0$
        - Generally, nHitsDedx $\leqslant$ nHitsFit $\leqslant$ nHitsPoss
    (d) DCA: distance of the closest approach from the primary vertex position to the track trajectory
    (e) DCA$_z$: z-coordinate of the DCA vector
    (f) signed DCA$_{xy}$: projection of the DCA vector to the xy-plane with a sign determined by the angle between the DCA vector and the momentum vector

in the xy-plane

(g) p_x: x-coordinate of the momentum

(h) p_y: y-coordinate of the momentum

(i) p_z: z-coordinate of the momentum

(j) $n\sigma_{\text{proton}}$: quantification of the $\mathrm{d}E/\mathrm{d}x$ deviation between the measured and proton theoretical values

(k) TOF match flag: matching status between the TPC track and the TOF hit (0: no match, positive: yes)

(l) TOF local Y: local y-coordinate of the track hit position on the TOF module

(m) TOF local Z: local z-coordinate of the track hit position on the TOF module

(n) β: velocity measured by TOF

3.2 Run Selection

A run refers to a continuous period of data collection during which the detector system operates under specific experimental configurations and conditions. Each run typically spans a few minutes to half an hour and involves many events of collisions. The data sets include thousands of runs, summarized in Table 3.2.

Table 3.2 Information of the runs in the data sets.

$\sqrt{s_{\mathrm{NN}}}$ (GeV)	Period of Run IDs	Number of Runs	Number of Bad Runs
7.7	22031042–22121018	2696	374
11.5	20342002–21055017	1957	274

Runs can be classified as “bad” ones due to some anomalies in the detector systems or data acquisition processes, which can introduce significant biases. It is necessary and crucial to remove such runs, enhancing the quality of the data and the reliability of the results.

3.2.1 Run-by-Run QA

A run-by-run Quality Assurance (QA) study is performed to identify bad runs. We select several key variables capable of reflecting the quality of each run, which are listed in Table 3.3. Here, $V_x^{\text{center}} = V_y^{\text{center}} = 0$ for V_r. The signs $\langle\cdot\rangle_{\text{event}}$ and $\sigma_{\text{event}}(\cdot)$ represent

Table 3.3 Selected variables for run-by-run Quality Assurance (QA).

Detector	Event Level	Track Level
TPC	V_z, V_r, RefMult, $\left\langle \text{signed DCA}_{xy} \right\rangle_{\text{event}}$, $\sigma_{\text{event}}\left(\text{signed DCA}_{xy}\right)$, $\langle \text{DCA}_z \rangle_{\text{event}}$, $\sigma_{\text{event}}\left(\text{DCA}_z\right)$	nHitsFit, nHitsFit/nHitsPoss, nHitsDedx, DCA, p_{T}, φ, η, $\mathrm{d}E/\mathrm{d}x$, $n\sigma_{\text{proton}}$
TOF	nTofMatch	$1/\beta$

the average and standard deviation of a track-level quantity in an event, respectively.

Some basic selection criteria are applied to extract these variables.

1. Run level
   (a) Not marked as an official bad run
2. Event level
   (a) $|V_z| < 50$ cm
   (b) $V_r < 2$ cm
3. Track level
   (a) nHitsFit > 10
   (b) nHitsDedx > 5 (only for $\mathrm{d}E/\mathrm{d}x$ and $n\sigma_{\mathrm{proton}}$)
   (c) DCA < 3 cm
   (d) $-32.76799 < n\sigma_{\mathrm{proton}} < 32.76699$ (only for $n\sigma_{\mathrm{proton}}$)
   (e) $\beta \geqslant 10^{-5}$ (only for $1/\beta$)

Averages within each run are calculated for all the QA variables in Table 3.3. Figures 3.1 and 3.2 show the run index dependence for some variables for the $\sqrt{s_{\mathrm{NN}}}$ = 7.7 GeV and $\sqrt{s_{\mathrm{NN}}}$ = 11.5 GeV data sets, respectively. The run index denotes the serial number of a run within the data set.

We utilize the STAR official run-by-run QA algorithm [136] to identify bad runs. Firstly, a run is marked “global bad” if any of its variables fall outside the range of $\mu \pm 10\sigma$ over the entire run duration. Secondly, the runs are segmented into several

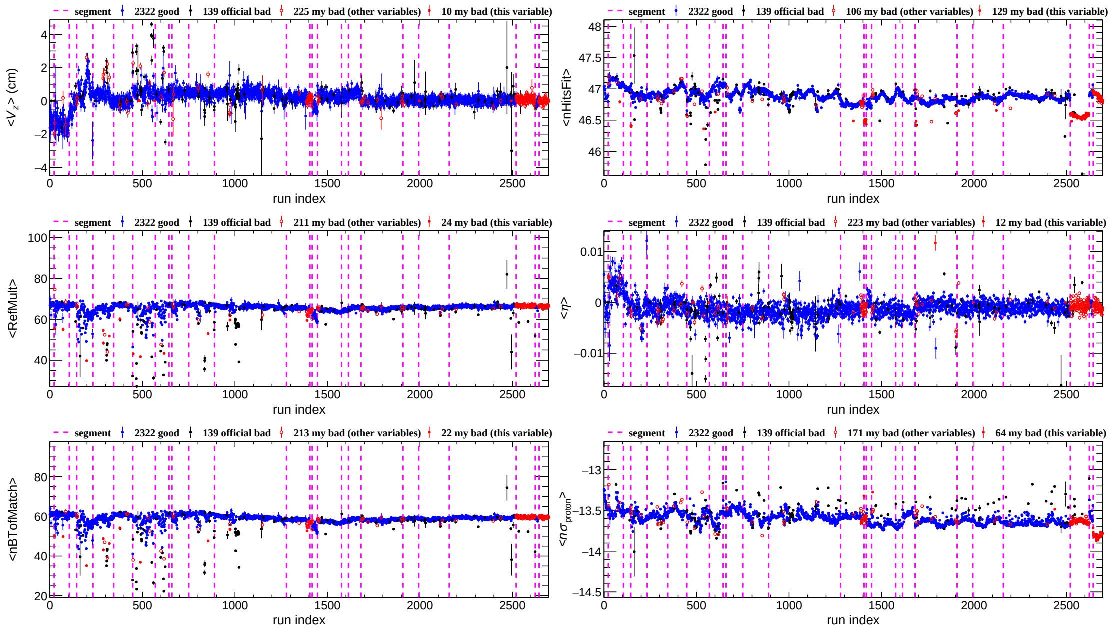

Figure 3.1 (Color online) Run-by-run QA of V_z, RefMult, nTofMatch (left), nHitsFit, η and $n\sigma_{\mathrm{proton}}$ (right) for the $\sqrt{s_{\mathrm{NN}}} = 7.7$ GeV data set. Magenta vertical lines represent the segments for the local run regions.

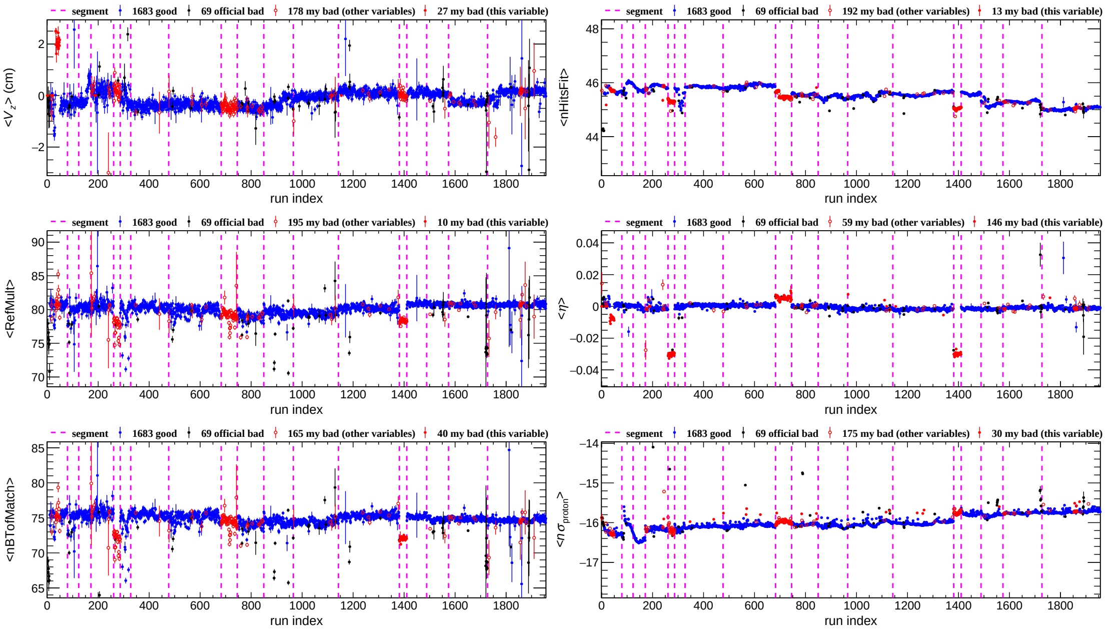

Figure 3.2 (Color online) Run-by-run QA of V_z, RefMult, nTofMatch (left), nHitsFit, η and $n\sigma_{\text{proton}}$ (right) for the $\sqrt{s_{\text{NN}}}$ = 11.5 GeV data set. Magenta vertical lines represent the segments for the local run regions.

stable regions, and a run is flagged as “local bad” if any of its variables exceed $\mu \pm 5\sigma$ within its specific region. This second procedure is repeated iteratively until no new bad runs are categorized. Segments of the local run regions are shwon as magenta vertical lines in Figures 3.1 and 3.2. It is evident that some variables exhibit clusters of runs deviating significantly from the majority, indicating long periods of abnormal conditions. All of the identified bad runs are removed from the following analysis.

3.3 Event Selection

An event refers to a single instance of a particle collision that triggers the detector system and is subsequently recorded for analysis. However, not all recorded events are of sufficient quality, and some of them may be affected by various issues. These poorly reconstructed events can introduce distortions in the data and should be rejected.

Table 3.4 Selection criteria of events and numbers of events after all selections.

$\sqrt{s_{\text{NN}}}$ (GeV)	Trigger ID	$\lvert V_z\rvert <$ (cm)	$V_r <$ (cm)	Center of (V_x, V_y) (cm)	Bad-DCA Rejection	Pileup Rejection	Events (Million)
7.7	8100[1-4]0	50	1	(−0.2902, −0.2632)	√	√	45
11.5	7100[0-2]0			(−0.2208, −0.2161)	√	√	110

The event selection criteria and numbers after all selections in this analysis are summarized in Table 3.4. We select the events with minimum bias triggers, the most popular set of triggers. If signals trigger the forward detectors, BBC, ZDC, VPD and EPD, they are collected as an event with as little bias as possible. Figures 3.3 and 3.4

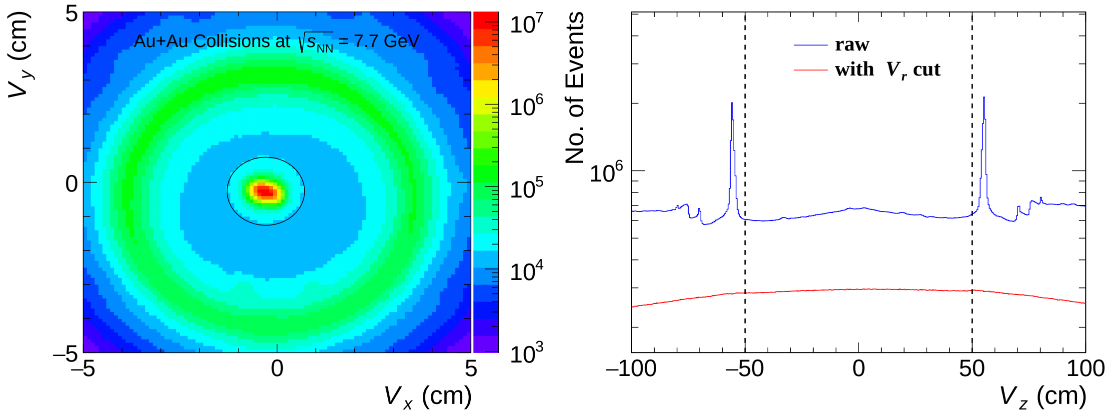

Figure 3.3 (Color online) Distributions of V_x-V_y (left) and V_z (right) of events in the $\sqrt{s_{\mathrm{NN}}}$ = 7.7 GeV data set. Peaks in the raw V_z distribution are induced by the interactions between beams and beam pipes at $z \sim \pm 55$ cm and can be removed by V_r cut. The V_z and V_r cut boundaries are shown as black lines.

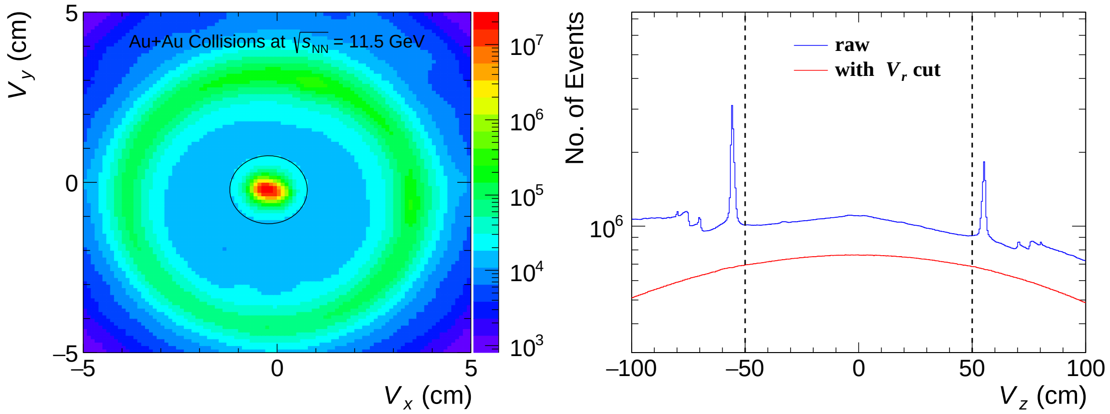

Figure 3.4 (Color online) Distributions of V_x-V_y (left) and V_z (right) of events in the $\sqrt{s_{\mathrm{NN}}}$ = 11.5 GeV data set. The V_z distribution after the V_r cut has a stronger peak shape compared to $\sqrt{s_{\mathrm{NN}}}$ = 7.7 GeV due to different beam energies. The V_z and V_r cut boundaries are shown as black lines.

present the distributions of the event primary vertex positions in the two data sets. Two beam pipes terminate at $z \sim \pm 55$ cm, resulting in two distinct peaks in the V_z distributions due to the interactions between the beams and the surrounding materials. These contributions are effectively removed by applying a tight V_r cut. In this analysis, we apply a cut of $V_r < 1$ cm with a shifted center, tighter than the commonly used cut of $V_r < 2$ cm, to suppress the background noise as expected. The V_z cut ensures that collisions take place around the center of the detector system, making the the mid-rapidity phase space covered by TPC and TOF.

3.3.1 Bad-DCA Event Rejection

In the BES-I analysis of net-proton number fluctuations [98], it was found that some events undergo unstable beam conditions during the data collection and inaccurate

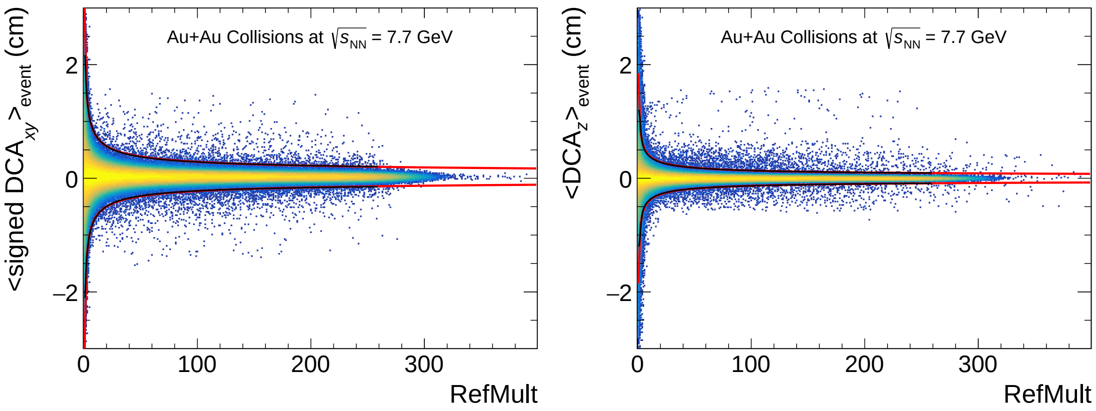

Figure 3.5 (Color online) $\langle \text{signed DCA}_{xy} \rangle_{\text{event}}$ (left) and $\langle \text{DCA}_z \rangle_{\text{event}}$ (right) as functions of RefMult in the $\sqrt{s_{\text{NN}}}$ = 7.7 GeV data set. The colors in the band represent the event numbers on logarithmic scales. Red curves are the parameterizations of black curves as $\mu \pm 6\sigma$.

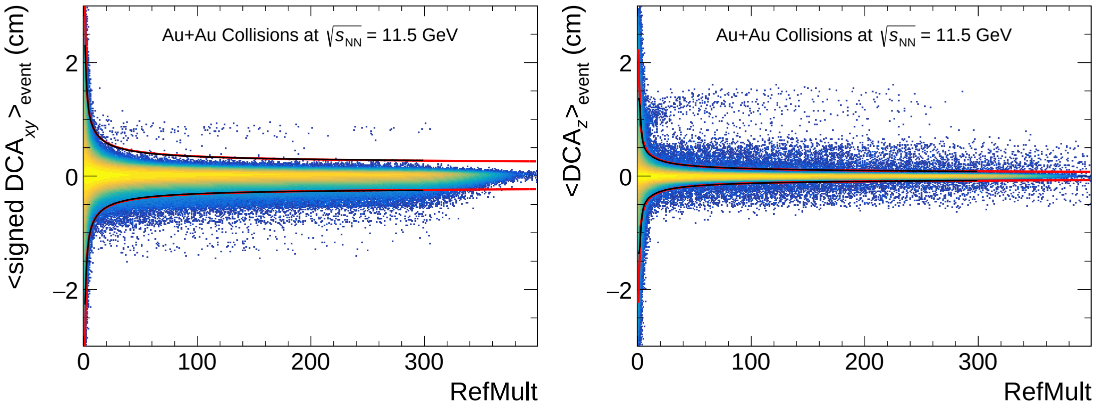

Figure 3.6 (Color online) $\langle \text{signed DCA}_{xy} \rangle_{\text{event}}$ (left) and $\langle \text{DCA}_z \rangle_{\text{event}}$ (right) as functions of RefMult in the $\sqrt{s_{\text{NN}}}$ = 11.5 GeV data set. The colors in the band represent the event numbers on logarithmic scales. Red curves are the parameterizations of black curves as $\mu \pm 6\sigma$.

space-charge calibration of TPC. These events can induce a tail on the left hand of the net-proton number distributions, and the kurtosis is enhanced since it characterizes the tailedness. The distorted fluctuations are not from the realistic collisions or from the physical signals as what we want. The track DCA was used to identify these events effectively, and a possible reason could be that it connects reconstruction and calibration of the primary vertex position (event level) and the track trajectory (track level).

In BES-II, a similar issue is also observed, and we employ $\langle \text{signed DCA}_{xy} \rangle_{\text{event}}$ and $\langle \text{DCA}_z \rangle_{\text{event}}$ for the bad-DCA event rejection. A set of basic track cuts is applied: nHitsFit > 10 and DCA < 3 cm. Figures 3.5 and 3.6 show the correlations of RefMult with $\langle \text{signed DCA}_{xy} \rangle_{\text{event}}$ in the left panels and $\langle \text{DCA}_z \rangle_{\text{event}}$ in the right panels in the two data sets. Considering the one-dimensional distributions of $\langle \text{signed DCA}_{xy} \rangle_{\text{event}}$ and $\langle \text{DCA}_z \rangle_{\text{event}}$ in each RefMult slice, the means are always close to zero, but the widths have a clear RefMult dependence, especially for low-RefMult events. It is worth to mention that there are suspicious tails far away from the main bands, which are likely from a data issue and are not suitable to be taken into account in the analysis. The black curves draw the $\mu \pm 6\sigma$ boundaries of the one-dimensional distributions in each RefMult slice, and they are parameterized by

$$y = p_0 + \frac{p_1}{x^{p_2}}, \tag{3.1}$$

shown as the red curves. The events beyond the red curves represent the 6σ outliers and will be rejected.

3.3.2 Pileup Event Rejection

In experiments, beams are composed of many bunches, each of which contains a large number of ions. When two bunches cross each other, ions in a bunch participate in collisions nearly simultaneously, especially under the conditions of high collision rates. If multiple collision occur within such a short time interval that the detector system can not separate them when recording the signals, a pileup event is reconstructed as considered to be a single collision. In a pileup event, the tracks are always belonging to at least two different realistic single collisions, and the reconstructed primary-vertex position may not be accurate. Since a pileup event is produced by merging multiple single collision, it is more likely to be of a high multiplicity and, therefore, be identified as a central collision. Pileup events should be removed before the analysis, especially for the high-sensitivity fluctuation measurement in central collisions.

TPC is relatively slow compared to other detectors. Ionization electrons drift across the entire volume of the chamber for tens of microseconds to generate signals, which limits its ability to distinguish between single events and pileup events. In contrast, TOF operates with a timing resolution around 100 ps, providing a prompt timing response much faster than TPC. The distinct difference in the timing resolutions between TPC and TOF could introduce a substantial suppression of the successful matching fraction between TOF hits and TPC tracks.

In this analysis, pileup events are identified and removed by investigating correlations between charged-particle multiplicities measured by TPC and TOF. RefMult is used as the TPC multiplicity. We define nTofBeta as the TOF multiplicity, which quantifies the number of TOF hits which are matched with TPC tracks and have reasonable velocity values calculated. Its tracks cuts are: nHitsFit > 10, DCA < 3 cm, TOF match flag > 0 and $0.1 < \beta < 1.1$. This quantity does not only include the geometry information from the TOF match flag, but also carry the timing capability from the β calculation, which would provide an excellent identification for the pileup events.

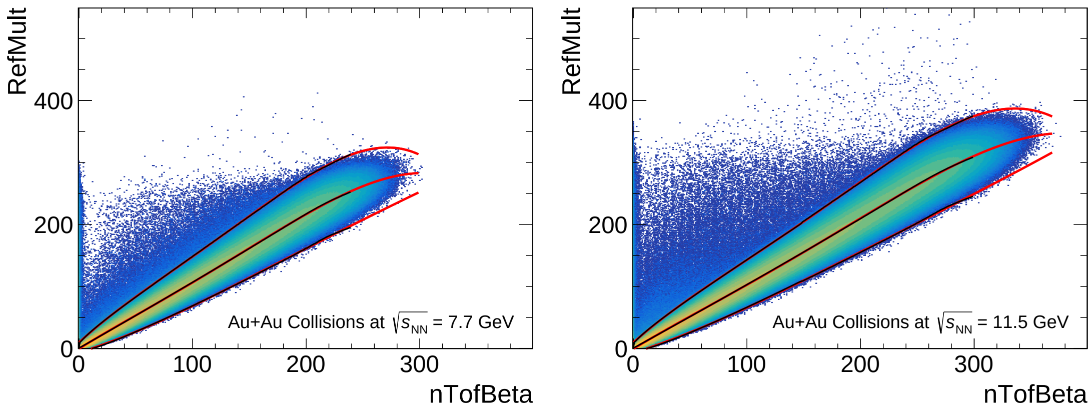

Figure 3.7 (Color online) Correlations between RefMult and nTofBeta in the $\sqrt{s_{\mathrm{NN}}}$ = 7.7 GeV (left) and 11.5 GeV (right) data sets. The colors in the band represent the event numbers on logarithmic scales. Red curves are the parameterizations of black curves as $\mathrm{mode} - 3.6\sigma$ **and** $\mathrm{mode} + 3.6(1 + S)\sigma$**.**

Figure 3.7 presents the two-dimensional distributions of RefMult and nTofBeta in the $\sqrt{s_{\mathrm{NN}}}$ = 7.7 GeV data set in the left panel and $\sqrt{s_{\mathrm{NN}}}$ = 11.5 GeV data set in the right panel. The colors, from red to blue, in the band characterize the distributions of event counts from higher to lower on a logarithmic scale. We can see a strong positive correlation between the TPC and TOF multiplicities from the main band. There is also a little fraction of events falling out of the band, typically with significantly smaller TOF multiplicity compared to the main band, shown as the blue tail band in the figure. This contribution is from the pileup events, inducing low TOF matching efficiency due to the high timing sensitivity of TOF. For the energy dependence, a higher pileup fraction can be observed from the larger and heavier pileup band in the $\sqrt{s_{\mathrm{NN}}}$ = 11.5 GeV data set, which results from the higher collision rate compared to 7.7 GeV.

To remove the pileup events, we apply similar method to the the bad-DCA event rejection. In each nTofBeta slice, a one-dimensional distribution is obtained and fitted using a double-NBD function. The NBD function is expressed in Equation 1.122. In the double-NBD fit, The first NBD function describes the main body including the peak, while the second one is for the pileup tail. Two values, $\mathrm{mode} - 3.6\sigma$ and $\mathrm{mode} + 3.6(1 + S)\sigma$, are calculated using parameters of the first NBD function, and they are shown as the black curves in Figure 3.7. Red curves denote polynomial functions fitted to the black curves, and events out of the red curves are removed as identified pileup events.

3.4 Track Selection

Tracks are selected by a few quality cuts summaized in Table 3.5, which are the same as the BES-I analysis. The number of fitting points for a track is required to exceed 20, ensuring that the track trajectory and momentum are reconstructed with high quality. Additionally, the number of fitting points should also be higher than 52% of the maximum possible number for that track, which accounts for issues like multiple counts from split tracks due to irrelevant hits in the TPC sectors. Considering the availability of using measured $\mathrm{d}E/\mathrm{d}x$ for PID, the fitting point number for the $\mathrm{d}E/\mathrm{d}x$ calculation has to be larger than 5. In experiments, secondary charged particles can arise from interactions between high-energy particles and the beam pipes or detector materials, contributing background noise. To isolate primary particles from heavy-ion collisions, the DCA, quantifying the distance between the primary vertex and the track trajectory, is constrained to be less than 1 cm.

Table 3.5 Track quality cuts.

nHitsFit >	nHitsFit/nHitsPoss >	nHitsDedx >	DCA < (cm)
20	0.52	5	1

Figure 3.8 shows the distributions of nHitsFit (top left), nHitsFit/nHitsPoss (bottom left), nHitsDedx (top right) and DCA (bottom right) of tracks in the $\sqrt{s_{\mathrm{NN}}} = 11.5$ GeV data set with the red dashed lines describing the cut boundaries.

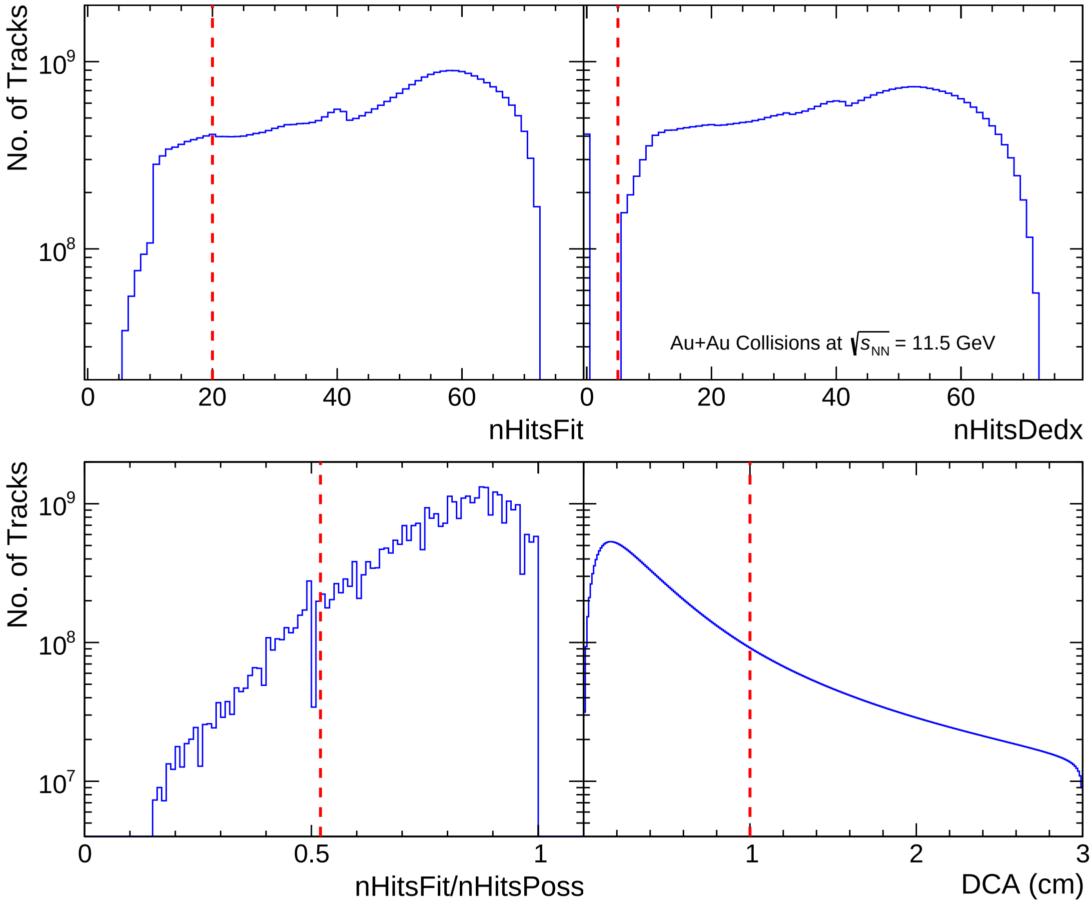

Figure 3.8 (Color online) Distributions of nHitsFit (top left), nHitsFit/nHitsPoss (bottom left), nHitsDedx (top right) and DCA (bottom right) of tracks in the $\sqrt{s_{\mathrm{NN}}}$ = 11.5 GeV data set. Red dashed lines denote the cut boundaries.

Track kinematic cuts are presented in Table 3.6. The default set maintains the same phase space as BES-I. In the acceptance dependence study, the higher cut of p_{T} will be reduced to 0.8, 1.0, 1.2, 1.4, 1.6 and 1.8 GeV/c, and the higher cut of $|y|$ will be decreased to 0.1, 0.2, 0.3 and 0.4 or increased to 0.6 and 0.7 taking advantage of the iTPC upgrade.

Table 3.6 Track kinematic cuts.

	$p_{\mathrm{T}} >$ (GeV/c)	$p_{\mathrm{T}} <$ (GeV/c)	$\|y\| <$
Default	0.4	2.0	0.5
Varied		0.8, 1.0, 1.2, 1.4, 1.6, 1.8	0.5
		2.0	0.1, 0.2, 0.3, 0.4, 0.6, 0.7

For PID, the TPC $n\sigma_{\mathrm{proton}}$ and the TOF m^2 are employed to find proton and antiproton candidates. Using the $\mathrm{d}E/\mathrm{d}x$ measured by TPC, we define the TPC $n\sigma_{\mathrm{X}}$ by

$$n\sigma_{\mathrm{X}} = \frac{1}{\sigma_{\mathrm{R}}} \ln \frac{(\mathrm{d}E/\mathrm{d}x)|_{\mathrm{measured}}}{(\mathrm{d}E/\mathrm{d}x)|_{\mathrm{expected\ X}}}, \tag{3.2}$$

where σ_{R} is the $\mathrm{d}E/\mathrm{d}x$ resolution of TPC, and $\left.\frac{\mathrm{d}E}{\mathrm{d}x}\right|_{\mathrm{expected\ X}}$ is the expected value for the particle species X by the Bichsel function [128]. It is obvious that $n\sigma_{\mathrm{X}}$ quantifies how the measured $\mathrm{d}E/\mathrm{d}x$ deviates from the expected value. Based on the definition of $n\sigma_{\mathrm{X}}$, its expected value is around zero. The distribution of $n\sigma_{\mathrm{X}}$ at a given momentum is expected to approximate a Gaussian distribution function with $\mu = 0$ and $\sigma = 1$. The Gaussian shape is expected by the characteristics of the detector response, and the mean and the standard deviation are based on the definition of $n\sigma_{\mathrm{X}}$. The calculation of TOF m^2 is expressed by Equation (2.5).

The p/q and η dependences of TPC $n\sigma_{\mathrm{proton}}$ and TOF m^2 of tracks in the $\sqrt{s_{\mathrm{NN}}} = 11.5$ GeV data set are presented in Figure 3.9. The corresponding expected peak positions for (anti)protons are shown as black dashed lines. We can see that both m^2 distributions peak at the expected value $m^2_{\mathrm{proton}} = 0.88\ \mathrm{GeV}^2/c^4$, and the peak position shows negligible p/q and η dependences, which suggests an excellent calibration for TOF. However, the calibration for TPC $n\sigma_{\mathrm{proton}}$ might not be so good, resulting in a shift of $\langle n\sigma_{\mathrm{proton}} \rangle$. We can also find that the $\langle n\sigma_{\mathrm{proton}} \rangle$ shift has a clear p dependence and a hint of η dependence. Similar phenomenons are observed also in the 7.7 GeV data set. That is to say, a differential TPC $\langle n\sigma_{\mathrm{proton}} \rangle$ recalibration in each two-dimensional phase space bin is required for the (anti)proton measurement. Details will be discussed in Section 3.4.1.

We consider three types of PID selection criteria as summarized in Table 3.7. Note that $n\sigma_{\mathrm{proton}}$ here is that after the recalibration with a mean at zero.

When we utilize the TOF β for PID, a cut of TOF $|\mathrm{local\ Y}| < 1.8$ cm is always

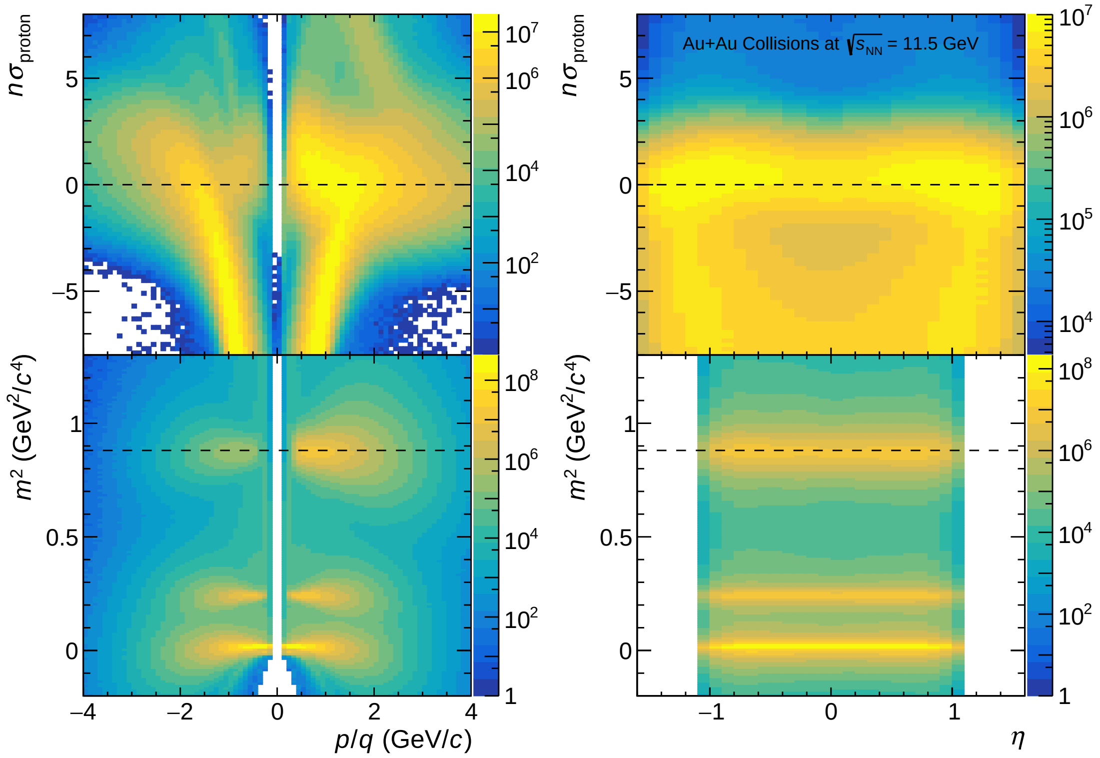

Figure 3.9 (Color online) Distributions of TPC $n\sigma_{\rm proton}$ (top) and TOF m^2 (bottom) versus p/q (left) and η (right) of tracks in the $\sqrt{s_{\rm NN}}$ = 11.5 GeV data set. Black dashed lines denote the expected peak positions for (anti)protons: $n\sigma_{\rm proton}$ = 0 and m^2 = 0.88 GeV^2/c^4. A clear p dependence and a hint of η dependence of the $\langle n\sigma_{\rm proton}\rangle$ shift are observed.

Table 3.7 Types of PID selection criteria.

PID Type	TPC Cut	TOF Cut	Default Phase Space
TPC	$\lvert n\sigma_{\rm proton}\rvert < 2$	/	$p_{\rm T} < 0.8$ GeV/c
TPC asymmetric	$0 < n\sigma_{\rm proton} < 2$	/	/
TPC+TOF	$\lvert n\sigma_{\rm proton}\rvert < 2$	TOF match flag > 0 TOF |local Y| < 1.8 cm 0.6 GeV^2/c^4 < m^2 < 1.2 GeV^2/c^4	$p_{\rm T} > 0.8$ GeV/c

required. Figure 3.10 shows the distribution of TOF local Y and local Z of tracks in the $\sqrt{s_{\rm NN}}$ = 11.5 GeV data set. A TOF hit with the local coordinate far away from the center of the module is likely to be mismatched to a TPC track, especially in the high-multiplicity environment created by the heavy-ion collisions. This cut selects tracks hitting around the centers of the TOF modules, which are expected to carry high-quality and clean matching information.

The reason why we do not require TOF at low $p_{\rm T}$ is its limited acceptance and the inefficiency cased by a fraction of tracks missed by a TOF match, especially for low-$p_{\rm T}$ tracks. However, the maximum momentum for the separation between pions/kaons and protons of the TPC dE/ dx is around 1 GeV/c. For (anti)protons with $p_{\rm T}$ ~ 0.8 GeV/c and $|y|$ ~ 0.5, the momentum is approximately 1 GeV/c. Considering the high sensitivity of the higher-order fluctuations, we should identify a group of clean protons and

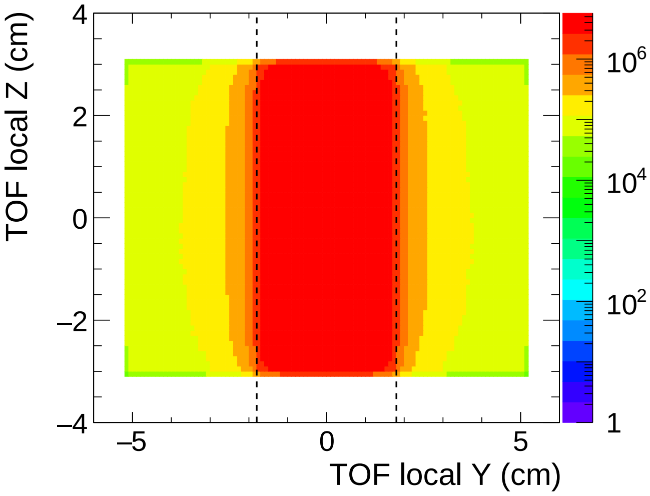

Figure 3.10 (Color online) Distribution of TOF local Y and local Z of tracks in the $\sqrt{s_{\mathrm{NN}}}$ = 11.5 GeV data set. The black dashed lines represent the cut boundaries.

avoid contaminating particles from contributing the measured signals. The approach is utilizing the TPC asymmetric PID or the TPC+TOF PID to reject contaminating particles and improve the proton and antiproton purities. The bin-by-bin purity is required to be always higher than 90% in this analysis. The actually used PID cuts will be determined in Section 3.4.4 based on the acceptance coverages of the detectors to be studied in Section 3.4.2 and the purity distributions to be studied in Section 3.4.3.

3.4.1 TPC PID Recalibration

Before the analysis, $n\sigma_{\mathrm{proton}}$ should be recalibrated to shift its mean back to zero. As shown in Figure 3.9, the calibration for TOF m^2 is good with a correct and stable peak at the expected m^2_{proton}. Thus, we use the TOF PID cut to identify pure (anti)protons, and find the current mean of $n\sigma_{\mathrm{proton}}$ in each two-dimensional phase space bin of p_{T} and η. Because the conditions of the experiments and calibrations may differ over runs, the

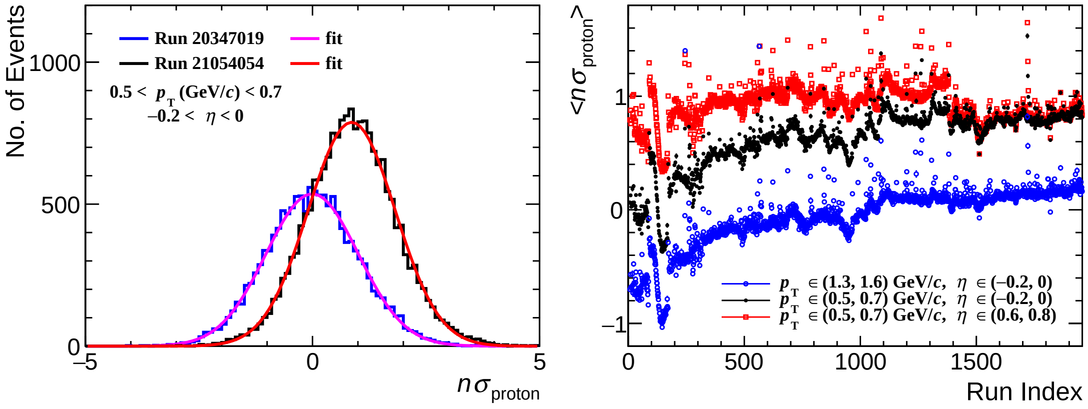

Figure 3.11 (Color online) Gaussian fits of $n\sigma_{\mathrm{proton}}$ (left) and run dependence of $\langle n\sigma_{\mathrm{proton}} \rangle$ (right) in two-dimensional phase space bins of p_{T} and η in the $\sqrt{s_{\mathrm{NN}}}$ = 11.5 GeV data set. Clear run, p_{T} and η dependence can be observed.

run dependence of $\left\langle n\sigma_{\text{proton}} \right\rangle$ is also studied. Figure 3.11 presents the recalibration of $n\sigma_{\text{proton}}$ in the $\sqrt{s_{\text{NN}}} = 11.5$ GeV data set. The left panel shows the $n\sigma_{\text{proton}}$ distributions after TOF PID in the same phase space from different runs, with a run dependence observed. Gaussian fits are applied to obtain the $\left\langle n\sigma_{\text{proton}} \right\rangle$ summarized in the right panel. This phenomenon is also observed in the $\sqrt{s_{\text{NN}}} = 7.7$ GeV data set. Hence, a run-, p_{T}- and η-dependent TPC $n\sigma_{\text{proton}}$ recalibration is performed using the mean to shift it back.

3.4.2 Acceptance

It is crucial to make sure that the acceptance where we take the measurement is fully covered by the detectors. Lack of coverage can lead to loss of signals. Figure 3.12 compares the (anti)proton acceptances of TPC in the y-p_{T} phase space between BES-I and BES-II with the same event and tracks cuts. The black square encloses the acceptance of the BES-I measurement, which is also the default acceptance in this analysis. It is obvious that the iTPC upgrade strongly enlarges the acceptance and provide an opportunity to achieve the measurement up to $|y| < 0.7$ within the dashed square.

Then we are going to check the acceptance in details by studying its dependence. As known, the acceptance coverage is determined by the geometry, which is correlated to the position of the detector relative to the primary vertex of the event, that is, V_z. Figure 3.13 shows the acceptances for (anti)protons in the $\sqrt{s_{\text{NN}}} = 11.5$ GeV data set. The color represents the distribution of the measured yield on a logarithmic scale. The track quality cuts are mentioned before including nHitsFit > 20. Left and right panels

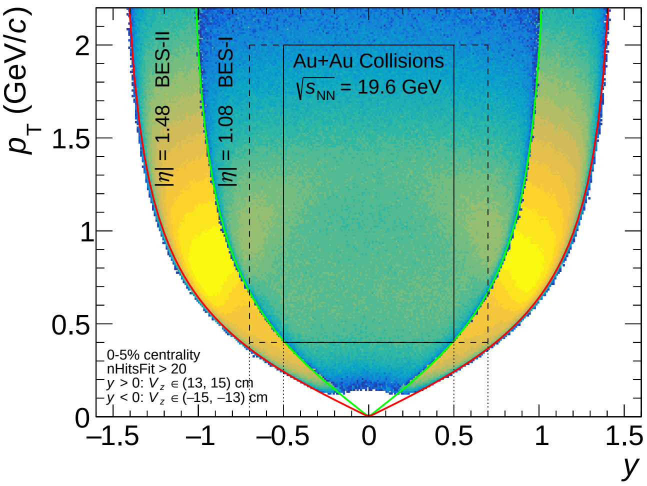

Figure 3.12 (Color online) Comparison of the (anti)proton acceptances of TPC in the y-p_{T} phase space between BES-I and BES-II. Both acceptance bands are obtained from the events at $\left|V_z\right| \sim 15$ cm and the tracks with nHitsFit > 20. The curves draw the acceptance boundaries: BES-I $\eta = 1.08$ and BES-II $\eta = 1.48$.

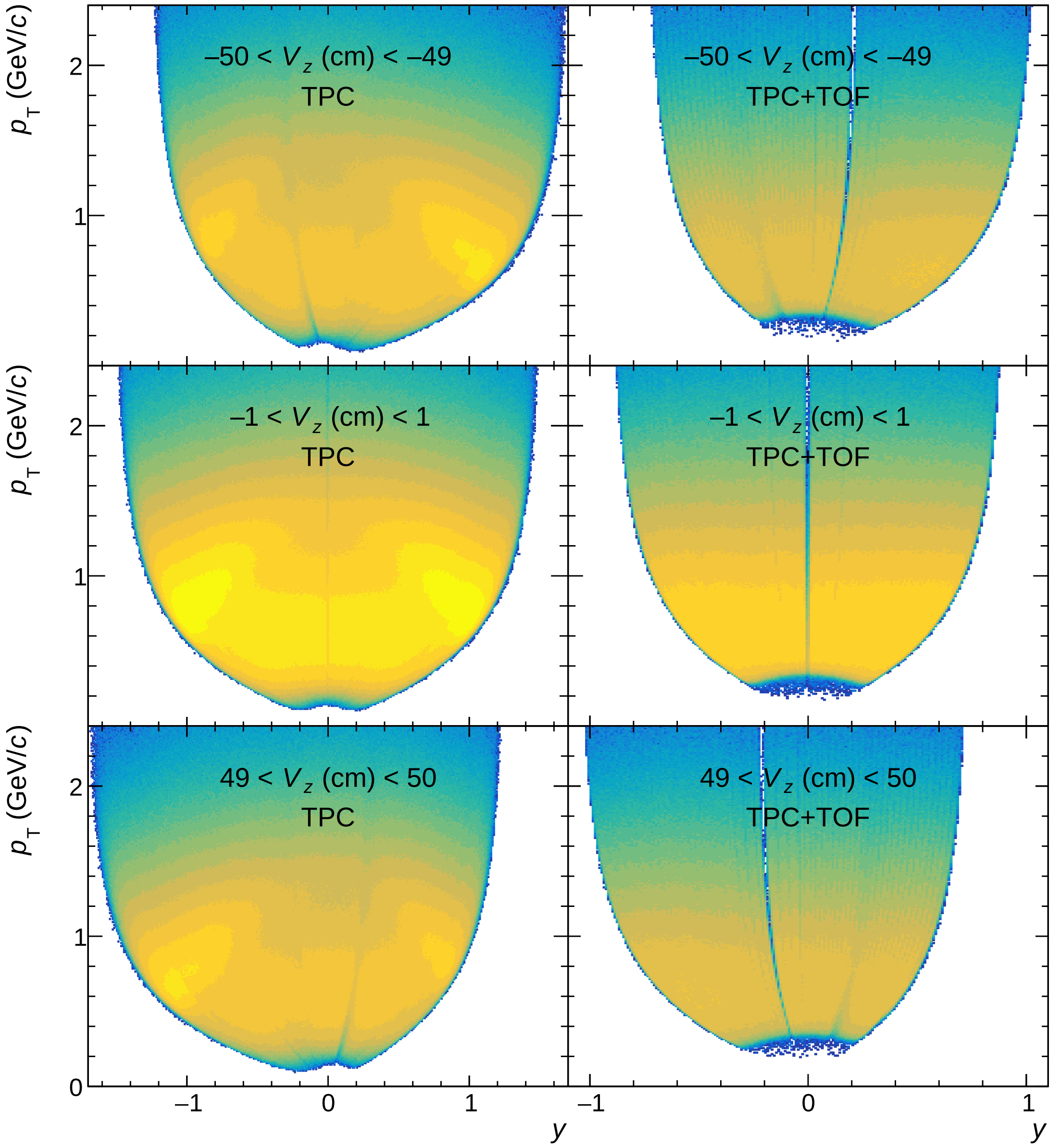

Figure 3.13 (Color online) Acceptances for (anti)protons measured by TPC and TPC+TOF in various V_z bins in the $\sqrt{s_{\mathrm{NN}}}$ = 11.5 GeV data set. Left (right) panels represent the acceptances by TPC (TPC+TOF). From top to bottom, the V_z bins are (−50, −49) cm, (−1, 1) cm and (49, 50) cm, respectively. Both TPC and TOF coverages strongly depend on the V_z range. The track quality cuts include nHitsFit > 20. Contaminating particles contribute to the peaks at large $|y|$ in the TPC plots. The dips in the yield distributions come from the central gap of TPC and TOF at $z \sim 0$ and the beam pipes at $|z| \sim 55$ cm.

are obtained using TPC PID and TPC+TOF PID, respectively. From top to bottom, V_z increases from negative to positive signs. A clear V_z dependence of the acceptance is observed. For $|V_z| < 1$ cm, the acceptance is symmetric with respect to $y = 0$. For positive (negative) V_z, the band moves towards negative (positive) y, because the θ or η coverage is limited if V_z and y have the same sign.

In the yield distributions meausred by TPC, there are two clear peaks at large $|y|$. They come from the contaminating particles, such as pions and kaons, which have com-

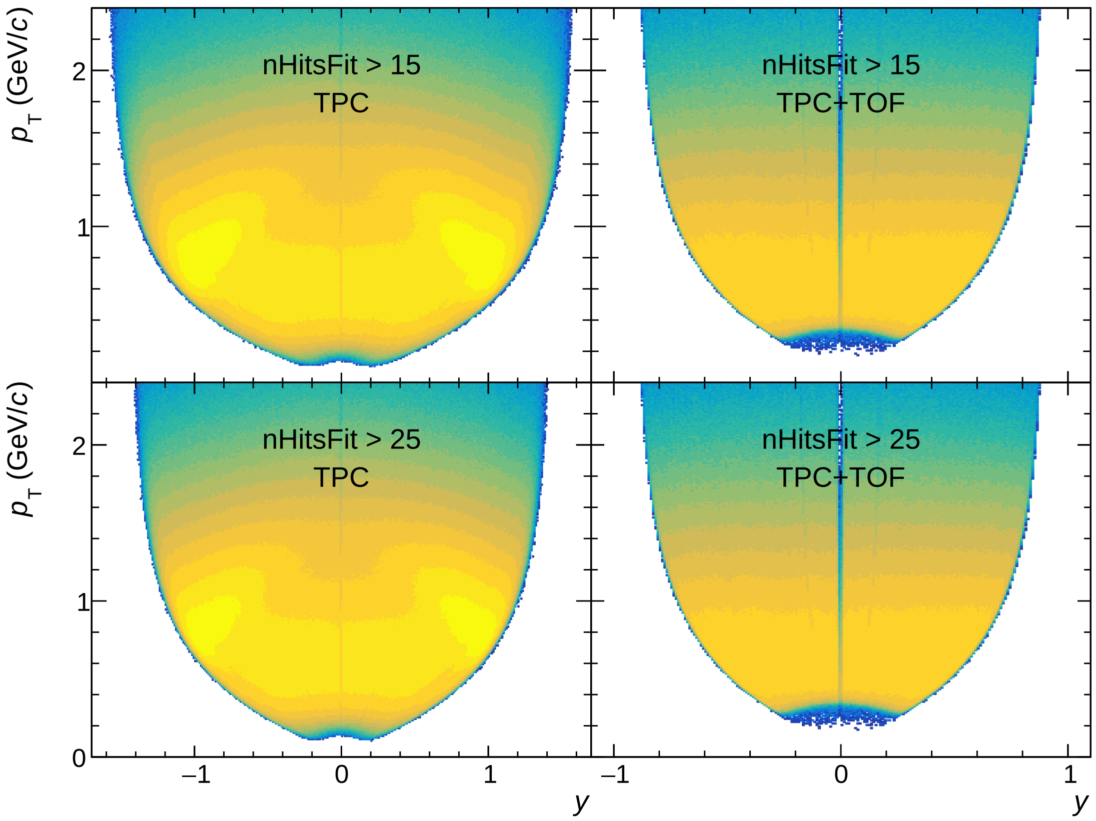

Figure 3.14 (Color online) Acceptances for (anti)protons measured by TPC and TPC+TOF from various nHitsFit cuts in the $\sqrt{s_{\rm NN}}$ = 11.5 GeV data set. Left (right) panels represent the acceptances by TPC (TPC+TOF). Top and bottom panels are using nHitsFit > 15 and nHitsFit > 25, respectively. The nHitsFit cut can reduce the TPC coverage but does not affect the TOF coverage.

parable dE/ dx with (anti)protons in that p region. Note that there is a dip at the centers of the yield distributions measured by TPC and TPC+TOF from $\left|V_z\right| < 1$ cm, which results from the central gap between west and east halves of TPC and TOF. Besides, there are two other dips in the plots from $\left|V_z\right| \sim 50$ cm. For $V_z \sim -50$ cm, a dip is at a negative y, and for $V_z \sim 50$ cm, another dip is at positive y. The two dips come from the beam pipes at $z \sim \pm 55$ cm, which cause lower counts of charged particles due to secondary reactions.

We also study the effect of nHitsFit on the acceptance coverage, shown in Figure 3.14. All the plots are taken from events with $V_z \sim 0$. Top panels show the acceptance from nHitsFit > 15, while bottom panels are obtained by nHitsFit > 25. For the coverage of TPC, the tighter nHitsFit cut leads to the smaller acceptance, because tracks capable of undergoing more fitting points should fly with smaller $|\eta|$. However, there is no clear nHitsFit cut dependence of the acceptance of TOF. As known, TOF is surrounding TPC, so the requirement for a track matched with a TOF hit is naturally tighter than the nHitsFit cut.

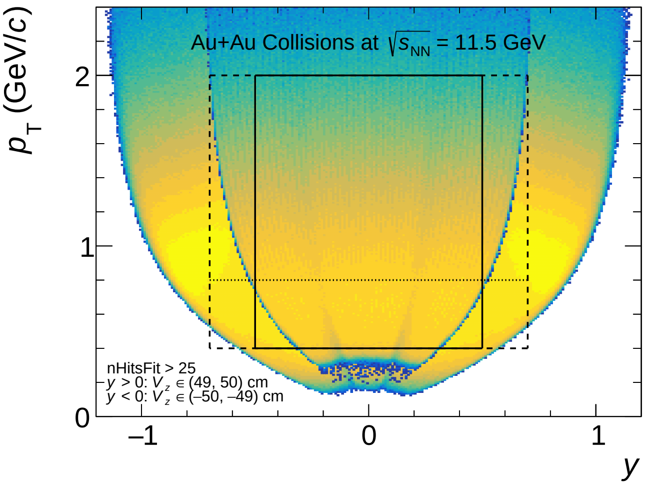

Figure 3.15 (Color online) Acceptances for (anti)protons measured by TPC and TPC+TOF in the worst case in the $\sqrt{s_{\mathrm{NN}}}$ = 11.5 GeV data set. The larger (smaller) band represents the acceptance from TPC (TPC+TOF). Tracks from the following cuts contribute to the acceptances: nHitsFit > 25; $y > 0$ from 49 cm $< V_z <$ 50 cm and $y < 0$ from −50 cm $< V_z <$ −49 cm. The dashed line represents the minimum p for the TOF PID utilization. The solid square encloses the default acceptance, while the dash square is for the y extension.

Because we are taking event-by-event measurement for the fluctuations, the phase space where we measure (anti)protons is required to be fully covered by the detectors in all the events. If not, the net-proton numbers in some events are artificially reduced as a bias on the measured fluctuations, and the signals will be distorted due to these "incomplete" events. Thus, we should check the measured phase space is fully covered by the detectors in the worst case in our analysis. Considering the V_z dependence, the maximum $|V_z|$ is 50 cm, and the acceptance is reduced to the minimum if y has the same sign as V_z. For nHitsFit, although the default cut is 20, the tightest cut is 25 when we study the systematic uncertainties in Section 3.9. Figure 3.15 shows the acceptance in the worst case, which represents nHitsFit > 25, and tracks with positive (negative) rapidities are selected from the events in 49 cm $< V_z <$ 50 cm (−50 cm $< V_z <$ −49 cm). There are two bands in the figure. The larger band represents the acceptance of (anti)protons measured by TPC, and the smaller one denotes the coverage of TPC+TOF. The solid square encloses the default acceptance in our analysis: 0.4 GeV/c $< p_{\mathrm{T}} <$ 2.0 GeV/c and $|y| < 0.5$, which is fully covered by TPC. We require TOF over the horizontal dotted line at p_{T} = 0.8 GeV/c, where the TOF has a full acceptance. Hence, the default acceptance and PID cut are available based on the acceptance check.

However, if we want to extend the rapidity range to $|y| < 0.7$, shown as the dashed box, both TPC and TOF lack part of the coverage. The solution could be reducing the $|V_z|$ cut, and the worst case would be better with larger acceptance. The acceptance where we take the measurement should be fully covered by TPC, and TOF is require to have a full acceptance in the phase space where it is utilized. As discussed, the PID cut depends on the proton and antiproton purity distributions in the phase space, so how to solve the acceptance problem will be determined after we introduce the purity study.

3.4.3 Purity

The higher-order fluctuations are very sensitive to the contaminating particles. To have a clean result on the measured net-proton numbers, we should ensure the bin-by-bin proton and antiproton purities in the measured phase space are always higher than 90%. For the purity, which is defined by the fraction of true particles of interest in the particle candidates, the approach for the calculation is to estimate the fraction of protons or antiprotons within the positively or negatively charged particles which are identified as protons or antiprotons by the detectors.

1. From TPC

To ensure the purities of protons and antiprotons from TPC, we perform multi-Gaussian fits for the $n\sigma_{\text{proton}}$ distributions of positively and negatively charged particles within each two-dimensional bin of p_{T} and y, respectively. Figure 3.16 shows the fitting details in several phase space bins. The procedures in each bin are illustrated as follows:

1. Fit the distribution of negatively charged particles with a double-Gaussian function, and determine the heights, means and widths of the peaks of pions and kaons,
2. Fit the distribution of positively charged particles with a quadruple-Gaussian function using the pion and kaon means and widths obtained in Step 1, and determine the height, mean and width of the proton peak,
3. Fit the distribution of negatively charged particles with a triple-Gaussian function using the pion and kaon heights, means and widths obtained in Step 1 and the proton mean and width obtained in Step 2, and determine the height of the antiproton peak,
4. Compute the PID cut efficiency and the purities of protons and antiprotons.

We find that the Gaussian distribution can describe the (anti)proton contribution well. In each panel, the vertical dashed lines are the cut boundaries of $\left|n\sigma_{\text{proton}}\right| < 2$. The PID cut efficiency, to be discussed in Section 3.7, is calculated by the ratio of the integral of the proton (antiproton) Gaussian function within $\left|n\sigma_{\text{proton}}\right| < 2$ divided by the total integral of the proton (antiproton) Gaussian function. The PID cut efficiency is always comparable to 95%, consistent with the 2σ probability of the Gaussian distribution. This supports that the width of $n\sigma_{\text{proton}}$ is around 1. There could be four purity numbers in the text "purity = A (B), C (D)", which represent

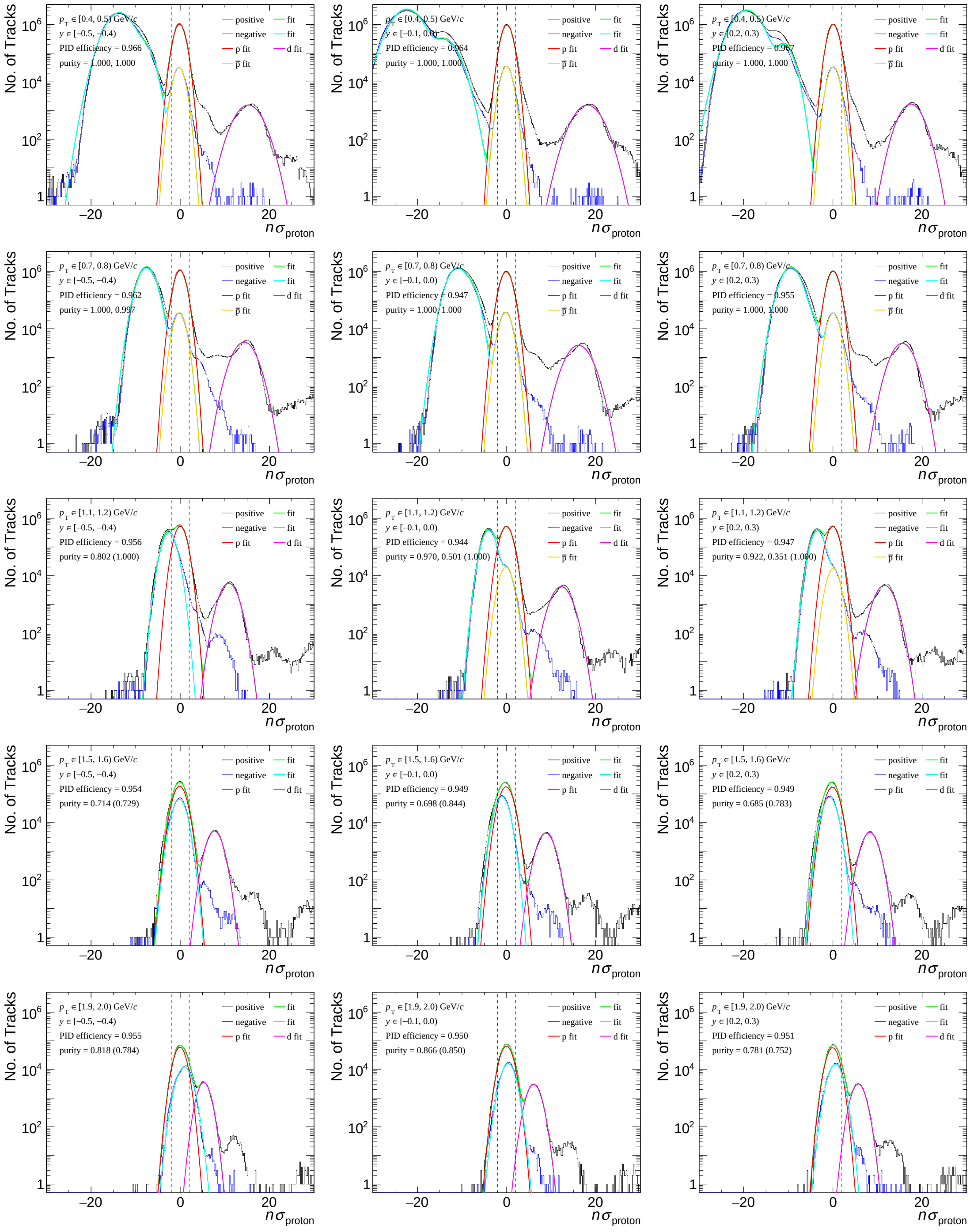

Figure 3.16 (Color online) Details of multi-Gaussian fits for the $n\sigma_{\rm proton}$ distributions of positively and negatively charged particles in a few two-dimensional bins of p_T and y in the $\sqrt{s_{\rm NN}}$ = 11.5 GeV data set. The PID cut efficiency and the purities of protons and antiprotons are calculated accordingly.

- A: proton purity within $|n\sigma_{\rm proton}| < 2$,
- B: proton purity within $0 < n\sigma_{\rm proton} < 2$,
- C: antiproton purity within $|n\sigma_{\rm proton}| < 2$,
- D: antiproton purity within $0 < n\sigma_{\rm proton} < 2$.

The purity is obtained by the ratio of the integral of the proton (antiproton) Gaussian function within the $n\sigma_{\text{proton}}$ cut window divided by the integral of the measured distribution of positively (negatively) charged particles within the $n\sigma_{\text{proton}}$ cut window. At low p, both purities are almost 100%, because pion and kaon contributions are far away from the $n\sigma_{\text{proton}}$ cut range. As p increases, the $n\sigma_{\text{proton}}$ peaks of pions and kaons merge together and move towards zero due to the trend of overlapping $\mathrm{d}E/\mathrm{d}x$. At $p_{\mathrm{T}} > 0.8$ GeV/c at mid-rapidity, pions start contaminate (anti)protons. Due to the low antiproton yield at the low $\sqrt{s_{\mathrm{NN}}}$, the antiproton purity drops significantly. Protons can protect their purity at higher p_{T} and larger y until pions merge their peaks completely. Hence, it is a challenge to have the antiproton high enough for this analysis. It can be found that the asymmetric cut window, $0 < n\sigma_{\text{proton}} < 2$, can effectively enhance the purity, because the $n\sigma_{\text{proton}}$ peaks of the contaminating particles always distribute on the negative side in the momentum region of $p \lesssim 1.6$ GeV/c. Note that such cut throws away half number of the pure (anti)protons and leads to an additional 50% factor of the PID cut efficiency. If the purity is not higher than 90%, we can choose whether to utilize TOF PID or the asymmetric $n\sigma_{\text{proton}}$ cut.

2. From TOF

We also check the purities of protons and antiprotons from TOF. Similarly, multi-Student's-t fits are used to describe the m^2 distributions of positively and negatively charged particles within each two-dimensional bins of p_{T} and y, respectively. A Log-Normal function may also be included for the background in the distribution, which is belived to come from some TOF hits mismatched with the TPC tracks. The fitting procedures, as well as the calculations of the PID cut efficiency and the purities, are similar to the case of $n\sigma_{\text{proton}}$. Both purity numbers of protons and antiprotons are listed in each panel, which are calculated within the vertical dashed lines corresponding to $0.6\ \mathrm{GeV}^2/c^4 < m^2 < 1.2\ \mathrm{GeV}^2/c^4$. We can see a very high purity, nearly 100%, from the TOF PID, suggesting an excellent capability of TOF. Note that the Student's-t function, which is symmetric, might not describe perfectly the m^2 peak of (anti)protons where we see a hint of asymmetry. However, the contaminating fraction is reasonably estimated to be negligible and supports the extreme purity. The little difference of the purity number from 100% is mainly due to the imperfect fitting.

From this study, we can observe a high purity at low p and a low purity at relatively high p from TPC, and the purity from TOF PID is always comparable to 100%. The purity will be considered when we determine the PID cuts.

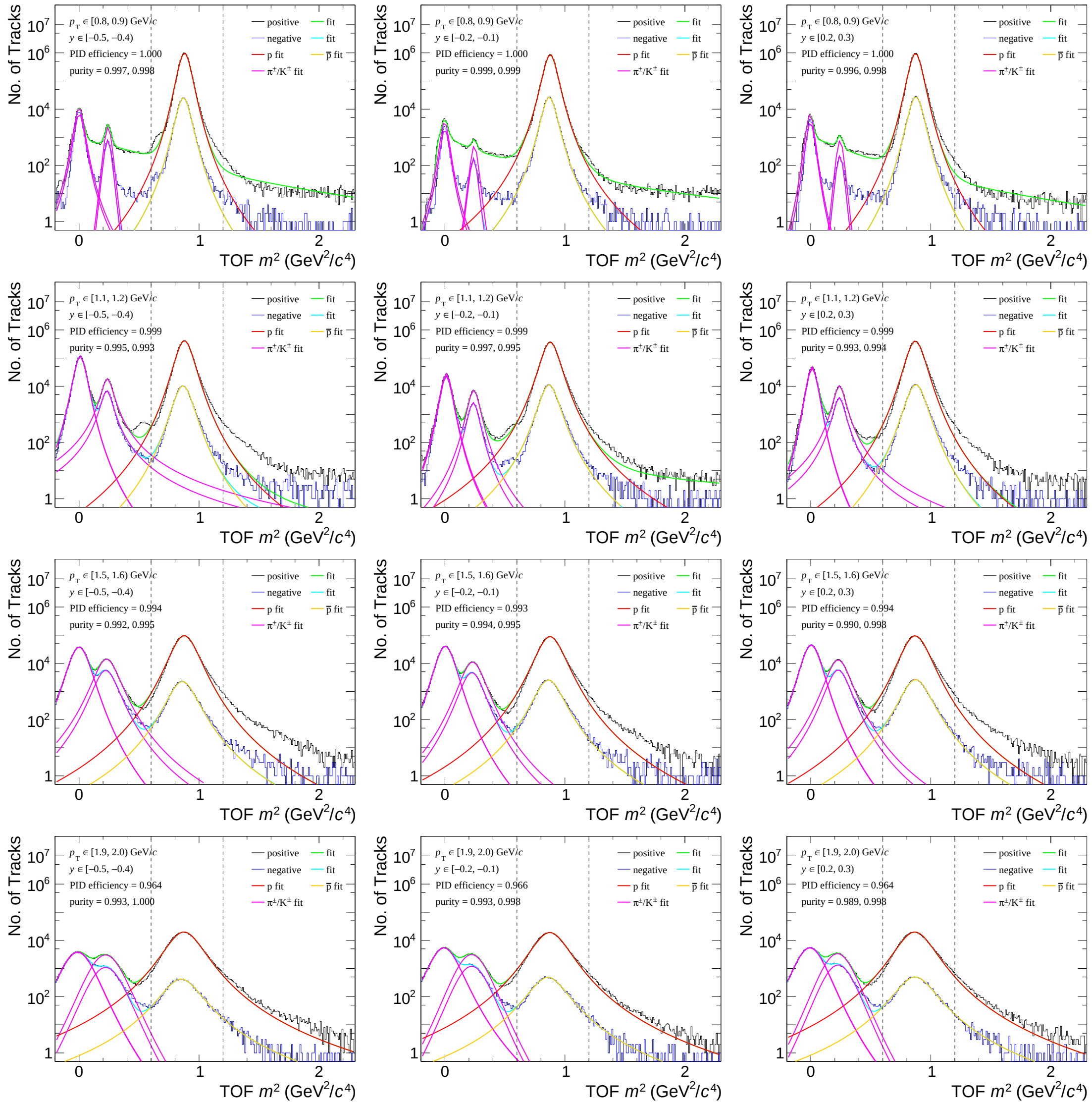

Figure 3.17 (Color online) Details of multi-Student's-t fits for the m^2 distributions of positively and negatively charged particles in a few two-dimensional bins of p_T and y in the $\sqrt{s_{NN}}$ = 11.5 GeV data set. A Log-Normal function may also be included to describe the background in the distribution. The PID cut efficiency and the purities of protons and antiprotons are calculated accordingly.

3.4.4 PID Cut Determination

So far, we have met two challenges:

1. Lack of acceptance for y extension for both TPC and TOF,
2. Low purity at high p for TPC,

and also two possible solutions:

1. The acceptance is enlarged by reducing the $|V_z|$ cut,
2. The purity can be enhanced by either the asymmetric $n\sigma_{\text{proton}}$ cut or the TOF PID,

with a few disadvantages:

1. Event statistics are suppressed by a tighter $|V_z|$ cut,
2. TOF has a clearly smaller coverage compared to TPC and may need an even

narrower V_z window to have enough acceptance,

3. The efficiency will be 50% lower if the asymmetric $n\sigma_{\mathrm{proton}}$ cut is applied.

Considering the issues of the acceptance and the purity, we are going to discuss how to determine the PID cuts. There are three sets of PID cuts classified into cases with different y ranges listed in Table 3.8. As we discussed before, the purity from TOF PID is always high, so it will not be checked again in this section.

Table 3.8 Three sets of PID cuts and corresponding y ranges.

PID Cut 1	$\|y\| < 0.5$
PID Cut 2	$\|y\| < 0.6$
PID Cut 3	$\|y\| < 0.7$

The determination of the PID cuts goes through the following steps:

1. Check the acceptance of TPC,
2. Check the purity distribution,
3. For phase space bins where purity < 90%, two choices:
    (a) Require TOF, check the acceptance of TOF, and reduce the $\left|V_z\right|$ cut if needed,
    (b) Check the purity from TPC asymmetric $n\sigma_{\mathrm{proton}}$ cut, and apply this cut if available and an additiaon factor of 50% on the PID efficiency.

Note that all the acceptance bands in this study are obtained based on the cut of nHitsFit > 25 as the tightest cut to be used in the systematic uncertainty calculation.

1. PID Cut 1

Figure 3.18 shows the acceptances and purities to be studied for PID Cut 1 in the $\sqrt{s_{\mathrm{NN}}}$ = 7.7 GeV (left) and 11.5 GeV (right) data sets. In each panel, there are two bands for the acceptances, the larger and smaller of which come from TPC and TPC+TOF, respectively. In both bands, tracks with positive (negative) rapidities are taken from events within 49 cm < V_z < 50 cm (−50 cm < V_z < −49 cm). Let us first focus on the $\sqrt{s_{\mathrm{NN}}}$ = 11.5 GeV data set on the right-hand side. In the phase space of 0.4 GeV/c < p_{T} < 2.0 GeV/c and $|y| < 0.5$, TPC has enough coverage, and the region of p_{T} > 0.8 GeV/c, where the TOF PID is used as the default case, is fully covered by TOF. There is no issue on the acceptance. For the purity, each phase space cell holds two purity numbers from TPC $\left|n\sigma_{\mathrm{proton}}\right| < 2$: the black one is for protons, and the red ons is for antiprotons. Within the black square, the phase space of p_{T} < 0.8 GeV/c, the TPC PID is only required, and both purities of protons and antiprotons are found to be almost 100%. In other words, the default acceptance and PID cut are fine for the $\sqrt{s_{\mathrm{NN}}}$ = 11.5 GeV data set.

In the left panel representing the $\sqrt{s_{\mathrm{NN}}}$ = 7.7 GeV data set, it is clear that the the

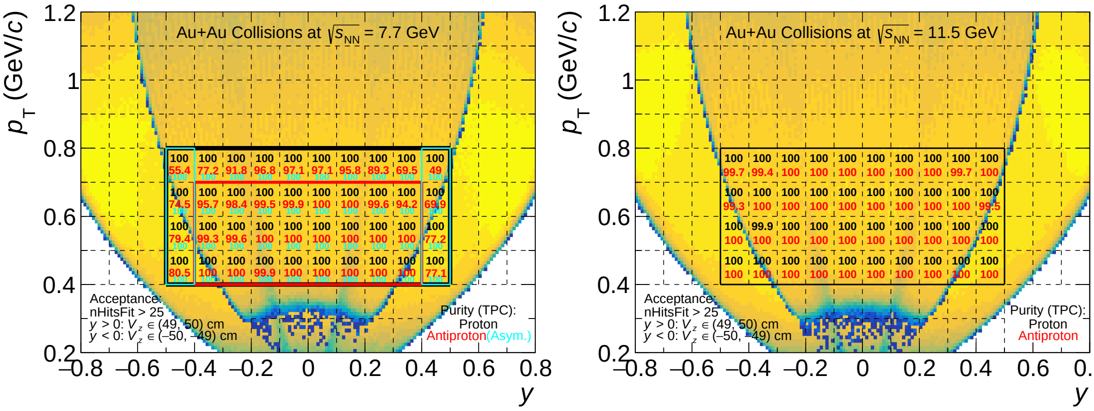

Figure 3.18 (Color online) Acceptances from TPC and TPC+TOF and purites from TPC used to determine PID Cut 1 in the $\sqrt{s_{NN}}$ = 7.7 GeV (left) and 11.5 GeV (right) data sets. Acceptance bands are obtained from tracks selected by nHitsFit > 25 from events in 49 cm < V_z < 50 cm for $y > 0$ and −50 cm < V_z < −49 cm for $y < 0$. Black, red and cyan purity numbers are for protons from TPC, antiprotons from TPC and antiprotons from the TPC asymmetric $n\sigma_{\text{proton}}$ cut, respectively.

default acceptance is also fully covered by TPC. This is natural because the geometry condition is not affected by $\sqrt{s_{NN}}$. There are three purity numbers in each cell, where the black and red ones are of the same definitions in the right panel. An additional cyan number is from the TPC asymmetric $n\sigma_{\text{proton}}$ cut of $0 < n\sigma_{\text{proton}} < 2$, found to enhance the antiproton purity compared to the red. The default PID cut is applying TPC PID only within the black square. Here, the proton purity is high enough, but there is an issue of the antiproton purity. Compared to the $\sqrt{s_{NN}}$ = 11.5 GeV data set, the purity is lower due to the lower antiproton yield at lower $\sqrt{s_{NN}}$. It is required to reduce the TPC PID phase space for antiprotons to the red box. However, in the cyan boxes, which are not fully covered by TOF and have a low antiproton purity, we can utilize the asymmetric PID cut. It has been checked that the the cyan numbers are higher than 90% here.

Hence, PID Cut 1 for both data sets is summarized as

1. 7.7 GeV ($|V_z| < 50$ cm):
   (a) Protons:
      - TPC: [0.4 GeV/c < p_T < 0.8 GeV/c, $|y| < 0.5$],
      - TPC+TOF: otherwise,
   (b) Antiprotons:
      - TPC: [0.4 GeV/c < p_T < 0.7 GeV/c, $|y| < 0.4$],
      - TPC asymmetric: [0.4 GeV/c < p_T < 0.8 GeV/c, $0.4 < |y| < 0.5$],
      - TPC+TOF: otherwise,
2. 11.5 GeV ($|V_z| < 50$ cm):
   (a) Protons:

  - TPC: [0.4 GeV/c < p_{T} < 0.8 GeV/c, $|y|$ < 0.5],
  - TPC+TOF: otherwise,

(b) Antiprotons:

  - TPC: [0.4 GeV/c < p_{T} < 0.8 GeV/c, $|y|$ < 0.5],
  - TPC+TOF: otherwise.

Based on this cut, the bin-by-bin proton and antiproton purities are higher than 99% in both data sets, expect only a couple of bins with antiproton purity > 94% for the $\sqrt{s_{\mathrm{NN}}}$ = 7.7 GeV data set.

2. PID Cut 2

In the right panel of Figure 3.19, in the 11.5 GeV data set, the $\left|V_z\right|$ cut should be reduced to 45 cm to have full TPC coverage in $|y|$ < 0.6. This is limited by the TPC geometry and expected to be the same for all data sets with iTPC. The purity numbers are defined the same as those in Figure 3.18. The proton purity within the black box is good, so we apply the default PID cut for protons. For antiprotons, the TPC PID is applied in the red box. There are six low-purity cells not fully covered by TOF, enclosed by the cyan boxes. Thus, we apply the TPC asymmetric cut here to improve the antiproton purity up to the cyan numbers.

There are more low-purity bins in 7.7 GeV data set, shown by the left panel of Figure 3.19. As seen for the two cells of 0.8 GeV/c < p_{T} < 0.9 GeV/c and 0.5 < $|y|$ < 0.6, the antiproton purity is below 90% even the TPC asymmetric cut is applied, so the only solution is reducing the $\left|V_z\right|$ cut down to 20 cm to make TOF cover them. Based on the $\left|V_z\right|$ cut, the phase space bins of the TPC PID and TPC asymmetric PID

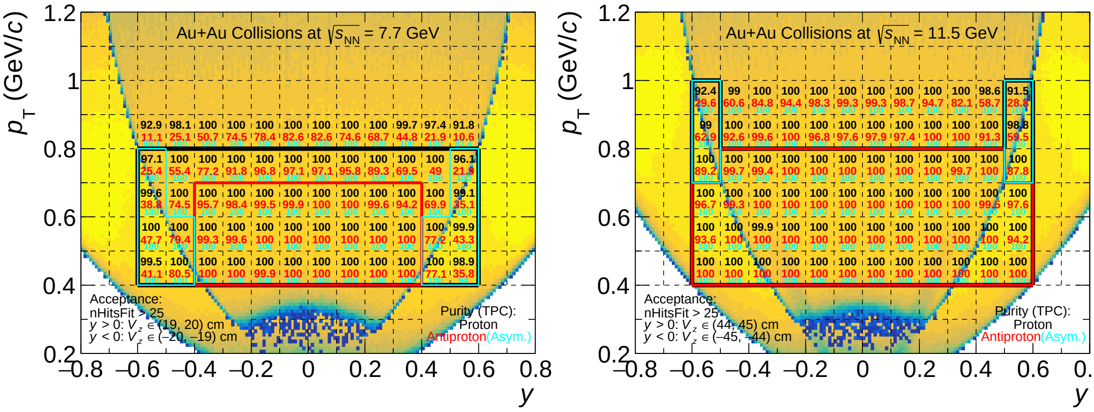

Figure 3.19 (Color online) Acceptances from TPC and TPC+TOF and purites from TPC used to determine PID Cut 2 in the $\sqrt{s_{\mathrm{NN}}}$ = 7.7 GeV (left) and 11.5 GeV (right) data sets. Acceptance bands are obtained from tracks selected by nHitsFit > 25. The event cut is 19 cm < V_z < 20 cm (−20 cm < V_z < −19 cm) for y > 0 (y < 0) for the 7.7 GeV data set, and 49 cm < V_z < 50 cm (−50 cm < V_z < −49 cm) for y > 0 (y < 0) for the 11.5 GeV data set. Black, red and cyan purity numbers are for protons from TPC, antiprotons from TPC and antiprotons from the TPC asymmetric $n\sigma_{\mathrm{proton}}$ cut, respectively.

for antiprotons are located within the red and cyan boxes, respectively.

We determine PID Cut 2 as

1. 7.7 GeV ($|V_z| < 20$ cm):
    - (a) Protons:
        - TPC: [0.4 GeV/c < p_{T} < 0.8 GeV/c, $|y| < 0.6$],
        - TPC+TOF: otherwise,
    - (b) Antiprotons:
        - TPC: [0.4 GeV/c < p_{T} < 0.7 GeV/c, $|y| < 0.4$],
        - TPC asymmetric: [0.4 GeV/c < p_{T} < 0.6 GeV/c, $0.4 < |y| < 0.5$] and [0.4 GeV/c < p_{T} < 0.8 GeV/c, $0.5 < |y| < 0.6$],
        - TPC+TOF: otherwise,
2. 11.5 GeV ($|V_z| < 45$ cm):
    - (a) Protons:
        - TPC: [0.4 GeV/c < p_{T} < 0.8 GeV/c, $|y| < 0.5$] and [0.4 GeV/c < p_{T} < 1.0 GeV/c, $0.5 < |y| < 0.6$],
        - TPC+TOF: otherwise,
    - (b) Antiprotons:
        - TPC: [0.4 GeV/c < p_{T} < 0.8 GeV/c, $|y| < 0.5$] and [0.4 GeV/c < p_{T} < 0.7 GeV/c, $0.5 < |y| < 0.6$],
        - TPC asymmetric: [0.7 GeV/c < p_{T} < 1.0 GeV/c, $0.5 < |y| < 0.6$],
        - TPC+TOF: otherwise.

Based on this cut, the bin-by-bin proton and antiproton purities are higher than 99% in both data sets, expect only a couple of bins with purity > 91%.

3. PID Cut 3

Similarly, if the analysis is going to $|y| < 0.7$, the $|V_z|$ cut should be reduced to 15 cm due to the geometry of TPC. Figure 3.20 presents the acceptances at $|V_z| \sim 15$ cm for both $\sqrt{s_{\mathrm{NN}}} = 7.7$ GeV data set in the left panel and 11.5 GeV data set in the right panel. It is found that there are always a couple of bins within $|y| < 0.7$ holding the antiproton purity below 90%, no matter whether TPC asymmetric PID or the TPC+TOF PID is applied. Hence, we focus on the proton analysis for $|y| < 0.7$. Note that at higher energies, the antiproton purity should be higher and may make the rapidity extension possible for antiprotons. While at low energies, due to the low yield of antiprotons, the proton contributions dominate in the net-proton fluctuations. In both panels, through the checks of the acceptance and the purity, proton are identified by TPC within the black boxes, and the TPC asymmetric PID is applied within magenta squares.

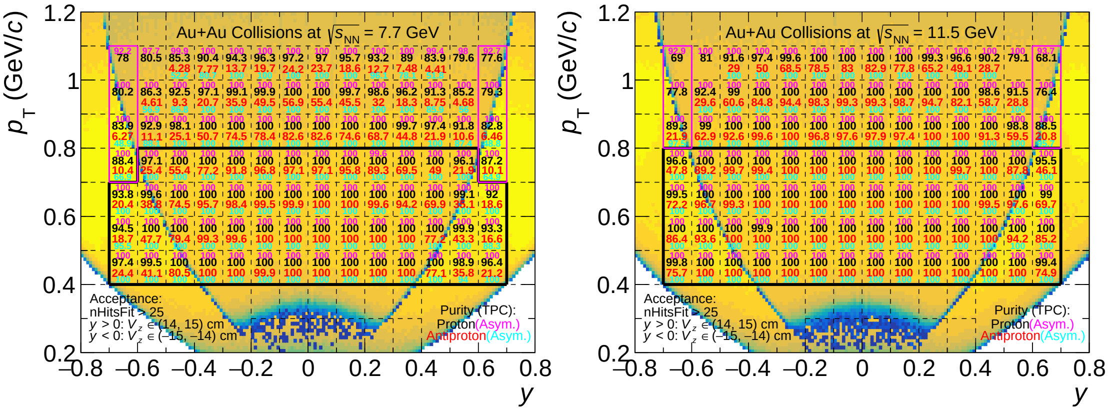

Figure 3.20 (Color online) Acceptances from TPC and TPC+TOF and purites from TPC used to determine PID Cut 3 in the $\sqrt{s_{\mathrm{NN}}}$ = 7.7 GeV (left) and 11.5 GeV (right) data sets. Acceptance bands are obtained from tracks selected by nHitsFit > 25 from events in 14 cm < V_z < 15 cm for $y > 0$ and −15 cm < V_z < −14 cm for $y < 0$. Magenta, black, red and cyan purity numbers are for protons from the TPC asymmetric $n\sigma_{\mathrm{proton}}$ cut, protons from TPC, antiprotons from TPC and antiprotons from the TPC asymmetric $n\sigma_{\mathrm{proton}}$ cut, respectively.

Based on the study, PID Cut 3 represents

1. 7.7 GeV ($|V_z| < 15$ cm):
   - (a) Protons:
     - TPC: [0.4 GeV/c < p_{T} < 0.8 GeV/c, $|y| < 0.6$] and [0.4 GeV/c < p_{T} < 0.7 GeV/c, $0.6 < |y| < 0.7$],
     - TPC asymmetric: [0.7 GeV/c < p_{T} < 1.1 GeV/c, $0.6 < |y| < 0.7$],
     - TPC+TOF: otherwise,
2. 11.5 GeV ($|V_z| < 15$ cm):
   - (a) Protons:
     - TPC: [0.4 GeV/c < p_{T} < 0.8 GeV/c, $|y| < 0.7$],
     - TPC asymmetric: [0.8 GeV/c < p_{T} < 1.1 GeV/c, $0.6 < |y| < 0.7$],
     - TPC+TOF: otherwise.

Based on this cut, the bin-by-bin proton purity is higher than 99% in both data sets, expect only a couple of bins with purity > 92%.

3.5 Centrality Definition

Centrality in heavy-ion collisions refers to the geometric extent of the interaction zone where the collisions occur. It is a key concept reflecting the volume of the collision system and providing insight into the collision dynamics of an event, including the energy density, temperature and magnetic field achieved in the collision zone. Thus, the collision centrality dependence of a measured quantity is usually studied in experiments. The net-proton number fluctuations belong to the bulk properties of the system and are also strongly affected by the collision centrality.

3.5.1 In Model

There are several variables which can be utilized to define the centrality. Here, we introduce the Glauber model [137], popular in the description of the collision centrality in experimental data. In this model, various centralities of collision events can be simulated, and the initial nucleons in each atomic nucleus are based on the Wood-Saxon potential [138].

Figure 3.21 [137] shows the geometry of the heavy-ion collisions, with side and beam-line views in panel (a) and (b), respectively. Two ellipses represent the colliding ions containing nucleons. The impact parameter b quantifies the perpendicular distance between the centers of the two ions. The overlap area of two ions in the transverse plane increases as b is reduced, and reaches a maximum in a head-on collision with $b = 0$ and fully overlapping ions. In other words, b measures how close a collision event is to a head-on collision and defines the centrality. For central collisions, ions overlap significantly with small b, while peripheral collisions carry larger b where the overlap of the ions is smaller. The left panel in Figure 3.22 [137] shows the distributions of b in various simulated collision systems. However, b can not be directly measured in experiments, since it is difficult to know the initial geometry for each collision.

Figure 3.23 [137] illustrates a event simulated by the Glauber model for a Au+Au collision event at $\sqrt{s_{\mathrm{NN}}} = 200$ GeV with the impact parameter $b = 6$ fm. Circles with darker and lighter colors represent participating and spectating nucleons, respectively, which are identified by whether they participate in the reactions. It is clear that most of the participating nucleons distribute in the overlap zone, where reactions focus. The

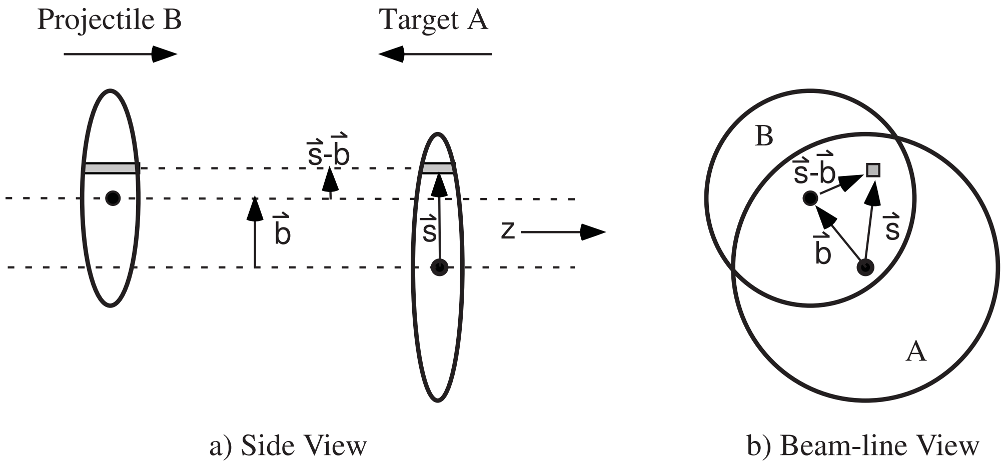

a) Side View b) Beam-line View

Figure 3.21 (Color online) A sketch of the heavy-ion collision geometry in the Optical Glauber Model, with side (a) and beam-line (b) views. Figure is taken from Reference [137].

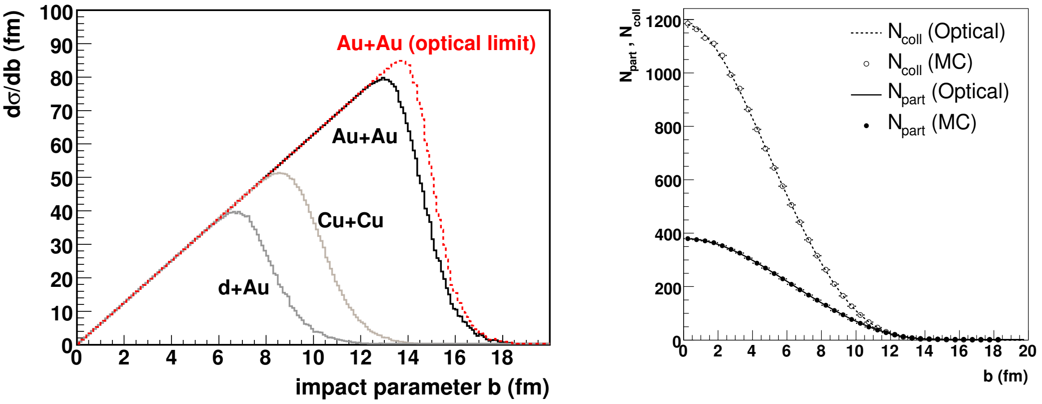

Figure 3.22 (Color online) Distributions of b (left) and numbers of participating nucleons (N_{part}) and binary nucleon-nucleon collisions (N_{coll}) as functions of b (right) in various collision systems from Glauber Monte Carlo calculations. Figure is taken from Reference [137].

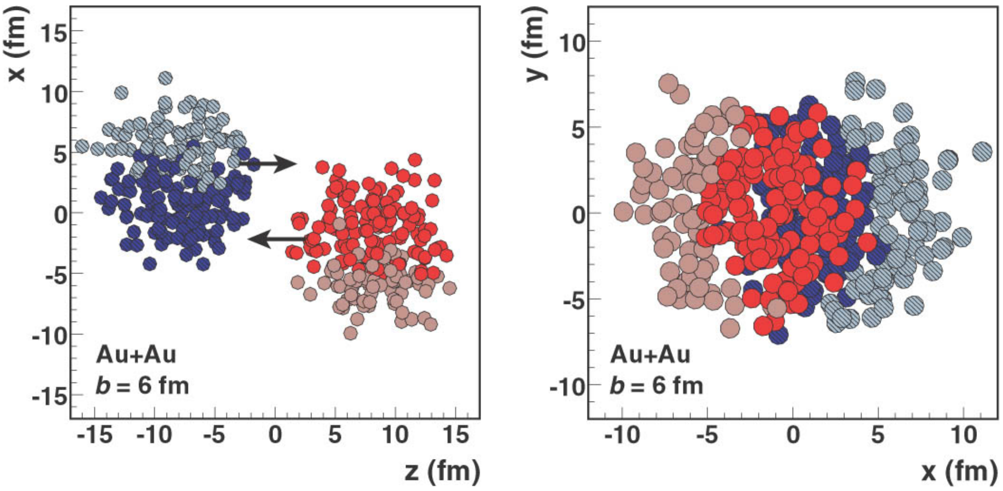

Figure 3.23 (Color online) A sketch of a Glauber Monte Carlo Au+Au collision event at $\sqrt{s_{\text{NN}}} = 200$ GeV with the impact parameter $b = 6$ fm, with side (left) and beam-line (right) views. Participating and spectating nucleons are drawn by darker and lighter colors, respectively. Figure is taken from Reference [137].

number of participating nucleons (N_{part}) has a maximum of the total nucleon number of the two colliding ions. It can reflect the overlap area, as a choice of the centrality definition correlated to b. In the Glauber model, reactions can be modelled into independent binary nucleon-nucleon collisions, the number of which (N_{coll}) also reflects the reaction intensity and the centrality. The right panel in Figure 3.22 [137] shows the correlations of N_{part} and N_{coll} to b in various simulated collision systems. To be more clearly, N_{part} and N_{coll} characterize the soft and hard processes, respectively. Neither of N_{part} and N_{coll} is the final-state quantities and cannot be obtained event-by-event in realistic experiments.

The Glauber model simulates the reactions in collision events and obtains the particles at the final state. The charged-particle multiplicity (N_{ch}) is experimentally mea-

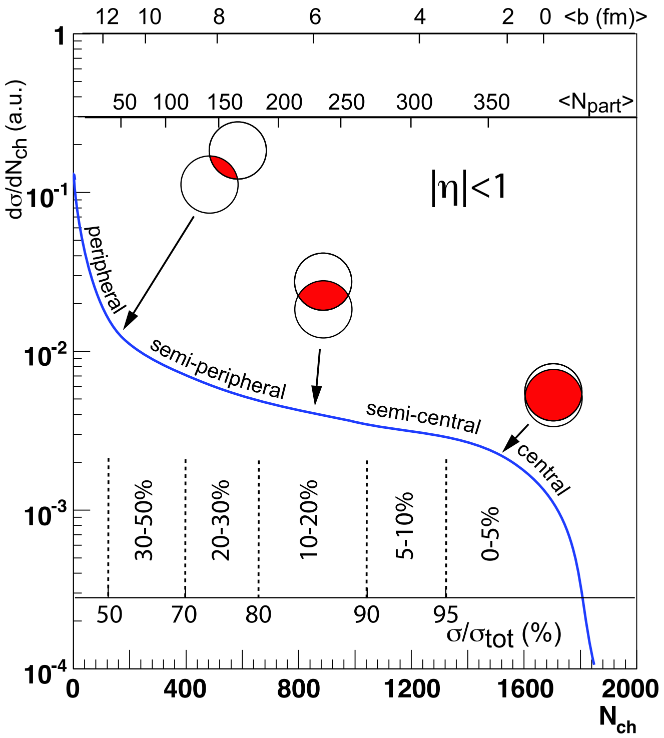

Figure 3.24 (Color online) An example of the distribution of the charged-particle multiplicity (N_{ch}) and its correlation with the Glabuer simulated b and N_{part}. Figure is taken from Reference [137].

surable and expected to reflect the centrality. Figure 3.24 [137] presents the correlation between the final-state N_{ch} and the simulated b and N_{part}. The more central collision, with the smaller b, holds the larger reaction area and the more participating nucleons and binary collisions, which are likely to produce more charged particles at the final state.

3.5.2 In Experiment

Experimentalists find several observables to determine the centrality for each collision event, such as the number of spectators flying out along the beam line counted by forward detectors and the total energy deposited in some detectors. The most popular one is N_{ch} as discussed.

1. Definition

In STAR, the official centrality determination is using RefMult as the reference multiplicity of charged particles within $|\eta| < 0.5$. It includes protons and antiprotons and can contribute to the net-proton fluctuations through a so-called self-correlation (or auto-correlation) [139-140]. If we count the same particle species in both the multiplicity for centrality and the particle number fluctuations, the multiplicity naturally classify events with more analyzed particles as more central events. The self-correlation effect

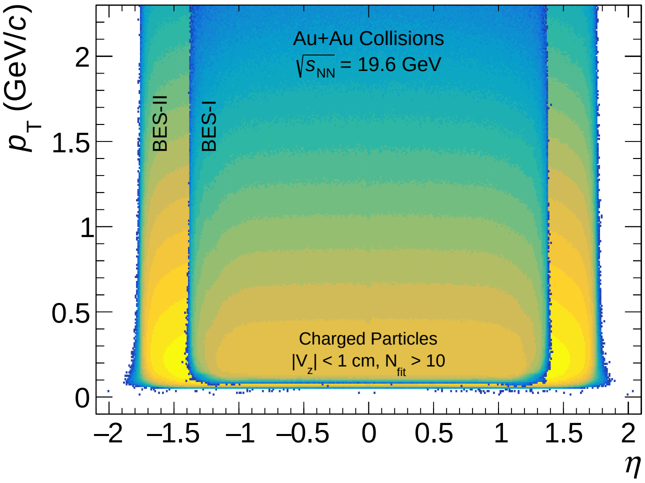

Figure 3.25 (Color online) Comparison of the charged-particle acceptances measured by TPC in the η-p_T phase space between BES-I and BES-II. Both acceptance bands are obtained from the events at $|V_z| < 1$ cm and the tracks with nHitsFit > 10.

may distort the fluctuation magnitudes and reflect false physical pictures. Therefore, we do not use RefMult for the centrality determination.

Because the charged-particle multiplicity is not fully determined by the initial centrality through a fixed correlation, the system volume fluctuates even if we select a fixed charged-particle multiplicity. Related model studies suggests that a larger multiplicity can suppress the volume fluctuations [139-141] and characterize the realistic collision centrality better. That is easy to understand that the minimum segment of the multiplicity is 1 unit and a larger multiplicity have more bins to reflect the centrality with better resolution. The volume fluctuations can also contribute to the measured fluctuations, but they are not the signals which we want to observe for the signals of the phase structure.

In this analysis, we define two charged-particle multiplicities, RefMult3 and RefMult3X, using the following cuts:

1. Track quality cuts
    (a) nHitsFit > 10
    (b) DCA < 3 cm
2. Kinematic cuts
    - $|\eta| < 1.0$ for RefMult3
    - $|\eta| < 1.6$ for RefMult3X
3. PID cuts
    - $n\sigma_{\text{proton}} < -3$
      if TPC PID available, TOF PID unavailable,
    - $m^2 < 0.4$ GeV^2/c^4

if TPC PID unavailable, TOF PID available,

- $n\sigma_{\text{proton}} < -3$, $m^2 < 0.4\ \text{GeV}^2/c^4$
  if TPC PID available, TOF PID available,

where TPC PID available ⇔ nHitsDedx > 5, and TOF PID available ⇔ TOF match flag > 0, $|\text{local Y}| < 1.8$ cm and $\beta \geqslant 10^{-5}$. The PID cuts here exclude protons and antiprotons to avoid the self-correction, and actually they select charged pions and kaons. RefMult3 keeps the same definition with $|\eta| < 1.0$ as BES-I. Taking advantage of iTPC, the $|\eta|$ cut can be extended up to 1.6 for the RefMult3X definition. The validation of the $|\eta|$ extension is confirmed by the charged-particle acceptances shown by Figure 3.25.

2. Correction

Now we consider to correct the multiplicity for each event considering two artificial negative contributions to the multiplicity. The geometry of the detector, determined by the collision primary-vertex position, influences the acceptance coverage and the detection efficiency, and the TPC occupancy, depending on the collision luminosity, also has an effect on the detection efficiency. Both of them suppress the multiplicity, which requires V_z and ZDC coincidence rate corrections. In the V_z correction, the first step is fitting the tail of the multiplicity distribution in each V_z bin by

$$f(\text{mult}) = A(1 + \text{erf}(-\sigma(\text{mult} - h))), \tag{3.3}$$

where h describes the high-end point position, and erf represents the error function. An example for RefMult3X within $-50\ \text{cm} < V_z < -49\ \text{cm}$ in the $\sqrt{s_{\text{NN}}} = 11.5$ data set is shown in the top left panel of Figure 3.26. Then, the dependence of h on V_z, presented as the black markers in the bottom left panel, is parameterized by the sextic function

$$f\left(V_z\right) = \sum_{i=0}^{6} p_i V_z^i, \tag{3.4}$$

shown as the red curve. We apply a bin-by-bin V_z correction and obtain the corrected multiplicity in each V_z bin as

$$\text{mult}_{\text{corr}} = \left\lfloor \frac{p_0}{h}\text{mult} + \text{random}(0, 1) \right\rfloor, \tag{3.5}$$

where h is taken by its value in this V_z bin. The corrected multiplicity is rounded to an adjacent integer based on a random number between 0 and 1 generated by random(0, 1). In the top right panel, it is found that the corrected distribution does not have a V_z dependence, and the h value becomes nearly constant in the bottom left panel.

The bottom right panel of Figure 3.26 presents the mean of RefMult3X as a function of the ZDC coincidence rate. The mean value is taken with a lower threshold of the

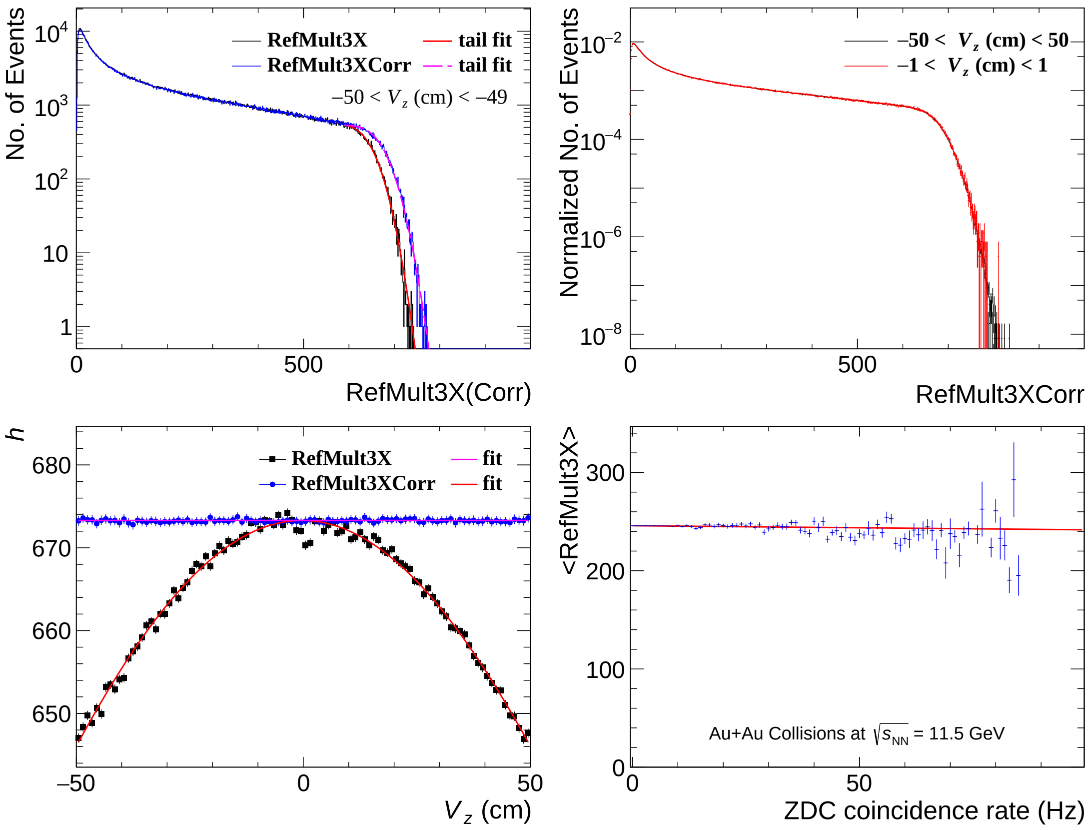

Figure 3.26 (Color online) Details of V_z and ZDC coincidence rate corrections for RefMult3X in the $\sqrt{s_{\mathrm{NN}}}$ = 11.5 GeV data set. Top left: V_z correction within -50 cm $< V_z < -49$ cm; top right: V_z-corrected distributions within $|V_z| < 50$ cm and $|V_z| < 1$ cm; bottom left: tail parameters before and after V_z correction; bottom right: dependence on ZDC coincidence rate.

multiplicity to reject the background. The red line denotes a linear parameterization. A clear dependence on the ZDC coincidence rate cannot be observed, so we do not take the luminosity correction into account.

The RefMult3 and RefMult3X distributions after the V_z correction in both data sets are presented in Figure 3.27, compared to RefMult3 in BES-I. The BES-II RefMult3 is observed to be a little bit larger than BES-I because of the enhanced detection efficiency and the reduced p_{T} threshold by iTPC. With a broader $|\eta|$ cut window, RefMult3X is even larger. As expected, the larger multiplicity distributes in the more bins and introduces the better centrality resolution. Hence, the resolution: RefMult3 (BES-I) < RefMult3 (BES-II) < RefMult3X (BES-II), which is one of the upgrade in the BES-II analysis. The effect of the centrality resolution will be studied in both model simulation and experimental data.

3. Glauber Fit

The collision centrality is usually expressed as a percentage of the total collision cross-section, where 0% represents the most central (head-on) collisions and 100% rep-

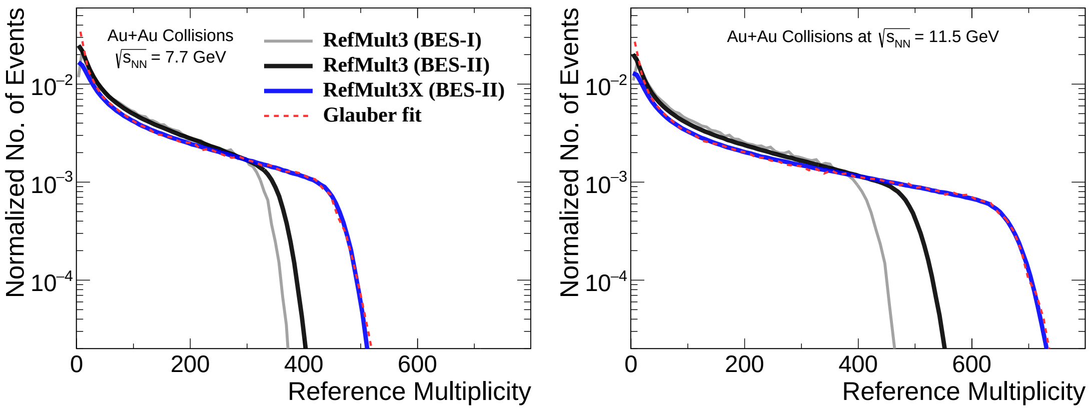

Figure 3.27 (Color online) Distributions of RefMult3 (BES-I and BES-II) and RefMult3X (BES-II) in the $\sqrt{s_{NN}}$ = 7.7 GeV (left) and 11.5 GeV (right) data sets. RefMult3 in BES-II is larger than that in BES-I and smaller than RefMult3X.

Table 3.9 Multiplicity cuts and $\langle N_{\text{part}} \rangle$ for various centrality classes. In each cell, the top (bottom) number represents the multiplicity cut ($\langle N_{\text{part}} \rangle$) value.

$\sqrt{s_{NN}}$	7.7 GeV		11.5 GeV	
Multiplicity	RefMult3	RefMult3X	RefMult3	RefMult3X
0–5%	290 338.5	376 339.5	408 340.2	553 340.8
5–10%	240 288.2	310 288.1	338 288.6	459 288.6
10–20%	164 224.1	212 223.8	232 224.4	316 224.6
20–30%	110 158.0	142 157.9	156 158.5	213 158.6
30–40%	71 108.4	92 108.5	101 108.9	138 109.0
40–50%	44 71.6	56 71.3	62 71.6	84 71.4
50–60%	25 44.4	32 43.9	35 44.1	48 44.0
60–70%	13 25.1	17 25.1	19 25.3	25 25.0
70–80%	7 13.5	8 13.0	9 13.3	12 12.9

resents the most peripheral (edge-on) collisions, and events are classified into various centrality classes by the intervals of the percentages. However, there is a trigger inefficiency with a significant suppression on recording low-multiplicity events. We need to use the Glauber Mont Carlo model to describe the experimental multiplicity, particularly the shape of the multiplicity distribution at low multiplicities. It is more important that the centrality parameters, b, N_{part} and N_{coll}, can be modelled.

We go through the STAR official approach. A number of Glauber events are simulated with a few input parameters, such as the types of the colliding nuclei, the collision energy and the cross section of the p+p collision at the same collision energy. As one of the initial parameters, b is randomly allocated. The contribution from N_{coll} as the hard component and N_{part} as the soft component to N_{ch} can be expressed by

$$N_{\mathrm{ch}} = n_{\mathrm{pp}} \left(xN_{\mathrm{coll}} + (1-x)\frac{N_{\mathrm{part}}}{2} \right), \tag{3.6}$$

where n_{pp} is the charged-particle multiplicity in p+p collisions, and x quantifies the fraction of the hard process. Actually, the N_{ch} calculated from this formula is not consistent with the experimentally measured multiplicity. An NBD fit is required through the following procedures:

1. Define $m = xN_{\mathrm{coll}} + (1-x)\frac{N_{\mathrm{part}}}{2}$,
2. Sample m times from NBD, expressed below, to get the ideal multiplicity,

$$\mathrm{NBD}(n) = \frac{\Gamma(n+k)}{\Gamma(n+1)\Gamma(k)} \left(\frac{\mu/k}{1+\mu/k} \right)^{n} (1+\mu/k)^{-k}, \tag{3.7}$$

3. Reduce the ideal multiplicity by a factor of $1-\varepsilon$, where the efficiency ε is

$$\varepsilon = 0.98 \left(1 - \frac{d}{540} \mathrm{mult}_{\mathrm{ideal}} \right). \tag{3.8}$$

There are four free fitting parameters:

1. $\mu = \langle n_{\mathrm{pp}} \rangle$,
2. k controls the shape including the sharpness of the upper edge of the Glauber multiplicity,
3. x is the hardness parameter,
4. d describes the multiplicity dependence of inefficiency.

By tuning the four parameters, the simulated multiplicity from Glauber is determined to have the the minimum χ^2 characterizing the difference from the measured multiplicity. Note that the Glauber fit is only taken for semi-central to central events, since the model cannot describe the multiplicity distribution of peripheral events in experiments, which is suppressed by the trigger inefficiency. The RefMult3X distributions from the Glauber fits are shown as red dashed curves in Figure 3.27.

The centrality classes are divided into several percentages from 0% to 80%, and the multiplicity cuts and $\langle N_{\mathrm{part}} \rangle$ are summarized in Table 3.9.

The difference of the multiplicity distributions between the Glauber model and the experiment induced by the trigger inefficiency is studied by the reweighting procedure. The trigger inefficiency is assumed to be 0% for 0–20% centrality, and the ratio of model/experiment in the 20–80% centrality class is parameterized by

$$f(x) = p_0 + \frac{p_1}{p_2 x + p_3} + p_4 \left(p_2 x + p_3 \right) + p_5 \left(p_2 x + p_3 \right)^2 + \frac{p_6}{\left(p_2 x + p_3 \right)^2}. \tag{3.9}$$

In the following cumulant measurement, this value is applied to each event as a weight.

3.6 Centrality Bin Width Correction

Measured fluctuations are usually presented in broad centrality classes. The finite centrality bin width leads to a varied multiplicity in a range, introducing an additional volume fluctuation effect and enhance the measured particle fluctuations, which contribute as a background or distortion [139-140]. To suppress the contribution of the volume fluctuations within a centrality class, it is easy to classify events into as narrow centrality bins as possible, that is, single-value multiplicity bins. In a broad centrality class, we can combine cumulants in each multiplicity bin with the number of events as the weight. This is the Centrality Bin Width Correction (CBWC) [139], and the formula is expressed by

$$C_r = \frac{\sum\limits_i n_i C_{r,i}}{\sum\limits_i n_i}, \tag{3.10}$$

where n_i and $C_{r,i}$ are the number of events and the rth-order cumulant in the ith multiplicity bin. The summation is taken over all the multiplicity bins in the centrality class. In this calculation, $C_{r,i}$ is obtained in the finest centrality bin with as small volume fluctuation as possible and contributes to C_r in a broad centrality class without a significant enhancement from the volume fluctuation.

3.7 Efficiency Correction

A number of particles are lost by the detectors based on a probability due to finite detection efficiency or some other effects. The efficiency can be defined by the ratio of the number of measured particles divided by the true number of produced particles. For some measurements on the first-order fluctuation, that is, mean, such as particle yields, the true number can be simply calculated by dividing the measured number by the efficiency. However, the contribution of the efficiency to the higher-order fluctuations is not simply a factor. To remove or suppress the effect of finite efficiency on the measured fluctuations, detailed studies are required.

3.7.1 Formula Derivation

The efficiency effect results from the detector response, which can be assumed to be binomial. Mathematically, for a particle group of interest, suppose the produced true number X, as a non-negative integer, is a stochastic variable following the probability mass function $P(X)$. The binomial efficiency is $\alpha \in [0, 1]$ and makes the measured number x, as non-negative integer not larger than X, follows

$$\tilde{P}(x) = \sum_{X} P(X)\mathscr{B}_{X,\alpha}(x), \tag{3.11}$$

where

$$\mathscr{B}_{X,\alpha}(x) = \frac{X!}{x!(X-x)!}\alpha^{x}(1-\alpha)^{X-x} \tag{3.12}$$

denotes the probability mass function of the binomial distribution with $\alpha = \dfrac{\langle x\rangle}{\langle X\rangle}$.

Note that non-binomial effects from efficiency can be estimated through an unfolding approach [142-143], and the results are found to agree well with the binomial assumption [98]. Hence, we only consider the binomial efficiency correction in this analysis.

For M particle group of interest, suppose the produced numbers $\boldsymbol{X} = \left(X_1, X_2, \cdots, X_M\right)$ are non-negative integer stochastic variables following the probability mass function $P(\boldsymbol{X})$. The linear combination of the produced numbers with the numerical coefficients $\boldsymbol{a} = \left(a_1, a_2, \cdots, a_M\right)$ is expressed by

$$Q_{(\boldsymbol{a})} = \boldsymbol{a}\cdot\boldsymbol{X} = \sum_{i=1}^{M} a_i X_i. \tag{3.13}$$

This quantity denotes the total conserved charge of these particles if a_i is the conserved charge carried by the ith particle species. The cumulant and factorial cumulant of Q can be derived from their generating functions as

$$\left\langle Q^{r}_{(\boldsymbol{a})}Q^{s}_{(\boldsymbol{b})}\right\rangle_{\mathrm{c}} = \partial^{r}_{(\boldsymbol{a})}\partial^{s}_{(\boldsymbol{b})}G_{\mathrm{c}}(\boldsymbol{\theta})\Big|_{\boldsymbol{\theta}=0}, \tag{3.14}$$

$$G_{\mathrm{c}}(\boldsymbol{\theta}) = \ln\sum_{\boldsymbol{X}} P(\boldsymbol{X})\mathrm{e}^{\boldsymbol{\theta}\cdot\boldsymbol{X}} = \ln\left\langle \mathrm{e}^{\boldsymbol{\theta}\cdot\boldsymbol{X}}\right\rangle, \tag{3.15}$$

$$\left\langle Q^{r}_{(\boldsymbol{a})}Q^{s}_{(\boldsymbol{b})}\right\rangle_{\mathrm{fc}} = \bar{\partial}^{r}_{(\boldsymbol{a})}\bar{\partial}^{s}_{(\boldsymbol{b})}G_{\mathrm{fc}}(\boldsymbol{u})\Big|_{\boldsymbol{u}=1}, \tag{3.16}$$

$$G_{\mathrm{fc}}(\boldsymbol{u}) = \ln\sum_{\boldsymbol{X}} \tilde{P}(\boldsymbol{X})\prod_{i=1}^{M} u_i^{X_i} = \ln\left\langle \prod_{i=1}^{M} u_i^{X_i}\right\rangle \tag{3.17}$$

with

$$\partial_{(\boldsymbol{a})} = \sum_{i=0}^{M} a_i\partial_{\theta_i}, \tag{3.18}$$

$$\bar{\partial}_{(\boldsymbol{a})} = \sum_{i=0}^{M} a_i\partial_{u_i}. \tag{3.19}$$

The relations between cumulants and factorial cumulants based on these definitions are derived in References [144-145].

Due to the effect of the binomial efficiencies $\boldsymbol{\alpha} = \left(\alpha_1, \alpha_2, \cdots, \alpha_M\right) \in [0,1]^M$, the measured numbers $\boldsymbol{x} = \left(x_1, x_2, \cdots, x_M\right)$ follows the probability mass function

$$\tilde{P}(\boldsymbol{x}) = \sum_{\boldsymbol{X}} P(\boldsymbol{X}) \prod_{i=1}^{M} \mathscr{B}_{X_i,\alpha_i}\left(x_i\right) \tag{3.20}$$

with $\alpha_i = \dfrac{\langle x_i \rangle}{\langle X_i \rangle}$. The linear combination of the measured numbers is expressed by

$$q_{(\boldsymbol{a})} = \boldsymbol{a} \cdot \boldsymbol{x} = \sum_{i=1}^{M} a_i x_i. \tag{3.21}$$

The cumulants and factorial cumulants can also be given by the generation functions as

$$\left\langle q^r_{(\boldsymbol{a})} q^s_{(\boldsymbol{b})} \right\rangle_{\mathrm{c}} = \partial^r_{(\boldsymbol{a})} \partial^s_{(\boldsymbol{b})} \tilde{G}_{\mathrm{c}}(\boldsymbol{\theta}) \Big|_{\boldsymbol{\theta}=0}, \tag{3.22}$$

$$\tilde{G}_{\mathrm{c}}(\boldsymbol{\theta}) = \ln \sum_{\boldsymbol{x}} P(\boldsymbol{x}) \mathrm{e}^{\boldsymbol{\theta}\cdot\boldsymbol{x}} = \ln \left\langle \mathrm{e}^{\boldsymbol{\theta}\cdot\boldsymbol{x}} \right\rangle, \tag{3.23}$$

$$\left\langle q^r_{(\boldsymbol{a})} q^s_{(\boldsymbol{b})} \right\rangle_{\mathrm{fc}} = \bar{\partial}^r_{(\boldsymbol{a})} \bar{\partial}^s_{(\boldsymbol{b})} \tilde{G}_{\mathrm{fc}}(\boldsymbol{u}) \Big|_{\boldsymbol{u}=1}, \tag{3.24}$$

$$\tilde{G}_{\mathrm{fc}}(\boldsymbol{u}) = \ln \sum_{\boldsymbol{x}} \tilde{P}(\boldsymbol{x}) \prod_{i=1}^{M} u_i^{x_i} = \ln \left\langle \prod_{i=1}^{M} u_i^{x_i} \right\rangle. \tag{3.25}$$

The generating functions of factorial cumulants with and without the effect of the binomial efficiency can be connected directly by

$$\begin{aligned} \tilde{G}_{\mathrm{fc}}(\boldsymbol{u}) &= \ln \sum_{\boldsymbol{X}} P(\boldsymbol{X}) \sum_{\boldsymbol{x}} \prod_{i=1}^{M} \mathscr{B}_{X_i,\alpha_i}\left(x_i\right) u_i^{x_i} \\ &= \ln \sum_{\boldsymbol{X}} P(\boldsymbol{x}) \prod_{i=1}^{M} \left(\alpha_i u_i + \left(1 - \alpha_i\right)\right) \\ &= G_{\mathrm{fc}}(\boldsymbol{u}'), \end{aligned} \tag{3.26}$$

where the second line is obtained by the binomial expansion, and $u_i' = \alpha_i u_i + \left(1 - \alpha_i\right)$ $(i = 1, 2, \cdots, M)$.

The relation between the produced and the measured cumulants can be derived by three steps:

$$\begin{tikzcd} \left\langle Q^r_{(\boldsymbol{a})} Q^s_{(\boldsymbol{b})} \right\rangle_{\mathrm{c}} \arrow[r, leftrightarrow] & \left\langle Q^r_{(\boldsymbol{a})} Q^s_{(\boldsymbol{b})} \right\rangle_{\mathrm{fc}} \arrow[d, leftrightarrow] \\ \left\langle q^r_{(\boldsymbol{a})} q^s_{(\boldsymbol{b})} \right\rangle_{\mathrm{c}} \arrow[r, leftrightarrow] & \left\langle q^r_{(\boldsymbol{a})} q^s_{(\boldsymbol{b})} \right\rangle_{\mathrm{fc}} \end{tikzcd}$$

The efficiency correction formulae for diagonal cumulants up to the fourth order are given by [144-145]

$$\left\langle Q_{(1,0)} \right\rangle_{\mathrm{c}} = \left\langle q_{(1,1)} \right\rangle_{\mathrm{c}}, \tag{3.27}$$

$$\left\langle Q_{(1,0)}^2 \right\rangle_{\mathrm{c}} = \left\langle q_{(1,1)}^2 \right\rangle_{\mathrm{c}} + \left\langle q_{(2,1)} \right\rangle_{\mathrm{c}} - \left\langle q_{(2,2)} \right\rangle_{\mathrm{c}}, \tag{3.28}$$

$$\begin{aligned}\left\langle Q_{(1,0)}^3 \right\rangle_{\mathrm{c}} = {} & \left\langle q_{(1,1)}^3 \right\rangle_{\mathrm{c}} + 3\left\langle q_{(1,1)} q_{(2,1)} \right\rangle_{\mathrm{c}} - 3\left\langle q_{(1,1)} q_{(2,2)} \right\rangle_{\mathrm{c}} \\ & + \left\langle q_{(3,1)} \right\rangle_{\mathrm{c}} - 3\left\langle q_{(3,2)} \right\rangle_{\mathrm{c}} + 2\left\langle q_{(3,3)} \right\rangle_{\mathrm{c}},\end{aligned} \tag{3.29}$$

$$\begin{aligned}\left\langle Q_{(1,0)}^4 \right\rangle_{\mathrm{c}} = {} & \left\langle q_{(1,1)}^4 \right\rangle_{\mathrm{c}} + 6\left\langle q_{(1,1)}^2 q_{(2,1)} \right\rangle_{\mathrm{c}} - 6\left\langle q_{(1,1)}^2 q_{(2,2)} \right\rangle_{\mathrm{c}} + 4\left\langle q_{(1,1)} q_{(3,1)} \right\rangle_{\mathrm{c}} \\ & - 12\left\langle q_{(1,1)} q_{(3,2)} \right\rangle_{\mathrm{c}} + 8\left\langle q_{(1,1)} q_{(3,3)} \right\rangle_{\mathrm{c}} + 3\left\langle q_{(2,1)}^2 \right\rangle_{\mathrm{c}} - 6\left\langle q_{(2,1)} q_{(2,2)} \right\rangle_{\mathrm{c}} \\ & + 3\left\langle q_{(2,2)}^2 \right\rangle_{\mathrm{c}} + \left\langle q_{(4,1)} \right\rangle_{\mathrm{c}} - 7\left\langle q_{(4,2)} \right\rangle_{\mathrm{c}} + 12\left\langle q_{(4,3)} \right\rangle_{\mathrm{c}} - 6\left\langle q_{(4,4)} \right\rangle_{\mathrm{c}},\end{aligned} \tag{3.30}$$

where

$$Q_{(r,s)} = Q_{(\boldsymbol{a}^r/\boldsymbol{\alpha}^s)} = \sum_{i=1}^{M} \frac{a_i^r}{\alpha_i^s} X_i, \tag{3.31}$$

$$q_{(r,s)} = q_{(\boldsymbol{a}^r/\boldsymbol{\alpha}^s)} = \sum_{i=1}^{M} \frac{a_i^r}{\alpha_i^s} x_i. \tag{3.32}$$

Those for hyper-order cumulants are put into Appendix A.

If $M \to \infty$, which means infinite groups of particles, x_i $(i = 0, 1, \cdots)$ can only be 0 or 1, and we have [146]

$$q_{(r,s)} = \sum_{i=1}^{x_{\mathrm{total}}} \frac{a_i^r}{\alpha_i^s}, \tag{3.33}$$

where $x_{\mathrm{total}} = \sum\limits_{i=1}^{M} x_i$, by ignoring contributions from zero counts. That is to say, $q_{(r,s)}$ does not take particle groups into account any more. The basic object for $q_{(r,s)}$ and α_i $(i = 0, 1, \cdots)$ turn to each single measured particle. Connected to the experimental analysis, the efficiency is calculated on the track basis, so this approach is called the track-by-track efficiency correction.

In the previous measurement [98], the bin-by-bin efficiency correction [147] was performed using the averaged efficiencies of individual protons and antiprotons calculated within two p_{T} bins. The track-by-track efficiency correction offers enhanced simplicity and accuracy compared to the former method. One of our studies [148] highlights that the non-uniformity of the track efficiency could influence the corrected fluctuations, indicating that using average efficiency within phase space bins should be done with caution. Additionally, another analysis [149] suggests that event-by-event fluctuations in efficiency can also impact the result and should be considered. Thus, it is essential to incorporate the detailed form of the efficiency distribution or its differential dependence which can be more effectively managed through the track-by-track efficiency correction.

3.7.2 Efficiency Calculation

1. TPC Tracking Efficiency

TPC misses a fraction of particles when reconstructing their tracks. The probability of a particle being tracked by TPC, characterizing the tracking capability of TPC, is called the TPC tracking efficiency. It depends on the track momentum vector, the detector geometry relative to the track trajectory, and the TPC occupancy. For the track momentum vector, we study the p_{T} and y dependence; for the relative geometry, it is reflected by V_z; for the occupancy, the efficiency has a little dependence on the event multiplicity.

In STAR, a Monte Carlo simulation, called embedding, is used to estimate the TPC tracking efficiency. The procedure is generating Monte Carlo tracks and embedding them into real events containing real tracks. The detector response to these tracks is simulated using the GEANT toolkit [150-152]. Tracks are reconstructed based on the simulation, and the efficiency is calculated by

$$\varepsilon_{\text{TPC tracking}} = \frac{N_{\text{reconstructed}}}{N_{\text{embedded}}} \tag{3.34}$$

as the fraction of the reconstructed tracks, which include all of the track quality cuts.

The TPC tracking efficiency is calculated in four-dimensional bins of centrality, V_z, p_{T} and y to study the detailed dependence. The centrality dependence is found to be weak. Figure 3.28 presents the TPC tracking efficiency of protons in the 0–5% centrality class. There are 14 panels representing y bins from -0.7 – -0.6 to 0.6–0.7. In each panel, markers show 5 V_z bins from -50 – -30 cm and 30–50 cm. In mid-rapidity bins, efficiencies in different V_z bins are consistent with each other. At forward/backward y, a clear V_z ordering of the efficiency can be observed, with smaller efficiency in the bins of V_z carrying the same sign as y. This effect results from the geometry, similar to the V_z dependence of acceptance.

Taking advantage of the iTPC upgrade, the TPC tracking efficiency at mid-rapidity in BES-II is about 10% higher than BES-I, and the enhancement at low p_{T} or for-

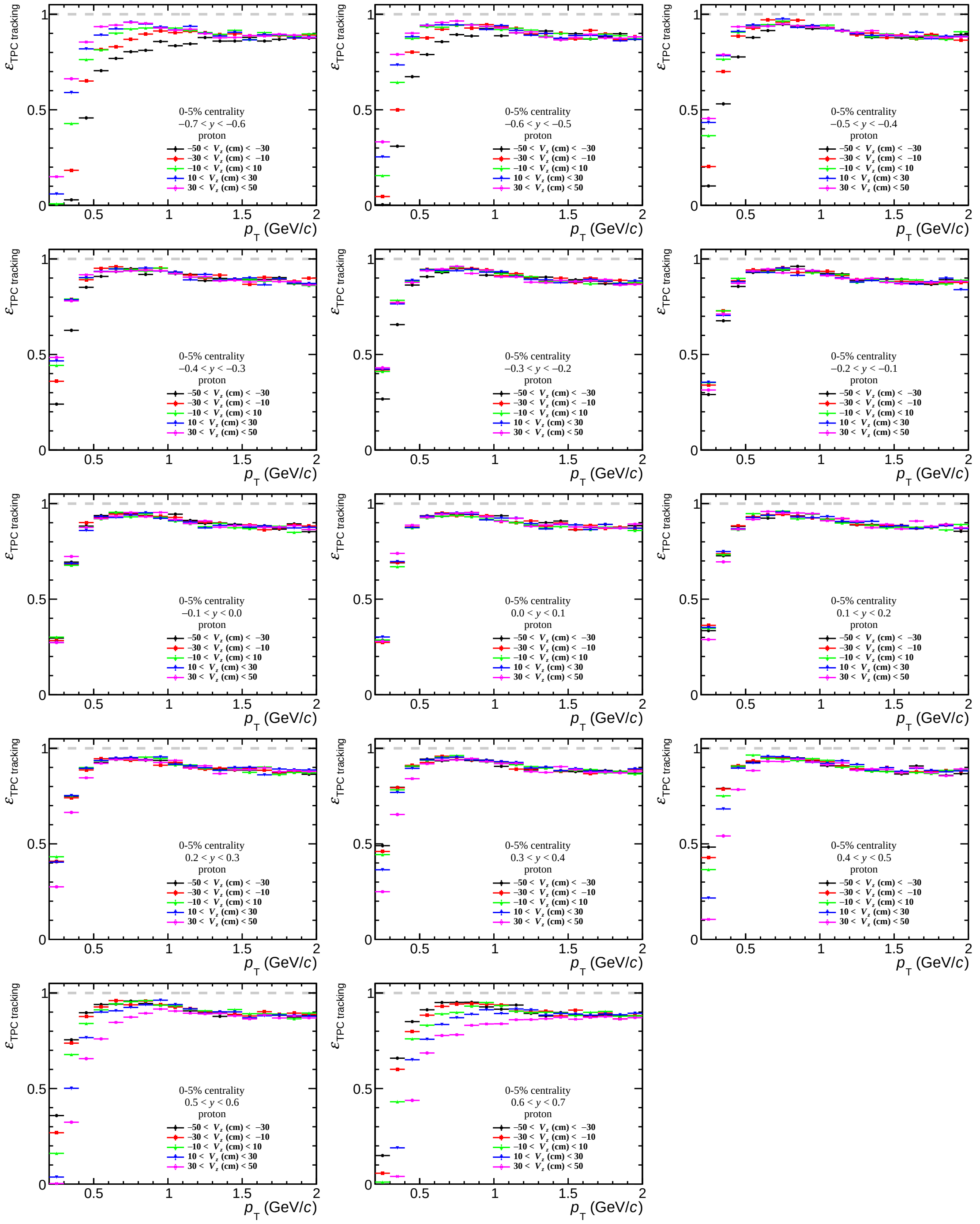

Figure 3.28 (Color online) TPC tracking efficiency of protons as a function of $p_{\rm T}$ in various V_z and y bins in the 0–5% centrality class in the $\sqrt{s_{\rm NN}} = 11.5$ GeV data set. Each panel represent a y bin, and markers show the $p_{\rm T}$ dependence in different V_z bins.

ward/backward rapidity is much stronger.

2. TPC PID cut Efficiency

The default TPC PID cut is $|n\sigma_{\rm proton}| < 2$, and it loses a fraction of (anti)protons due to the Gaussian width. In Section 3.4.3, the TPC PID cut efficiency has been extracted from the multi-Gaussian fit for $n\sigma_{\text{proton}}$ by

$$\varepsilon_{\text{TPC PID}} = \frac{N_{\text{TPC PID}}}{N_{\text{(anti)proton, no TPC PID}}}, \tag{3.35}$$

where the numerator counts the number of (anti)protons passing the $n\sigma_{\text{proton}}$ cut, while the denominator denotes the total (anti)protons without an $n\sigma_{\text{proton}}$ cut estimated from the $n\sigma_{\text{proton}}$ fit. In Figure 3.16, the efficiency is found comparable to 95% as the Gaussian 2σ area. Note that the PID cut efficiency is reduced by a factor of 50% in the phase space bins where the TPC asymmetric PID cut is applied.

3. TOF Matching Efficiency

The TOF matching efficiency represents the probability of a track that is matched with a TOF hit and is calculated by

$$\varepsilon_{\text{TOF matching}} = \frac{N_{\text{TPC PID, TOF match}}}{N_{\text{TPC PID}}}, \tag{3.36}$$

where “TPC PID” includes the track quality cuts and TPC PID cuts, and “TOF match” requires the cuts of TOF match flag > 0, TOF $|\text{local Y}| < 1.8$ cm and $\beta \geqslant 10^{-5}$. It is also obtained in four-dimensional bins of centrality, V_z, p_{T} and y, and the distributions in the 0–5% centrality class from the $\sqrt{s_{\text{NN}}} = 11.5$ GeV data set are shown in Figure 3.29. It is obvious that the y and V_z dependences follow the same trend as the TPC tracking efficiency but are much more significant, because the TOF acceptance coverage is smaller and provides a stronger edge effect. We can find a clear suppression of the TOF matching efficiency within [-50 cm $< V_z < -30$ cm, $0.1 < y < 0.2$] and [30 cm $< V_z < 50$ cm, $-0.2 < y < -0.1$] due to the limited matching capability for tracks crossing the central gap of the detector system between the east and west halves.

4. TOF PID cut Efficiency

The TOF PID cut also misses counting a few (anti)protons. Similar to the TPC PID cut efficiency, the TOF PID cut efficiency is calculated by

$$\varepsilon_{\text{TOF PID}} = \frac{N_{\text{TOF PID}}}{N_{\text{(anti)proton, no TOF PID}}}, \tag{3.37}$$

where the denominator represents the estimated total number of (anti)protons without a m^2 cut based on the multi-Student’s-t fit for m^2 in Section 3.4.3. A negligible inefficiency from the TOF PID cut is observed in Figure 3.17, so we do not include this contribution in the efficiency correction.

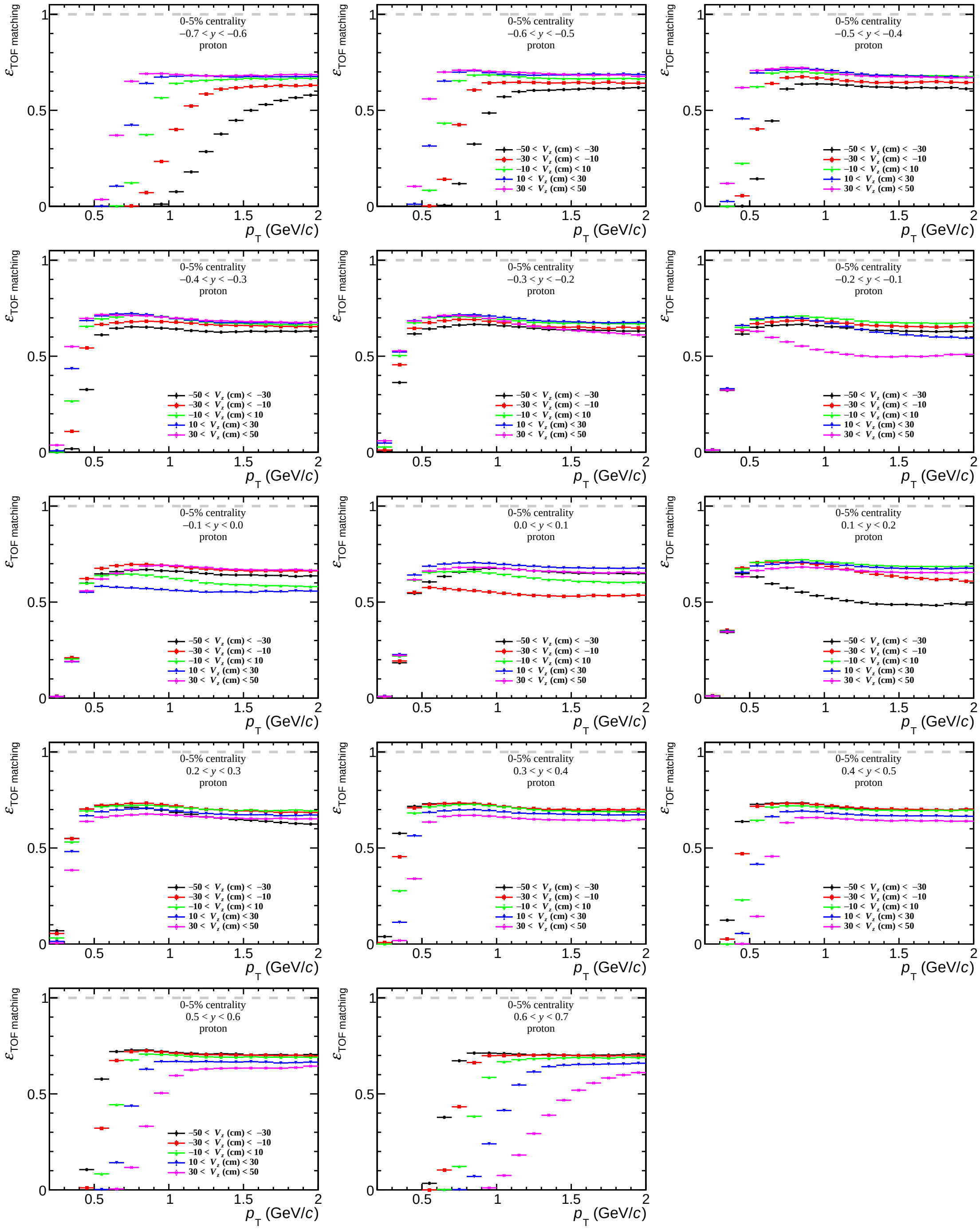

Figure 3.29 (Color online) TOF matching efficiency of protons as a function of p_{T} in various V_z and y bins in the 0–5% centrality class from the $\sqrt{s_{\mathrm{NN}}}$ = 11.5 GeV data set. Each panel represent a y bin, and markers show the p_{T} dependence in different V_z bins.

3.8 Statistical Uncertainty Estimation

In experiments, we use the statistical measures of the sample (produced frequency distribution) to estimate those of the population (true probability distribution), and the statistical uncertainties quantify the statistical fluctuations induced by the limited statistics. Statistical errors of the higher-order fluctuations are the more complicated, including contributions from the more and higher-order correlations. Here, we introduce two calculation methods for the statistical errors: analytical method and bootstrap method.

3.8.1 Analytical Method

This method utilizes analytical formulae derived using statistics based on one of our studies [153]. We start with the covariance of two estimated moments given by [154]

$$
\begin{aligned}
n \cdot \mathrm{Cov}\left(\langle \widehat{X_1 X_2 \cdots X_r} \rangle, \langle \widehat{Y_1 Y_2 \cdots Y_s} \rangle\right) &= \langle X_1 X_2 \cdots X_r Y_1 Y_2 \cdots Y_s \rangle \\
&\quad - \langle X_1 X_2 \cdots X_r \rangle \langle Y_1 Y_2 \cdots Y_s \rangle ,
\end{aligned}
\tag{3.38}
$$

where X_i $(i = 1, 2, \cdots, r)$ and Y_j $(j = 1, 2, \cdots, s)$ are stochastic variables and n denotes the number of samples. A hat $(\hat{\cdot})$ represents that the quantity is estimated from samples.

Using the relation between moments and cumulants expressed in Section 1.8, we can propagate the covariances of estimated moments into the (co)variances between estimated cumulants. Formulae are summarized in Reference [153], some of which for cumulants up to the fourth order are listed in Appendix B.

1. For Efficiency-Uncorrected Cumulant

From the univariate case, variances, as squares of the statistical errors, of efficiency-uncorrected cumulants can be obtained directly as [154]

$$n \cdot \mathrm{Var}\left(\hat{C}_1\right) = C_2, \tag{3.39}$$

$$n \cdot \mathrm{Var}\left(\hat{C}_2\right) = C_4 + 2C_2^2, \tag{3.40}$$

$$n \cdot \mathrm{Var}\left(\hat{C}_3\right) = C_6 + 9C_4C_2 + 9C_3^2 + 6C_2^3, \tag{3.41}$$

$$
\begin{aligned}
n \cdot \mathrm{Var}\left(\hat{C}_4\right) &= C_8 + 16C_6C_2 + 48C_5C_3 + 34C_4^2 \\
&\quad + 72C_4C_2^2 + 144C_3^2C_2 + 24C_2^4,
\end{aligned}
\tag{3.42}
$$

$$
\begin{aligned}
n \cdot \mathrm{Var}\left(\hat{C}_5\right) &= C_{10} + 25C_8C_2 + 100C_7C_3 + 200C_6C_4 \\
&\quad + 125C_5^2 + 200C_6C_2^2 + 1200C_5C_3C_2 + 850C_4^2C_2 \\
&\quad + 1500C_4C_3^2 + 600C_4C_2^3 + 1800C_3^2C_2^2 + 120C_2^5,
\end{aligned}
\tag{3.43}
$$

$$
\begin{aligned}
n \cdot \mathrm{Var}\left(\hat{C}_6\right) &= C_{12} + 36C_{10}C_2 + 180C_9C_3 + 465C_8C_4 + 780C_7C_5 + 461C_6^2 \\
&\quad + 450C_8C_2^2 + 3600C_7C_3C_2 + 7200C_6C_4C_2 + 6300C_6C_3^2 \\
&\quad + 4500C_5^2C_2 + 21600C_5C_4C_3 + 4950C_4^3 + 2400C_6C_2^3 \\
&\quad + 21600C_5C_3C_2^2 + 15300C_4^2C_2^2 + 54000C_4C_3^2C_2 \\
&\quad + 8100C_3^4 + 5400C_4C_2^4 + 21600C_3^2C_2^3 + 720C_2^6,
\end{aligned}
\tag{3.44}
$$

and the covariances are given by

$$n \cdot \mathrm{Cov}\left(\widehat{C}_r, \widehat{C}_1\right) = C_{r+1}, \tag{3.45}$$

$$n \cdot \mathrm{Cov}\left(\widehat{C}_3, \widehat{C}_2\right) = C_5 + 6C_3C_2, \tag{3.46}$$

$$n \cdot \mathrm{Cov}\left(\widehat{C}_4, \widehat{C}_2\right) = C_6 + 8C_4C_2 + 6C_3^2, \tag{3.47}$$

$$n \cdot \mathrm{Cov}\left(\widehat{C}_5, \widehat{C}_2\right) = C_7 + 10C_5C_2 + 20C_4C_3, \tag{3.48}$$

$$n \cdot \mathrm{Cov}\left(\widehat{C}_6, \widehat{C}_2\right) = C_8 + 12C_6C_2 + 30C_5C_3 + 20C_4^2. \tag{3.49}$$

For cumulant ratios, the variances can be calculated using the error propagation formula by

$$\mathrm{Var}\left(\frac{\widehat{C}_r}{\widehat{C}_s}\right) = \frac{\mathrm{Var}\left(\widehat{C}_r\right)}{C_s^2} + \frac{C_r^2\,\mathrm{Var}\left(\widehat{C}_s\right)}{C_s^4} - \frac{2C_r\,\mathrm{Cov}\left(\widehat{C}_r, \widehat{C}_s\right)}{C_s^3}. \tag{3.50}$$

The variance of the CBWC-ed cumulant can also be obtained analytically by the error propagation as

$$\mathrm{Var}\left(\widehat{C}_r\right) = \frac{\sum_i n_i^2\,\mathrm{Var}\left(\widehat{C}_{r,i}\right)}{\left(\sum_i n_i\right)^2}. \tag{3.51}$$

2. For Efficiency-Corrected Cumulant

Based on the (co)variance formulae for the multivariate case, the variances of the efficiency-corrected cumulants derived in Section 3.7.1 are expressed by

$$n \cdot \mathrm{Var}\left(\widehat{C}_1^{\mathrm{corr}}\right) = \left\langle q_{(1,1)}^2 \right\rangle_{\mathrm{c}}, \tag{3.52}$$

$$\begin{aligned} n \cdot \mathrm{Var}\left(\widehat{C}_2^{\mathrm{corr}}\right) = &\left\langle q_{(1,1)}^4 \right\rangle_{\mathrm{c}} + 2\left\langle q_{(1,1)}^2 \right\rangle_{\mathrm{c}}^2 + 2\left\langle q_{(1,1)}^2 q_{(2,1)} \right\rangle_{\mathrm{c}} - 2\left\langle q_{(1,1)}^2 q_{(2,2)} \right\rangle_{\mathrm{c}} \\ &+ \left\langle q_{(2,1)}^2 \right\rangle_{\mathrm{c}} - 2\left\langle q_{(2,1)} q_{(2,2)} \right\rangle_{\mathrm{c}} + \left\langle q_{(2,2)}^2 \right\rangle_{\mathrm{c}}, \end{aligned} \tag{3.53}$$

and the covariances can also be obtained as

$$n \cdot \mathrm{Cov}\left(\widehat{C}_2^{\mathrm{corr}}, \widehat{C}_1^{\mathrm{corr}}\right) = \left\langle q_{(1,1)}^3 \right\rangle_{\mathrm{c}} + \left\langle q_{(1,1)} q_{(2,1)} \right\rangle_{\mathrm{c}} - \left\langle q_{(1,1)} q_{(2,2)} \right\rangle_{\mathrm{c}}, \tag{3.54}$$

$$\begin{aligned} n \cdot \mathrm{Cov}\left(\widehat{C}_3^{\mathrm{corr}}, \widehat{C}_1^{\mathrm{corr}}\right) = &\left\langle q_{(1,1)}^4 \right\rangle_{\mathrm{c}} + 3\left\langle q_{(1,1)}^2 q_{(2,1)} \right\rangle_{\mathrm{c}} - 3\left\langle q_{(1,1)}^2 q_{(2,2)} \right\rangle_{\mathrm{c}} \\ &+ \left\langle q_{(1,1)} q_{(3,1)} \right\rangle_{\mathrm{c}} - 3\left\langle q_{(1,1)} q_{(3,2)} \right\rangle_{\mathrm{c}} + 2\left\langle q_{(1,1)} q_{(3,3)} \right\rangle_{\mathrm{c}}. \end{aligned} \tag{3.55}$$

Results for higher orders are presented in Reference [153]. Statistical errors of cumulant ratios and CBWC-ed cumulants are calculated similarly to the efficiency-uncorrected case.

The statistical uncertainty estimation for efficiency-corrected cumulants has been tested in a toy Monte Carlo simulation in Reference [153]. The probability of a cumulant touching the true value within the estimated statistical error is found to be around 68%, and the errors are consistent with those calculated through the bootstrap method to be discussed later, shown in Figure 3.30 [153], supporting the validation of the analytical derivation.

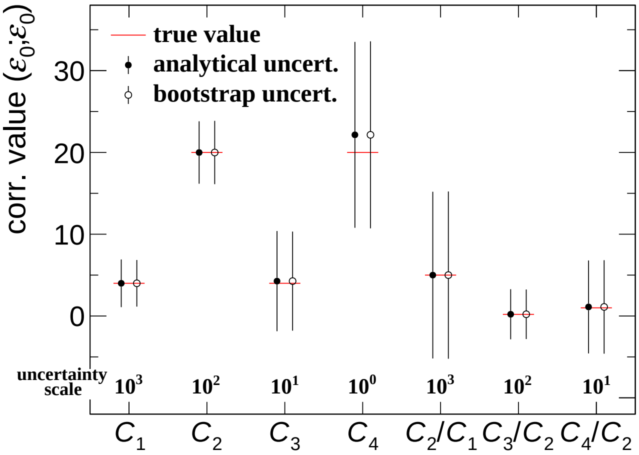

Figure 3.30 (Color online) Comparison between statistical errors from the analytical method and the bootstrap method in a toy Monte Carlo simulation. Figure is taken from Reference [153].

From the formulae, it can be extracted that

$$\mathrm{Cov}\left(\widehat{C}_r^{\mathrm{corr}}, \widehat{C}_s^{\mathrm{corr}}\right) \propto \frac{1}{n}\frac{C_{r+s}}{\varepsilon^{r+s}}. \tag{3.56}$$

This is to say, the statistical error approaches 0 when $n \to \infty$ and can be suppressed by a higher efficiency. The upgrade in BES-II provides improved statistics and enhanced detector efficiency, which contributes to the precision of the measurement. We can also find the errors for higher-orders more sensitive to the efficiency and even higher-order fluctuations. For example, the statistical error of the sixth-order cumulant includes the contribution from the fluctuation up to the twelfth order and plenty of terms characterizing complicated correlations.

Our study [153] also concludes in both analytical and Monte Carlo analyses that

$$\mathrm{Var}\left(\widehat{C}_r\right) \leqslant \mathrm{Var}\left(\widehat{C}_r^{\mathrm{corr}}(\bar{\varepsilon})\right) \leqslant \mathrm{Var}\left(\widehat{C}_r^{\mathrm{corr}}(\varepsilon)\right), \tag{3.57}$$

where $\widehat{C}_r$ represents the cumulant estimated from a sample without a finite efficiency. The estimated cumulants corrected by the efficiencies $\bar{\varepsilon}$ and ε are marked by $\widehat{C}_r^{\mathrm{corr}}(\bar{\varepsilon})$ and $\widehat{C}_r^{\mathrm{corr}}(\varepsilon)$, respectively, and $\bar{\varepsilon}$ is a constant efficiency with the same average as ε. The former inequality suggests the statistical error decreases down to the minimum as the efficiency increases to 100%; while the latter inequality means the statistical error can also be enhanced by the non-uniformity of the efficiency, or called the track-by-track efficiency fluctuation. For suppressing the statistical uncertainty, this study concludes that improving statistics, enhancing efficiency and reducing efficiency non-uniformity are effective approaches.

3.8.2 Bootstrap Method

This method is based on the Monte Carlo resampling procedure [147]. The primary procedure is generating many new samples by independently and randomly sampling events from the real data. Suppose the number of the bootstrap samples is B, and the quantity of interest is X. It is easy to calculate Φ in each bootstrap sample, marked as Φ_b $(b = 1, 2, \cdots, B)$ for the bth sample. Then, the variance of the measured quantity Φ is given by the variance of Φ_b as

$$\begin{aligned}\mathrm{Var}(\Phi) &= \frac{1}{B-1}\sum_{b=1}^{B}\left(\Phi_b - \frac{1}{B}\sum_{b\prime=1}^{B}\Phi_{b\prime}\right)^2 \\ &= \frac{B}{B-1}\left(\frac{1}{B}\sum_{b=1}^{B}\Phi_b^2 - \left(\frac{1}{B}\sum_{b=1}^{B}\Phi_b\right)^2\right).\end{aligned} \tag{3.58}$$

The variance of the quantity from the resampled samples reflect the statistical fluctuations including intrinsic correlations. Thus, the bootstrap method is logically simple, but serves as a really computation-intensive approach.

3.9 Systematic Uncertainty Estimation

The accuracy and reliability of the experimental results are characterized by the systematic uncertainties. The main idea is to check the systematic variations of the measured quantities by tuning the data selection criteria, which can reflect contributions and effects related to the detector performance and calibration, measurement techniques and background noises.

In this analysis, we change the cuts from five sources listed in Table 3.10 to observe systematic variations. The nHitsFit cut checks the tracking and calibration performance; the DCA cut extracts the background effect; the PID cuts study the contribution from contaminating particles; and the efficiency variation tests the stability of the result based on the current understanding on the efficiency estimation. The systematic error of the efficiency was 5% in BES-I [98], while it is estimated to be 2.5% in BES-II due to the

Table 3.10 Cuts for systematic uncertainty estimation.

Cut	Default	Varied			
nHitsFit	> 20	> 15	> 18	> 22	> 25
DCA (cm)	< 1	< 0.8	< 0.9	< 1.1	< 1.2
$\left\|n\sigma_{\text{proton}}\right\|$	< 2	< 1.6	< 1.8	< 2.2	< 2.5
m^2 (GeV$^2/c^4$)	0.6–1.2	0.5–1.1	0.55–1.15	0.65–1.25	0.7–1.3
Efficiency	Default	× 0.975		× 1.025	

improved performance with iTPC. Note that efficiency is recalculated for each varied cut, and TPC asymmetric PID also follows each varied $|n\sigma_{\text{proton}}|$ cut.

The systematic error is calculated using the Barlow check [155] to judge whether the variation of the measured value is from the statistical fluctuation or not when we change the cut. The procedures are discussed as follows.

Suppose there is an observable Y, and the measured central value and statistical uncertainty based on the default cut are Y_{def} and $\sigma_{\text{stat,def}}$, respectively. In total S systematic sources, for the sth ($s = 1, 2, \cdots, S$) source with N_s varied cuts, the measured central value and statistical uncertainty are $Y_{s,i}$ and $\sigma_{\text{stat},s,i}$ from the ith ($i = 1, 2, \cdots, N_s$) varied cut, respectively, and we mark

$$Y^2_{\text{diff},s,i} = \left(Y_{s,i} - Y_{\text{def}}\right)^2, \tag{3.59}$$

$$\sigma^2_{\text{stat,diff},s,i} = \left|\sigma^2_{\text{stat},s,i} - \sigma^2_{\text{stat,def}}\right|. \tag{3.60}$$

If

$$Y^2_{\text{diff},s,i} > \sigma^2_{\text{stat,diff},s,i}, \tag{3.61}$$

this varied cut passes the Barlow check, and its systematic contribution

$$\sigma_{\text{sys},s,i} = \sqrt{Y^2_{\text{diff},s,i} - \sigma^2_{\text{stat,diff},s,i}}. \tag{3.62}$$

If a varied cut fail to pass the Barlow check, its systematic contribution is 0.

The systematic contribution of the sth source is given by

$$\sigma_{\text{sys},s} = \begin{cases} \sqrt{\frac{1}{n_s}\sum_{i=1}^{N_s} \sigma^2_{\text{sys},s,i}} & \text{if } n_s > 0, \\ 0 & \text{if } n_s = 0, \end{cases} \tag{3.63}$$

where n_s is the number of cuts passing the Barlow check in the sth source.

The total systematic uncertainty of the observable is obtained as the quadratic sum of the contribution from all sources by

$$\sigma_{\text{sys}} = \sqrt{\sum_{s=1}^{S} \sigma^2_{\text{sys},s}}. \tag{3.64}$$

Table 3.11 Systematics of net-proton number C_4/C_2 from RefMult3X centrality classes in Au+Au collisions at $\sqrt{s_{\mathrm{NN}}} = 7.7$ GeV.

Net-Proton C_4/C_2			0–5%	5–10%	10–20%	20–30%	30–40%	40–50%	50–60%	60–70%	70–80%
Central Value			0.4119	0.5283	0.7190	0.5916	0.7015	0.7621	0.7903	0.8160	0.7912
Statistical Error			0.2469	0.2085	0.1039	0.0656	0.0438	0.0284	0.0190	0.0140	0.0091
Systematic Error			0.1302	0.1102	0.0296	0.0246	0.0268	0.0154	0.0090	0.0066	0.0066
1	nHitsFit	a) 15	−0.0014	0.0045	−0.0083	−0.0022	0.0024	0.0005	0.0009	0.0003	0.0003
		b) 18	0.0045	−0.0014	−0.0037	−0.0042	0.0016	−0.0004	0.0009	0.0002	0.0005
		c) 22	0.0071	0.0138	0.0032	0.0055	−0.0000	0.0018	0.0008	0.0003	−0.0001
		d) 25	−0.0071	−0.0269	0.0171	−0.0015	−0.0003	0.0026	0.0017	0.0027	−0.0004
		Σ	0.0000	0.0061	0.0105	0.0028	0.0016	0.0000	0.0005	0.0012	0.0002
			0.0%	1.2%	1.5%	0.5%	0.2%	0.0%	0.1%	0.2%	0.0%
2	DCA	a) 0.8	−0.0207	0.0009	−0.0125	0.0067	0.0077	−0.0034	−0.0091	−0.0092	−0.0102
		b) 0.9	−0.0861	−0.0279	−0.0210	−0.0058	0.0004	−0.0015	−0.0062	−0.0042	−0.0042
		c) 1.1	0.0203	−0.0406	−0.0041	−0.0106	0.0045	0.0073	−0.0007	−0.0001	0.0029
		d) 1.2	−0.0066	−0.0066	−0.0438	−0.0096	0.0170	0.0125	−0.0003	0.0037	0.0050
		Σ	0.0607	0.0285	0.0246	0.0067	0.0115	0.0096	0.0074	0.0058	0.0061
			14.7%	5.4%	3.4%	1.1%	1.6%	1.3%	0.9%	0.7%	0.8%
3	$n\sigma_{\mathrm{proton}}$	a) 1.6	0.1702	0.0244	0.0025	0.0224	−0.0466	−0.0105	−0.0091	0.0001	−0.0005
		b) 1.8	−0.0329	0.0428	−0.0268	0.0294	−0.0238	−0.0138	−0.0042	−0.0041	0.0007
		c) 2.2	−0.0416	−0.0837	0.0140	−0.0141	−0.0114	−0.0022	−0.0005	0.0002	−0.0012
		d) 2.5	−0.0294	−0.1476	0.0089	−0.0094	−0.0115	−0.0027	0.0028	0.0035	0.0016
		Σ	0.1129	0.1037	0.0119	0.0224	0.0238	0.0119	0.0047	0.0028	0.0000
			27.4%	19.6%	1.7%	3.8%	3.4%	1.6%	0.6%	0.3%	0.0%
4	m^2	a) (0.50,1.10)	−0.0076	0.0293	0.0085	0.0100	0.0034	0.0020	−0.0023	−0.0009	−0.0014
		b) (0.55,1.15)	−0.0035	−0.0038	0.0032	0.0047	−0.0016	−0.0017	0.0020	0.0006	−0.0007
		c) (0.65,1.25)	−0.0187	0.0146	0.0064	−0.0105	−0.0061	−0.0013	−0.0014	0.0001	0.0006
		d) (0.70,1.30)	−0.0298	0.0256	0.0049	−0.0077	0.0004	−0.0031	−0.0022	0.0005	0.0012
		Σ	0.0226	0.0231	0.0045	0.0073	0.0037	0.0019	0.0019	0.0007	0.0009
			5.5%	4.4%	0.6%	1.2%	0.5%	0.3%	0.2%	0.1%	0.1%
5	Efficiency	a) ×0.975	−0.0086	−0.0086	0.0023	−0.0100	−0.0047	−0.0038	−0.0029	−0.0016	−0.0036
		b) ×1.025	0.0086	0.0083	−0.0016	0.0095	0.0046	0.0037	0.0029	0.0017	0.0035
		Σ	0.0000	0.0000	0.0000	0.0000	0.0000	0.0000	0.0000	0.0000	0.0023
			0.0%	0.0%	0.0%	0.0%	0.0%	0.0%	0.0%	0.0%	0.3%

Table 3.12 Systematics of net-proton number C_4/C_2 from RefMult3X centrality classes in Au+Au collisions at $\sqrt{s_{\mathrm{NN}}} = 11.5$ GeV.

Net-Proton C_4/C_2			0–5%	5–10%	10–20%	20–30%	30–40%	40–50%	50–60%	60–70%	70–80%
Central Value			0.4012	0.6026	0.5895	0.4831	0.6243	0.6255	0.6592	0.6941	0.7125
Statistical Error			0.1347	0.1063	0.0552	0.0362	0.0229	0.0153	0.0098	0.0067	0.0044
Systematic Error			0.0647	0.0848	0.0362	0.0120	0.0162	0.0066	0.0084	0.0055	0.0066
1	nHitsFit	a) 15	−0.0006	−0.0031	−0.0035	−0.0021	0.0005	0.0007	0.0002	−0.0002	−0.0001
		b) 18	−0.0002	−0.0032	−0.0040	−0.0017	−0.0004	0.0008	0.0001	−0.0000	−0.0001
		c) 22	0.0131	0.0127	0.0023	−0.0010	−0.0002	0.0002	0.0002	0.0003	0.0002
		d) 25	0.0358	0.0323	0.0004	0.0021	0.0015	0.0022	−0.0009	0.0006	0.0002
		Σ	0.0224	0.0212	0.0029	0.0006	0.0000	0.0013	0.0001	0.0002	0.0001
			5.6%	3.5%	0.5%	0.1%	0.0%	0.2%	0.0%	0.0%	0.0%
2	DCA	a) 0.8	−0.0036	−0.0790	−0.0465	0.0128	0.0042	−0.0023	0.0023	0.0009	−0.0044
		b) 0.9	−0.0558	−0.0562	−0.0115	0.0023	−0.0006	−0.0007	0.0059	−0.0007	−0.0021
		c) 1.1	0.0395	0.0295	−0.0269	−0.0015	−0.0051	−0.0015	−0.0008	0.0011	−0.0010
		d) 1.2	−0.0071	0.0172	−0.0376	0.0118	−0.0185	−0.0029	−0.0006	0.0011	0.0005
		Σ	0.0477	0.0504	0.0331	0.0118	0.0097	0.0019	0.0044	0.0010	0.0028
			11.9%	8.4%	5.6%	2.4%	1.5%	0.3%	0.7%	0.1%	0.4%
3	$n\sigma_{\mathrm{proton}}$	a) 1.6	0.0078	0.1069	0.0117	−0.0019	−0.0210	0.0091	−0.0053	−0.0019	0.0018
		b) 1.8	0.0251	0.0476	0.0246	−0.0101	−0.0133	−0.0011	−0.0062	−0.0010	−0.0000
		c) 2.2	−0.0525	−0.0151	−0.0095	0.0086	−0.0130	0.0070	0.0039	−0.0014	0.0006
		d) 2.5	−0.0487	−0.0342	−0.0246	0.0032	−0.0037	0.0021	−0.0029	−0.0008	0.0011
		Σ	0.0364	0.0631	0.0144	0.0000	0.0129	0.0048	0.0046	0.0000	0.0001
			9.1%	10.5%	2.4%	0.0%	2.1%	0.8%	0.7%	0.0%	0.0%
4	m^2	a) (0.50,1.10)	−0.0129	−0.0019	−0.0006	−0.0018	0.0027	−0.0015	−0.0010	−0.0006	0.0004
		b) (0.55,1.15)	0.0090	0.0022	−0.0015	−0.0012	0.0013	−0.0010	0.0002	−0.0004	−0.0001
		c) (0.65,1.25)	−0.0100	0.0150	0.0015	0.0030	−0.0005	0.0009	−0.0008	0.0002	0.0002
		d) (0.70,1.30)	0.0020	0.0008	0.0019	0.0037	−0.0001	−0.0006	−0.0004	0.0008	0.0001
		Σ	0.0091	0.0149	0.0013	0.0018	0.0020	0.0003	0.0007	0.0000	0.0004
			2.3%	2.5%	0.2%	0.4%	0.3%	0.1%	0.1%	0.0%	0.1%
5	Efficiency	a) ×0.975	−0.0120	0.0025	−0.0024	−0.0127	−0.0057	−0.0067	−0.0064	−0.0059	−0.0062
		b) ×1.025	0.0115	−0.0015	0.0028	0.0120	0.0056	0.0066	0.0062	0.0057	0.0059
		Σ	0.0000	0.0000	0.0000	0.0000	0.0000	0.0039	0.0054	0.0054	0.0059
			0.0%	0.0%	0.0%	0.0%	0.0%	0.6%	0.8%	0.8%	0.8%

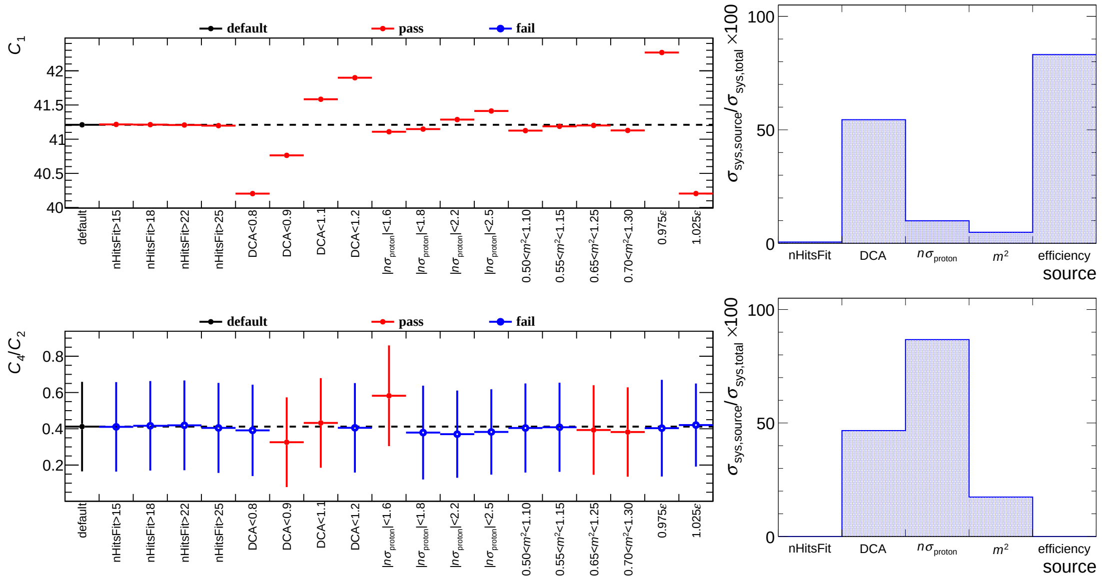

Figure 3.31 (Color online) Measured values using various cuts (left) and contribution fractions of the systematic errors from various sources (right) for C_1 (top) and C_4/C_2 (bottom) in the 0–5% centrality class defined by RefMult3X from the $\sqrt{s_{\mathrm{NN}}}$ = 7.7 GeV data set.

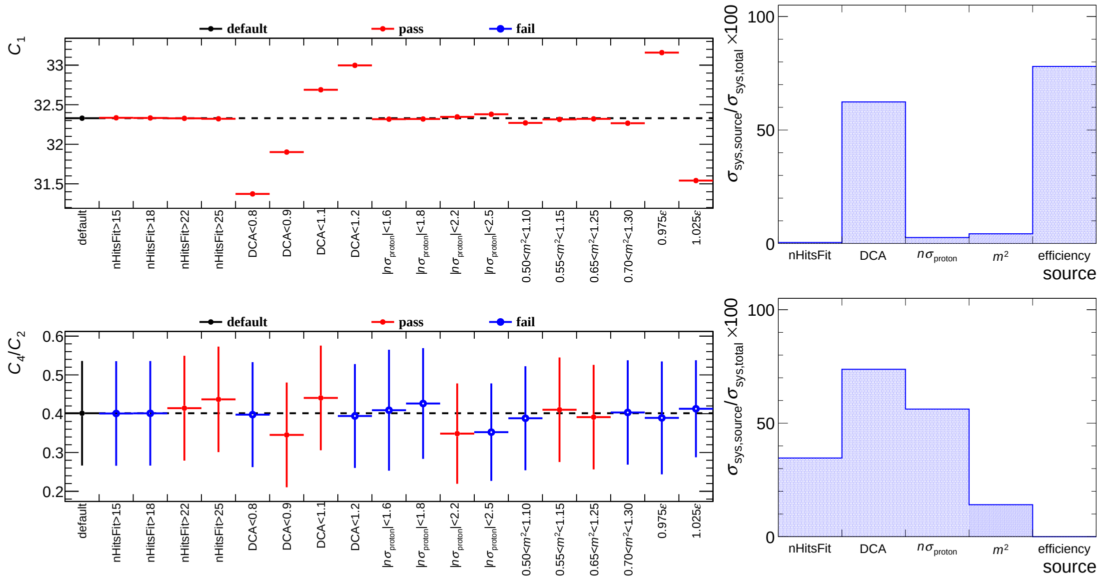

Figure 3.32 (Color online) Measured values using various cuts (left) and contribution fractions of the systematic errors from various sources (right) for C_1 (top) and C_4/C_2 (bottom) in the 0–5% centrality class defined by RefMult3X from the $\sqrt{s_{\mathrm{NN}}}$ = 11.5 GeV data set.

Details of systematics of net-proton number C_4/C_2 in RefMult3X centrality classes from the $\sqrt{s_{\mathrm{NN}}} = 7.7$ GeV and 11.5 GeV data sets are summarized in Tables 3.11 and 3.12, respectively. The first few rows show central values, statistical errors and systematic errors in various centrality classes. For each systematic source, the variation of the central value is shown corresponding to each varied cut, and a red number represents failure of the Barlow check. The "Σ" row and the next row summarize the absolute and relative systematic errors from this cut, respectively.

More clearly, the systematic contributions in the 0–5% centrality class defined by RefMult3X from the $\sqrt{s_{\mathrm{NN}}}$ = 7.7 GeV and 11.5 GeV data sets shown in Figures 3.31 and 3.32, respectively. Left panels present the measured values as functions of cuts, and right panels summarize the fraction of the systematic contribution from various sources, with top (bottom) panels for C_1 (C_4/C_2). Note that the quadratic sum of the bars in each right panel is 100%. For C_1, systematic contributions from the DCA and the efficiency strongly dominate in both data sets. The DCA systematics reflect the effect of the background, such as secondary particles, and the contribution from the efficiency is 2.5%, exactly equal to its variation. For C_4/C_2, the leading sources are the DCA and the $n\sigma_{\mathrm{proton}}$ cut. The variation of the efficiency value can not pass the Barlow check, indicating that C_4/C_2 is not sensitive to the efficiency.

3.10 Centrality Resolution Study

This section focuses on the effect of centrality resolution on the experimentally measured fluctuations. Figure 3.33 shows cumulants and cumulant ratios in Au+Au collisions at $\sqrt{s_{\mathrm{NN}}}$ = 11.5 GeV. BES-II results in centrality classes from RefMult3 and RefMult3X are compared to BES-I using RefMult3. A systematic trend is observed that for C_2, C_3, C_4, C_2/C_1, C_3/C_2 and C_4/C_2, results from BES-I RefMult3 > BES-II RefMult3 > BES-II RefMult3X, which is opposite to the ordering of multiplicity values from the distributions in the bottom left panel. The larger multiplicity is believed to have the better centrality resolution, so the better resolution would induce lower cumulants and cumulant ratios. For C_4/C_2 in central events, all points from various centrality definitions are consistent with each other within uncertainties, suggesting a weak dependence on the resolution.

A new multiplicity called RefMult3E is included, defined the same as RefMult3 but with an efficiency = 0.83. In other words, RefMult3E randomly samples tracks counted by RefMult3 with a probability of 0.83. The tail position and shape of the RefMult3E distribution overlap BES-I RefMult3 to mimic the centrality resolution. We can see that cumulants and ratios from RefMult3E are higher compared to those from BES-II RefMult3, and get closer to those from BES-I RefMult3 in most of the cases. By tuning the centrality resolution to be similar to BES-I, the BES-II result reproduces BES-I with good consistency, especially for C_2/C_1 and C_4/C_2, as well as C_3/C_2 in central to semi-central events. The difference between BES-I and BES-II is likely to result from the effect of centrality resolution.

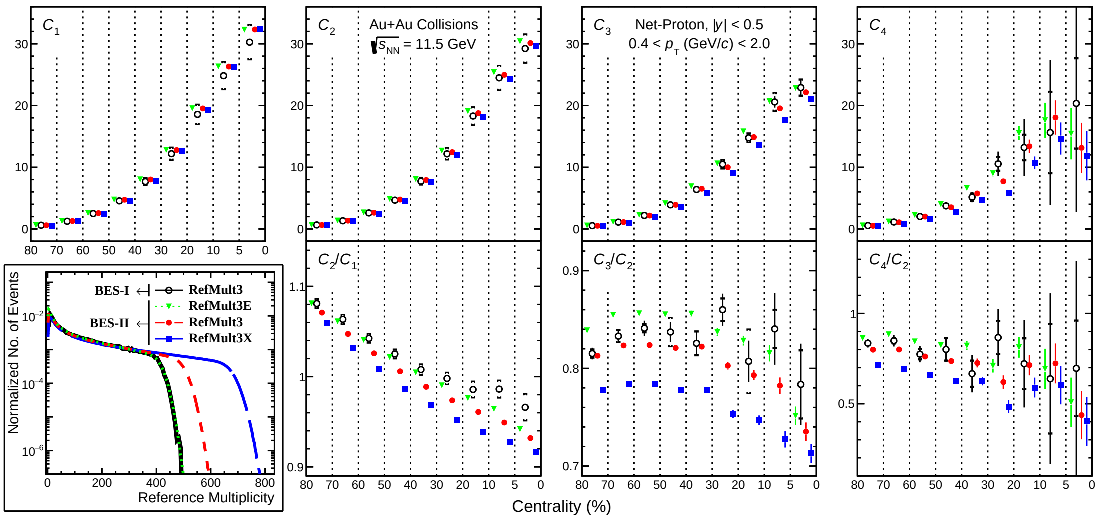

Figure 3.33 (Color online) Distributions of reference multiplicities (bottom left) and collision centrality dependence of net-proton number cumulants and their ratios up to the fourth order in Au+Au collisions at $\sqrt{s_{\mathrm{NN}}}$ = 11.5 GeV. Various multiplicities are shown: BES-I and BES-II RefMult3 ($|\eta| < 1.0$), BES-II RefMult3X ($|\eta| < 1.6$) and BES-II RefMult3E, which comes from BES-II RefMult3 with efficiency = 0.83 to have similar distribution to BES-I RefMult3. BES-II results carry statistical uncertainties only.

3.11 UrQMD Analysis

We perform the UrQMD [87-89] analysis for the study on the model side, including the baseline expectation and some effects. UrQMD events are simulated for Au+Au collisions at each collision energy, and the comparison to the experimental result will be discussed in Section 4.5. Here presents the UrQMD analysis based on a part of the produced statistics for $\sqrt{s_{\mathrm{NN}}}$ = 7.7 GeV to study the centrality resolution, because the multiplicity at the lowest $\sqrt{s_{\mathrm{NN}}}$ should be the smallest and contribute the most significantly to the effect of centrality resolution.

The input b randomly distributes in 0–16 fm, and the final state of the simulation is at $t = 50$ fm/c. Since there is no N_{part} provided by the original UrQMD code, we calculate it on an event-by-event basis as the difference between the total number of the nucleons in the two colliding nuclei at the initial state and the number of the nucleons which have never participated in an inelastic collision at the final state. Events with zero N_{part} are removed from the analysis, and there are about 68 million events analyzed.

We define the multiplicities using charged pions and kaons within different η windows and with different efficiency values to tune the centrality resolution:

1. RefMult3E: $\pi^{\pm}$ and $\mathrm{K}^{\pm}$ within $|\eta| < 1.0$ with efficiency = 0.83,
2. RefMult3: $\pi^{\pm}$ and $\mathrm{K}^{\pm}$ within $|\eta| < 1.0$,
3. RefMult3XE: $\pi^{\pm}$ and $\mathrm{K}^{\pm}$ within $|\eta| < 1.6$ with efficiency = 0.83,
4. RefMult3X: $\pi^{\pm}$ and $\mathrm{K}^{\pm}$ within $|\eta| < 1.6$,

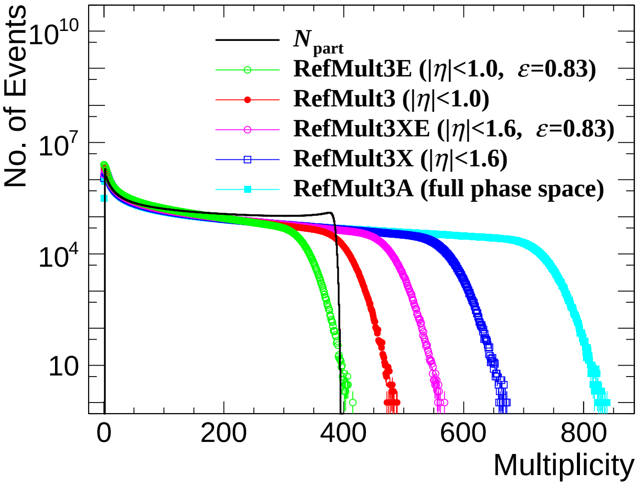

Figure 3.34 (Color online) Multiplicity distributions including RefMult3E, RefMult3, RefMult3XE, RefMult3X and RefMult3A in the UrQMD Au+Au collisions at $\sqrt{s_{\rm NN}}$ = 7.7 GeV.

5. RefMult3A: $\pi^{\pm}$ and $K^{\pm}$ with no η cut (full phase space).

The efficiency value 83% is determined by making the RefMult3X tail positions in UrQMD and experimental data comparable to each other. The multiplicity distributions including $N_{\rm part}$ are presented in Figure 3.34. The clear ordering from smallest to largest is: RefMult3E < RefMult3 < RefMult3XE < RefMult3X < RefMult3A. Centrality classes from 0–5%, 5–10%, 10-20% to 70–80% are individually defined these multiplicities.

The correlations between $N_{\rm part}$ and RefMult3/3X are studied. Figure 3.35 shows the $N_{\rm part}$ distributions drawn by the black curve, red curves and blue curves representing the entire $N_{\rm part}$ distribution, the $N_{\rm part}$ distributions in centrality classes defined by RefMult3 and the $N_{\rm part}$ distributions in centrality classes defined by RefMult3X, respectively. Obviously, $N_{\rm part}$ and RefMult3/3X select different groups of events in each centrality class.

The details of the centrality definitions are studied using $N_{\rm part}$, RefMult3 and RefMult3X, summarized in Table 3.13. In each cell, the top number is $\sigma\left(N_{\rm part}\right)$ as the standard deviation of $N_{\rm part}$ over the events within the centrality class defined by the multiplicity. The bottom number denotes the fraction of common events within the centrality class defined by the multiplicity compared to the same centrality class defined by $N_{\rm part}$ which is calculated by $\dfrac{N_{\rm events}\left(\text{mult. cent.} = N_{\rm part}\ \text{cent.} = i\right)}{N_{\rm events}\left(N_{\rm part}\ \text{cent.} = i\right)}$ for the ith centrality. For $\sigma\left(N_{\rm part}\right)$, the $N_{\rm part}$ centrality always holds the minimum number, because it takes sharp $N_{\rm part}$ cuts to determine the centrality. The comparison also shows larger values of $\sigma\left(N_{\rm part}\right)$ from the RefMult3 centralities than that from the RefMult3X centralities, because the red curves are wider than the blue curves in Figure 3.35, suggesting larger

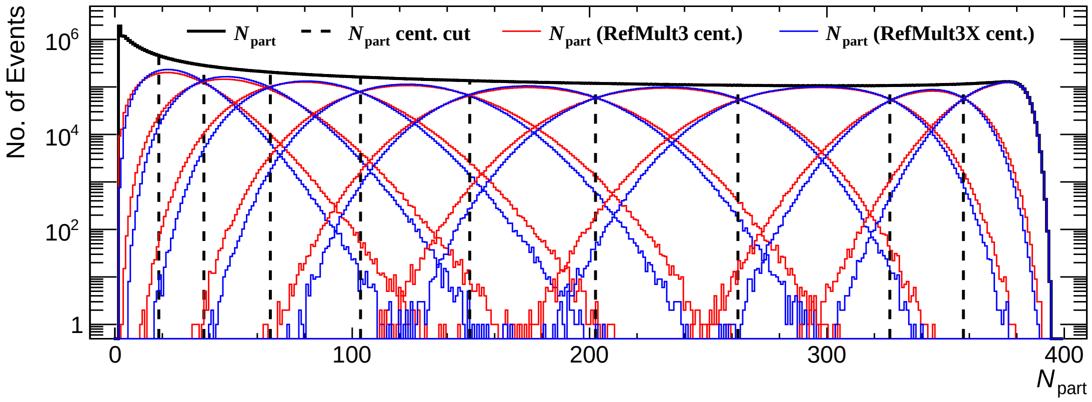

Figure 3.35 (Color online) Distributions of $N_{\rm part}$ in the UrQMD Au+Au collisions at $\sqrt{s_{\rm NN}}$ = 7.7 GeV. Black curve represents the entire distribution, and the red and blue curves denote the $N_{\rm part}$ distributions from various centrality classes defined by RefMult3 and RefMult3X respectively. Black dashed lines show the centrality boundaries of $N_{\rm part}$.

Table 3.13 Standard deviations of $N_{\rm part}$ and fractions of common events with $N_{\rm part}$ for various centrality classes defined by $N_{\rm part}$, RefMult3 and RefMult3X. In each cell, the top (bottom) number represents $\sigma\left(N_{\rm part}\right)$ (the fraction of common events within the same centrality class defined by $N_{\rm part}$).

Multiplicity	$N_{\rm part}$	RefMult3	RefMult3X
0–5%	8.1 100%	11.5 84.8%	10.8 86.2%
5–10%	9.0 100%	16.4 65.0%	15.1 68.5%
10–20%	18.5 100%	25.9 77.2%	24.5 79.2%
20–30%	17.3 100%	27.2 71.6%	25.7 74.8%
30–40%	15.3 100%	26.5 67.0%	25.0 71.5%
40–50%	13.3 100%	24.8 64.2%	22.8 66.9%
50–60%	11.0 100%	21.9 62.0%	20.0 64.2%
60–70%	8.1 100%	17.8 54.1%	16.4 60.7%
70–80%	5.5 100%	13.8 49.8%	12.4 56.4%

volume fluctuations from RefMult3. For the fraction of common events, the numbers from the $N_{\rm part}$ centralities are naturally 100%, and the RefMult3 centralities have lower common fractions than RefMult3X, which can also be observed by comparing the overlap areas between red and blue curves in Figure 3.35. This means that the RefMult3X centrality definition is “closer” to $N_{\rm part}$. If RefMult3E, RefMult3XE and RefMult3A are also taken into consideration, the same trend can be observed, which indicates that the larger multiplicity provides the better centrality resolution: RefMult3E < RefMult3 < RefMult3XE < RefMult3X < RefMult3A.

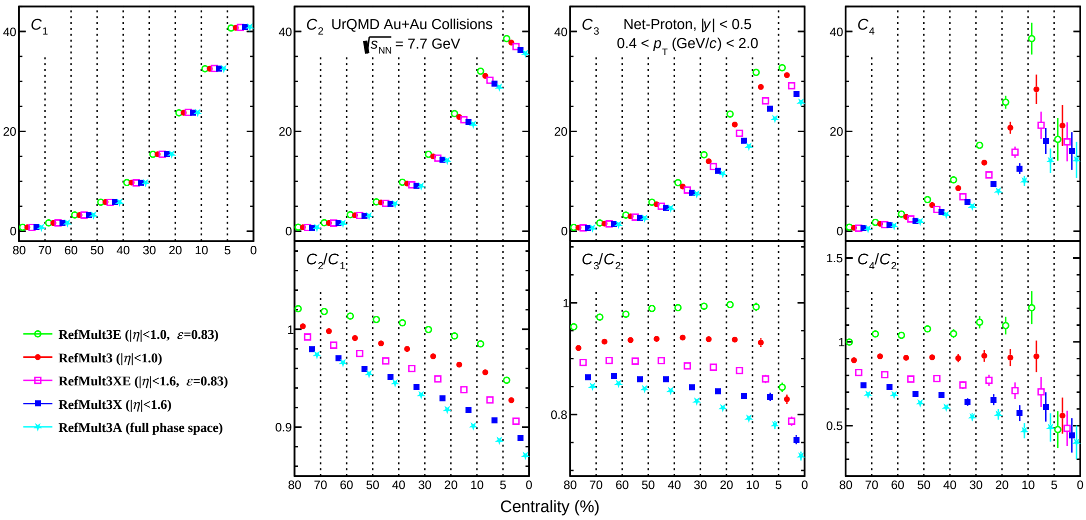

Figure 3.36 (Color online) Collision centrality dependence of net-proton number cumulants and their ratios up to the fourth order in UrQMD Au+Au collisions at $\sqrt{s_{\mathrm{NN}}}$ = 7.7 GeV.

Protons and antiprotons are extracted within the same acceptance as the default case in the experimental analysis: [0.4 GeV/c < p_{T} < 2.0 GeV/c, $|y|$ < 0.5]. Net-proton number cumulants and ratios up to the fourth order with CBWC performed are shown in Figure 3.36. In each centrality class, five points are drawn representing the results from difference centrality definitions. For cumulants from the second order to the fourth order, it can be directly found that the better centrality resolution from the larger multiplicity leads to the lower cumulants and ratios, which denotes a clear centrality resolution ordering. This phenomenon could be explained by two sub-effects. The first one is the event selection in a centrality class. Within each centrality class, different centrality definitions select different groups of events. The larger multiplicity provides the smaller volume fluctuation of the events as discussed, which suppresses the volume fluctuation effect on the measured fluctuations. The second one is the binning process for CBWC. The larger multiplicity has more integer bins to divide the events with better accuracy of the collision centrality, so the volume fluctuation in the multiplicity bin is smaller, which contributes less to the CBWC-ed cumulants. That is to say, the centrality resolution ordering of the cumulants comes from the volume fluctuation induced by the centrality definition by the multiplicity.

Comparing all the centrality definitions, the best resolution is taken from RefMult3A, which does not require a phase space cut, so the lowest cumulants and ratios come from RefMult3A centrality classes. However, results from RefMult3X are very close to those from RefMult3A, indicating a saturation of the centrality resolution effect. Furthermore, if we focus on the C_4/C_2 in the 0–5% centrality class, those points from different centrality definitions are consistent with each other within uncertainties. In other words, C_4/C_2 in the 0–5% centrality is not sensitive to the centrality resolution, and these is also a hint for other orders. The reason could be that N_{part} in top central events is constrained by its maximum value as the total nucleon number of the initial colliding nuclei.

This UrQMD study provides an important reference for the experimental data analysis, including the expected phenomenon and the potential reason of the centrality resolution effect. Two points to be emphasized are the saturation of the effect from RefMul3X and the insensitivity of C_4/C_2 in central events to the resolution, which supports our fluctuation measurement especially for C_4/C_2 in the 0–5% centrality class determined by RefMult3X.

Chapter 4 Results

4.1 Event-by-Event Distributions

This section discusses the event-by-event net-proton, proton and antiproton number distributions shown in Figure 4.1. Protons and antiprotons are selected within the default phase space [0.4 GeV/c < p_{T} < 2.0 GeV/c, $|y|$ < 0.5]. All the distributions are not corrected for the finite efficiency.

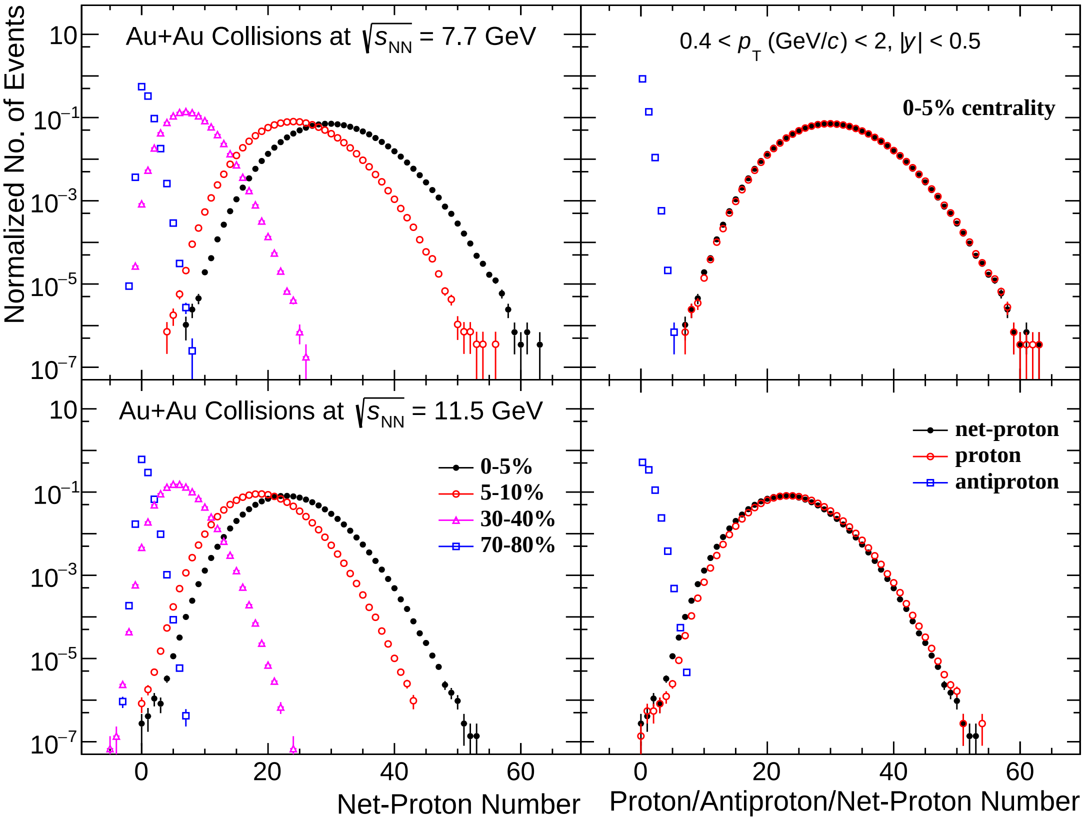

Figure 4.1 (Color online) Efficiency-uncorrected distributions of event-by-event proton, antiproton and net-proton numbers in Au+Au collision at $\sqrt{s_{\mathrm{NN}}}$ = 7.7 GeV (top) and 11.5 GeV (bottom). Left panels show the net-proton number distributions in the 0–5%, 5–10%, 30–40% and 70–80% centrality classes, while right panels show the proton, antiproton and net-proton number distributions from top 5% central events.

Top and bottom panels show the distributions taken in Au+Au collisions at $\sqrt{s_{\mathrm{NN}}}$ = 7.7 GeV and 11.5 GeV, respectively. Left panels draw the net-proton number distributions from central to peripheral centrality classes. The more central events produce the larger net-proton numbers with wider distributions. Right panels compare the proton, antiproton and net-proton number distributions in the 0–5% centrality class. Because of the relatively low collision energy, antiprotons are much less than protons and provide smaller contributions to the net-proton numbers. If we observe the collision energy dependence of the net-proton number distribution in central events, it is easy to find that the mean from $\sqrt{s_{\mathrm{NN}}}$ = 7.7 GeV is larger than that from $\sqrt{s_{\mathrm{NN}}}$ = 11.5 GeV, which results from the stronger effect of baryon stopping phenomenon at the lower energy. More initial nucleons stay at the central collision zone and increase the net-baryon number.

4.2 Collision Centrality Dependence

This section discusses the collision centrality dependence of cumulants of net-proton, proton and antiproton numbers and factorial cumulants of proton and antiproton numbers up to the sixth order and their ratios. With the efficiency correction and CBWC performed, all the results in this section are obtained within the default phase space [$0.4\ \mathrm{GeV}/c < p_{\mathrm{T}} < 2.0\ \mathrm{GeV}/c$, $|y| < 0.5$] from nine default centrality classes of 0–5%, 5–10%, 10–20%, 20–30%, 30–40%, 40–50%, 50–60%, 60–70% and 70–80% in Au+Au collisions. Plots in this section include top panels for $\sqrt{s_{\mathrm{NN}}}$ = 7.7 GeV and bottom panels for $\sqrt{s_{\mathrm{NN}}}$ = 11.5 GeV. Data points are shown as functions of $\langle N_{\mathrm{part}} \rangle$. For the descriptions of markers, stars, circles and squares denote results from BES-I using the RefMult3 centrality, BES-II using the RefMult3 centrality and BES-II using the RefMult3X centrality, respectively. Statistical errors are drawn as vertical bars, and systematic errors are expressed by brackets for BES-I and vertical shaded bands for BES-II. For the cumulants and factorial cumulants and their ratios from BES-I for comparison, those up to the fourth order in the nine centrality classes are taken from References [83,98], and the hyper-order results in the 0–40% and 50–60% centrality classes are taken from Reference [102].

Figure 4.2 presents the centrality dependence of net-proton number cumulants up to the fourth order. Cumulants show a increasing trend from peripheral to central events because the more central collisions produce the more net-particles. BES-I and BES-II results agree well with each other within uncertainties, supporting this measurement. Because of the PID cut efficiency included in the BES-II efficiency correction, C_1 is systematically higher than BES-I. For higher-order cumulants beyond the first order, a qualitative trend is observed: RefMult3X (BES-II) < RefMult3 (BES-II) < RefMult3 (BES-I), implying the centrality resolution effect as discussed.

Figure 4.3 presents the centrality dependence of ratios of net-proton number cumulants up to the fourth order, including C_2/C_1, C_3/C_2 and C_4/C_2. All the cumulant ratios show a decreasing trend from peripheral to central events. A strong effect of

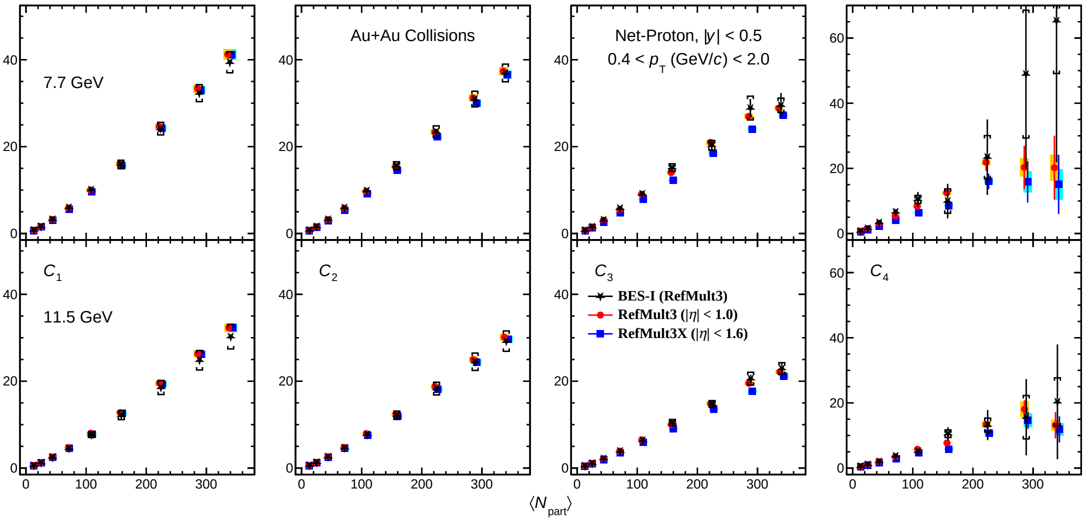

Figure 4.2 (Color online) Collision centrality dependence of net-proton number cumulants up to the fourth order (C_1, C_2, C_3 and C_4) in Au+Au collisions at $\sqrt{s_{NN}}$ = 7.7 GeV (top) and 11.5 GeV (bottom).

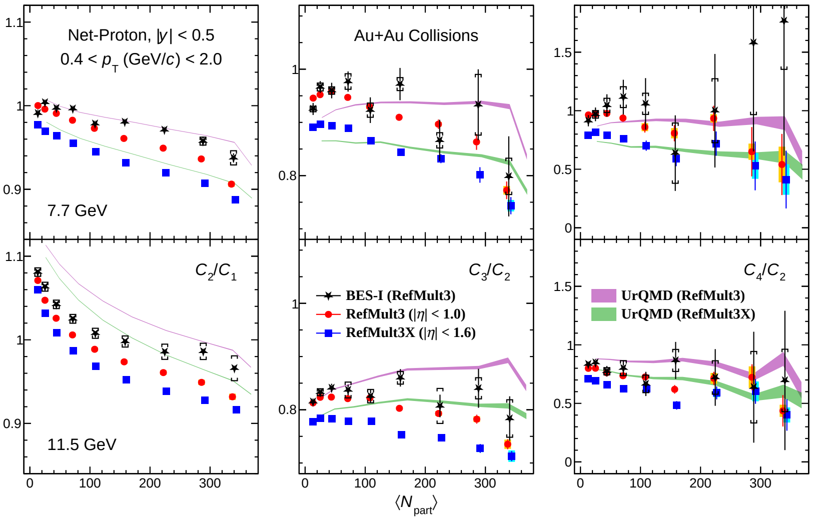

Figure 4.3 (Color online) Collision centrality dependence of net-proton number cumulant ratios up to the fourth order (C_2/C_1, C_3/C_2 and C_4/C_2) in Au+Au collisions at $\sqrt{s_{NN}}$ = 7.7 GeV (top) and 11.5 GeV (bottom).

the centrality resolution can be seen, contributing significantly to C_2/C_1 and C_3/C_2. For C_4/C_2 in top central events, the three points are consistent within uncertainties, which suggests a weak effect of the centrality resolution. Results from both centrality definitions and both collision energies in the UrQMD simulations are also drawn for comparison and show similar centrality dependence trends and similar centrality resolution effect to the experimental data Note that the $\langle N_{\text{part}} \rangle$ values in UrQMD are calculated the same as Section 3.11, while those drawn for the experimental results are obtained from Glauber. The model dependence leads to different abscissae of UrQMD and data in each centrality class.

To compare the BES-I and BES-II results, we quantify the deviations of net-proton

Table 4.1 Deviations of net-proton number C_4/C_2 between BES-I and BES-II results. RefMult3 is used for the centrality determination.

$\sqrt{s_{NN}}$ (GeV)	0–5%	70–80%
7.7	1.0σ	0.9σ
11.5	0.4σ	1.3σ

Table 4.2 Reduction factors of uncertainties of net-proton number C_4/C_2 in 0–5% central events in BES-II compared to BES-I.

$\sqrt{s_{NN}}$ (GeV)	Stat.	Sys.
7.7	4.7	3.2
11.5	4.4	5.1

number C_4/C_2 in central and peripheral events using RefMult3 as the centrality determination in Table 4.1. Consistency within $\sim 1\sigma$ is observed. Furthermore, uncertainties are strongly suppressed in BES-II comapared to BES-I, and the reduction factors of statistical and systematic errors of net-proton number C_4/C_2 in 0–5% central events are summarized in Table 4.2. Taking advantage of several upgrades in BES-II, we have much better precision in both statistical and systematic cases.

Figure 4.4 presents the centrality dependence of hyper-order net-proton number cumulants, C_5 and C_6, as well as their ratios C_5/C_1 and C_6/C_2. Black stars represent the BES-I hyper-order cumulant ratios in the 50–60% and 0–40% centrality classes. For peripheral events, BES-I and BES-II results are consistent. However, in the 0–40% centrality class, C_5/C_1 and C_6/C_2 from $\sqrt{s_{NN}}$ = 7.7 GeV and C_6/C_2 from $\sqrt{s_{NN}}$ = 11.5 GeV measured in this analysis, which deviate from BES-I, are either positive or consistent with zero. Considering the large errors, no significant centrality resolution effect can be discussed. One solution to the error suppression in BES-II is

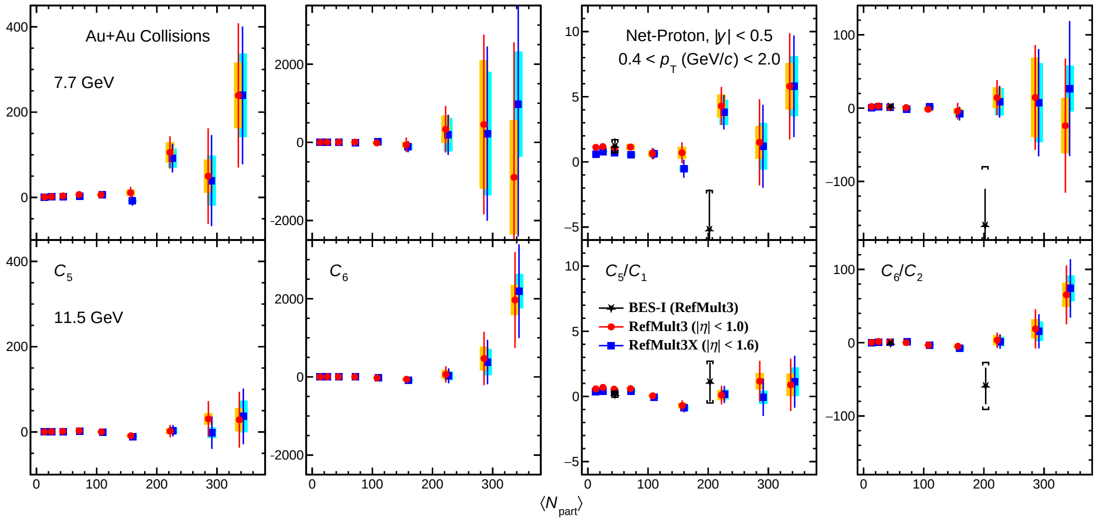

Figure 4.4 (Color online) Collision centrality dependence of hyper-order net-proton number cumulants and cumulant ratios (C_5, C_6, C_5/C_1 and C_6/C_2) in Au+Au collisions at $\sqrt{s_{NN}}$ = 7.7 GeV (top) and 11.5 GeV (bottom).

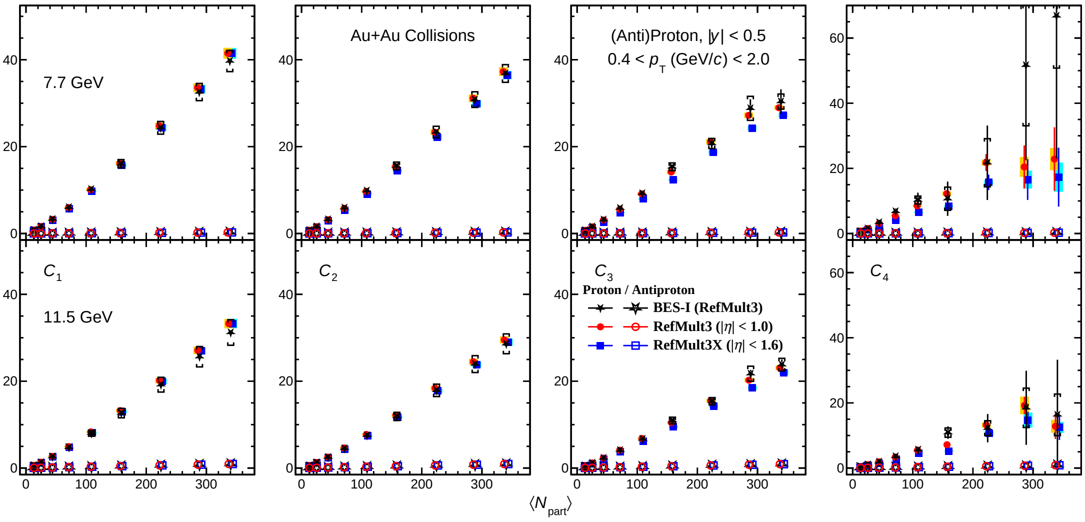

Figure 4.5 (Color online) Collision centrality dependence of proton and antiproton number cumulants up to the fourth order (C_1, C_2, C_3 and C_4) in Au+Au collisions at $\sqrt{s_{NN}}$ = 7.7 GeV (top) and 11.5 GeV (bottom).

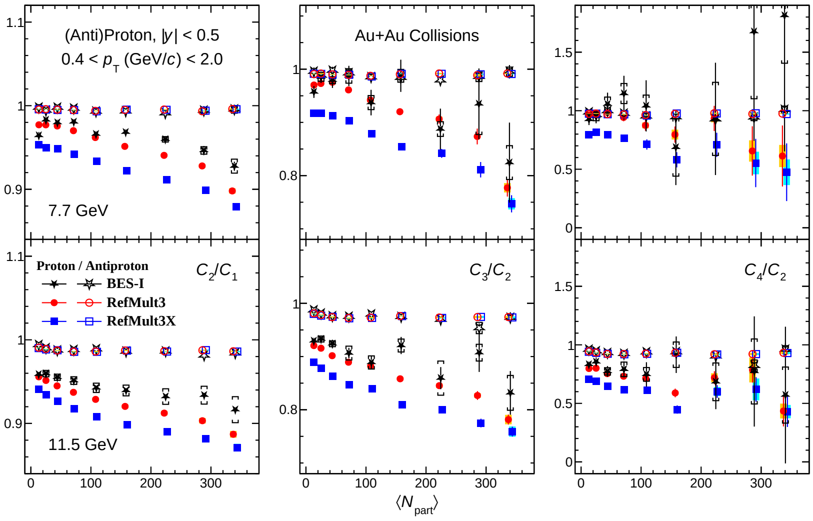

Figure 4.6 (Color online) Collision centrality dependence of proton and antiproton number cumulant ratios up to the fourth order (C_2/C_1, C_3/C_2 and C_4/C_2) in Au+Au collisions at $\sqrt{s_{NN}}$ = 7.7 GeV (top) and 11.5 GeV (bottom).

combining the current central and semi-central centrality classes into 0–40% for more statistics, which could be included in the future work.

Figure 4.5 presents the centrality dependence of proton and antiproton number cumulants up to the fourth order. Solid (open) markers represent proton (antiproton) results. Antiproton number cumulants are always around zero due to the low antiproton yields at low collision energies, and the proton contributions dominate the net-proton results. Good agreement can be found between BES-I and BES-II measurements.

Figure 4.6 presents the centrality dependence of proton and antiproton number cumulants ratios. Antiproton number cumulant ratios are close to unity because of the

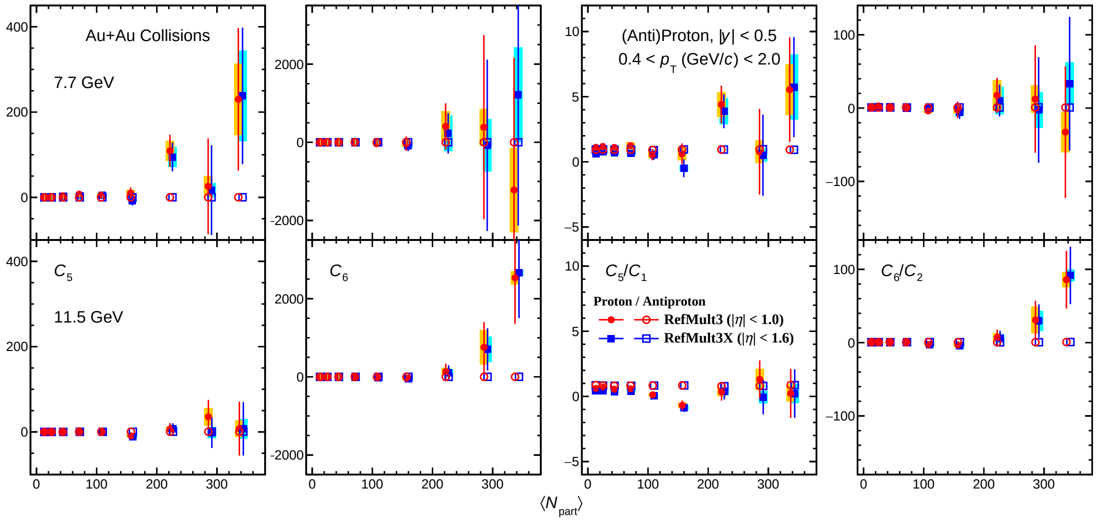

Figure 4.7 (Color online) Collision centrality dependence of hyper-order proton and antiproton number cumulants and cumulant ratios (C_5, C_6, C_5/C_1 and C_6/C_2) in Au+Au collisions at $\sqrt{s_{\mathrm{NN}}}$ = 7.7 GeV (top) and 11.5 GeV (bottom).

Poisson limit for small particle numbers. For $\sqrt{s_{\mathrm{NN}}}$ = 11.5 GeV, a hint of a decreasing trend in antiproton number cumulant ratios can be found as $\langle N_{\mathrm{part}} \rangle$ increases, which is qualitatively consistent with proton cumulant ratios. The phenomenons of proton cumulant ratios are quite similar to the net-proton results.

Figure 4.7 presents the centrality dependence of hyper-order proton and antiproton number cumulants and cumulant ratios. The antiproton number C_5 (C_5/C_1) and C_6 (C_6/C_2) are around zero (unity), behaving similarly to the lower orders. In central events, proton number C_5/C_1 is positive at $\sqrt{s_{\mathrm{NN}}}$ = 7.7 GeV but consistent with zero at $\sqrt{s_{\mathrm{NN}}}$ = 11.5 GeV; C_6/C_2 is consistent with zero at $\sqrt{s_{\mathrm{NN}}}$ = 7.7 GeV but positive at $\sqrt{s_{\mathrm{NN}}}$ = 11.5 GeV.

Figure 4.8 presents the centrality dependence of proton and antiproton number factorial cumulants up to the fourth order. Antiproton results at both collision energies are always around zero. The proton number κ_2 is progressively negative, indicating a negative two-particle correlation inside protons. The increasing proton number κ_3 suggests a positive three-proton correlation. The proton number κ_4 fluctuates around zero.

Figure 4.9 presents the centrality dependence of proton and antiproton number factorial cumulant ratios. The BES-II results from this analysis are found to agree well with BES-I and carry much smaller uncertainties. Antiproton number factorial cumulant ratios show quite small deviations from the Poisson baseline at zero, while there seems to be negative κ_2/κ_1. For proton results, it is clear to see increasingly negative κ_2/κ_1 induced by the stronger two-proton anti-correlation in the more central events due to

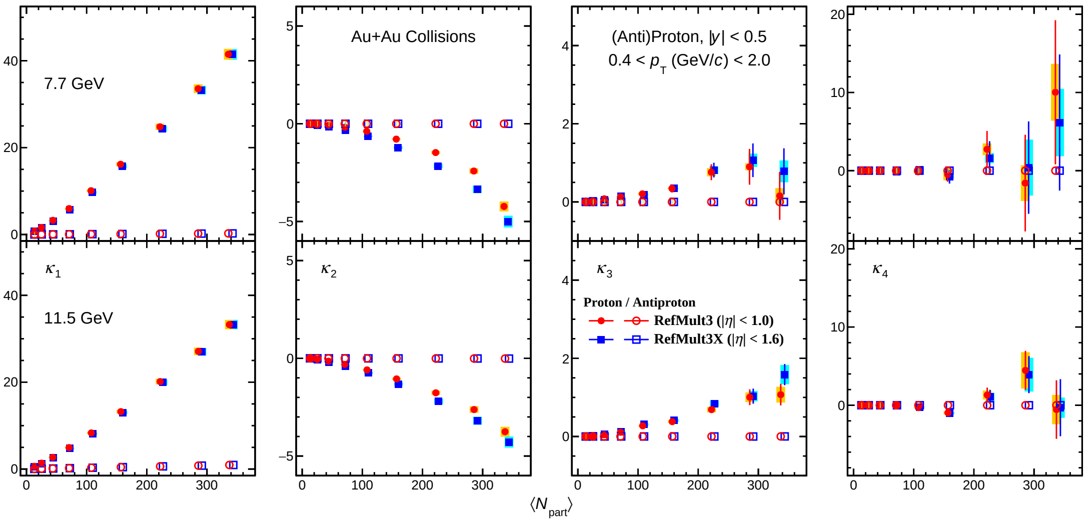

Figure 4.8 (Color online) Collision centrality dependence of proton and antiproton number factorial cumulants up to the fourth order (κ_1, κ_2, κ_3 and κ_4) in Au+Au collisions at $\sqrt{s_{\mathrm{NN}}}$ = 7.7 GeV (top) and 11.5 GeV (bottom).

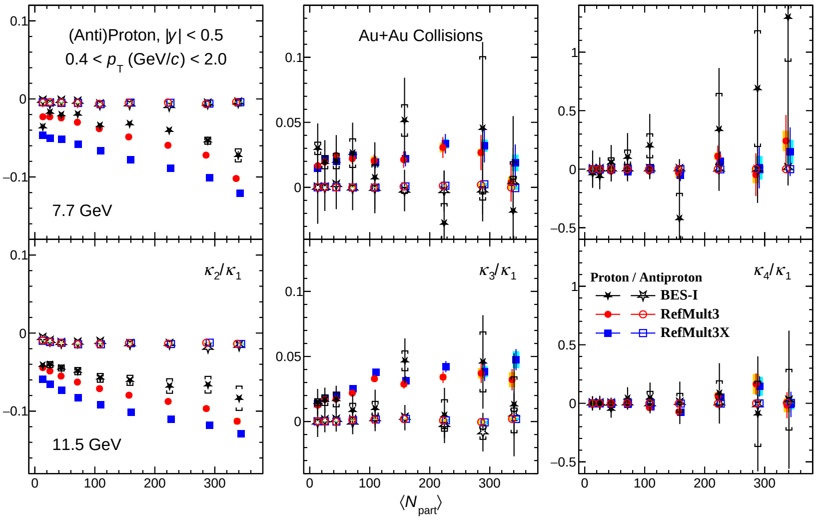

Figure 4.9 (Color online) Collision centrality dependence of proton and antiproton number factorial cumulant ratios up to the fourth order (κ_2/κ_1, κ_3/κ_1 and κ_4/κ_1) in Au+Au collisions at $\sqrt{s_{\mathrm{NN}}}$ = 7.7 GeV (top) and 11.5 GeV (bottom).

net-baryon number conservation; κ_3/κ_1 is likely to be increasingly positive; however, no significant centrality dependence can be observed in κ_4/κ_1 related to a four-proton correlation. We can extract centrality resolution effect on proton number factorial cumulant ratios, including κ_2/κ_1 and a hint for κ_3/κ_1: better resolution provides larger deviation from zero.

Figure 4.10 presents the centrality dependence of hyper-order proton and antiproton number factorial cumulants and factorial cumulant ratios. The proton number κ_5 and κ_6 in the 0–40% and 50–60% centrality classes from BES-I are shown for comparison. The BES-I negative κ_5 from $\sqrt{s_{\mathrm{NN}}}$ = 7.7 GeV and negative κ_6 from $\sqrt{s_{\mathrm{NN}}}$ = 11.5 GeV

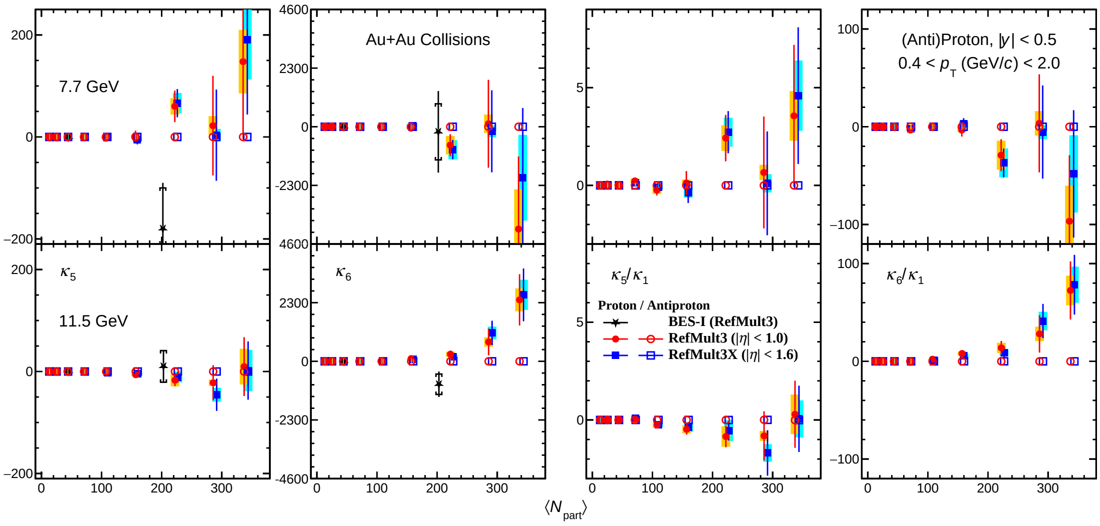

Figure 4.10 (Color online) Collision centrality dependence of hyper-order proton and antiproton number factorial cumulants and factorial cumulant ratios (κ_5, κ_6, κ_5/κ_1 and κ_6/κ_1) in Au+Au collisions at $\sqrt{s_{\mathrm{NN}}}$ = 7.7 GeV (top) and 11.5 GeV (bottom).

can not be reproduced. In BES-II central events, there is positive proton number κ_5/κ_1 from $\sqrt{s_{\mathrm{NN}}}$ = 7.7 GeV. The proton number κ_6/κ_1 from $\sqrt{s_{\mathrm{NN}}}$ = 11.5 GeV is progressively positive from peripheral to central events. Multi-antiproton correlations are close to zero like lower orders.

4.3 Rapidity Dependence

This section discusses the y dependence of cumulants of net-proton, proton and antiproton numbers and factorial cumulants of proton and antiproton numbers up to the fourth order and their ratios. With the efficiency correction and CBWC performed, all the results in this section are obtained within the phase space [0.4 GeV/c < p_{T} < 2.0 GeV/c, $|y| < |y|_{\mathrm{max}}$] in 0–5% central Au+Au collisions, where $|y|_{\mathrm{max}}$ = 0.1, 0.2, 0.3, 0.4, 0.5 for net-proton, proton and antiproton results using PID Cut 1; $|y|_{\mathrm{max}}$ = 0.6 for net-proton, proton and antiproton results using PID Cut 2; and $|y|_{\mathrm{max}}$ = 0.7 for proton results using PID Cut 3. Plots in this section include top panels for $\sqrt{s_{\mathrm{NN}}}$ = 7.7 GeV and bottom panels for $\sqrt{s_{\mathrm{NN}}}$ = 11.5 GeV. For the descriptions of markers, stars, circles and squares denote results from BES-I using the RefMult3 centrality, BES-II using the RefMult3 centrality and BES-II using the RefMult3X centrality, respectively. Statistical errors are drawn as vertical bars, and systematic errors are expressed by brackets for BES-I and vertical shaded bands for BES-II. The cumulants and factorial cumulants and their ratios within $|y|$ < 0.1, 0.2, 0.3, 0.4, 0.5 from BES-I [98] are shown for comparison.

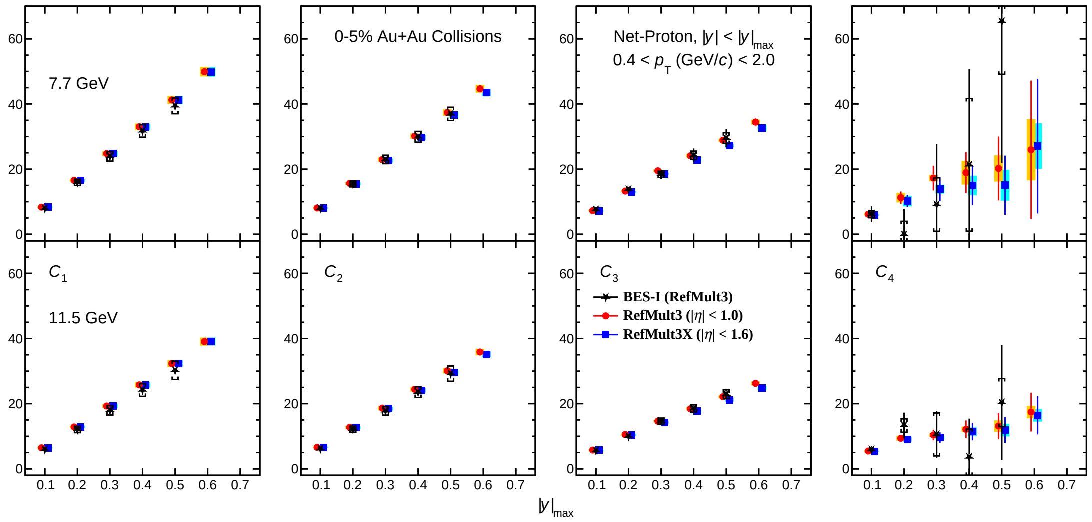

Figure 4.11 (Color online) Rapidity (y) dependence of net-proton number cumulants up to the fourth order (C_1, C_2, C_3 and C_4) in Au+Au collisions at $\sqrt{s_{\text{NN}}}$ = 7.7 GeV (top) and 11.5 GeV (bottom).

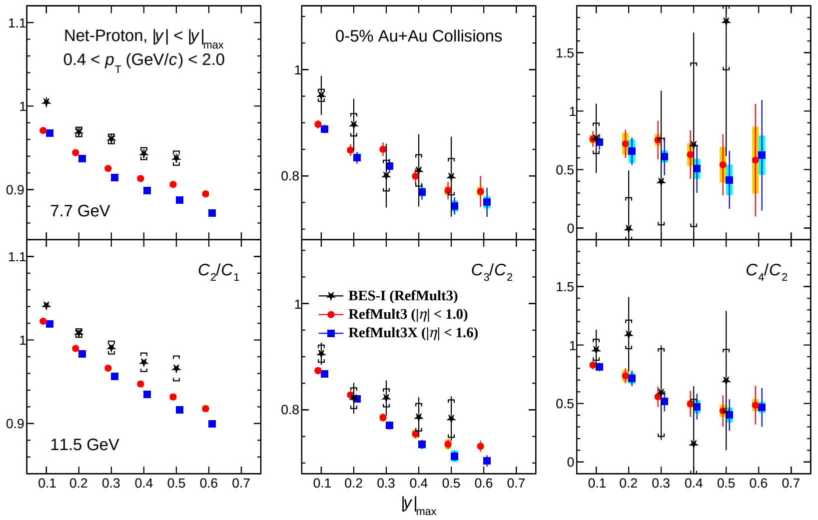

Figure 4.12 (Color online) Rapidity (y) dependence of net-proton number cumulant ratios up to the fourth order (C_2/C_1, C_3/C_2 and C_4/C_2) in Au+Au collisions at $\sqrt{s_{\text{NN}}}$ = 7.7 GeV (top) and 11.5 GeV (bottom).

Figure 4.11 presents the y dependence of net-proton number cumulants up to the fourth order. Cumulants monotonically increase as the y windows expands due to more net-particles counted. For the cases of $|y|_{\text{max}} \leqslant 0.5$, the BES-II results show a good agreement with the BES-I results and produce a little bit higher C_1 because the PID cut efficiency is included in the efficiency correction. Cumulants within $|y| < 0.6$ follow a smooth trend compared to those within narrower y windows. To extend $|y|$ up to 0.6, the event $|V_z|$ cut is reduced from 50 cm to 20 cm (45 cm) for the $\sqrt{s_{\text{NN}}}$ = 7.7 GeV (11.5 GeV) data set, which causes lower statistics and larger statistical uncertainties comapred to the results from the default acceptance.

Figure 4.12 presents the y dependence of net-proton number cumulant ratios.

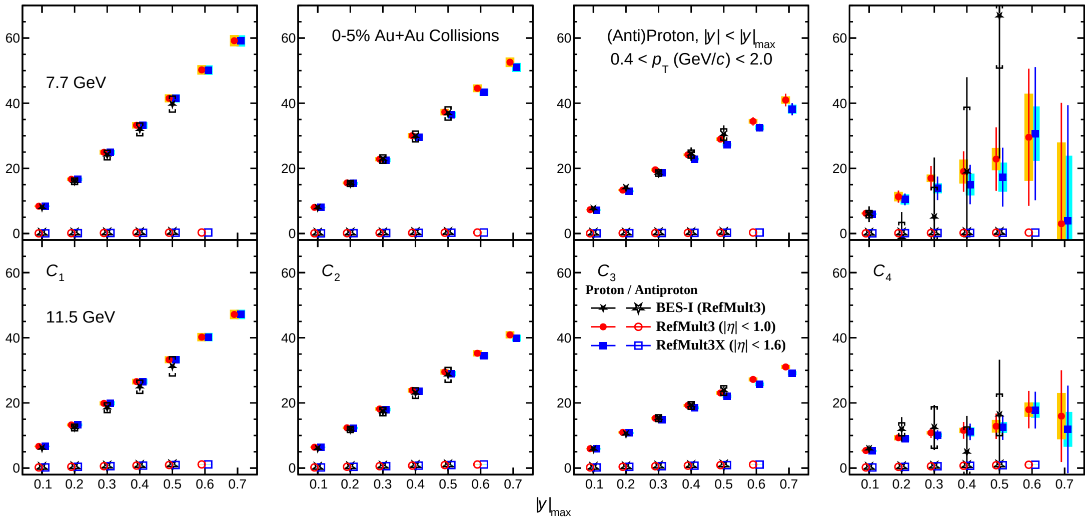

Figure 4.13 (Color online) Rapidity (y) dependence of proton and antiproton number cumulants up to the fourth order (C_1, C_2, C_3 and C_4) in Au+Au collisions at $\sqrt{s_{\mathrm{NN}}}$ = 7.7 GeV (top) and 11.5 GeV (bottom).

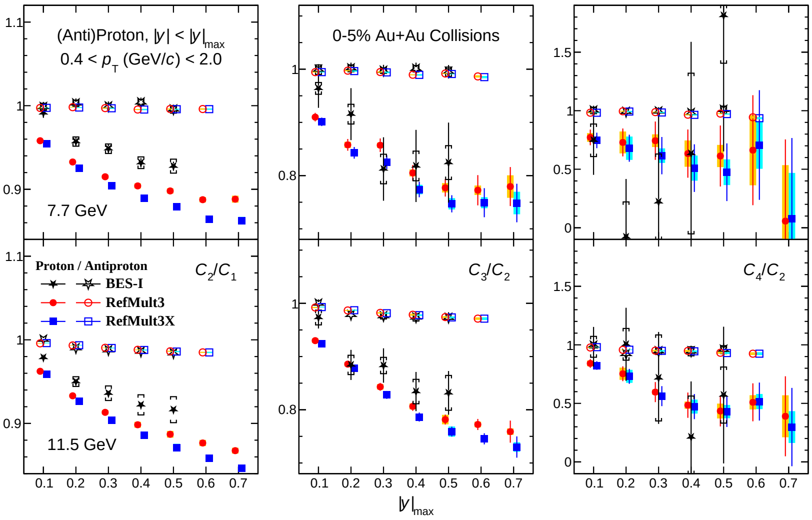

Figure 4.14 (Color online) Rapidity (y) dependence of proton and antiproton number cumulant ratios up to the fourth order (C_2/C_1, C_3/C_2 and C_4/C_2) in Au+Au collisions at $\sqrt{s_{\mathrm{NN}}}$ = 7.7 GeV (top) and 11.5 GeV (bottom).

Within various y windows in central events, a clear effect of the centrality resolution can always be observed on C_2/C_1 and C_3/C_2, while the effect is weak on C_4/C_2. There is a decreasing trend in all the cumulant ratios as the y window expands, which is opposite to the cumulants before taking ratios.

Figure 4.13 presents the y dependence of proton and antiproton number cumulants up to the fourth order. Solid markers denote proton number cumulants, while open markers are for those of antiproton numbers. It can also be seen that antiproton number cumulants are around zero within all y windows at both energies. Proton number cumulants are similar to net-proton number cumulants. A slight hint of smaller C_4 within

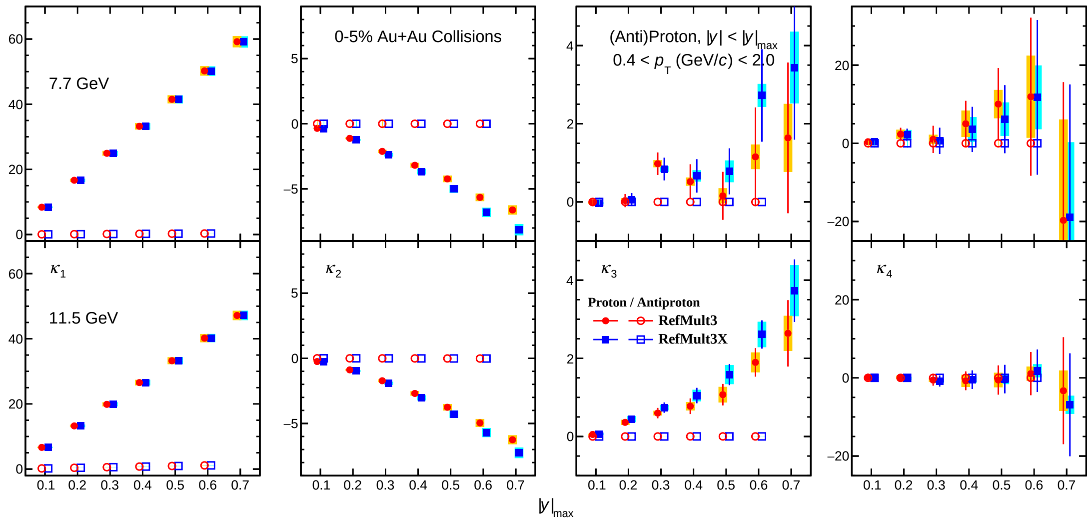

Figure 4.15 (Color online) Rapidity (y) dependence of proton and antiproton number factorial cumulants up to the fourth order (κ_1, κ_2, κ_3 and κ_4) in Au+Au collisions at $\sqrt{s_{\mathrm{NN}}} = 7.7$ GeV (top) and 11.5 GeV (bottom).

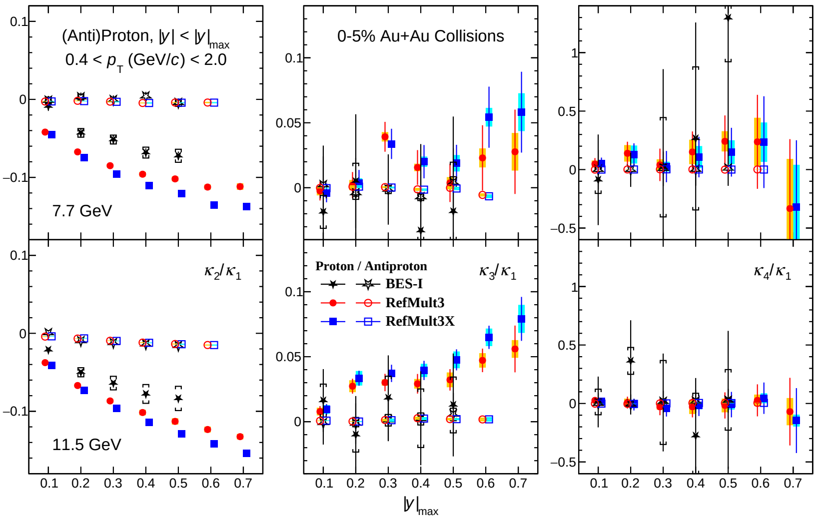

Figure 4.16 (Color online) Rapidity (y) dependence of proton and antiproton number factorial cumulant ratios up to the fourth order (κ_2/κ_1, κ_3/κ_1 and κ_4/κ_1) in Au+Au collisions at $\sqrt{s_{\mathrm{NN}}} = 7.7$ GeV (top) and 11.5 GeV (bottom).

$|y| < 0.7$ can be seen, but the uncertainties are large due to the reduced $|V_z|$ cut down to 15 cm.

Figure 4.14 presents the y dependence of proton and antiproton number cumulants ratios. The extended $|y|_{\mathrm{max}}$ up to 0.7 is applied for proton results. It can be clearly observed that all the cumulant ratios of proton and antiproton numbers are reduced by the increasing $|y|_{\mathrm{max}}$. The results within $|y| < 0.6$ and $|y| < 0.7$, carrying significant uncertainties, seem to follow the decreasing trend from narrower y windows.

Figure 4.15 presents the y dependence of proton and antiproton number factorial cumulants up to the fourth order. Focusing on the proton results, the second order and third order show opposite signs and trends as functions of $|y|_{\mathrm{max}}$. They progressively deviate from zero as the y acceptance expands. However, for the fourth order, the results are always consistent with zero within large error bars. Antiproton number factorial cumulants are always close to zero.

Figure 4.16 presents the y dependence of proton and antiproton number factorial cumulant ratios. Similar trends are observed to the factorial cumulants, indicating a negative two-proton correlation and a positive three-proton correlation which become stronger in a broader y window. The y dependence of κ_4/κ_1 is not significant considering the uncertainties. It is also observed that the better centrality resolution results in proton number κ_2/κ_1 and κ_3/κ_1 the farther from the Poisson baseline at zero.

4.4 Transverse Momentum Dependence

This section discusses the p_{T} dependence of cumulants of net-proton, proton and antiproton numbers and factorial cumulants of proton and antiproton numbers up to the fourth order and their ratios. With the efficiency correction and CBWC performed, all the results in this section are obtained within the phase space [$0.4\ \mathrm{GeV}/c < p_{\mathrm{T}} < p_{\mathrm{T}}^{\mathrm{max}}$, $|y| < 0.5$] in 0–5% central Au+Au collisions, where $p_{\mathrm{T}}^{\mathrm{max}} = 0.8$, 1.0, 1.2, 1.4, 1.6, 1.8, 2.0 GeV/c. Plots in this section include top panels for $\sqrt{s_{\mathrm{NN}}} = 7.7$ GeV and bottom panels for $\sqrt{s_{\mathrm{NN}}} = 11.5$ GeV. For the descriptions of markers, stars, circles and squares denote results from BES-I using the RefMult3 centrality, BES-II using the RefMult3 centrality and BES-II using the RefMult3X centrality, respectively. Statistical errors are drawn as vertical bars, and systematic errors are expressed by brackets for BES-I and vertical shaded bands for BES-II. The cumulants and factorial cumulants and their ratios within $0.4\ \mathrm{GeV}/c < p_{\mathrm{T}} < 1.0$, 1.2, 1.4, 1.6, 2.0 GeV/c from BES-I [98] are shown for comparison.

Figure 4.17 presents the p_{T} dependence of net-proton number cumulants up to the fourth order. Cumulants smoothly increase for a larger p_{T} window, and a saturation is likely to exist for $p_{\mathrm{T}}^{\mathrm{max}} = 2.0$ GeV/c. The BES-II results, with slightly higher C_1, show a good agreement with BES-I.

Figure 4.18 presents the p_{T} dependence of net-proton number cumulant ratios. Good consistency is found when comparing BES-I and BES-II measurements. There is a decreasing trend for C_2/C_1 and C_3/C_2, as well as C_4/C_2 at $\sqrt{s_{\mathrm{NN}}} = 11.5$ GeV. For C_4/C_2 at $\sqrt{s_{\mathrm{NN}}} = 7.7$ GeV, an enhancement appears at $p_{\mathrm{T}}^{\mathrm{max}} = 0.8$ GeV/c, which could come from the Poisson limit approaching unity. There is also a saturation phenomenon

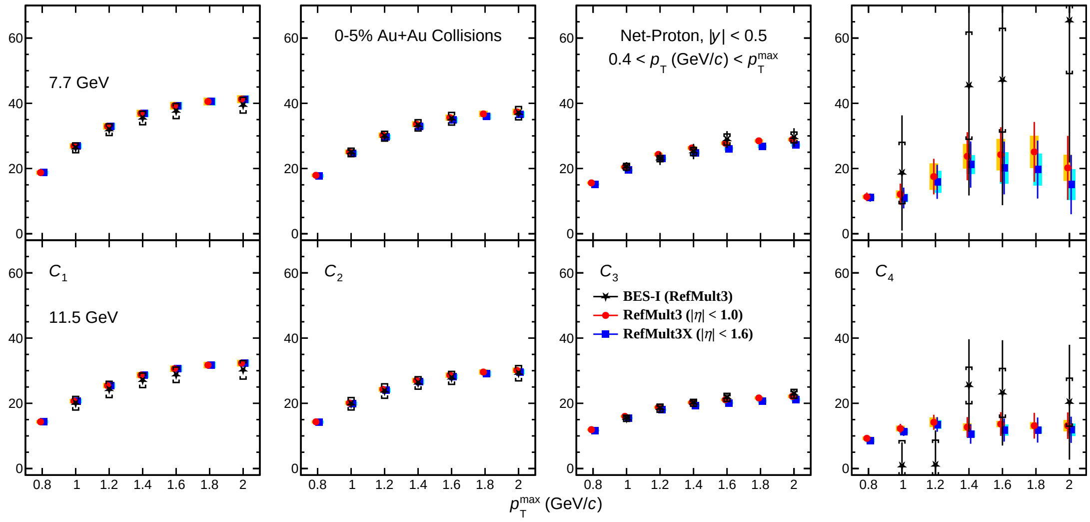

Figure 4.17 (Color online) Transverse momentum (p_T) dependence of net-proton number cumulants up to the fourth order (C_1, C_2, C_3 and C_4) in Au+Au collisions at $\sqrt{s_{NN}}$ = 7.7 GeV (top) and 11.5 GeV (bottom).

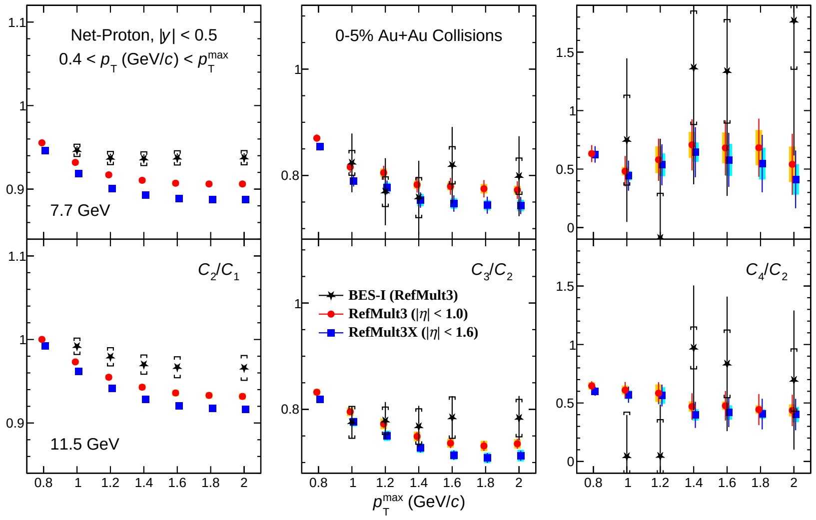

Figure 4.18 (Color online) Transverse momentum (p_T) dependence of net-proton number cumulant ratios up to the fourth order (C_2/C_1, C_3/C_2 and C_4/C_2) in Au+Au collisions at $\sqrt{s_{NN}}$ = 7.7 GeV (top) and 11.5 GeV (bottom).

for high p_T^{max}.

Figure 4.19 presents the p_T dependence of proton and antiproton number cumulants up to the fourth order. The centrality resolution effect also exists for C_2/C_1 and C_3/C_2 in various p_T windows from central events. No clear p_T dependence can be observed for antiproton results due to the small values. The proton number cumulants show similar behaviors to the net-proton number cumulants, because the proton serves as the dominant source.

Figure 4.20 presents the p_T dependence of proton and antiproton number cumulant ratios. As p_T^{max} increases, a smoothly decreasing trend is shown in both proton

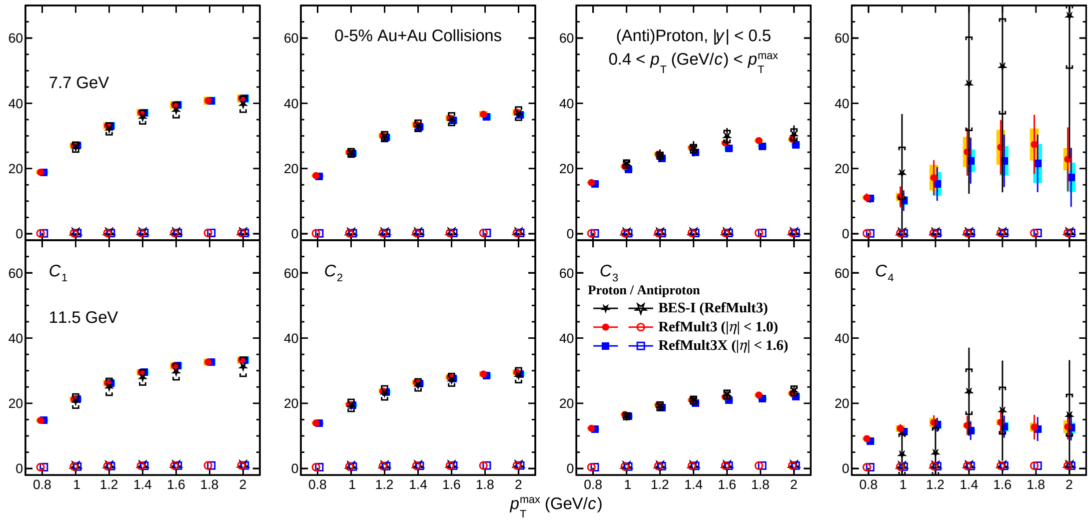

Figure 4.19 (Color online) Transverse momentum (p_T) dependence of proton and antiproton number cumulants up to the fourth order (C_1, C_2, C_3 and C_4) in Au+Au collisions at $\sqrt{s_{NN}}$ = 7.7 GeV (top) and 11.5 GeV (bottom).

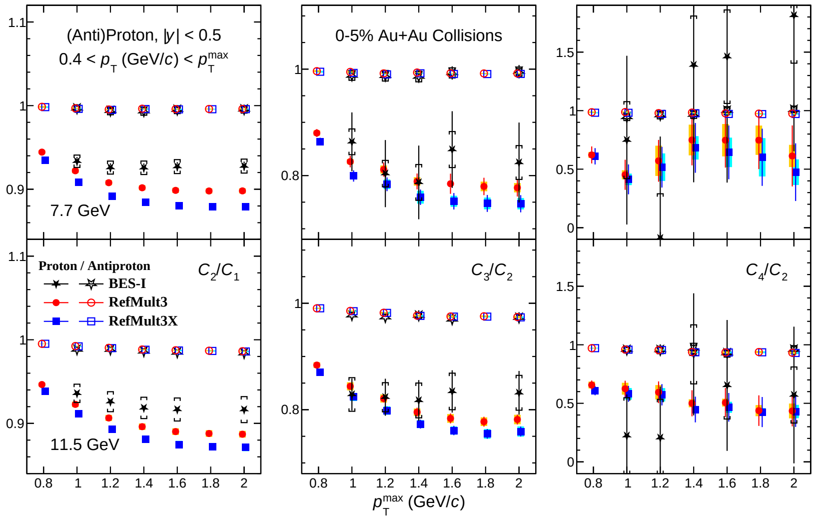

Figure 4.20 (Color online) Transverse momentum (p_T) dependence of proton and antiproton number cumulant ratios up to the fourth order (C_2/C_1, C_3/C_2 and C_4/C_2) in Au+Au collisions at $\sqrt{s_{NN}}$ = 7.7 GeV (top) and 11.5 GeV (bottom).

and antiproton results, although the antiproton ones stay close to unity as the Poisson baseline.

Figure 4.21 presents the p_T dependence of proton and antiproton number factorial cumulants up to the fourth order. Similar to the y dependence, κ_2 decreases and κ_3 increases as the phase space becomes larger. For κ_4, positive values can be seen in a few p_T windows at $\sqrt{s_{NN}}$ = 7.7 GeV, but those at $\sqrt{s_{NN}}$ = 11.5 GeV always touch zero within errors.

Figure 4.22 presents the p_T dependence of proton and antiproton number factorial cumulant ratios. The behaviors as the p_T acceptance expands, similar to factorial cumu-

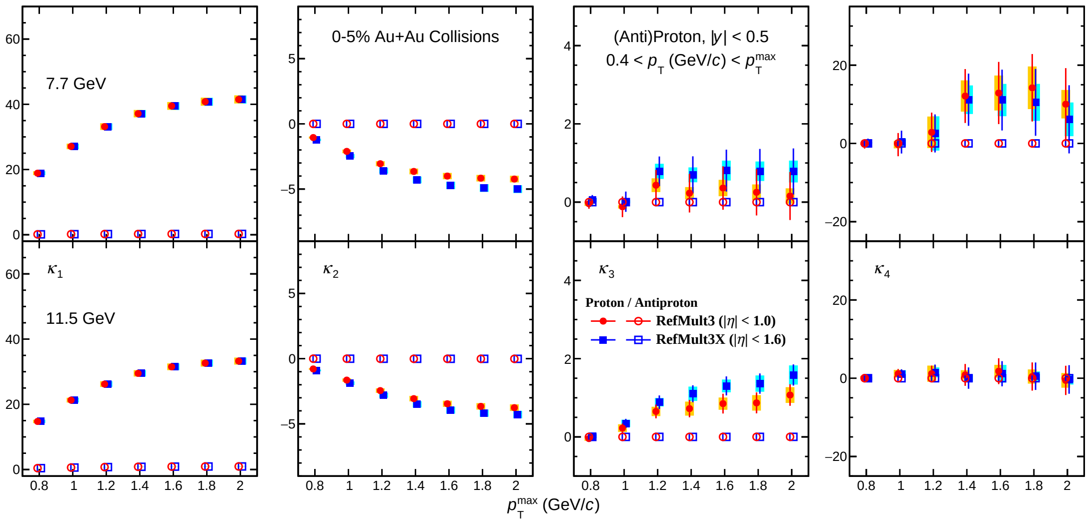

Figure 4.21   (Color online) Transverse momentum (p_T) dependence of proton and antiproton number factorial cumulants up to the fourth order (κ_1, κ_2, κ_3 and κ_4) in Au+Au collisions at $\sqrt{s_{NN}}$ = 7.7 GeV (top) and 11.5 GeV (bottom).

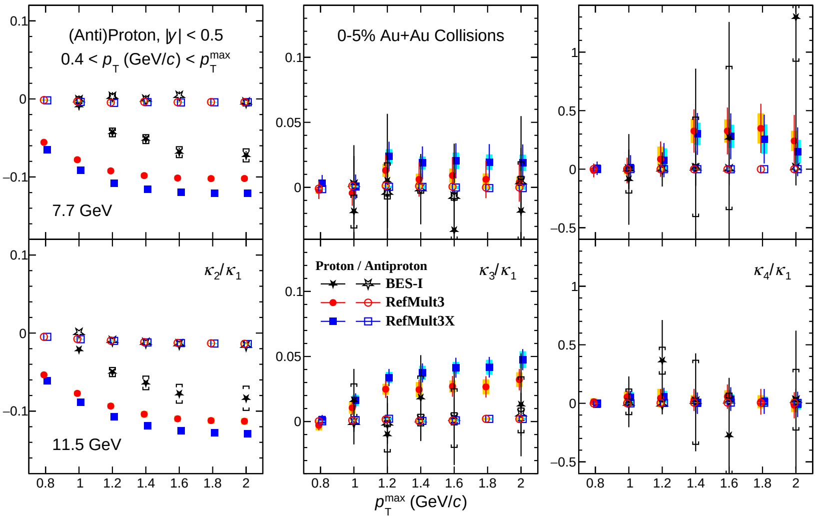

Figure 4.22   (Color online) Transverse momentum (p_T) dependence of proton and antiproton number factorial cumulant ratios up to the fourth order (κ_2/κ_1, κ_3/κ_1 and κ_4/κ_1) in Au+Au collisions at $\sqrt{s_{NN}}$ = 7.7 GeV (top) and 11.5 GeV (bottom).

lants, suggest increasing a two-proton anti-correlation and a three-proton correlation at both energies, as well as a positive four-proton correlation at $\sqrt{s_{NN}}$ = 7.7 GeV. Effect of centrality resolution is still seen in proton number κ_2/κ_1 and κ_3/κ_1.

4.5   Collision Energy Dependence

This section discusses the $\sqrt{s_{NN}}$ dependence of ratios of net-proton number cumulants and factorial cumulants up to the fourth order. With the efficiency correction and CBWC performed, all the results in this section are obtained within the default phase space [0.4 GeV/c < p_T < 2.0 GeV/c, $|y|$ < 0.5] in central (0–5%) and peripheral (70–

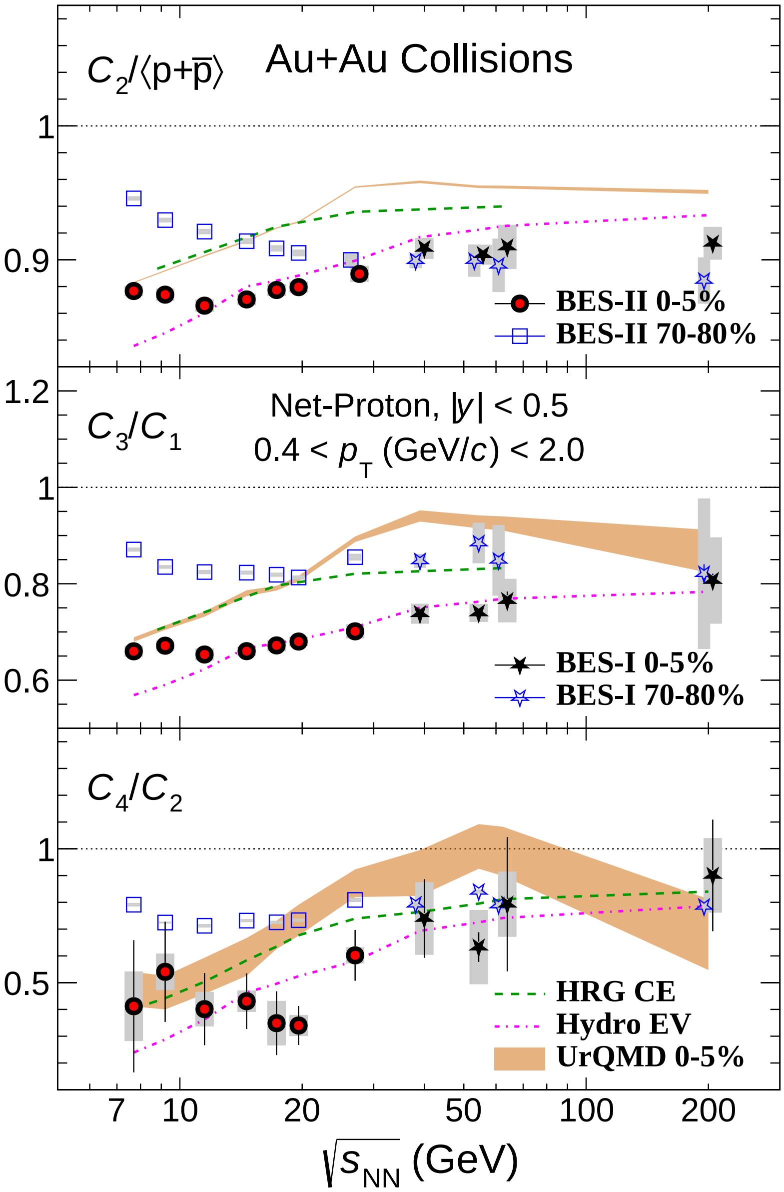

Figure 4.23 (Color online) Collision energy ($\sqrt{s_{\mathrm{NN}}}$) dependence of net-proton number cumulant ratios up to the fourth order ($C_2/\langle \mathrm{p}+\bar{\mathrm{p}}\rangle$, C_3/C_1 and C_4/C_2) in Au+Au collisions. The BES-I result is taken from Reference [83,98]. This analysis contributes to the STAR BES-II result [134-135].

80%) Au+Au collisions. The BES-I result is taken from References [83,98], and the BES-II result has just been released by the STAR Collaboration [134-135]. This analysis contributes to and plays a key role in the STAR BES-II measurement of net-proton number fluctuations.

Figure 4.23 presents the $\sqrt{s_{\mathrm{NN}}}$ dependence of net-proton number cumulant ratios, including $C_2/\langle \mathrm{p}+\bar{\mathrm{p}}\rangle$ in the top panel, C_3/C_1 in the middle panel and C_4/C_2 in the bottom panel. Here, $\langle \mathrm{p}+\bar{\mathrm{p}}\rangle$ represents the mean of the event-by-event number of protons and antiprotons. Solid and open markers denote the cumulant ratios in central and peripheral events, respectively. Stars show the BES-I result using RefMult3, and the circles and squares are from BES-II including this analysis for $\sqrt{s_{\mathrm{NN}}}$ = 7.7 GeV and 11.5 GeV. Note that the BES-II $\sqrt{s_{\mathrm{NN}}}$ = 27 GeV data set was taken before the iTPC upgrade and the centrality is defined by RefMult3. Data points from other BES-II data sets are from RefMult3X centrality classes.

The measured cumulant ratios in central events follow a decreasing trend as $\sqrt{s_{\mathrm{NN}}}$ decreases and stop dropping at low energies with a hint of rising $C_2/\langle \mathrm{p}+\bar{\mathrm{p}}\rangle$. In peripheral events, C_3/C_1 and C_4/C_2 show weak energy dependence, but $C_2/\langle \mathrm{p}+\bar{\mathrm{p}}\rangle$ continuously increases for the decreasing $\sqrt{s_{\mathrm{NN}}}$. Results in peripheral events are always higher than those in central events except $C_2/\langle \mathrm{p}+\bar{\mathrm{p}}\rangle$ at $\sqrt{s_{\mathrm{NN}}} \gtrsim 30$ GeV.

In each panel, the dotted line is at unity, corresponding to the Skellam expectation as the purely statistical baseline. Clear suppression is observed in all the cumulant ratios, which is stronger in central events compared to peripheral events. Three model predictions without a critical point but considering the net-baryon number conservation are shown for comparison. The HRG model describing the baryonic charge by the canonical ensemble [94] is labelled by “HRG CE”. The calculation based on the hydrodynamics of the system evolution with excluded volume [156] is shown as “Hydro EV”. The UrQMD simulation [87-89] is also performed with the same techniques as the experimental data analysis such as the centrality determination (RefMult3X for $\sqrt{s_{\mathrm{NN}}} \leqslant 19.6$ GeV and RefMult3 for $\sqrt{s_{\mathrm{NN}}} \geqslant 27$ GeV) and CBWC. The former two model expectations monotonically decrease as $\sqrt{s_{\mathrm{NN}}}$ decreases, and the UrQMD calculation in 0–5% central events also shows a decreasing trend at $\sqrt{s_{\mathrm{NN}}} \gtrsim 40$ GeV. However, none of the models can quantitatively reproduce the measurement well at all energies. For C_4/C_2, model calculations are consistent with the experimental data at $\sqrt{s_{\mathrm{NN}}} \gtrsim 30$ GeV and at $\sqrt{s_{\mathrm{NN}}} \lesssim 15$ GeV. At $\sqrt{s_{\mathrm{NN}}} \sim 20$ GeV, three models carry a smooth $\sqrt{s_{\mathrm{NN}}}$ dependence, and a dip could exist in the deviation between experimental and model results.

Figure 4.24 presents the $\sqrt{s_{\mathrm{NN}}}$ dependence of proton number factorial cumulant ratios, including κ_2/κ_1 in the top panel, κ_3/κ_1 in the middle panel and κ_4/κ_1 in the bottom panel. The dotted line at zero in each panel represents the Poisson baseline. We can clearly observe a negative two-proton correlation and a positive three-proton correlation in both central and peripheral collisions at each energy, while κ_4/κ_1 touches zero with large errors. Factorial cumulant ratios in peripheral events show weak $\sqrt{s_{\mathrm{NN}}}$ dependence and are closer to zero than central events. Focusing on the 0–5% centrality, all of the results suggest a hint of a non-monotonic behavior. κ_2/κ_1 and κ_3/κ_1 show a dip and a peak at $\sqrt{s_{\mathrm{NN}}} \sim 11.5$ GeV, respectively. For a decreasing collision energy,

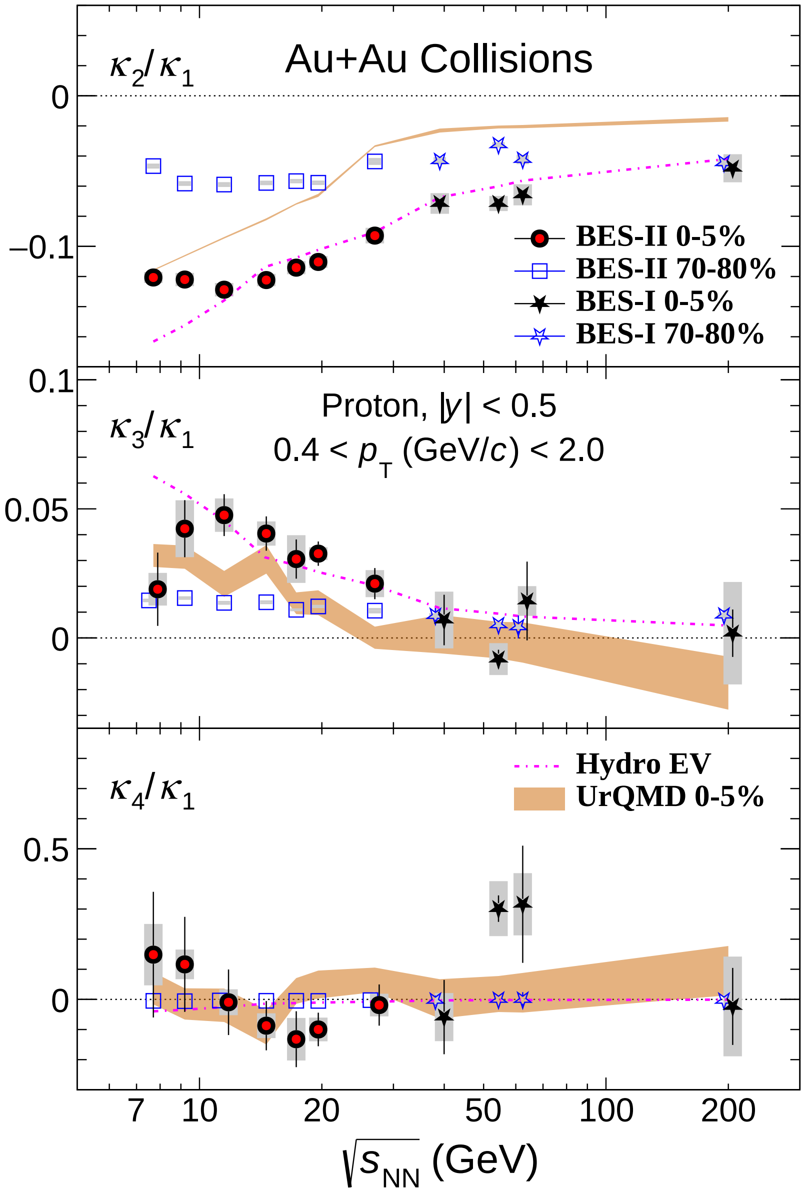

Figure 4.24 (Color online) Collision energy ($\sqrt{s_{NN}}$) dependence of proton number factorial cumulant ratios up to the fourth order (κ_2/κ_1, κ_3/κ_1 and κ_4/κ_1) in Au+Au collisions. The BES-I result is taken from Reference [83,98]. This analysis contributes to the STAR BES-II result [134-135].

κ_4/κ_1 decreases to be negative from zero and is likely to reach a minimum at $\sqrt{s_{NN}}$ around 17.3 GeV. Then it goes up and touches zero again at lower energies. However, models without a critical point expect roughly monotonic trends.

Figure 4.25 presents the $\sqrt{s_{NN}}$ dependence of antiproton number factorial cumulant ratios, including κ_2/κ_1 in the top panel, κ_3/κ_1 in the middle panel and κ_4/κ_1 in the bottom panel. The two-antiproton correlations in both central and peripheral events are more strongly negative at the higher collision energy, similar to the case of protons. Models reproduce the trends and the sign. However, we can not observed clear a three-antiproton or a four-antiproton correlation. κ_3/κ_1 and κ_4/κ_1 are close to zero with no

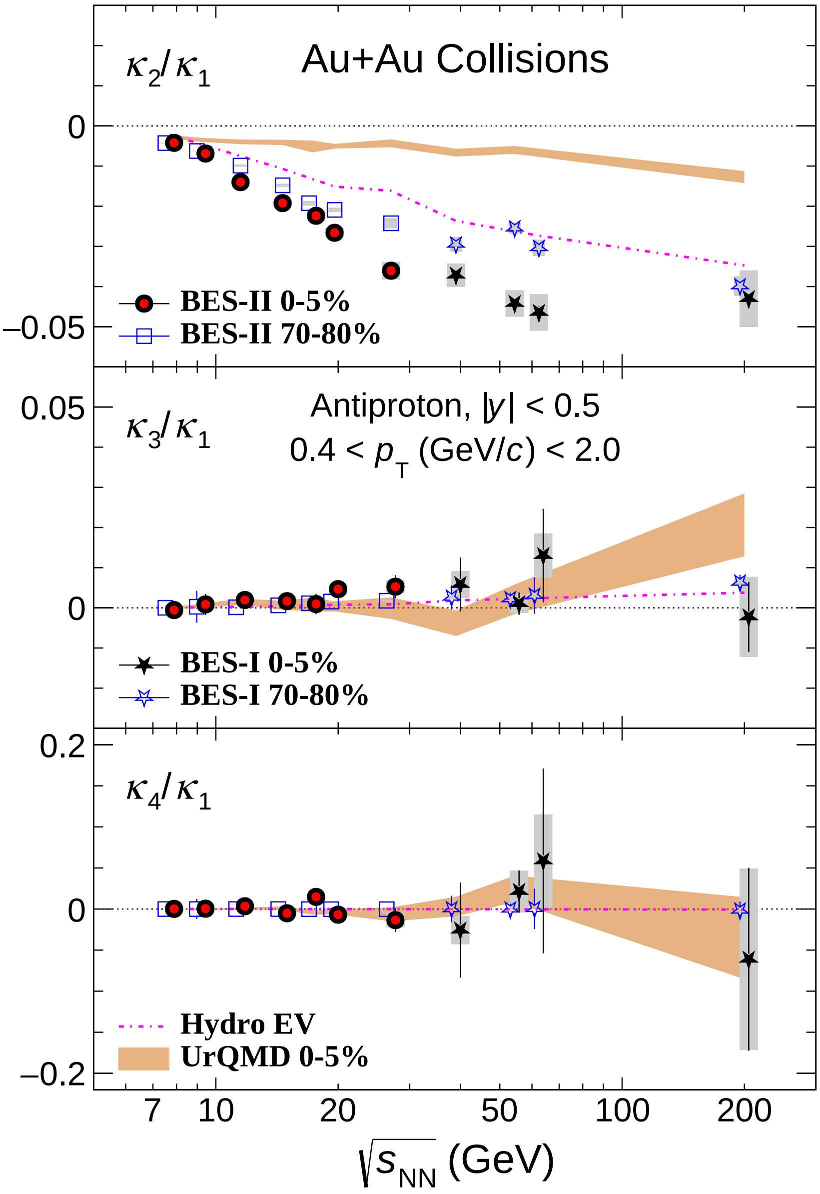

Figure 4.25 (Color online) Collision energy ($\sqrt{s_{\mathrm{NN}}}$) dependence of antiproton number factorial cumulant ratios up to the fourth order (κ_2/κ_1, κ_3/κ_1 and κ_4/κ_1) in Au+Au collisions. The BES-I result is taken from Reference [83,98]. This analysis contributes to the STAR BES-II result [134-135].

significant energy dependence, and such behaviors are also seen in models.

The deviations of net-proton number C_4/C_2 in central events from non-critical references, including the peripheral data and models without a critical point, are quantified as functions of $\sqrt{s_{\mathrm{NN}}}$ and plotted in Figure 4.26. The significance of the deviation is obtained as the difference of C_4/C_2 between the 0–5% data and the reference normalized by the quadratic sum of the errors of the 0–5% data and the reference. At $\sqrt{s_{\mathrm{NN}}} = 200$ GeV, the experimental data in central events also show good consistency with the four references. As $\sqrt{s_{\mathrm{NN}}}$ decreases, deviations become larger. All the references provide a maximum deviation at $\sqrt{s_{\mathrm{NN}}} \sim 20$ GeV, forming obvious dips with

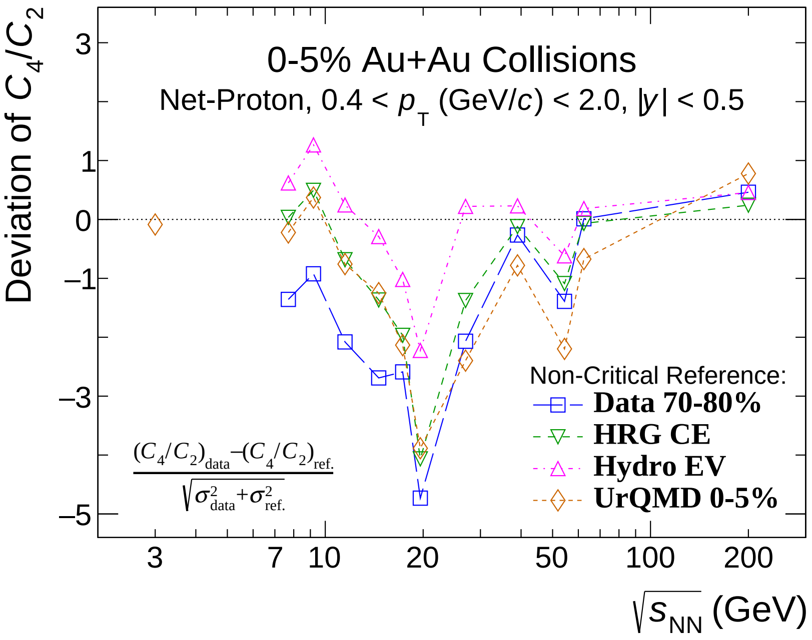

Figure 4.26 (Color online) Collision energy ($\sqrt{s_{NN}}$) dependence of deviations of net-proton number C_4/C_2 in 0–5% central events from several non-critical references in Au+Au collisions. The number represents the difference normalized by the total error, which is shown on the bottom left. Each marker represents a distinct reference taken for the calculation of the deviation.

Table 4.3 Overall deviations of net-proton number C_4/C_2 in 0–5% central events from several non-critical references in Au+Au collisions at $\sqrt{s_{NN}}$ from 7.7 GeV to 27 GeV in BES-I and BES-II.

Reference	Data 70–80%	HRG CE	Hydro EV	UrQMD 0–5%
BES-I	1.5σ	1.7σ	1.4σ	2.1σ
BES-II	5.4σ	3.2σ	0.5σ	3.5σ

2–5σ. At lower $\sqrt{s_{NN}}$, deviations are smaller and closer to zero, suggesting C_4/C_2 is returning to the predicted baseline. The result at $\sqrt{s_{NN}} = 3$ GeV taken from the STAR FXT measurement [99-100] agrees with the UrQMD calculation quite well.

Table 4.3 lists the overall deviations of net-proton number C_4/C_2 in central events from peripheral events and models without a critical point in the range of $\sqrt{s_{NN}} = 7.7$–27 GeV. The significance is estimated by the χ^2 test and also compared to BES-I. We find the overall deviation highly improved up to a significance level of 5.4σ in BES-II due to the precision measurement.

Chapter 5 Summary and outlook

5.1 Summary

This thesis reports the exploration of the QCD phase structure, especially the conjectured critical point, through the measurement of event-by-event fluctuations of proton (including antiproton and net-proton) numbers in Au+Au collisions at RHIC. The data with large statistics are collected by the STAR experiment with the iTPC upgrade from BES-II. Detailed analysis is presented for $\sqrt{s_{\mathrm{NN}}}$ = 7.7 GeV and 11.5 GeV, including net-proton, proton and antiproton number cumulants and proton and antiproton number factorial cumulants with respect to dependences on collision centrality (up to the sixth order), rapidity and transverse momentum (up to the fourth order). The default phase space of the measurement is [0.4 GeV/c $< p_{\mathrm{T}} <$ 2.0 GeV/c, $|y| < 0.5$], and the rapidity is extended to ± 0.6 for net-proton and antiproton numbers and ± 0.7 for proton numbers for the rapidity dependence. The collision energy dependence of fourth-order cumulant and factorial cumulant ratios is also discussed.

Data QA — Run, event and track selections are performed to remove background and distortion from fluctuations. Bad runs are rejected after a procedure of run-by-run QA. Inaccurately calibrated events are identified by abnormal values of track DCA in these events. Pileup events are found using the multiplicity correlation between TPC and TOF. For tracks, the energy loss parameter $n\sigma_{\mathrm{proton}}$ measured by TPC is recalibrated in each two-dimensional phase space bin and each run for high PID accuracy. Through studying V_z and nHitsFit dependences of (anti)proton acceptances from TPC and TOF, the measured phase space for each event is checked to be fully covered by the detectors with various cuts. Bin-by-bin proton and antiproton purities are estimated by fitting TPC $n\sigma_{\mathrm{proton}}$ and TOF m^2, required to be always higher than 90%. Purities from TOF PID are found always comparable to 100%, and those from TPC PID are also nearly 100% at low momenta. Three sets of PID cuts are defined individually for $|y| < 0.5$, 0.6 and 0.7 considering the purity requirement and the acceptance coverage, and puities are higher than 99% in most of phase space bins.

Techniques — The collision centrality is defined using two multiplicities, RefMult3 and RefMult3X, both of which exclude protons and antiprotons to avoid the effect of the self-correlation. With the upgraded iTPC, RefMult3, keeping the same cut of $|\eta| < 1.0$ as BES-I, becomes larger than BES-I, and RefMult3X extends $|\eta|$ to 1.6 to be even larger. The larger multiplicity provides the better centrality resolution as expected. The centrality bin width correction is applied to suppress the volume fluctuation within each broad centrality class. The TPC tracking efficiency and the TOF matching efficiency are calculated in the four-dimensional dependence on centrality, V_z, y and p_{T}, and the PID cut efficiency is also introduced. The TPC tracking efficiency is found to be higher than BES-I, especially at low p_{T}. The efficiency correction based on the binomial assumption is applied on the track-by-track basis. Statistical uncertainties are estimated using the analytical method and the bootstrap method which are tested to produce consistent results. Systematic uncertainties are studied by tuning track quality cuts, PID cuts and the efficiency to extract the systematic variation through the Barlow check. The leading sources of systematics for C_1 are DCA and the efficiency, while those for C_4/C_2 are DCA and $n\sigma_{\mathrm{proton}}$.

Centrality Resolution — A clear effect of centrality resolution is observed in both the experiment and the UrQMD model. Better centrality resolution induces lower cumulants/ratios from the second to the fourth orders, except C_4/C_2 in central events, which is not sensitive to the resolution. In the experiment, with applying an efficiency on BES-II RefMult3 to mimic the BES-I centrality resolution, the result agrees better with BES-I, suggesting the difference between BES-I and BES-II could be induced by such effect. In the model, the larger multiplicity is tested to provide the better centrality resolution with the smaller volume fluctuation. Additionally, the effect when taking RefMult3X for centrality determination is found to be saturated compared to that when taking the multiplicity in the full phase space.

Results — Cumulants and factorial cumulants are measured based on two centrality determinations using RefMult3 and RefMult3X. Most of BES-I and BES-II measurements are consistent within uncertainties, and both statistical and systematic errors in BES-II are strongly reduced. For example, the BES-II net-proton number C_4/C_2 results agree with BES-I within $\sim 1\sigma$, with errors suppressed by a factor of 3–5. The centrality resolution has a strong effect on the suppression of C_2/C_1 and a weak effect on C_4/C_2 in central events. Proton contribution dominates the net-proton number fluctuations, while the antiproton number cumulants and factorial cumulants stay around the statistical baselines. The rapidity and transverse momentum dependences show smooth trends consistent with BES-I, and the points of the extended rapidities carry larger uncertainties due to the reduced statistics.

The collision energy dependence of cumulant and factorial cumulant ratios shows a clear physical picture. In the 0–5% centrality class, all of the net-proton number $C_2/\langle \mathrm{p} + \bar{\mathrm{p}} \rangle$, C_3/C_1 and C_4/C_2 are below unity, the statistical baseline. Proton number factorial cumulant ratios suggest a negative two-proton correlation and a positive three-proton correlation. κ_2/κ_1 and κ_3/κ_1 and κ_4/κ_1 in central events show a hint of non-monotonic collision energy dependence with a potential minimum at $\sqrt{s_{\mathrm{NN}}} \sim 11.5$ GeV, maximum at $\sqrt{s_{\mathrm{NN}}} \sim 11.5$ GeV and minimum at $\sqrt{s_{\mathrm{NN}}} \sim 17.3$ GeV, respectively. Three models without a critical point, HRG CE, Hydro EV and UrQMD (0–5%), are taken into comparison. All of their expectations follow a monotonically decreasing trend as the collision energy decreases, and none of them can quantitatively describe the experimental results well. The measured C_4/C_2 in the 0–5% centrality class show a dip at $\sqrt{s_{\mathrm{NN}}} \sim 19.6$ GeV relative to non-critical references including the 70–80% experimental data and the three models. Based on different references, the deviation at $\sqrt{s_{\mathrm{NN}}} = 19.6$ GeV is 2–5σ and the significance of the overall deviation within $\sqrt{s_{\mathrm{NN}}} = 7.7$–27 GeV reaches up to 5.4σ, much higher than BES-I.

In summary, this study utilizes enlarged statistics, upgraded detectors and improved data analysis techniques and obtains the result with better centrality resolution, better statistical precision, better control on systematics and better acceptance coverage compared to BES-I. A significant deviation of high-order fluctuations is observed relative to various references without a critical point. The precision measurement provides better understanding on the QCD phase structure and helps improve related theoretical studies and future experiments.

5.2 Outlook

Detailed Acceptance Scan — So far, there have been several measurements for the (net-)proton number fluctuations in Au+Au collisions at RHIC, including the BES-I collider analysis at $\sqrt{s_{\mathrm{NN}}} = 7.7$–200 GeV corresponding to $\mu_B = 420$–25 MeV, the BES-II FXT analysis at $\sqrt{s_{\mathrm{NN}}} = 3$ GeV corresponding to $\mu_B = 750$ MeV and this analysis based on the BES-II collider experiments at $\sqrt{s_{\mathrm{NN}}} = 7.7$–27 GeV. Several hints and implications about the QCD phase structure have been obtained from these analyses. There still remain several important studies to be done based on the BES-II collider data. For example, the acceptance dependence at all collision energies has not been finalized yet. As is theoretically studied [64], it provides a stronger signature of fluctuations and correlations from the measurement within the extended acceptance window. Furthermore, a theoretical study [157] suggests a new idea for the rapidity scan within $|y - y_c| < \Delta y/2$. By varying y_c, the system locates at different positions in the phase diagram, which could serve as a probe of the critical regime with finer resolution

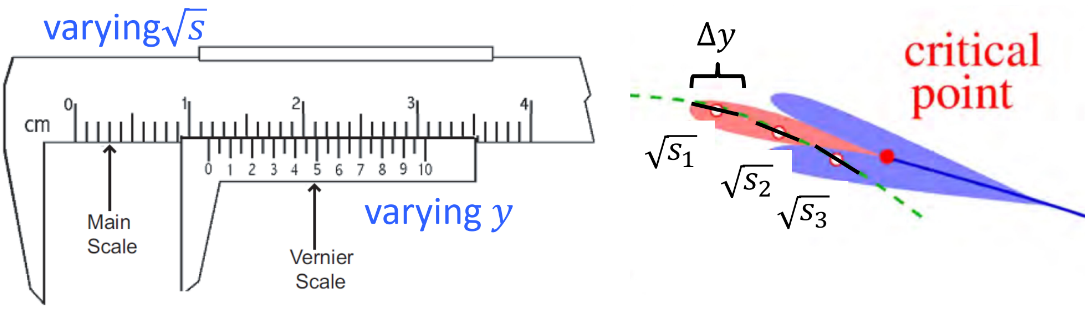

Figure 5.1 (Color online) Illustration of the collision energy scan and the rapidity scan. Figure is taken from Reference [158].

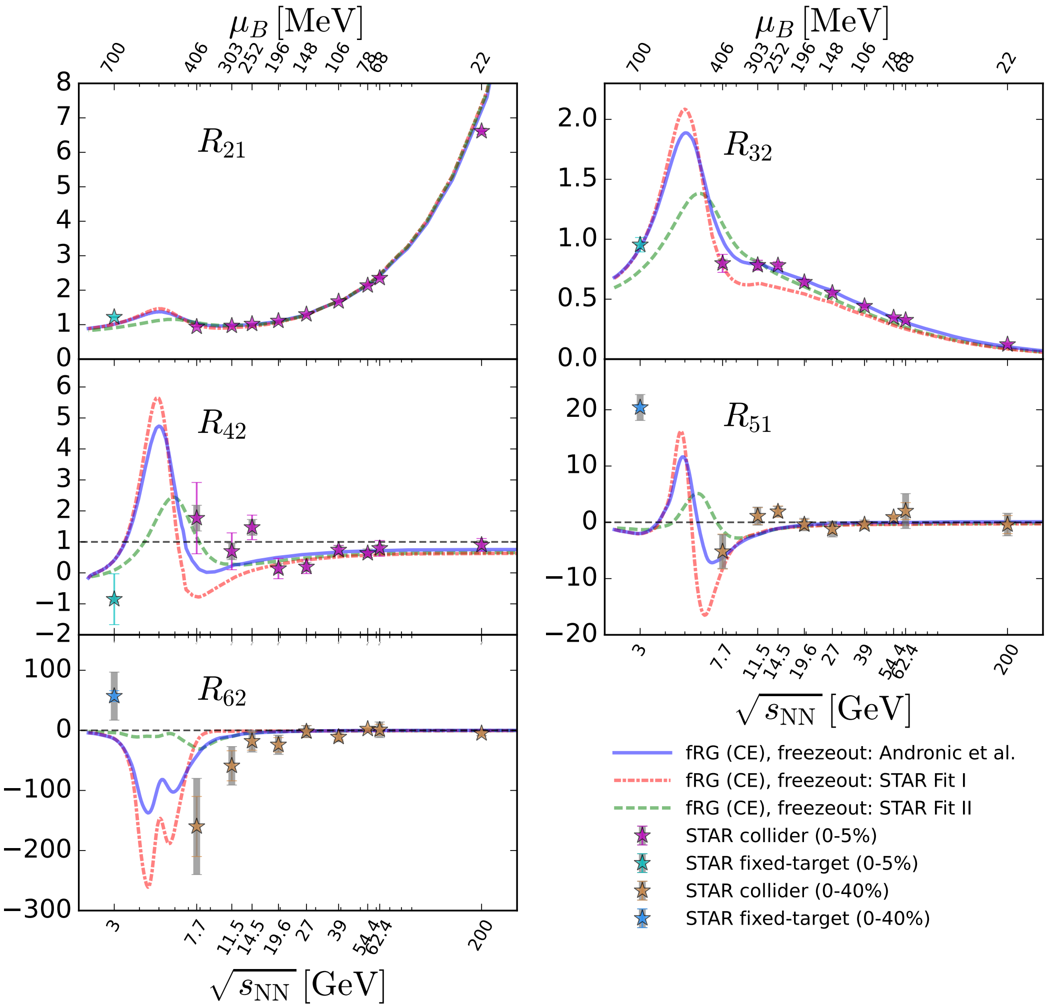

Figure 5.2 (Color online) Net-baryon number fluctuations of different orders as functions of $\sqrt{s_{\rm NN}}$ calculated by FRG on three different freeze-out curves. Here, R_{ij} represents C_i/C_j. Figure is taken from Reference [159].

than the collision energy scan, illustrated by Figure 5.1 [158].

Extended Energy Range — The other part of BES-II is the FXT mode for Au+Au collision experiments covering $\sqrt{s_{\rm NN}}$ = 3–13.7 GeV, which presents a promising opportunity for further measurements extending μ_B up to ~750 MeV. The information of the data sets is summarized in Table 2.2. To scan the QCD phase diagram in details and look for the potential impact on our understanding, it is essential to explore the current energy gap between $\sqrt{s_{\mathrm{NN}}}$ = 3 GeV and 7.7 GeV using the FXT data. The FRG calculation predicts there might be many additional important structures in the $\sqrt{s_{\mathrm{NN}}}$ dependence of net-baryon number cumulant ratios within the absent energy range [159], shown in Figure 5.2. Measurements at $\sqrt{s_{\mathrm{NN}}} < 7.7$ GeV could show interesting information related to the QCD phase structure.

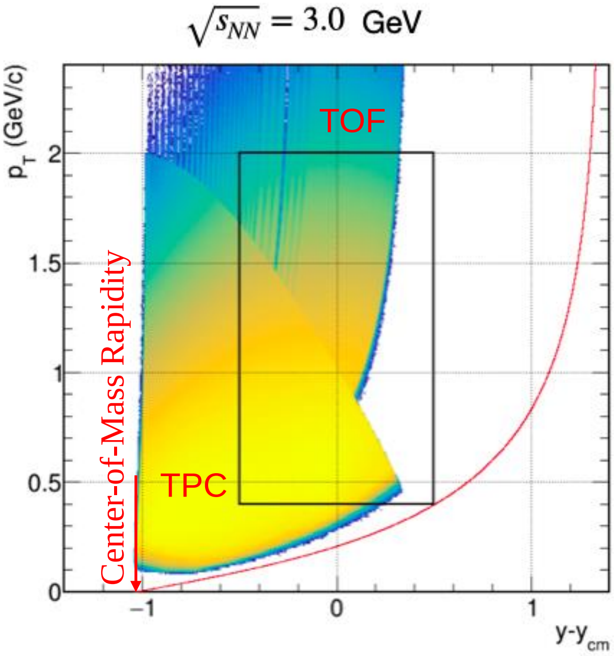

Figure 5.3 (Color online) Acceptance of protons in the $\sqrt{s_{\mathrm{NN}}}$ = 3 GeV data set with the expected boundary extended by the iTPC upgrade in Run-21. Figure is taken from Reference [160].

Upgraded Detectors — It is worth emphasizing that since 2019, the iTPC upgrade has been ready to enlarge the acceptance coverage, and eTOF has been installed to help PID at forward rapidities. Note that signals in a smaller acceptance could be reduced to be closer to the Poisson baseline. The completed analysis for the Run-18 $\sqrt{s_{\mathrm{NN}}}$ = 3 GeV data set does not utilize the upgraded detectors, and the proton measurement is taken within $-0.5 < y < 0$, half of the mid-rapidity window in the collider analysis. In the new $\sqrt{s_{\mathrm{NN}}}$ = 3 GeV data set taken in the year 2021, we may extend the rapidity window to $|y| < 0.5$ according to the expected boundary of the proton acceptance extended by the iTPC upgrade in Figure 5.3 [160]. Besides, due to the small multiplicities at low $\sqrt{s_{\mathrm{NN}}}$, the volume fluctuations are enhanced and can strongly influence the measured signals, studied at $\sqrt{s_{\mathrm{NN}}}$ = 3 GeV in Reference [100]. The upgraded iTPC provides larger multiplicities and improves the centrality resolution for the new FXT measurements, which is definitely an important part required by the sensitive observation.

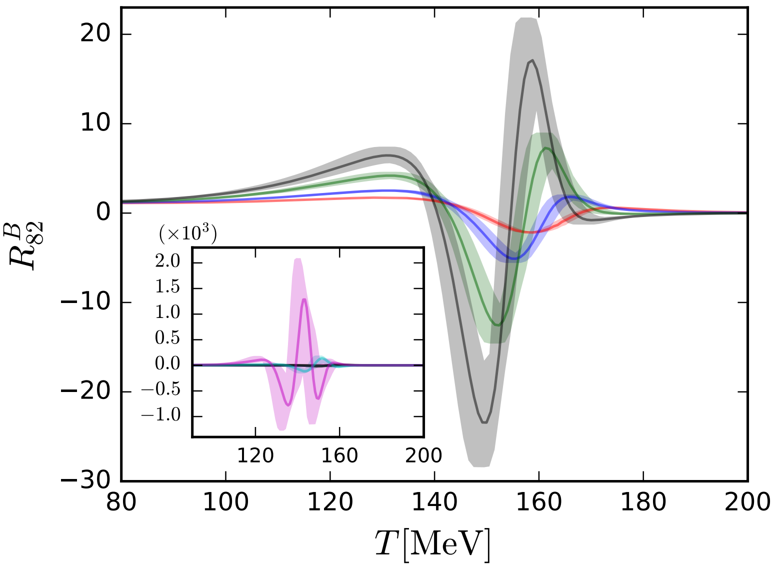

Figure 5.4 (Color online) Net-baryon number C_8/C_2 (R_{82}) as a function of T at several values of μ_B from the FRG calculation. Figure is taken from Reference [80].

Hyper-Order Fluctuations — As discussed, the higher-order fluctuations carry the larger statistical errors and are the more hungry for the statistics. The Run-21 data set for $\sqrt{s_{\rm NN}}$ = 3 GeV includes 2.1 billion events, and the proposed Au+Au collision experiments in 2023 and 2025 are proposed to take around 20 billion events [103]. The extremely high statistics enable us to measure the hyper-order fluctuations with high precision. It might also be possible to extend the cumulants up to the seventh and eighth orders, which are predicted to be sensitive to the phase structure in details including the crossover phase transition. Figure 5.4 [80] shows the behavior of the net-baryon number C_8/C_2 from the FRG calculation.

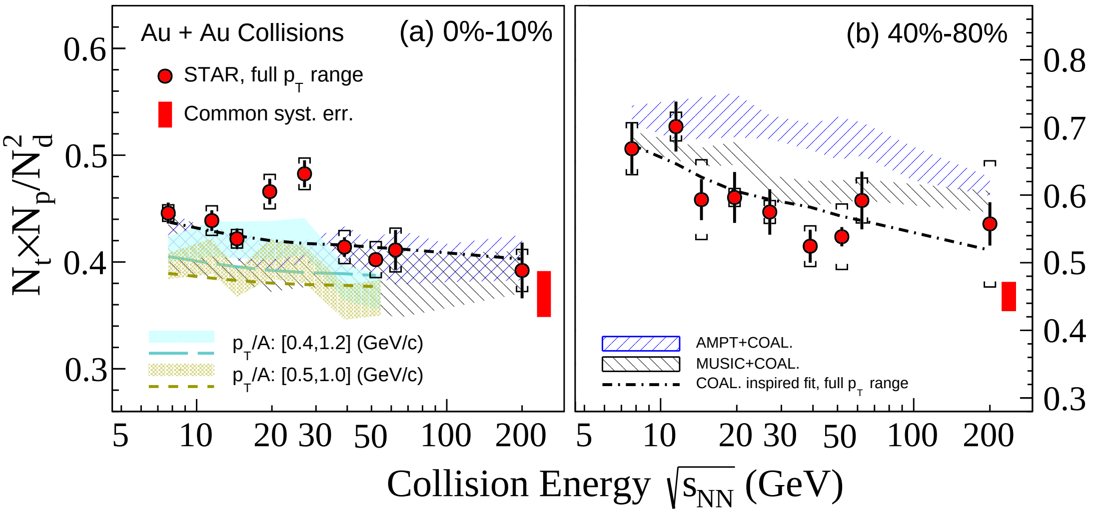

Figure 5.5 (Color online) Collision energy dependence of the triton (t) yield ratio (N_tN_p/N_d^2) measured by STAR in BES-I. Figure is taken from Reference [161].

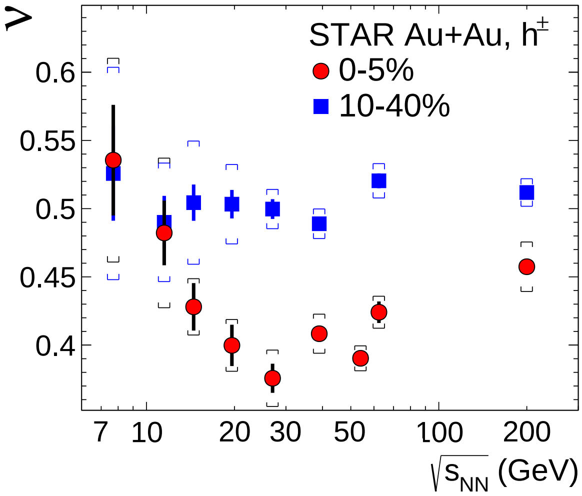

Figure 5.6 (Color online) Collision energy dependence of the scaling exponent (ν) from the intermittency of charged hadrons (h$^{\pm}$) measured by STAR in BES-I. Figure is taken from Reference [162].

More Observables — The QCD phase structure, including the existence and properties of the critical point, also needs to be confirmed by several different conclusive observables for strong evidence, such as net-charged-hadron and net-charged-kaon number fluctuations and baryon-strangeness correlations. Figures 5.5 and 5.6 [162] present the collision energy dependence of the triton (t) yield ratio (N_tN_p/N_d^2) and the scaling exponent (ν) of the charged-hadron intermittency measured by STAR from BES-I.

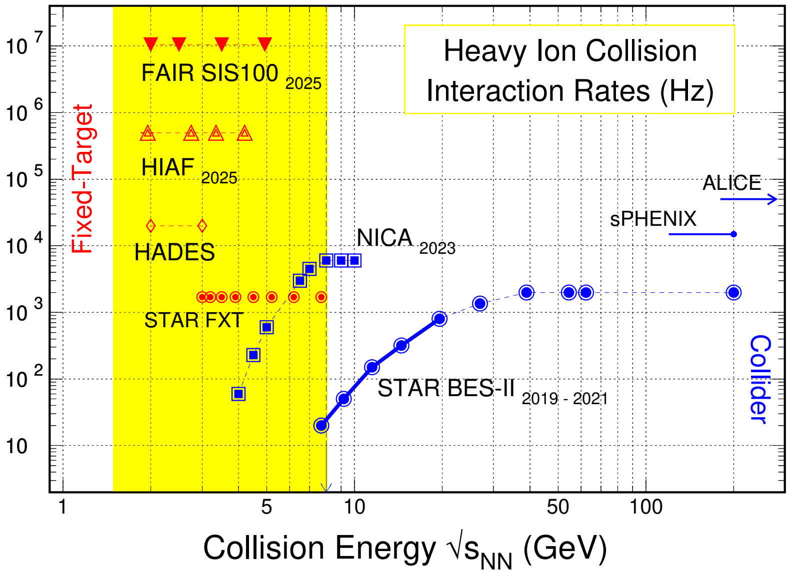

Figure 5.7 (Color online) Interaction rates of heavy-ion collisions as functions of $\sqrt{s_{\mathrm{NN}}}$ for various facilities. Blue and red markers represent collider and FXT experiments, respectively. Figure is taken from Reference [9].

Both of the measurements are sensitive to the density fluctuations in the collision system, particularly for neutrons in the former. Clearly non-monotonic behaviors are found at 19.6 GeV $\lesssim \sqrt{s_{\mathrm{NN}}} \lesssim$ 27 GeV in central events, which do not exist in the peripheral results. Such observations support the critical signals and can be further studied with higher precision in BES-II.

Future Facilities — Figure 5.7 summarizes $\sqrt{s_{\mathrm{NN}}}$ dependence of the heavy-ion collision interaction rates of various facilities. Collider and FXT experiments are drawn as blue and red markers, respectively. There are several accelerators under construction or nearly ready for running. NICA ($\sqrt{s_{\mathrm{NN}}}$ = 4–10 GeV), FAIR ($\sqrt{s_{\mathrm{NN}}}$ = 2–5 GeV) and HIAF focus on the relatively low energies and have much higher collision rates compared to RHIC BES. Related measurements can be done using the new data collected by these future experiments. The opportunity will help us explore the QCD phase structure in the high-baryon-density region.

Bibliography

[1] Cush. Standard Model of Elementary Particles[EB/OL]. https://commons.wikimedia.org/wiki/File:Standard_Model_of_Elementary_Particles.svg.

[2] AAD G, et al. Observation of a new particle in the search for the Standard Model Higgs boson with the ATLAS detector at the LHC[J/OL]. Phys. Lett. B, 2012, 716: 1-29. arXiv: `1207.7214 [hep-ex]`. DOI: 10.1016/j.physletb.2012.08.020.

[3] CHATRCHYAN S, et al. Observation of a New Boson at a Mass of 125 GeV with the CMS Experiment at the LHC[J/OL]. Phys. Lett. B, 2012, 716: 30-61. arXiv: `1207.7235 [hep-ex]`. DOI: 10.1016/j.physletb.2012.08.021.

[4] GROSS D J, WILCZEK F. Ultraviolet Behavior of Nonabelian Gauge Theories[J/OL]. Phys. Rev. Lett., 1973, 30: 1343-1346. DOI: 10.1103/PhysRevLett.30.1343.

[5] POLITZER H D. Reliable Perturbative Results for Strong Interactions?[J/OL]. Phys. Rev. Lett., 1973, 30: 1346-1349. DOI: 10.1103/PhysRevLett.30.1346.

[6] GROSS D J, WILCZEK F. Asymptotically Free Gauge Theories - I[J/OL]. Phys. Rev. D, 1973, 8: 3633-3652. DOI: 10.1103/PhysRevD.8.3633.

[7] BETHKE S. Experimental tests of asymptotic freedom[J/OL]. Prog. Part. Nucl. Phys., 2007, 58: 351-386. arXiv: hep-ex/0606035. DOI: 10.1016/j.ppnp.2006.06.001.

[8] NAVAS S, et al. Review of particle physics[J/OL]. Phys. Rev. D, 2024, 110(3): 030001. DOI: 10.1103/PhysRevD.110.030001.

[9] MOHANTY B, XU N. QCD Critical Point and High Baryon Density Matter[C/OL]// Criticality in QCD and the Hadron Resonance Gas. 2021. arXiv: `2101.09210 [nucl-ex]`.

[10] FUKUSHIMA K, HATSUDA T. The phase diagram of dense QCD[J/OL]. Rept. Prog. Phys., 2011, 74: 014001. arXiv: `1005.4814 [hep-ph]`. DOI: 10.1088/0034-4885/74/1/014001.

[11] Particle Data Group. History of the Universe[EB/OL]. https://particleadventure.org/history-universe.html.

[12] BASS S A, GYULASSY M, STOECKER H, et al. Signatures of quark gluon plasma formation in high-energy heavy ion collisions: A Critical review[J/OL]. J. Phys. G, 1999, 25: R1-R57. arXiv: hep-ph/9810281. DOI: 10.1088/0954-3899/25/3/013.

[13] HEINZ U W, JACOB M. Evidence for a new state of matter: An Assessment of the results from the CERN lead beam program[J/OL]. 2000. arXiv: nucl-th/0002042.

[14] ARSENE I, et al. Quark gluon plasma and color glass condensate at RHIC? The Perspective from the BRAHMS experiment[J/OL]. Nucl. Phys. A, 2005, 757: 1-27. arXiv: nucl-ex/04

10020. DOI: 10.1016/j.nuclphysa.2005.02.130.

[15] BACK B B, et al. The PHOBOS perspective on discoveries at RHIC[J/OL]. Nucl. Phys. A, 2005, 757: 28-101. arXiv: nucl-ex/0410022. DOI: 10.1016/j.nuclphysa.2005.03.084.

[16] ADAMS J, et al. Experimental and theoretical challenges in the search for the quark gluon plasma: The STAR Collaboration's critical assessment of the evidence from RHIC collisions [J/OL]. Nucl. Phys. A, 2005, 757: 102-183. arXiv: nucl-ex/0501009. DOI: 10.1016/j.nuclphysa.2005.03.085.

[17] ADCOX K, et al. Formation of dense partonic matter in relativistic nucleus-nucleus collisions at RHIC: Experimental evaluation by the PHENIX collaboration[J/OL]. Nucl. Phys. A, 2005, 757: 184-283. arXiv: nucl-ex/0410003. DOI: 10.1016/j.nuclphysa.2005.03.086.

[18] GYULASSY M, MCLERRAN L. New forms of QCD matter discovered at RHIC[J/OL]. Nucl. Phys. A, 2005, 750: 30-63. arXiv: nucl-th/0405013. DOI: 10.1016/j.nuclphysa.2004.10.034.

[19] ROMATSCHKE P, ROMATSCHKE U. Viscosity Information from Relativistic Nuclear Collisions: How Perfect is the Fluid Observed at RHIC?[J/OL]. Phys. Rev. Lett., 2007, 99: 172301. arXiv: 0706.1522 `[nucl-th]`. DOI: 10.1103/PhysRevLett.99.172301.

[20] AKIBA Y, et al. The Hot QCD White Paper: Exploring the Phases of QCD at RHIC and the LHC[J/OL]. 2015. arXiv: 1502.02730 `[nucl-ex]`.

[21] WILSON K G. Confinement of Quarks[J/OL]. Phys. Rev. D, 1974, 10: 2445-2459. DOI: 10.1103/PhysRevD.10.2445.

[22] AOKI Y, ENDRODI G, FODOR Z, et al. The Order of the quantum chromodynamics transition predicted by the standard model of particle physics[J/OL]. Nature, 2006, 443: 675-678. arXiv: hep-lat/0611014. DOI: 10.1038/nature05120.

[23] BORSANYI S, FODOR Z, HOELBLING C, et al. Is there still any T_c mystery in lattice QCD? Results with physical masses in the continuum limit III[J/OL]. JHEP, 2010, 09: 073. arXiv: 1005.3508 `[hep-lat]`. DOI: 10.1007/JHEP09(2010)073.

[24] GUPTA S, LUO X, MOHANTY B, et al. Scale for the Phase Diagram of Quantum Chromodynamics[J/OL]. Science, 2011, 332: 1525-1528. arXiv: 1105.3934 `[hep-ph]`. DOI: 10.1126/science.1204621.

[25] BORSANYI S, FODOR Z, HOELBLING C, et al. Full result for the QCD equation of state with 2+1 flavors[J/OL]. Phys. Lett. B, 2014, 730: 99-104. arXiv: 1309.5258 `[hep-lat]`. DOI: 10.1016/j.physletb.2014.01.007.

[26] BAZAVOV A, et al. Chiral crossover in QCD at zero and non-zero chemical potentials [J/OL]. Phys. Lett. B, 2019, 795: 15-21. arXiv: 1812.08235 `[hep-lat]`. DOI: 10.1016/j.physletb.2019.05.013.

[27] ALFORD M G, RAJAGOPAL K, WILCZEK F. QCD at finite baryon density: Nucleon droplets and color superconductivity[J/OL]. Phys. Lett. B, 1998, 422: 247-256. arXiv: hep-ph/9711395. DOI: 10.1016/S0370-2693(98)00051-3.

[28] HALASZ A M, JACKSON A D, SHROCK R E, et al. On the phase diagram of QCD[J/OL]. Phys. Rev. D, 1998, 58: 096007. arXiv: hep-ph/9804290. DOI: 10.1103/PhysRevD.58.096007.

[29] De FORCRAND P, PHILIPSEN O. The QCD phase diagram for small densities from imaginary chemical potential[J/OL]. Nucl. Phys. B, 2002, 642: 290-306. arXiv: hep-lat/0205016. DOI: 10.1016/S0550-3213(02)00626-0.

[30] ENDRODI G, FODOR Z, KATZ S D, et al. The QCD phase diagram at nonzero quark density[J/OL]. JHEP, 2011, 04: 001. arXiv: 1102.1356 [hep-lat]. DOI: 10.1007/JHEP04(2011)001.

[31] FODOR Z, KATZ S D. Critical point of QCD at finite T and μ, lattice results for physical quark masses[J/OL]. JHEP, 2004, 04: 050. arXiv: hep-lat/0402006. DOI: 10.1088/1126-6708/2004/04/050.

[32] EJIRI S. Canonical partition function and finite density phase transition in lattice QCD [J/OL]. Phys. Rev. D, 2008, 78: 074507. arXiv: 0804.3227 [hep-lat]. DOI: 10.1103/PhysRevD.78.074507.

[33] GAVAI R V, GUPTA S. Pressure and nonlinear susceptibilities in QCD at finite chemical potentials[J/OL]. Phys. Rev. D, 2003, 68: 034506. arXiv: hep-lat/0303013. DOI: 10.1103/PhysRevD.68.034506.

[34] PHILIPSEN O. Towards the chiral critical surface of QCD[J/OL]. Nucl. Phys. A, 2009, 830: 713C-716C. arXiv: 0907.4668 [hep-ph]. DOI: 10.1016/j.nuclphysa.2009.10.064.

[35] DATTA S, GAVAI R V, GUPTA S. Quark number susceptibilities and equation of state at finite chemical potential in staggered QCD with $N_t = 8$[J/OL]. Phys. Rev. D, 2017, 95(5): 054512. arXiv: 1612.06673 [hep-lat]. DOI: 10.1103/PhysRevD.95.054512.

[36] SCAVENIUS O, MOCSY A, MISHUSTIN I N, et al. Chiral phase transition within effective models with constituent quarks[J/OL]. Phys. Rev. C, 2001, 64: 045202. arXiv: nucl-th/0007030. DOI: 10.1103/PhysRevC.64.045202.

[37] XU K, LI Z, HUANG M. QCD critical end point from a realistic PNJL model[J/OL]. EPJ Web Conf., 2018, 192: 00019. arXiv: 1810.03524 [hep-ph]. DOI: 10.1051/epjconf/201819200019.

[38] ISSERSTEDT P, BUBALLA M, FISCHER C S, et al. Baryon number fluctuations in the QCD phase diagram from Dyson-Schwinger equations[J/OL]. Phys. Rev. D, 2019, 100(7): 074011. arXiv: 1906.11644 [hep-ph]. DOI: 10.1103/PhysRevD.100.074011.

[39] FU W J, PAWLOWSKI J M, RENNECKE F. QCD phase structure at finite temperature and density[J/OL]. Phys. Rev. D, 2020, 101(5): 054032. arXiv: 1909.02991 `[hep-ph]`. DOI: 10.1103/PhysRevD.101.054032.

[40] PANDAV A, MALLICK D, MOHANTY B. Search for the QCD critical point in high energy nuclear collisions[J/OL]. Prog. Part. Nucl. Phys., 2022, 125: 103960. arXiv: 2203.07817 `[nucl-ex]`. DOI: 10.1016/j.ppnp.2022.103960.

[41] SHEN C. Sketch of relativistic heavy-ion collisions[EB/OL]. https://u.osu.edu/vishnu/2014/08/06/sketch-of-relativistic-heavy-ion-collisions/.

[42] CITRON Z, et al. Report from Working Group 5: Future physics opportunities for high-density QCD at the LHC with heavy-ion and proton beams[J/OL]. CERN Yellow Rep. Monogr., 2019, 7: 1159-1410. arXiv: 1812.06772 `[hep-ph]`. DOI: 10.23731/CYRM-2019-007.1159.

[43] CLEYMANS J, OESCHLER H, REDLICH K, et al. Comparison of chemical freeze-out criteria in heavy-ion collisions[J/OL]. Phys. Rev. C, 2006, 73: 034905. arXiv: hep-ph/0511094. DOI: 10.1103/PhysRevC.73.034905.

[44] STEPHANOV M A, RAJAGOPAL K, SHURYAK E V. Event-by-event fluctuations in heavy ion collisions and the QCD critical point[J/OL]. Phys. Rev. D, 1999, 60: 114028. arXiv: hep-ph/9903292. DOI: 10.1103/PhysRevD.60.114028.

[45] ASAKAWA M, HEINZ U W, MULLER B. Fluctuation probes of quark deconfinement [J/OL]. Phys. Rev. Lett., 2000, 85: 2072-2075. arXiv: hep-ph/0003169. DOI: 10.1103/PhysRevLett.85.2072.

[46] JEON S, KOCH V. Event by event fluctuations[M/OL]//HWA R C, WANG X N. Quark-gluon plasma 3. 2004: 430-490. arXiv: hep-ph/0304012. DOI: 10.1142/9789812795533_0007.

[47] KOCH V. Hadronic Fluctuations and Correlations[M/OL]//STOCK R. Relativistic Heavy Ion Physics. 2010: 626-652. arXiv: 0810.2520 `[nucl-th]`. DOI: 10.1007/978-3-642-01539-7_20.

[48] STEPHANOV M A. Non-Gaussian fluctuations near the QCD critical point[J/OL]. Phys. Rev. Lett., 2009, 102: 032301. arXiv: 0809.3450 `[hep-ph]`. DOI: 10.1103/PhysRevLett.102.032301.

[49] CHENG M, et al. Baryon Number, Strangeness and Electric Charge Fluctuations in QCD at High Temperature[J/OL]. Phys. Rev. D, 2009, 79: 074505. arXiv: 0811.1006 `[hep-lat]`. DOI: 10.1103/PhysRevD.79.074505.

[50] ASAKAWA M, EJIRI S, KITAZAWA M. Third moments of conserved charges as probes of QCD phase structure[J/OL]. Phys. Rev. Lett., 2009, 103: 262301. arXiv: 0904.2089

`[nucl-th]`. DOI: 10.1103/PhysRevLett.103.262301.

[51] STEPHANOV M A. On the sign of kurtosis near the QCD critical point[J/OL]. Phys. Rev. Lett., 2011, 107: 052301. arXiv: 1104.1627 `[hep-ph]`. DOI: 10.1103/PhysRevLett.107.052301.

[52] BAZAVOV A, et al. Fluctuations and Correlations of net baryon number, electric charge, and strangeness: A comparison of lattice QCD results with the hadron resonance gas model [J/OL]. Phys. Rev. D, 2012, 86: 034509. arXiv: 1203.0784 `[hep-lat]`. DOI: 10.1103/PhysRevD.86.034509.

[53] MORITA K, FRIMAN B, REDLICH K. Criticality of the net-baryon number probability distribution at finite density[J/OL]. Phys. Lett. B, 2015, 741: 178-183. arXiv: 1402.5982 `[hep-ph]`. DOI: 10.1016/j.physletb.2014.12.037.

[54] HATTA Y, STEPHANOV M A. Proton number fluctuation as a signal of the QCD critical endpoint[J/OL]. Phys. Rev. Lett., 2003, 91: 102003. arXiv: hep-ph/0302002. DOI: 10.1103/PhysRevLett.91.102003.

[55] ATHANASIOU C, RAJAGOPAL K, STEPHANOV M. Using Higher Moments of Fluctuations and their Ratios in the Search for the QCD Critical Point[J/OL]. Phys. Rev. D, 2010, 82: 074008. arXiv: 1006.4636 `[hep-ph]`. DOI: 10.1103/PhysRevD.82.074008.

[56] KITAZAWA M, ASAKAWA M. Revealing baryon number fluctuations from proton number fluctuations in relativistic heavy ion collisions[J/OL]. Phys. Rev. C, 2012, 85: 021901. arXiv: 1107.2755 `[nucl-th]`. DOI: 10.1103/PhysRevC.85.021901.

[57] KITAZAWA M, ASAKAWA M. Relation between baryon number fluctuations and experimentally observed proton number fluctuations in relativistic heavy ion collisions[J/OL]. Phys. Rev. C, 2012, 86: 024904. arXiv: 1205.3292 `[nucl-th]`. DOI: 10.1103/PhysRevC.86.024904.

[58] HE S, LUO X, NARA Y, et al. Effects of Nuclear Potential on the Cumulants of Net-Proton and Net-Baryon Multiplicity Distributions in Au+Au Collisions at $\sqrt{s_{\mathrm{NN}}} = 5\,\mathrm{GeV}$[J/OL]. Phys. Lett. B, 2016, 762: 296-300. arXiv: 1607.06376 `[nucl-ex]`. DOI: 10.1016/j.physletb.2016.09.053.

[59] HE S, LUO X. Proton Cumulants and Correlation Functions in Au + Au Collisions at $\sqrt{s_{\mathrm{NN}}}$ = 7.7–200 GeV from UrQMD Model[J/OL]. Phys. Lett. B, 2017, 774: 623-629. arXiv: 1704.00423 `[nucl-ex]`. DOI: 10.1016/j.physletb.2017.10.030.

[60] GAVAI R V, GUPTA S. Lattice QCD predictions for shapes of event distributions along the freezeout curve in heavy-ion collisions[J/OL]. Phys. Lett. B, 2011, 696: 459-463. arXiv: 1001.3796 `[hep-lat]`. DOI: 10.1016/j.physletb.2011.01.006.

[61] DING H T, KARSCH F, MUKHERJEE S. Thermodynamics of strong-interaction matter

from Lattice QCD[J/OL]. Int. J. Mod. Phys. E, 2015, 24(10): 1530007. arXiv: 1504.05274 [hep-lat]. DOI: 10.1142/S0218301315300076.

[62] BOWMAN E S, KAPUSTA J I. Critical Points in the Linear Sigma Model with Quarks [J/OL]. Phys. Rev. C, 2009, 79: 015202. arXiv: 0810.0042 [nucl-th]. DOI: 10.1103/PhysRevC.79.015202.

[63] BJORKEN J D. Highly Relativistic Nucleus-Nucleus Collisions: The Central Rapidity Region[J/OL]. Phys. Rev. D, 1983, 27: 140-151. DOI: 10.1103/PhysRevD.27.140.

[64] LING B, STEPHANOV M A. Acceptance dependence of fluctuation measures near the QCD critical point[J/OL]. Phys. Rev. C, 2016, 93(3): 034915. arXiv: 1512.09125 [nucl-th]. DOI: 10.1103/PhysRevC.93.034915.

[65] BZDAK A, KOCH V, STRODTHOFF N. Cumulants and correlation functions versus the QCD phase diagram[J/OL]. Phys. Rev. C, 2017, 95(5): 054906. arXiv: 1607.07375 [nucl-th]. DOI: 10.1103/PhysRevC.95.054906.

[66] STEPHANOV M. QCD Critical Point and Hydrodynamic Fluctuations in Relativistic Fluids [J/OL]. Acta Phys. Polon. B, 2024, 55(5): 5-A4. arXiv: 2403.03255 [nucl-th]. DOI: 10.5506/APhysPolB.55.5-A4.

[67] MUKHERJEE S, VENUGOPALAN R, YIN Y. Universal off-equilibrium scaling of critical cumulants in the QCD phase diagram[J/OL]. Phys. Rev. Lett., 2016, 117(22): 222301. arXiv: 1605.09341 [hep-ph]. DOI: 10.1103/PhysRevLett.117.222301.

[68] ASAKAWA M, KITAZAWA M, MÜLLER B. Issues with the search for critical point in QCD with relativistic heavy ion collisions[J/OL]. Phys. Rev. C, 2020, 101(3): 034913. arXiv: 1912.05840 [nucl-th]. DOI: 10.1103/PhysRevC.101.034913.

[69] RAJAGOPAL K, RIDGWAY G, WELLER R, et al. Understanding the out-of-equilibrium dynamics near a critical point in the QCD phase diagram[J/OL]. Phys. Rev. D, 2020, 102(9): 094025. arXiv: 1908.08539 [hep-ph]. DOI: 10.1103/PhysRevD.102.094025.

[70] PALHARES L F, FRAGA E S, KODAMA T. Finite-size effects and signatures of the QCD critical endpoint[J/OL]. J. Phys. G, 2010, 37: 094031. DOI: 10.1088/0954-3899/37/9/094031.

[71] PAN Z, CUI Z F, CHANG C H, et al. Finite-volume effects on phase transition in the Polyakov-loop extended Nambu–Jona-Lasinio model with a chiral chemical potential [J/OL]. Int. J. Mod. Phys. A, 2017, 32(13): 1750067. arXiv: 1611.07370 [hep-ph]. DOI: 10.1142/S0217751X17500671.

[72] STEPHANOV M A. Evolution of fluctuations near QCD critical point[J/OL]. Phys. Rev. D, 2010, 81: 054012. arXiv: 0911.1772 [hep-ph]. DOI: 10.1103/PhysRevD.81.054012.

[73] NAHRGANG M, BLUHM M, SCHAEFER T, et al. Diffusive dynamics of critical fluc-

tuations near the QCD critical point[J/OL]. Phys. Rev. D, 2019, 99(11): 116015. arXiv: 1804.05728 `[nucl-th]`. DOI: 10.1103/PhysRevD.99.116015.

[74] ZHANG Y, HE S, LIU H, et al. Effects of resonance weak decay and hadronic rescattering on the proton number fluctuations in Au+Au collisions at $\sqrt{s_{\mathrm{NN}}} = 5$ from a microscopic hadronic transport (JAM) model[J/OL]. Phys. Rev. C, 2020, 101(3): 034909. arXiv: 1905.01095 `[nucl-ex]`. DOI: 10.1103/PhysRevC.101.034909.

[75] NAHRGANG M, BLUHM M, ALBA P, et al. Impact of resonance regeneration and decay on the net-proton fluctuations in a hadron resonance gas[J/OL]. Eur. Phys. J. C, 2015, 75(12): 573. arXiv: 1402.1238 `[hep-ph]`. DOI: 10.1140/epjc/s10052-015-3775-0.

[76] BLUHM M, NAHRGANG M, BASS S A, et al. Impact of resonance decays on critical point signals in net-proton fluctuations[J/OL]. Eur. Phys. J. C, 2017, 77(4): 210. arXiv: 1612.03889 `[nucl-th]`. DOI: 10.1140/epjc/s10052-017-4771-3.

[77] FU J H. Higher moments of multiplicity fluctuations in a hadron-resonance gas with exact conservation laws[J/OL]. Phys. Rev. C, 2017, 96(3): 034905. arXiv: 1610.07138 `[nucl-th]`. DOI: 10.1103/PhysRevC.96.034905.

[78] PRUNEAU C A. Role of baryon number conservation in measurements of fluctuations [J/OL]. Phys. Rev. C, 2019, 100(3): 034905. arXiv: 1903.04591 `[nucl-th]`. DOI: 10.1103/PhysRevC.100.034905.

[79] BAZAVOV A, et al. Skewness, kurtosis, and the fifth and sixth order cumulants of net baryon-number distributions from lattice QCD confront high-statistics STAR data[J/OL]. Phys. Rev. D, 2020, 101(7): 074502. arXiv: 2001.08530 `[hep-lat]`. DOI: 10.1103/PhysRevD.101.074502.

[80] FU W J, LUO X, PAWLOWSKI J M, et al. Hyper-order baryon number fluctuations at finite temperature and density[J/OL]. Phys. Rev. D, 2021, 104(9): 094047. arXiv: 2101.06035 `[hep-ph]`. DOI: 10.1103/PhysRevD.104.094047.

[81] NONAKA T. Measurement of the Sixth-Order Cumulant of Net-Proton Distributions in Au+Au Collisions from the STAR Experiment[J/OL]. Nucl. Phys. A, 2021, 1005: 121882. arXiv: 2002.12505 `[nucl-ex]`. DOI: 10.1016/j.nuclphysa.2020.121882.

[82] PANDAV A. Measurement of cumulants of conserved charge multiplicity distributions in Au+Au collisions from the STAR experiment[J/OL]. Nucl. Phys. A, 2021, 1005: 121936. arXiv: 2003.12503 `[nucl-ex]`. DOI: 10.1016/j.nuclphysa.2020.121936.

[83] ADAM J, et al. Nonmonotonic Energy Dependence of Net-Proton Number Fluctuations [J/OL]. Phys. Rev. Lett., 2021, 126(9): 092301. arXiv: 2001.02852 `[nucl-ex]`. DOI: 10.1103/PhysRevLett.126.092301.

[84] ABDALLAH M, et al. Measurement of the Sixth-Order Cumulant of Net-Proton Multiplic-

ity Distributions in Au+Au Collisions at $\sqrt{s_{NN}} = 27$, 54.4, and 200 GeV at RHIC[J/OL]. Phys. Rev. Lett., 2021, 127(26): 262301. arXiv: 2105.14698 `[nucl-ex]`. DOI: 10.1103/PhysRevLett.127.262301.

[85] BRAUN-MUNZINGER P, REDLICH K, STACHEL J. Particle production in heavy ion collisions[J/OL]. 2003: 491-599. arXiv: nucl-th/0304013. DOI: 10.1142/9789812795533_0008.

[86] ANDRONIC A, BRAUN-MUNZINGER P, STACHEL J. Hadron production in central nucleus-nucleus collisions at chemical freeze-out[J/OL]. Nucl. Phys. A, 2006, 772: 167-199. arXiv: nucl-th/0511071. DOI: 10.1016/j.nuclphysa.2006.03.012.

[87] BASS S A, et al. Microscopic models for ultrarelativistic heavy ion collisions[J/OL]. Prog. Part. Nucl. Phys., 1998, 41: 255-369. arXiv: nucl-th/9803035. DOI: 10.1016/S0146-6410(98)00058-1.

[88] BLEICHER M, et al. Relativistic hadron hadron collisions in the ultrarelativistic quantum molecular dynamics model[J/OL]. J. Phys. G, 1999, 25: 1859-1896. arXiv: hep-ph/9909407. DOI: 10.1088/0954-3899/25/9/308.

[89] PETERSEN H, STEINHEIMER J, BURAU G, et al. A Fully Integrated Transport Approach to Heavy Ion Reactions with an Intermediate Hydrodynamic Stage[J/OL]. Phys. Rev. C, 2008, 78: 044901. arXiv: 0806.1695 `[nucl-th]`. DOI: 10.1103/PhysRevC.78.044901.

[90] KARSCH F, REDLICH K. Probing freeze-out conditions in heavy ion collisions with moments of charge fluctuations[J/OL]. Phys. Lett. B, 2011, 695: 136-142. arXiv: 1007.2581 `[hep-ph]`. DOI: 10.1016/j.physletb.2010.10.046.

[91] FU J. Higher moments of net-proton multiplicity distributions in heavy ion collisions at chemical freeze-out[J/OL]. Phys. Lett. B, 2013, 722: 144-150. DOI: 10.1016/j.physletb.2013.04.018.

[92] BRAUN-MUNZINGER P, FRIMAN B, KARSCH F, et al. Net-proton probability distribution in heavy ion collisions[J/OL]. Phys. Rev. C, 2011, 84: 064911. arXiv: 1107.4267 `[hep-ph]`. DOI: 10.1103/PhysRevC.84.064911.

[93] GARG P, MISHRA D K, NETRAKANTI P K, et al. Conserved number fluctuations in a hadron resonance gas model[J/OL]. Phys. Lett. B, 2013, 726: 691-696. arXiv: 1304.7133 `[nucl-ex]`. DOI: 10.1016/j.physletb.2013.09.019.

[94] BRAUN-MUNZINGER P, FRIMAN B, REDLICH K, et al. Relativistic nuclear collisions: Establishing a non-critical baseline for fluctuation measurements[J/OL]. Nucl. Phys. A, 2021, 1008: 122141. arXiv: 2007.02463 `[nucl-th]`. DOI: 10.1016/j.nuclphysa.2021.122141.

[95] HERMANS R. Negative and positive skew diagrams (English)[EB/OL]. https://commons

.wikimedia.org/wiki/File:Negative_and_positive_skew_diagrams_(English).svg.

[96] MarkSweep, Andel. Standard symmetric pdfs[EB / OL]. https://commons.wikimedia.org/wiki/File:Standard_symmetric_pdfs.svg.

[97] STAR. Studying the Phase Diagram of QCD Matter at RHIC[J / OL]. STAR Note, SN0598. https://drupal.star.bnl.gov/STAR/starnotes/public/sn0598.

[98] ABDALLAH M, et al. Cumulants and correlation functions of net-proton, proton, and antiproton multiplicity distributions in Au+Au collisions at energies available at the BNL Relativistic Heavy Ion Collider[J / OL]. Phys. Rev. C, 2021, 104(2): 024902. arXiv: 2101.12413 `[nucl-ex]`. DOI: 10.1103/PhysRevC.104.024902.

[99] ABDALLAH M S, et al. Measurements of Proton High Order Cumulants in $\sqrt{s_{NN}} = 3$ GeV Au+Au Collisions and Implications for the QCD Critical Point[J / OL]. Phys. Rev. Lett., 2022, 128(20): 202303. arXiv: 2112.00240 `[nucl-ex]`. DOI: 10.1103/PhysRevLett.128.202303.

[100] ABDALLAH M, et al. Higher-order cumulants and correlation functions of proton multiplicity distributions in $\sqrt{s_{NN}} = 3$ GeV Au+Au collisions at the RHIC STAR experiment [J / OL]. Phys. Rev. C, 2023, 107(2): 024908. arXiv: 2209.11940 `[nucl-ex]`. DOI: 10.1103/PhysRevC.107.024908.

[101] ADAMCZEWSKI-MUSCH J, et al. Proton-number fluctuations in $\sqrt{s_{NN}}$ =2.4 GeV Au + Au collisions studied with the High-Acceptance DiElectron Spectrometer (HADES)[J / OL]. Phys. Rev. C, 2020, 102(2): 024914. arXiv: 2002.08701 `[nucl-ex]`. DOI: 10.1103/PhysRevC.102.024914.

[102] ABOONA B, et al. Beam Energy Dependence of Fifth and Sixth-Order Net-proton Number Fluctuations in Au+Au Collisions at RHIC[J / OL]. Phys. Rev. Lett., 2023, 130(8): 082301. arXiv: 2207.09837 `[nucl-ex]`. DOI: 10.1103/PhysRevLett.130.082301.

[103] STAR. The STAR Beam Use Request for Run-23-25[J / OL]. STAR Note, SN0793. https://drupal.star.bnl.gov/STAR/starnotes/public/SN0793.

[104] STAR. Technical Design Report for the iTPC Upgrade[J / OL]. STAR Note, SN0644. https://drupal.star.bnl.gov/STAR/starnotes/public/sn0644.

[105] STAR, CBM eTOF Group. Physics Program for the STAR/CBM eTOF Upgrade[J / OL]. 2016. arXiv: 1609.05102 `[nucl-ex]`.

[106] ADAMS J, et al. The STAR Event Plane Detector[J / OL]. Nucl. Instrum. Meth. A, 2020, 968: 163970. arXiv: 1912.05243 `[physics.ins-det]`. DOI: 10.1016/j.nima.2020.163970.

[107] HARRISON M, PEGGS S G, ROSER T. The RHIC accelerator[J / OL]. Ann. Rev. Nucl. Part. Sci., 2002, 52: 425-469. DOI: 10.1146/annurev.nucl.52.050102.090650.

[108] HARRISON M, LUDLAM T, OZAKI S. RHIC project overview[J/OL]. Nucl. Instrum. Meth. A, 2003, 499: 235-244. DOI: 10.1016/S0168-9002(02)01937-X.

[109] Brookhaven National Laboratory. RHIC Run 24: Science Goals and Accelerator Advances [EB/OL]. https://www.bnl.gov/newsroom/news.php?a=221826.

[110] ADAMCZYK M, et al. The BRAHMS experiment at RHIC[J/OL]. Nucl. Instrum. Meth. A, 2003, 499: 437-468. DOI: 10.1016/S0168-9002(02)01949-6.

[111] ACKERMANN K H, et al. STAR detector overview[J/OL]. Nucl. Instrum. Meth. A, 2003, 499: 624-632. DOI: 10.1016/S0168-9002(02)01960-5.

[112] ADCOX K, et al. PHENIX detector overview[J/OL]. Nucl. Instrum. Meth. A, 2003, 499: 469-479. DOI: 10.1016/S0168-9002(02)01950-2.

[113] BACK B B, et al. The PHOBOS detector at RHIC[J/OL]. Nucl. Instrum. Meth. A, 2003, 499: 603-623. DOI: 10.1016/S0168-9002(02)01959-9.

[114] O'BRIEN E. The construction of the sPHENIX detector and status of its commissioning [J/OL]. EPJ Web Conf., 2024, 296: 01007. DOI: 10.1051/epjconf/202429601007.

[115] LI-JUAN R, ZHANG-BU X, CHI Y, et al. Global polarization of hyperons and spin alignment of vector mesons in quark matters[J/OL]. Acta Phys. Sin., 2023, 72(11): 112401. DOI: 10.7498/aps.72.20230496.

[116] ABDALLAH M, et al. Search for the chiral magnetic effect with isobar collisions at $\sqrt{s_{NN}}$ = 200 GeV by the STAR Collaboration at the BNL Relativistic Heavy Ion Collider[J/OL]. Phys. Rev. C, 2022, 105(1): 014901. arXiv: 2109.00131 `[nucl-ex]`. DOI: 10.1103/PhysRevC.105.014901.

[117] ALEKSEEV I, et al. Polarized proton collider at RHIC[J/OL]. Nucl. Instrum. Meth. A, 2003, 499: 392-414. DOI: 10.1016/S0168-9002(02)01946-0.

[118] STAR. STAR Images[EB/OL]. https://drupal.star.bnl.gov/STAR/public/img.

[119] ANDERSON M, et al. The STAR time projection chamber: a unique tool for studying high multiplicity events at RHIC[J/OL]. Nucl. Instrum. Meth. A, 2003, 499: 659-678. arXiv: nucl-ex/0301015. DOI: 10.1016/S0168-9002(02)01964-2.

[120] STAR. Proposal for a Large Area Time of Flight System for STAR[J/OL]. STAR Note, SN0621. https://drupal.star.bnl.gov/STAR/starnotes/public/sn0621.

[121] BEDDO M, et al. The STAR barrel electromagnetic calorimeter[J/OL]. Nucl. Instrum. Meth. A, 2003, 499: 725-739. DOI: 10.1016/S0168-9002(02)01970-8.

[122] BERGSMA F, et al. The STAR detector magnet subsystem[J/OL]. Nucl. Instrum. Meth. A, 2003, 499: 633-639. DOI: 10.1016/S0168-9002(02)01961-7.

[123] RUAN L, et al. Perspectives of a Midrapidity Dimuon Program at RHIC: A Novel and Compact Muon Telescope Detector[J/OL]. J. Phys. G, 2009, 36: 095001. arXiv: 0904.377

4 [nucl-ex]. DOI: 10.1088/0954-3899/36/9/095001.

[124] ALLGOWER C E, et al. The STAR endcap electromagnetic calorimeter[J/OL]. Nucl. Instrum. Meth. A, 2003, 499: 740-750. DOI: 10.1016/S0168-9002(02)01971-X.

[125] WHITTEN C A. The beam-beam counter: A local polarimeter at STAR[J/OL]. AIP Conf. Proc., 2008, 980(1): 390-396. DOI: 10.1063/1.2888113.

[126] LLOPE W J, et al. The STAR Vertex Position Detector[J/OL]. Nucl. Instrum. Meth. A, 2014, 759: 23-28. arXiv: 1403.6855 [physics.ins-det]. DOI: 10.1016/j.nima.2014.04.080.

[127] ADLER C, DENISOV A, GARCIA E, et al. The RHIC zero degree calorimeter[J/OL]. Nucl. Instrum. Meth. A, 2001, 470: 488-499. arXiv: nucl-ex/0008005. DOI: 10.1016/S0168-9002(01)00627-1.

[128] BICHSEL H. A method to improve tracking and particle identification in TPCs and silicon detectors[J/OL]. Nucl. Instrum. Meth. A, 2006, 562: 154-197. DOI: 10.1016/j.nima.2006.03.009.

[129] ADAMCZYK L, et al. Bulk Properties of the Medium Produced in Relativistic Heavy-Ion Collisions from the Beam Energy Scan Program[J/OL]. Phys. Rev. C, 2017, 96(4): 044904. arXiv: 1701.07065 [nucl-ex]. DOI: 10.1103/PhysRevC.96.044904.

[130] YANG Y. The STAR detector upgrades for the BES II and beyond physics program[J/OL]. Nucl. Phys. A, 2021, 1005: 121758. DOI: 10.1016/j.nuclphysa.2020.121758.

[131] LLOPE W J. The large-area time-of-flight (TOF) upgrade for the STAR detector[J/OL]. AIP Conf. Proc., 2009, 1099(1): 778-781. DOI: 10.1063/1.3120153.

[132] DONG X. The Time-Of-Flight Detector for RHIC/STAR and The Related Physics[J/OL]. AIP Conf. Proc., 2006, 865(1): 332-337. DOI: 10.1063/1.2398870.

[133] LLOPE W J, et al. The TOFp / pVPD time-of-flight system for STAR[J/OL]. Nucl. Instrum. Meth. A, 2004, 522: 252-273. arXiv: nucl-ex/0308022. DOI: 10.1016/j.nima.2003.11.414.

[134] PANDAV A. Precision Measurement of Net-proton Number Fluctuations in Au+Au Collisions at RHIC[Z]. Presented at the 15th Workshop on Critical Point and Onset of Deconfinement. Berkeley, California, USA, 2024.

[135] ZHANG Y. Precision Measurement of Net-proton Number Fluctuations in Au+Au Collisions at RHIC[Z]. Presented at the 21st International Conference on Strangeness in Quark Matter. Strasbourg, France, 2024.

[136] STAR. Bad Run QA[EB/OL]. https://github.com/star-bnl/star-sw/tree/main/StRoot/PWGTools/BadRunQA.

[137] MILLER M L, REYGERS K, SANDERS S J, et al. Glauber modeling in high energy nuclear collisions[J/OL]. Ann. Rev. Nucl. Part. Sci., 2007, 57: 205-243. arXiv: nucl-ex/0701025.

DOI: 10.1146/annurev.nucl.57.090506.123020.

[138] WOODS R D, SAXON D S. Diffuse Surface Optical Model for Nucleon-Nuclei Scattering [J/OL]. Phys. Rev., 1954, 95: 577-578. DOI: 10.1103/PhysRev.95.577.

[139] LUO X, XU J, MOHANTY B, et al. Volume fluctuation and auto-correlation effects in the moment analysis of net-proton multiplicity distributions in heavy-ion collisions[J/OL]. J. Phys. G, 2013, 40: 105104. arXiv: 1302.2332 `[nucl-ex]`. DOI: 10.1088/0954-3899/40/10/105104.

[140] CHATTERJEE A, ZHANG Y, ZENG J, et al. Effect of centrality selection on higher-order cumulants of net-proton multiplicity distributions in relativistic heavy-ion collisions[J/OL]. Phys. Rev. C, 2020, 101(3): 034902. arXiv: 1910.08004 `[nucl-ex]`. DOI: 10.1103/PhysRevC.101.034902.

[141] SUGIURA T, NONAKA T, ESUMI S. Volume fluctuation and multiplicity correlation in higher-order cumulants[J/OL]. Phys. Rev. C, 2019, 100(4): 044904. arXiv: 1903.02314 `[nucl-th]`. DOI: 10.1103/PhysRevC.100.044904.

[142] GARG P, MISHRA D K, NETRAKANTI P K, et al. Unfolding of event-by-event net-charge distributions in heavy-ion collision[J/OL]. J. Phys. G, 2013, 40: 055103. arXiv: 1211.2074 `[nucl-ex]`. DOI: 10.1088/0954-3899/40/5/055103.

[143] ESUMI S, NAKAGAWA K, NONAKA T. Reconstructing particle number distributions with convoluting volume fluctuations[J/OL]. Nucl. Instrum. Meth. A, 2021, 987: 164802. arXiv: 2002.11253 `[physics.data-an]`. DOI: 10.1016/j.nima.2020.164802.

[144] NONAKA T, KITAZAWA M, ESUMI S. More efficient formulas for efficiency correction of cumulants and effect of using averaged efficiency[J/OL]. Phys. Rev. C, 2017, 95(6): 064912. arXiv: 1702.07106 `[physics.data-an]`. DOI: 10.1103/PhysRevC.95.064912.

[145] KITAZAWA M, LUO X. Properties and uses of factorial cumulants in relativistic heavy-ion collisions[J/OL]. Phys. Rev. C, 2017, 96(2): 024910. arXiv: 1704.04909 `[nucl-th]`. DOI: 10.1103/PhysRevC.96.024910.

[146] LUO X, NONAKA T. Efficiency correction for cumulants of multiplicity distributions based on track-by-track efficiency[J/OL]. Phys. Rev. C, 2019, 99(4): 044917. arXiv: 1812.10303 `[physics.data-an]`. DOI: 10.1103/PhysRevC.99.044917.

[147] LUO X. Unified description of efficiency correction and error estimation for moments of conserved quantities in heavy-ion collisions[J/OL]. Phys. Rev. C, 2015, 91(3): 034907. arXiv: 1410.3914 `[physics.data-an]`. DOI: 10.1103/PhysRevC.94.059901.

[148] SI F, ZHANG Y, LUO X. Effect of non-uniform efficiency on higher-order cumulants in heavy-ion collisions *[J/OL]. Chin. Phys. C, 2021, 45(12): 124001. arXiv: 2105.13128

[physics.data-an]. DOI: 10.1088/1674-1137/ac24f6.

[149] HE S, LUO X. Event-by-Event Efficiency Fluctuations and Efficiency Correction for Cumulants of Superposed Multiplicity Distributions in Relativistic Heavy-ion Collision Experiments[J/OL]. Chin. Phys. C, 2018, 42(10): 104001. arXiv: 1802.02911 [physics.data-an]. DOI: 10.1088/1674-1137/42/10/104001.

[150] AGOSTINELLI S, et al. GEANT4–a simulation toolkit[J/OL]. Nucl. Instrum. Meth. A, 2003, 506: 250-303. DOI: 10.1016/S0168-9002(03)01368-8.

[151] ALLISON J, et al. Geant4 developments and applications[J/OL]. IEEE Trans. Nucl. Sci., 2006, 53: 270. DOI: 10.1109/TNS.2006.869826.

[152] ALLISON J, et al. Recent developments in Geant4[J/OL]. Nucl. Instrum. Meth. A, 2016, 835: 186-225. DOI: 10.1016/j.nima.2016.06.125.

[153] SI F, ZHANG Y. Statistical uncertainty estimation of higher-order cumulants with finite efficiency and its application in heavy-ion collisions[J/OL]. Phys. Rev. C, 2022, 105(2): 024907. arXiv: 2111.00238 [nucl-th]. DOI: 10.1103/PhysRevC.105.024907.

[154] STUART A, ORD J K. Kendall's Advanced Theory of Statistics, Volume 1: Distribution Theory[M]. 6th ed. London: Wiley, 1994.

[155] BARLOW R. Systematic errors: Facts and fictions[C/OL]//Conference on Advanced Statistical Techniques in Particle Physics. 2002: 134-144. arXiv: hep-ex/0207026.

[156] VOVCHENKO V, KOCH V, SHEN C. Proton number cumulants and correlation functions in Au-Au collisions at sNN=7.7–200 GeV from hydrodynamics[J/OL]. Phys. Rev. C, 2022, 105(1): 014904. arXiv: 2107.00163 [hep-ph]. DOI: 10.1103/PhysRevC.105.014904.

[157] BREWER J, MUKHERJEE S, RAJAGOPAL K, et al. Searching for the QCD critical point via the rapidity dependence of cumulants[J/OL]. Phys. Rev. C, 2018, 98(6): 061901. arXiv: 1804.10215 [hep-ph]. DOI: 10.1103/PhysRevC.98.061901.

[158] BREWER J. Searching for the QCD critical point via the rapidity dependence of cumulants [Z]. Presented at the 12th Workshop on Critical Point and Onset of Deconfinement. Corfu, Greece, 2018.

[159] FU W J, LUO X, PAWLOWSKI J M, et al. Ripples of the QCD Critical Point[J/OL]. 2023. arXiv: 2308.15508 [hep-ph].

[160] STAR. The STAR Beam Use Request for Run-21, Run-22 and data taking in 2023-25 [J/OL]. STAR Note, SN0755. https://drupal.star.bnl.gov/STAR/starnotes/public/sn0755.

[161] ABDULHAMID M, et al. Beam Energy Dependence of Triton Production and Yield Ratio ($N_t \times N_p/N_d^2$) in Au+Au Collisions at RHIC[J/OL]. Phys. Rev. Lett., 2023, 130: 202301. arXiv: 2209.08058 [nucl-ex]. DOI: 10.1103/PhysRevLett.130.202301.

[162] ABDULHAMID M, et al. Energy dependence of intermittency for charged hadrons in

Au+Au collisions at RHIC[J/OL]. Phys. Lett. B, 2023, 845: 138165. arXiv: 2301.11062 [nucl-ex]. DOI: 10.1016/j.physletb.2023.138165.

Appendix A Efficiency Correction Formulae for Hyper-Order Cumulants

Formulae of efficiency-corrected fifth- and sixth-order cumulants are expressed by [144]

$$\begin{aligned}
\left\langle Q^5_{(1,0)}\right\rangle_\mathrm{c} = {} & \left\langle q^5_{(1,1)}\right\rangle_\mathrm{c} + 10\left\langle q^3_{(1,1)}q_{(2,1)}\right\rangle_\mathrm{c} - 10\left\langle q^3_{(1,1)}q_{(2,2)}\right\rangle_\mathrm{c} + 10\left\langle q^2_{(1,1)}q_{(3,1)}\right\rangle_\mathrm{c} \\
& - 30\left\langle q^2_{(1,1)}q_{(3,2)}\right\rangle_\mathrm{c} + 20\left\langle q^2_{(1,1)}q_{(3,3)}\right\rangle_\mathrm{c} + 15\left\langle q^2_{(2,2)}q_{(1,1)}\right\rangle_\mathrm{c} \\
& + 15\left\langle q^2_{(2,1)}q_{(1,1)}\right\rangle_\mathrm{c} - 30\left\langle q_{(1,1)}q_{(2,1)}q_{(2,2)}\right\rangle_\mathrm{c} + 5\left\langle q_{(1,1)}q_{(4,1)}\right\rangle_\mathrm{c} \\
& - 35\left\langle q_{(1,1)}q_{(4,2)}\right\rangle_\mathrm{c} + 60\left\langle q_{(1,1)}q_{(4,3)}\right\rangle_\mathrm{c} - 30\left\langle q_{(1,1)}q_{(4,4)}\right\rangle_\mathrm{c} \\
& + 10\left\langle q_{(2,1)}q_{(3,1)}\right\rangle_\mathrm{c} - 30\left\langle q_{(2,1)}q_{(3,2)}\right\rangle_\mathrm{c} + 20\left\langle q_{(2,1)}q_{(3,3)}\right\rangle_\mathrm{c} \\
& - 10\left\langle q_{(2,2)}q_{(3,1)}\right\rangle_\mathrm{c} + 30\left\langle q_{(2,2)}q_{(3,2)}\right\rangle_\mathrm{c} - 20\left\langle q_{(2,2)}q_{(3,3)}\right\rangle_\mathrm{c} + \left\langle q_{(5,1)}\right\rangle_\mathrm{c} \\
& - 15\left\langle q_{(5,2)}\right\rangle_\mathrm{c} + 50\left\langle q_{(5,3)}\right\rangle_\mathrm{c} - 60\left\langle q_{(5,4)}\right\rangle_\mathrm{c} + 24\left\langle q_{(5,5)}\right\rangle_\mathrm{c},
\end{aligned} \tag{A.1}$$

$$\begin{aligned}
\left\langle Q^6_{(1,0)}\right\rangle_\mathrm{c} = {} & \left\langle q^6_{(1,1)}\right\rangle_\mathrm{c} + 15\left\langle q^4_{(1,1)}q_{(2,1)}\right\rangle_\mathrm{c} - 15\left\langle q^4_{(1,1)}q_{(2,2)}\right\rangle_\mathrm{c} + 20\left\langle q^3_{(1,1)}q_{(3,1)}\right\rangle_\mathrm{c} \\
& - 60\left\langle q^3_{(1,1)}q_{(3,2)}\right\rangle_\mathrm{c} + 40\left\langle q^3_{(1,1)}q_{(3,3)}\right\rangle_\mathrm{c} - 90\left\langle q^2_{(1,1)}q_{(2,2)}q_{(2,1)}\right\rangle_\mathrm{c} \\
& + 45\left\langle q^2_{(1,1)}q^2_{(2,1)}\right\rangle_\mathrm{c} + 45\left\langle q^2_{(1,1)}q^2_{(2,2)}\right\rangle_\mathrm{c} + 15\left\langle q^3_{(2,1)}\right\rangle_\mathrm{c} \\
& - 15\left\langle q^3_{(2,2)}\right\rangle_\mathrm{c} + 15\left\langle q^2_{(1,1)}q_{(4,1)}\right\rangle_\mathrm{c} - 105\left\langle q^2_{(1,1)}q_{(4,2)}\right\rangle_\mathrm{c} \\
& + 180\left\langle q^2_{(1,1)}q_{(4,3)}\right\rangle_\mathrm{c} - 90\left\langle q^2_{(1,1)}q_{(4,4)}\right\rangle_\mathrm{c} - 45\left\langle q^2_{(2,1)}q_{(2,2)}\right\rangle_\mathrm{c} \\
& + 45\left\langle q^2_{(2,2)}q_{(2,1)}\right\rangle_\mathrm{c} + 60\left\langle q_{(1,1)}q_{(2,1)}q_{(3,1)}\right\rangle_\mathrm{c} - 180\left\langle q_{(1,1)}q_{(2,1)}q_{(3,2)}\right\rangle_\mathrm{c} \\
& + 120\left\langle q_{(1,1)}q_{(2,1)}q_{(3,3)}\right\rangle_\mathrm{c} - 60\left\langle q_{(1,1)}q_{(2,2)}q_{(3,1)}\right\rangle_\mathrm{c} \\
& + 180\left\langle q_{(1,1)}q_{(2,2)}q_{(3,2)}\right\rangle_\mathrm{c} - 120\left\langle q_{(1,1)}q_{(2,2)}q_{(3,3)}\right\rangle_\mathrm{c} + 6\left\langle q_{(1,1)}q_{(5,1)}\right\rangle_\mathrm{c} \\
& - 90\left\langle q_{(1,1)}q_{(5,2)}\right\rangle_\mathrm{c} + 300\left\langle q_{(1,1)}q_{(5,3)}\right\rangle_\mathrm{c} - 360\left\langle q_{(1,1)}q_{(5,4)}\right\rangle_\mathrm{c} \\
& + 144\left\langle q_{(1,1)}q_{(5,5)}\right\rangle_\mathrm{c} + 15\left\langle q_{(2,1)}q_{(4,1)}\right\rangle_\mathrm{c} - 105\left\langle q_{(2,1)}q_{(4,2)}\right\rangle_\mathrm{c} \\
& + 180\left\langle q_{(2,1)}q_{(4,3)}\right\rangle_\mathrm{c} - 90\left\langle q_{(2,1)}q_{(4,4)}\right\rangle_\mathrm{c} - 15\left\langle q_{(2,2)}q_{(4,1)}\right\rangle_\mathrm{c} \\
& + 105\left\langle q_{(2,2)}q_{(4,2)}\right\rangle_\mathrm{c} - 180\left\langle q_{(2,2)}q_{(4,3)}\right\rangle_\mathrm{c} + 90\left\langle q_{(2,2)}q_{(4,4)}\right\rangle_\mathrm{c} \\
& + 10\left\langle q^2_{(3,1)}\right\rangle_\mathrm{c} - 60\left\langle q_{(3,1)}q_{(3,2)}\right\rangle_\mathrm{c} + 40\left\langle q_{(3,1)}q_{(3,3)}\right\rangle_\mathrm{c} + 90\left\langle q^2_{(3,2)}\right\rangle_\mathrm{c} \\
& - 120\left\langle q_{(3,2)}q_{(3,3)}\right\rangle_\mathrm{c} + 40\left\langle q^2_{(3,3)}\right\rangle_\mathrm{c} + \left\langle q_{(6,1)}\right\rangle_\mathrm{c} - 31\left\langle q_{(6,2)}\right\rangle_\mathrm{c} \\
& + 180\left\langle q_{(6,3)}\right\rangle_\mathrm{c} - 390\left\langle q_{(6,4)}\right\rangle_\mathrm{c} + 360\left\langle q_{(6,5)}\right\rangle_\mathrm{c} - 120\left\langle q_{(6,6)}\right\rangle_\mathrm{c}.
\end{aligned} \tag{A.2}$$

Appendix B Variances and Covariances of Estimated Cumulants

Here, we list some formulae for variances and covariances of estimated cumulants up to fourth order summarized in Reference [153] with P, Q, R, S, T and U representing stochastic variables and large n:

First-order cumulants:

$$n \cdot \mathrm{Cov}\left(\widehat{\langle P\rangle_\mathrm{c}}, \widehat{\langle Q\rangle_\mathrm{c}}\right) = \langle PQ\rangle_\mathrm{c}\,, \tag{B.1}$$

$$n \cdot \mathrm{Cov}\left(\widehat{\langle PQ\rangle_\mathrm{c}}, \widehat{\langle R\rangle_\mathrm{c}}\right) = \langle PQR\rangle_\mathrm{c}\,, \tag{B.2}$$

$$n \cdot \mathrm{Cov}\left(\widehat{\langle PQR\rangle_\mathrm{c}}, \widehat{\langle S\rangle_\mathrm{c}}\right) = \langle PQRS\rangle_\mathrm{c}\,, \tag{B.3}$$

$$n \cdot \mathrm{Cov}\left(\widehat{\langle PQRS\rangle_\mathrm{c}}, \widehat{\langle T\rangle_\mathrm{c}}\right) = \langle PQRST\rangle_\mathrm{c}\,. \tag{B.4}$$

Second-order cumulants:

$$n \cdot \mathrm{Cov}\left(\widehat{\langle PQ\rangle_\mathrm{c}}, \widehat{\langle RS\rangle_\mathrm{c}}\right) = \langle PQRS\rangle_\mathrm{c} + \langle PR\rangle_\mathrm{c}\langle QS\rangle_\mathrm{c} + \langle PS\rangle_\mathrm{c}\langle QR\rangle_\mathrm{c}\,, \tag{B.5}$$

$$\begin{aligned} n \cdot \mathrm{Cov}\left(\widehat{\langle PQR\rangle_\mathrm{c}}, \widehat{\langle ST\rangle_\mathrm{c}}\right) = {}& \langle PQRST\rangle_\mathrm{c} + \langle PQS\rangle_\mathrm{c}\langle RT\rangle_\mathrm{c} + \langle PQT\rangle_\mathrm{c}\langle RS\rangle_\mathrm{c} \\ & + \langle PRS\rangle_\mathrm{c}\langle QT\rangle_\mathrm{c} + \langle PRT\rangle_\mathrm{c}\langle QS\rangle_\mathrm{c} \\ & + \langle QRS\rangle_\mathrm{c}\langle PT\rangle_\mathrm{c} + \langle QRT\rangle_\mathrm{c}\langle PS\rangle_\mathrm{c}\,, \end{aligned} \tag{B.6}$$

$$\begin{aligned} n \cdot \mathrm{Cov}\left(\widehat{\langle PQRS\rangle_\mathrm{c}}, \widehat{\langle TU\rangle_\mathrm{c}}\right) = {}& \langle PQRSTU\rangle_\mathrm{c} + \langle PQRT\rangle_\mathrm{c}\langle SU\rangle_\mathrm{c} \\ & + \langle PQST\rangle_\mathrm{c}\langle RU\rangle_\mathrm{c} + \langle PRST\rangle_\mathrm{c}\langle QU\rangle_\mathrm{c} \\ & + \langle QRST\rangle_\mathrm{c}\langle PU\rangle_\mathrm{c} + \langle PQRU\rangle_\mathrm{c}\langle ST\rangle_\mathrm{c} \\ & + \langle PQSU\rangle_\mathrm{c}\langle RT\rangle_\mathrm{c} + \langle PRSU\rangle_\mathrm{c}\langle QT\rangle_\mathrm{c} \\ & + \langle QRSU\rangle_\mathrm{c}\langle PT\rangle_\mathrm{c} + \langle PQT\rangle_\mathrm{c}\langle RSU\rangle_\mathrm{c} \\ & + \langle PRT\rangle_\mathrm{c}\langle QSU\rangle_\mathrm{c} + \langle PST\rangle_\mathrm{c}\langle QRU\rangle_\mathrm{c} \\ & + \langle PQU\rangle_\mathrm{c}\langle RST\rangle_\mathrm{c} + \langle PRU\rangle_\mathrm{c}\langle QST\rangle_\mathrm{c} \\ & + \langle PSU\rangle_\mathrm{c}\langle QRT\rangle_\mathrm{c}\,. \end{aligned} \tag{B.7}$$

Third-order cumulants:

$$\begin{aligned} n \cdot \mathrm{Cov}\left(\widehat{\langle PQR\rangle_\mathrm{c}}, \widehat{\langle STU\rangle_\mathrm{c}}\right) = {}& \langle PQRSTU\rangle_\mathrm{c} + \langle PQST\rangle_\mathrm{c}\langle RU\rangle_\mathrm{c} \\ & + \langle PQSU\rangle_\mathrm{c}\langle RT\rangle_\mathrm{c} + \langle PQTU\rangle_\mathrm{c}\langle RS\rangle_\mathrm{c} \\ & + \langle PRST\rangle_\mathrm{c}\langle QU\rangle_\mathrm{c} + \langle PRSU\rangle_\mathrm{c}\langle QT\rangle_\mathrm{c} \\ & + \langle PRTU\rangle_\mathrm{c}\langle QS\rangle_\mathrm{c} + \langle QRST\rangle_\mathrm{c}\langle PU\rangle_\mathrm{c} \end{aligned}$$

$$\begin{aligned}
&+ \langle QRSU\rangle_\mathrm{c} \langle PT\rangle_\mathrm{c} + \langle QRTU\rangle_\mathrm{c} \langle PS\rangle_\mathrm{c} \\
&+ \langle PQS\rangle_\mathrm{c} \langle RTU\rangle_\mathrm{c} + \langle PQT\rangle_\mathrm{c} \langle RSU\rangle_\mathrm{c} \\
&+ \langle PQU\rangle_\mathrm{c} \langle RST\rangle_\mathrm{c} + \langle PRS\rangle_\mathrm{c} \langle QTU\rangle_\mathrm{c} \\
&+ \langle PRT\rangle_\mathrm{c} \langle QSU\rangle_\mathrm{c} + \langle PRU\rangle_\mathrm{c} \langle QST\rangle_\mathrm{c} \\
&+ \langle QRS\rangle_\mathrm{c} \langle PTU\rangle_\mathrm{c} + \langle QRT\rangle_\mathrm{c} \langle PSU\rangle_\mathrm{c} \\
&+ \langle QRU\rangle_\mathrm{c} \langle PST\rangle_\mathrm{c} + \langle PS\rangle_\mathrm{c} \langle QT\rangle_\mathrm{c} \langle RU\rangle_\mathrm{c} \\
&+ \langle PS\rangle_\mathrm{c} \langle QU\rangle_\mathrm{c} \langle RT\rangle_\mathrm{c} + \langle PT\rangle_\mathrm{c} \langle QS\rangle_\mathrm{c} \langle RU\rangle_\mathrm{c} \\
&+ \langle PT\rangle_\mathrm{c} \langle QU\rangle_\mathrm{c} \langle RS\rangle_\mathrm{c} + \langle PU\rangle_\mathrm{c} \langle QS\rangle_\mathrm{c} \langle RT\rangle_\mathrm{c} \\
&+ \langle PU\rangle_\mathrm{c} \langle QT\rangle_\mathrm{c} \langle RS\rangle_\mathrm{c} ,
\end{aligned} \tag{B.8}$$

$$\begin{aligned}
n \cdot \mathrm{Cov}\left(\widehat{\left\langle P^4\right\rangle_\mathrm{c}}, \widehat{\left\langle Q^3\right\rangle_\mathrm{c}}\right) = {}& \left\langle P^4 Q^3\right\rangle_\mathrm{c} + 12 \left\langle P^3 Q^2\right\rangle_\mathrm{c} \langle PQ\rangle_\mathrm{c} \\
&+ 12 \left\langle P^3 Q\right\rangle_\mathrm{c} \left\langle PQ^2\right\rangle_\mathrm{c} + 18 \left\langle P^2 Q^2\right\rangle_\mathrm{c} \left\langle P^2 Q\right\rangle_\mathrm{c} \\
&+ 36 \left\langle P^2 Q\right\rangle_\mathrm{c} \langle PQ\rangle_\mathrm{c}^2 ,
\end{aligned} \tag{B.9}$$

$$\begin{aligned}
n \cdot \mathrm{Cov}\left(\widehat{\left\langle P^4\right\rangle_\mathrm{c}}, \widehat{\left\langle P^2 Q\right\rangle_\mathrm{c}}\right) = {}& \left\langle P^6 Q\right\rangle_\mathrm{c} + 4 \left\langle P^5\right\rangle_\mathrm{c} \langle PQ\rangle_\mathrm{c} + 8 \left\langle P^4 Q\right\rangle_\mathrm{c} \left\langle P^2\right\rangle_\mathrm{c} \\
&+ 14 \left\langle P^4\right\rangle_\mathrm{c} \left\langle P^2 Q\right\rangle_\mathrm{c} + 16 \left\langle P^3 Q\right\rangle_\mathrm{c} \left\langle P^3\right\rangle_\mathrm{c} \\
&+ 24 \left\langle P^3\right\rangle_\mathrm{c} \left\langle P^2\right\rangle_\mathrm{c} \langle PQ\rangle_\mathrm{c} + 12 \left\langle P^2 Q\right\rangle_\mathrm{c} \left\langle P^2\right\rangle_\mathrm{c}^2 .
\end{aligned} \tag{B.10}$$

Fourth-order cumulants:

$$\begin{aligned}
n \cdot \mathrm{Var}\left(\widehat{\left\langle P^4\right\rangle_\mathrm{c}}\right) = {}& \left\langle P^8\right\rangle_\mathrm{c} + 16 \left\langle P^6\right\rangle_\mathrm{c} \left\langle P^2\right\rangle_\mathrm{c} + 48 \left\langle P^5\right\rangle_\mathrm{c} \left\langle P^3\right\rangle_\mathrm{c} \\
&+ 34 \left\langle P^4\right\rangle_\mathrm{c}^2 + 72 \left\langle P^4\right\rangle_\mathrm{c} \left\langle P^2\right\rangle_\mathrm{c}^2 \\
&+ 144 \left\langle P^3\right\rangle_\mathrm{c}^2 \left\langle P^2\right\rangle_\mathrm{c} + 24 \left\langle P^2\right\rangle_\mathrm{c}^4 .
\end{aligned} \tag{B.11}$$

Acknowledgements

Firstly, I would like to express my gratitude to my supervisors, whose invaluable guidance and support have been instrumental throughout my PhD study. I extend my heartfelt thanks to Prof. Dr. Yifei Zhang, my supervisor at USTC. From my undergraduate studies to my doctoral research, he has been a steadfast mentor, guiding me through the complexities of the field and igniting my scientific curiosity. His unwavering support has been crucial in shaping my academic journey and fostering my research skills. I am also profoundly grateful to Prof. Dr. Nu Xu, who has been an exceptional advisor throughout my doctoral research. His profound expertise and extensive guidance have been immensely beneficial, with his constructive feedback and insightful discussions making significant contributions to the advancement of this research.

Additionally, I deeply appreciate Prof. Dr. ShinIchi Esumi, my supervisor during my exchange period at University of Tsukuba. Over the past two years, his detailed discussions and constructive feedback have greatly enhanced my research. His guidance and support during my time abroad have been crucial to my academic growth. I would also like to thank other STAR members at Tsukuba, Prof. Dr. Takafumi Niida, Prof. Dr. Toshihiro Nonaka and Prof. Dr. Takahito Todoroki, for their important suggestions on my research. My gratitude extends to Moe Isshiki and Kosuke Okubo for providing substantial help with my studies and daily life abroad. I also wish to acknowledge CSC for the scholarship covering my expenses while in Japan.

Furthermore, I would like to thank the members of the STAR High Moment Group for their constructive discussions on this analysis throughout the past few years. I have greatly benefited from the invaluable advice and collaborative support provided by Prof. Dr. Nu Xu, Prof. Dr. Xin Dong, Prof. Dr. ShinIchi Esumi, Prof. Dr. Xiaofeng Luo, Prof. Dr. Bedangadas Mohanty, Prof. Dr. Toshihiro Nonaka, Dr. Ashish Pandav, Dr. Yu Zhang, Yige Huang, Bappaditya Mondal, Zachary Sweger, Yongcong Xu and Xin Zhang.

I would also like to thank the staff and students of the USTC group. My appreciation goes to Prof. Dr. Cheng Li, Prof. Dr. Ming Shao, Prof. Dr. Zebo Tang, Prof. Dr. Yongjie Sun, Prof. Dr. Wangmei Zha, Dr. Xiaozhi Bai, Dr. Kun Jiang, Dr. Shenghui Zhang, Dr. Zhen Liu, Dr. Xiaolong Chen, Dr. Yuanjing Ji, Dr. Pengfei Wang, Dr. Ziwei Li, Dr. Xinjian Wang, Dr. Jian Zhou, Dr. Yang Li, Dr. Ziyang Li and Dr. Kaifeng Shen for their guidance on my studies. I also extend my thanks to Xinyue Ju, Yitao

Wu, Tianqi Hu, Xiujun Li, Zheng Liang, Pengzhong Lu, Yuan Su, Junchao Wang, Yan Wang, Xin Wu, Kaiyang Wang, Senjie Zhu, Guangsheng Li, Xinbai Li, Zhenjun Xiong, Dongsheng Li, Yulou Yan, Yuan Zhang, Qiyan Cai and others.

Special thanks to the RHIC operation team and the STAR Collaboration for their successful work in completing the collection of invaluable experimental data.

Finally, I would like to express the deepest thanks to my family. Their unwavering understanding, support, encouragement and companionship have been my greatest source of strength throughout this journey. Their belief in me has been a constant motivation and has made this achievement possible.

Publications and Presentations

Papers

1. Charm and beauty isolation from heavy flavor decay electrons in p+p and Pb+Pb collisions at $\sqrt{s_{\mathrm{NN}}} = 5.02$ TeV at LHC
   Dongsheng Li, **Fan Si** (co-first), Yidan Zhao, Pengyu Zhou, Yifei Zhang, Xiujun Li, Chengxi Yang
   Physics Letters B 832, 137249 (2022), arXiv:2110.08769 [nucl-ex]
2. Statistical uncertainty estimation of higher-order cumulants with finite efficiency and its application in heavy-ion collisions
   Fan Si, Yifei Zhang
   Physical Review C 105, 024907 (2022), arXiv:2111.00238 [nucl-th]
3. Effect of non-uniform efficiency on higher-order cumulants in heavy-ion collisions
   Fan Si, Yifei Zhang, Xiaofeng Luo
   Chinese Physics C 45, 124001 (2021), arXiv:2105.13128 [physics.data-an]
4. Charm and Beauty Separation from Heavy Flavor Electron Measurements at RHIC
   Fan Si, Xiaolong Chen, Shenghui Zhang, Yifei Zhang
   Nuclear Physics Review 37(3), 684–689 (2020)
5. Charm and beauty isolation from heavy flavor decay electrons in Au+Au collisions at $\sqrt{s_{\mathrm{NN}}} = 200$ GeV at RHIC
   Fan Si, Xiao-Long Chen, Long Zhou, Yi-Fei Zhang, Sheng-Hui Zhang, Xin-Yue Ju, Xiu-Jun Li, Xin Dong, Nu Xu
   Physics Letters B 805, 135465 (2020), arXiv:1906.08974 [nucl-ex]
6. Temperature Fluctuation and the Specific Heat in Au+Au Collisions at Collision Energies from 5 to 200 GeV
   Xiujun Li, **Fan Si**, Zebang Fu, Yifei Zhang
   Nuclear Physics Review 36(4), 395–399 (2019)

Notes

1. Precision measurement of net-proton number fluctuations in Au+Au collisions at RHIC

Xin Dong, ShinIchi Esumi, Yige Huang, Xiaofeng Luo, Bedanga Mohanty, Bappaditya Mondal, Toshihiro Nonaka, Ashish Pandav, **Fan Si**, Nu Xu, Yifei Zhang, Yu Zhang (alphabetically)
STAR Note PSN0833

Presentations

1. Talk, "Precision Measurement of Net-proton Number Fluctuations in Au+Au Collisions at RHIC", iHIC 2024 — 2nd Symposium on Intermediate-energy Heavy Ion Collisions, Jul. 12–16, 2024, Beijing, China.
2. Talk, "Fluctuation measurements at RHIC-STAR", WHBM 2023 — Workshop on Highly Baryonic Matter at RHIC-BES and Future Facilities, Apr. 29–30, 2023, Tsukuba, Japan.
3. Poster, "Data-driven isolation for charm and beauty decay electrons at RHIC and LHC", 13th Conference on Particle Physics in China, Aug. 16–19, 2021, Qingdao, China (online).
4. Talk, "Data-driven isolation for charm and beauty decay electrons at RHIC and LHC", QPT 2021 — 14th Workshop on QCD Phase Transition and Relativistic Heavy-Ion Physics, Jul. 26–30, 2021, Guiyang, China.
5. Poster, "Charm and beauty isolation in heavy flavor electron measurements in Au+Au collisions at $\sqrt{s_{\mathrm{NN}}} = 200$ GeV at RHIC", Quark Matter 2019 — XXVIIIth International Conference on Ultra-relativistic Nucleus-Nucleus Collisions, Nov. 3–9, 2019, Wuhan, China.
6. Talk, "Charm and beauty isolation in heavy flavor electron measurements at RHIC", CNPC 2019 — 17th Conference on Nuclear Physics in China, Oct. 8–12, 2019, Wuhan, China.
7. Talk, "Charm and beauty isolation in heavy flavor electron measurements in Au+Au collisions at $\sqrt{s_{\mathrm{NN}}} = 200$ GeV at RHIC", QPT 2019 — 13th Workshop on QCD Phase Transition and Relativistic Heavy-Ion Physics, Aug. 16–20, 2019, Enshi, China.